UNIVERSITÀ DEGLI STUDI DI MILANO

DIPARTIMENTO DI CHIMICA

PhD Course in Chemistry

XXXV Cycle

VISIBLE LIGHT SENSITISED WO_3–BASED PHOTOANODES FOR SOLAR ASSISTED WATER OXIDATION

Chiara Nomellini

Matr. R12587

Supervisor – Prof. Elena Selli

Co-supervisor – Prof. Maria Vittoria Dozzi

PhD Course Coordinator – Prof. Daniele Passarella

Anno Accademico 2021-2022

Table of contents

Abstract

The need for stable, storable, accessible and renewable forms of energy has been insistently growing in the last decades, along with the concern about the ongoing climate changes connected to the extensive use of fossil fuels. The efficient exploitation of solar energy, that strikes the Earth's surface with a great amount of energy everyday, is a promising, though challenging, approach to the problem, with hydrogen produced from solar energy using photoelectrochemical water splitting representing an encouraging alternative.

This PhD thesis aims at contributing to deepening the knowledge of the working principles and intrinsic characteristics of photoanode materials, responsible for driving the water oxidation reaction, the kinetic bottleneck of overall water splitting. Focus of the work is the study of photoactive metal oxide-based materials, such as tungsten trioxide (WO_3), its ternary oxide derivative copper tungstate ($CuWO_4$) and bismuth vanadate ($BiVO_4$), which are among the most promising materials to be employed for these scopes.

Most of the experimental work here presented has been conducted at the UniMi Photocatalysis Group of the Università degli Studi di Milano, Italy, under the supervision of prof. Elena Selli; a fruitful collaboration with the group of prof. Sixto Giménez at the INAM Institute of the Universitat Jaume I of Castellón de la Plana, Spain, has led to the results outlined in Chapter 7 and partially in Chapter 5.

The present PhD thesis is organized as follows.

Chapter 1 presents an introduction to the grounds and aims at the origin of the work. An outline on the global energy demand and consumptions is drawn, evidencing that fossil fuels still represent the most widely used energy source. A brief description of the new, emerging renewable energy sources is presented, with a more detailed view on the hydrogen fuel, in particular on that produced from solar assisted water splitting.

Chapter 2 aims at giving the theoretical principles at the basis of photoelectrochemical water splitting. The main category of photocatalysts, *i.e.,* metal oxide semiconductors, is presented along with their physico-chemical properties. The peculiar characteristics that make them suitable photoactive systems for driving the water oxidation reaction are highlighted. Finally, the working mechanism and the requirements of combined tandem PEC cells are illustrated.

Chapter 3 is dedicated to both the experimental and theoretical methods, as well as the synthetic and characterization techniques, that have been used throughout my PhD for producing and interpreting the data presented in this thesis. A careful description of the employed experimental set ups, located in the laboratories of both prof. Selli and prof. Giménez, is also reported.

Chapter 4 starts with the description of the experimental work carried out during my studies, which was firstly focused on copper tungstate, a ternary oxide deriving from the more investigated tungsten oxide, which is characterized by a relatively smaller band gap enabling its sensitisation towards the visible portion of the solar spectrum. For the first time, the effects on photoactivity induced by doping this material with nickel ions have been systematically investigated and demonstrated by means of multiple physical and photoelectrochemical methods.

Chapter 5 deals with the study of the well-known WO_3–$BiVO_4$ heterojunction, a system combining two of the most promising photoanode materials. My work was focused on disclosing the effects on the overall performance of the composite material induced by selectively tuning the morphology of the tungsten oxide underlayer. WO_3 and WO_3–$BiVO_4$ photoanodes characterized by either a planar or a nanostructured morphology have been synthetized and multiple experimental techniques have been applied to ascertain the intrinsic

characteristics as well as the photoelectrochemical performances of the so obtained photoactive materials layers.

Chapter 6 is focused instead on the role played by the thickness of either the WO_3 and the $BiVO_4$ layer and their reciprocal balance in tuning the overall efficiency of the WO_3–$BiVO_4$ composite systems. Multiple heterojunction samples displaying a planar morphology have thus been systematically prepared by varying both the under- and the overlayer thicknesses. The thorough screening of these photoelectrodes allowed an in-depth investigation of the mechanisms of photocurrent generation, and in particular on the detrimental charge recombination paths which can be activated when varying the thicknesses of the two oxides.

Chapter 7 is dedicated to the characterization of the photoanodes presented in Chapter 6 by means of two advanced techniques: Electrochemical Impedance Spectroscopy (EIS) and Spectroelectrochemical (SEC) analyses. These techniques provide information on the charge storage and charge transfer mechanisms occurring in the WO_3–$BiVO_4$ heterojunction, in comparison with single-component samples. Additional insight was thus obtained into the role exerted by the metal oxides thickness on the overall behaviour of the composite photoanodes.

Finally, Chapter 8 provides an overview of the results discussed in this thesis, as well as the future perspectives of each investigated research line.

.

Chapter 1 - Renewable and solar energy sources

1.1 World energy consumption

At the beginning of the 1990s the increasing concern of the scientific community on the potential consequences of the arising climate change led the United Nations to create a secretariat dedicated to monitoring and battling the increase of the global mean temperature, the United Nations Framework Convention on Climate Change (UNFCCC). The first significant achievement of this panel was the agreement that led to the Kyoto protocol signed in 1995, in which the joining parties agreed to decrease their emissions of greenhouse gases by 5%.[1] Another historical agreement was signed in 2015, when 196 state parties negotiated and successively adopted the Paris Agreement, dealing with greenhouse gas emission mitigation and adaptation. The long-term goal of this treaty was to keep the increase in global average temperature below 2°C with respect to its pre-industrial level and to limit it to 1.5°C.[2] To reach this ambitious goal the signatory countries should drastically decrease their emissions and reach, by 2050, zero net emissions. The achievement of this goal soon proved to be extremely challenging, considering how vast the use of fossil-based fuels is, even today.

The theory of the greenhouse effect has been first formulated at the beginning of the 19th century, while the role of human activities in increasing greenhouse gas concentration has come under scrutiny only more than a century later, in the late 1950s, when the first monitoring of atmospheric carbon dioxide concentrations began.[3] Serious scientific interest in man's impact on global climate and the possible impacts of these changes on society where brought to public debate through conferences, research networks and assessments, particularly from 1970 onwards.

The concentration of carbon dioxide in the atmosphere has increased from approximately 277 parts per million (ppm) in 1750, at the beginning of the Industrial Era, to *ca.* 400 ppm in 2018.[4] The atmospheric CO_2 increase above pre-industrial levels was, initially, primarily caused by the release of carbon deriving from deforestation and other land use activities. While CO_2 emissions from fossil fuel use started before the Industrial Era, they became the dominant source of anthropogenic emissions only from 1950. Anthropogenic emissions occur on top of an active carbon cycle that drives carbon circulation between carbon reservoirs (atmosphere, oceans, biosphere) on timescales ranging from days to millennia.[5]

Recent researches have established a near-proportional relationship between global mean surface air temperature change and cumulative CO_2 emissions,[6,7] and the consequences of the rapid increase in carbon dioxide concentration are evident, as shown in **Figure 1.1**.

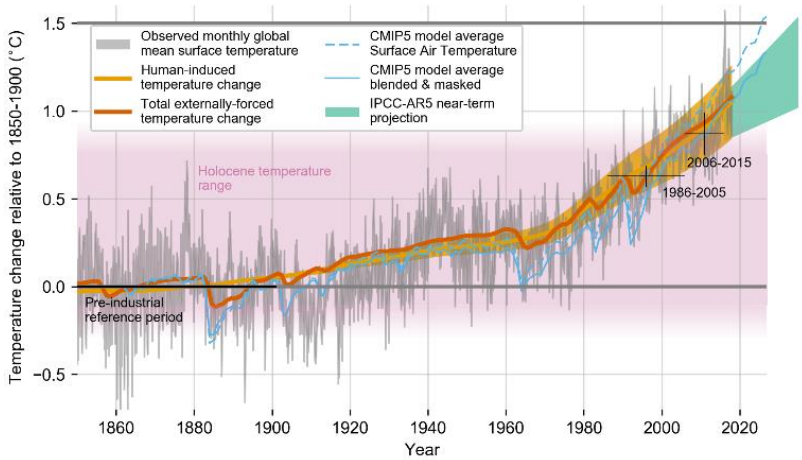

Figure 1.1 Evolution of global mean surface temperature (GMST) from 1850 to 2020. Human-induced (yellow) contributions to these GMST changes are highlighted. Figure taken from ref. 8.

Primary energy consumption has continued to rise year after year, reaching a peak of almost 600 Exajoules (10^{18} J) in 2019, with a lower rate consumption increase in most recent years. By observing the shares of energy sources to the global consumption (**Figure 1.2**), oil continues to hold the largest share of the energy mix, accounting for 33%, while coal is the second largest employed fuel with a share of 27%, even if this is its lowest recorded share since 2003. Natural gas (24%) and renewable energies (5%) are undergoing a rise in their share, while hydroelectricity has been stable for several years. In particular, in 2019 the growth in energy consumptions was driven by renewables, followed by natural gas, which together contributed to over three quarters of the net increase, reaching record values. The combination of slower growth in energy demand and a shift in the fuel mix away from coal and toward natural gas and renewables led to a significant slowdown in the growth of carbon emissions, that rose only by 0.5% in that year.

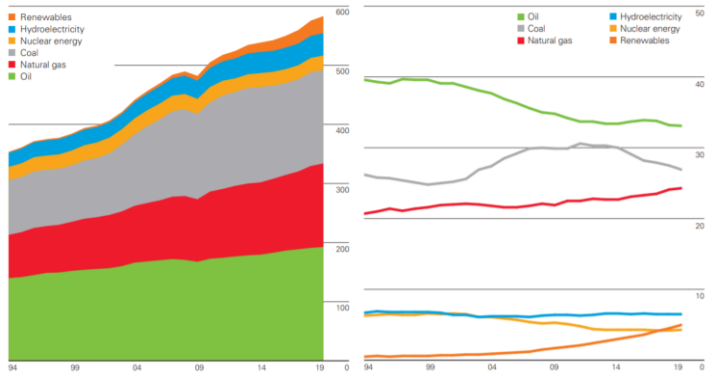

Figure 1.2 World energy consumptions in Exajoules (10^{18} J) and percent shares of global energy from 1994 to 2019. Figure taken from ref. 9.

Improving energy efficiency and reducing the energy demand are considered key mechanisms for limiting climate change. However, there are practical limitations associated with the constantly growing global population and, moreover, with the growing global economy of emerging countries.[10,11] At the global level, the correlation between increased wealth and increased energy consumption is indeed very strong.

Another fundamental solution to the ever-growing concerns on global warming, air pollution, and energy supply is to replace the current carbon-rich fossil fuels with renewable and environmentally friendly carbon-free or carbon-neutral energy sources. During the year 2020, commitments towards climate action greatly increased, with more than 20 countries

and the European Union committing to greenhouse gas emission reduction targets. These goals can be achieved only by simultaneously reducing energy demand and by switching energy consumption towards renewable energy sources.

1.2 Renewable energy sources

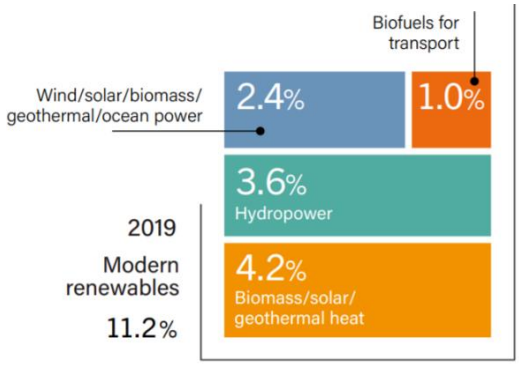

Figure 1.3 Estimated renewable share of total final energy consumption in 2019. Figure taken from ref. 12.

As of 2019, modern renewable energy accounted for an estimated 11.2% of the total final energy consumption, which rose from 8.7% one decade ago, *i.e.*, in 2009,[12] as **Figure 1.3** depicts. In 2020, despite the impacts of the global COVID-19 pandemic, renewable energy set a record in new power capacity, that reached its highest recorded share in the global electricity mix, accounting for 29%. Moreover, the costs of producing electricity from wind and solar energy have dropped significantly in recent years.

Renewable technologies are considered as clean sources of energy and an optimal use of these resources could minimize environmental impacts, produce minimum secondary wastes, and are considered sustainable based on current and future economic and social needs. Sun is the source of the entire class of these energies, the primary forms of solar energy being heat and light. Sunlight and heat are then transformed and absorbed by the environment in a multitude of ways; some of these transformations result in renewable energy sources such as biomass and wind energy. Renewable energy technologies provide an excellent opportunity for greenhouse gases emission mitigation and global warming reduction via substituting conventional energy sources. Renewable energy sources (RES) include biomass, hydropower, geothermal, solar, wind and marine energies. RES are the primary, domestic and clean or inexhaustible energy resources.

Hydropower is an essential energy source harnessed from water moving from higher to lower elevation levels, primarily to turn turbines and generate electricity. The primary

energy is provided by gravity and the height from which the water falls down on to the turbine and the potential energy of the stored water is given by the mass of the water and the gravity factor. Hydropower discharges practically no particulate pollution, can upgrade quickly, and it is capable of storing energy for many hours.[4]

Among the renewable energy technologies applied to electricity generation, **wind energy** ranks second only to hydroelectric in terms of installed capacity and is experiencing rapid growth. Today, wind energy for electricity production is a mature, competitive, and virtually pollution-free technology widely used in many areas of the world. Wind technology converts the energy available in wind to electricity or mechanical power through the use of wind turbines. The working mechanism of a wind turbine consists in the conversion of the motion of the wind into rotational energy that can be used to drive a generator. Wind turbines capture power from the wind by means of aerodynamically designed blades and convert it into rotating mechanical power.[13]

The term **biomass energy** refers to any source of energy produced from non-fossil biological materials. Biomass energy can come from ocean and freshwater habitats as well as from land. Biomass energy ranges from firewood to ethanol produced from corn or sugarcane, to methane captured from landfills. Although much of the recent debate on biomass energy has focused on ethanol, biodiesel and other liquid transportation fuels, the opportunities for biomass to become a source of direct combustion fuel are promising. With appropriate technologies, burning compacted biomass energy pellets as a heat source might be the most efficient commercial use of biomass energy.[14]

The estimation of the energy reserves available on earth demonstrates the dominant position of solar energy among all renewable and non-renewable energy sources.[15] The total sum of recoverable energy from all reserves is around 1% of the solar energy supplied to the earth surface by the sun in one year. Moreover, given that the same amount of energy from sunlight strikes the earth in 1 hour ($4.3 \cdot 10^{20}$ J) than all of the energy currently consumed on the planet in 1 year,[16,17] many studies are focused on how to capture, convert and store this type of energy in a cost-effective fashion.

1.2.1 Solar energy and solar fuels

Sunlight is a clean and renewable energy source that provides our planet with an intense flux of highly energetic photons, that can promote uphill reactions such as the photosynthetic fixation of CO_2 in biological systems. Solar energy, unlike fossil fuels, is present in all parts of the planet, even if with significant differences depending on the latitude. Since the Sun will continue to shine for billions of years, solar energy is inexhaustible on human time scale.[18] The spectrum of the Sun's solar radiation (**Figure 1.4**) is close to that of a black body, emitting radiation across most of the electromagnetic spectrum, with wavelengths ranging between 10^{-5} and 10^{5} nm. Before reaching the earth's surface, a part of the emitted light is absorbed by the stratosphere, the ozonosphere, and other different atmospheric layers; approximately, 40% of the radiation arriving to the earth reaches its surface. The radiation at sea level is composed of 5% ultraviolet light (with wavelength λ ranging from 280 to 400 nm), 50% of visible light (with λ from 400 to 900 nm), the remaining portion consisting in infrared and longer wavelength light (λ from 900 up to 4000 nm).

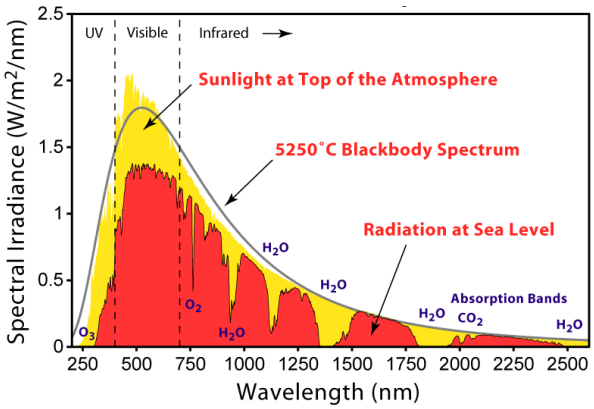

Figure 1.4 Solar emission spectra at the outside atmosphere and at sea level. Figure taken from ref. 19.

Since the solar spectrum at sea level can vary due to latitude or atmospheric conditions, scientific investigations dealing with solar light have to guarantee compliance with international standards, ensuring reproducibility of the light source employed in the experiments. The AM1.5G spectrum, which has been used in this thesis as the standard solar irradiation source, has been calculated from the reference AM0 solar spectrum (Air Mass zero, *i.e.*, the solar spectrum measured outside the Earth's atmosphere) under representative geometric and atmospheric conditions, which are: *i)* an air mass of 1.5 (condition in which

the Sun is about 41° above the horizon), *ii)* a cell tilted by 37° from the horizon, *iii)* the spectrum includes the surrounding ground (sky and ground), and for this reason it is called global, *iv)* the atmospheric conditions are from the US standard atmosphere, *v)* the haziness of a sunny clear day is considered, *vi)* the total irradiance is 100 mW/cm^2.[20] This spectrum is a good representative of the illumination conditions on a tilted flat plate array on a clear day without clouds near noon in the geographical mid latitudes.

The important advantages presented by solar energy exploitation are however mitigated by two relevant drawbacks: solar energy has a relatively low intensity, and it is intermittent on a local scale; this intermittence is mainly related to the dependence on weather conditions, as well as the alternation between day and night. Due to these limitations, to be a material contribution to primary energy supply, solar energy must be captured, converted, and stored. There are several technologies available for solar energy utilization, mainly represented by solar thermal energy, photovoltaics (PV) and solar fuels.

Solar thermal energy is composed by a group of technologies for harnessing solar energy to generate thermal energy for use in industry as well as in the residential and commercial sectors. Solar thermal collectors are classified as low-, medium-, or high-temperature collectors, and are employed in various fields.

Today, **photovoltaics** represents the most widely disseminated solar-based technology and is one of the fastest growing industries. Direct solar energy conversion to electricity is conventionally done using photovoltaic cells, which make use of the photovoltaic effect. The PV effect depends on the interaction of photons, with energy equal or greater than the band gap of PV materials. Some of the losses due to the band-gap limitations are avoided by combining semiconductors of different band gaps. However, solar energy has low energy density: PV modules require a large surface area for small amounts of energy generation.[13] Moreover, PV produces electricity, which has an intrinsic difficulty in terms of storage. Considering the intermittent nature of solar energy, converting solar energy into easily storable chemical energy or a fuel has emerged as an ideal option of solar energy utilization.

Arguably the most attractive method for this energy conversion and storage is in the form of chemical bonds, by production of cheap **solar fuels**. The conversion of abundant energy-poor molecules to energy-rich molecules using sunlight as energy source is one of the

biggest challenges of the twenty-first century. It is urgent to replace fossil fuels with solar fuels such as hydrogen from water, or methanol from water and carbon dioxide,[21] thus capturing and converting solar energy into chemical bonds.

To produce renewable fuels, energy must be harvested in a renewable way and used to convert simple building blocks, such as H_2O and CO_2, into liquid or gaseous fuels. Four main categories of solar fuels exist, each consisting of multiple options, characterized by different stages of development, efficiency, and cost. The first category is concentration: solar light is concentrated to generate heat, which can be used in thermal conversion processes or for electricity generation. Transformation consists in renewable energy being transformed into electricity, which is used to drive electroconversion processes such as electrolysis. Natural photosynthesis refers to natural biosystems that are able to transform H_2O, CO_2, and light into biomass, which subsequently can be converted into fuels, chemicals, heat, or electricity. Lastly, artificial photosynthesis includes a collection of direct but non-bio based conversion processes, which use photoactive materials that capture sunlight and thereby drive a photoconversion process in an artificial leaf, a photoelectrochemical cell, or employing photocatalytic powders.[22–24]

Examples of chemical fuels include hydrogen, methane, methanol, gasoline, diesel, etc. Except for hydrogen, all of these examples require a carbon source. While CO_2 is an obvious candidate in view of the environmental concerns discussed in **Section 1.1**, capturing CO_2 from the atmosphere has a huge entropic cost because of its dilute nature. Fossil fuel-based power plants seem attractive point-sources of highly concentrated CO_2, but if the ultimate goal is to completely avoid the use of fossil fuels this route couldn't be pursued. Direct photochemical conversion of CO_2 to a fuel seems to be even more challenging,[25] as the electrochemical half-reactions for the conversion of CO_2 to, *e.g.*, methanol or methane, involve complex six- and eight-electron transfer steps, respectively. Based on these considerations, the conversion of solar energy into hydrogen appears to be by far a much more attractive route.

1.3 Hydrogen as future fuel

Hydrogen is the lightest, simplest, and most plentiful of all chemical elements in the universe. However, it occurs only in combination with other elements, primarily with oxygen in water and with carbon, nitrogen, and oxygen in living materials and fossil fuels. Hydrogen is very clean in terms of emissions at the point of use; in fuel cells it is combined with oxygen without generating CO_2, the only produced by-product being water.[26] Hydrogen fuel is a sustainable energy carrier that will play an large role in the world energy scenario, helping the reduction of carbon emissions from transportation and industrial sectors; hydrogen is hence regarded by many as the fuel of the future. With the highest mass energy density of any other fuel and its clean combustion in air, hydrogen could be considered as the ultimate clean energy carrier. However, the realisation of a largely hydrogen-based renewable energy solution – the hydrogen economy – heavily depends on the development of cost-effective, green production technologies. For instance, the US Department of Energy stated that the price of hydrogen must reach 4 US$ kg^{-1} (including production, delivery and dispensing) before it can become competitive as an alternative to gasoline to be used in passenger vehicles.[27]

The most important industrial route of hydrogen production consists in the catalytic steam-reforming of hydrocarbons, involving the treatment of gaseous or vaporized hydrocarbons with steam at high temperature (650–950 °C) and high pressure (15–40 bar) over nickel-based catalysts.[28,29] Indeed, almost all hydrogen production is still based on raw fossil materials and only 4% is produced via water electrolysis. In view of the different hydrogen production pathways, hydrogen sources can be divided into different categories. *Grey hydrogen* mostly results from industrial by-products and its energy source is mainly composed of fossil fuels; moreover, the hydrogen production process is accompanied by carbon dioxide production and emission. In a modified *grey hydrogen* production method, if the carbon dioxide by-product can be captured, used, or stored, preventing pollution, then the resultant process is defined as *blue hydrogen* production. If H_2 is obtained through renewable energy sources, such as wind energy, solar energy, biomass energy and other green sources, then it is classified as *green hydrogen*.[17] Driven by the current growing concern about global climate change, efforts have been made to develop new alternative and environmentally friendly hydrogen sources, such as its photoelectrocatalytic production from natural resources such as water and solar energy.

1.3.1 Hydrogen from photoelectrochemical water splitting

Photoelectrochemical water splitting is based on the principles of heterogeneous catalysis, in which a solid material, usually a semiconductor, interacts with an incident radiation and increases the rate of a chemical reaction. This field of research has been the object of intense research efforts since 1972, year in which the photocatalytic splitting of water on TiO_2 electrodes has been discovered by Fujishima and Honda.[30]

PEC water splitting is usually carried out in a photoelectrochemical cell by two separate electrodes (that catalyse the two semi-reactions that compose the overall water splitting process), immersed in an electrolyte. One of the main advantages of this approach is that hydrogen and oxygen are produced at separate electrodes. This avoids serious safety concerns and allows the easy separation of these gases. A second advantage is that it can be carried out at room temperature, *i.e.*, there is no need for large-scale solar concentrators that would limit its application to large central facilities in sunny regions of the world. A third advantage is that a photoelectrochemical water splitting device can be constructed entirely from inorganic materials. This offers a degree of chemical robustness and durability that is difficult to achieve for organic or biological systems.

Solar energy driven water splitting decomposes water into its two main components:

$$2H_2O + h\nu \longrightarrow 2H_2 + O_2 \qquad E^0 = -1.23\,V \tag{1.1}$$

The overall electrochemical reaction of water splitting consists of both reduction and oxidation half-reactions (reaction potentials are reported against the reversible hydrogen electrode, RHE):

$$\begin{aligned} 2H^+ &\longrightarrow H_2 && E^0 = 0\,V \\ O_2 + 4H^+ + 4e^- &\longrightarrow 2H_2O && E^0 = 1.23\,V \end{aligned} \tag{1.2}$$

Since the standard potential of the overall reaction (**Equation 1.1**) is negative, water splitting is an uphill reaction ($\Delta G^0 = 237$ kJ·mol^{-1}) and energy must be given to the system for water splitting to occur. While a difference in bias of only 1.23 V should be sufficient to split water into H_2 and O_2, due to the overpotential required to overcome kinetic issues of the oxygen and hydrogen evolution reactions and to the energy losses caused by the transport of

charges, modern alkaline electrolysers usually operate at voltages above 1.8 V.[31] For this reason, only photons with wavelengths shorter than 700 nm (which account for *ca.* 40% of the solar spectrum) have enough energy to drive the water splitting reaction. Moreover, the efficiency of the water splitting reaction is limited by the large overpotential of the oxygen evolution reaction (OER), while the hydrogen evolution reaction (HER) can proceed at potentials close to the equilibrium potential. In the OER four electrons must be extracted from two water molecules in a multielectron process that must allow the stabilization of oxidized intermediates. Additionally, the extraction of electrons must be counterbalanced with the removal of protons, to avoid the creation of excess charge. Finally, all of these processes must be carried out in a way that prevents the catalyst to be degraded.[32] The understanding and optimization of the oxygen evolution step is thus a great challenge for solar-to-hydrogen conversion.

1.3.1.1 Natural and artificial photosynthesis: the Z-scheme

The process of conversion of a water molecule into chemical energy, in terms of hydrogen bonds, is the attempt of replicating one of the photosynthesis processes occurring in green plants.[33] Solar-to-chemical energy conversion is performed by plants through natural photosynthesis (NPS), in which oxygen and carbohydrates are produced from water and carbon dioxide using sunlight. The energy conversion efficiency of NPS can reach *ca.* 7% under optimum conditions. A potentially more controlled technology for the solar-to-chemical energy conversion process is artificial photosynthesis (APS), which aims to emulate NPS using man-made materials. Photosynthetic reactions are determined primarily by three reaction processes: light-harvesting processes, charge generation and separation processes, and catalytic reaction processes. The overall efficiency is determined by the balance of thermodynamics and kinetics of these steps. The light reaction of NPS occurs via a series of gradual electron transfer processes that create sufficient energy for water-splitting, known as the 'Z-scheme', depicted in **Figure 1.5**; two photosystems – photosystem I (PS I) and photosystem II (PS II) – collect light energy through an assembly of light-harvesting chlorophylls and pump electrons to a higher electronic state.[24,34]

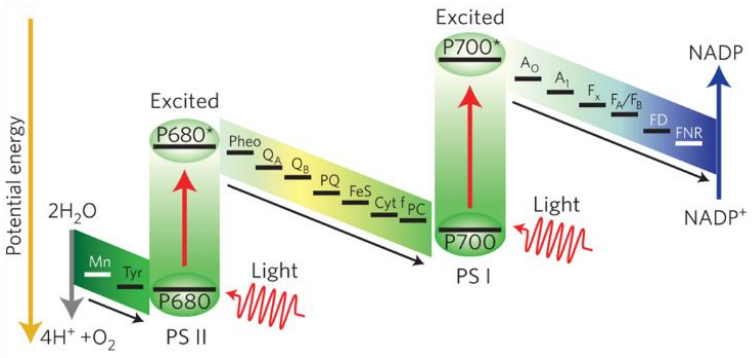

Figure 1.5 NPS charge-separation processes, including type I and II reaction centres (simplified Z-scheme). Figure taken from ref. 24.

At the donor side of PS II the water oxidation reaction occurs, yielding O_2. These processes ensure that the charge separation quantum efficiency is close to 100% under optimal conditions.

The Z-scheme mechanism which is behind NPS is mimicked in artificial photosynthesis by the two-step process depicted in **Figure 1.6**, in which two distinct photocatalysts drive the water oxidation and the hydrogen generation reaction, acting as **photoanode** and **photocathode**, respectively. As mentioned earlier in this section, the two photocatalysts are usually semiconductors, which can indeed absorb solar photons with energy greater than their band gap energy ($h\nu > E_g$); the solid-light interaction then leads to the excitation of an electron that is promoted to the conduction band (CB), leaving a hole in the valence band (VB) of the material.[35,36] These photogenerated charge carriers can thus take part into oxidation and reduction reactions, and the energy diagrams describing the working principles of a photoanode and a photocathode in the overall splitting of water are described in **Figure 1.6**. The oxidation of a water molecule by the photoanode (left-side of the image) can occur only if the top of the VB is more positive in energy with respect to the oxidation potential of H_2O to O_2. At the same time, a photocathode (right-side) can reduce protons only if the bottom of its CB is more negative than the reduction potential of H^+ to H_2.

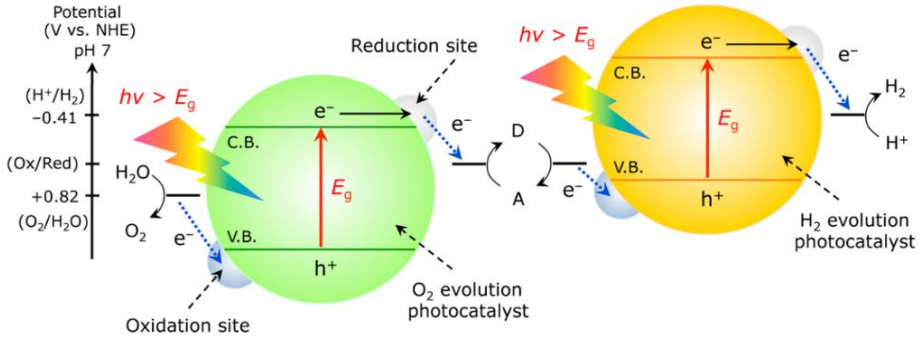

Figure 1.6 Schematic energy diagram of APS water splitting for a two-step (Z-scheme) photoexcitation system. Figure taken from ref. 37.

Another approach applied to the photocatalytic splitting of water consists in carrying out the two semi-reactions on the surface of a single photocatalyst, characterized by VB and CB energy levels that straddle the water oxidation and proton reduction potentials. However, finding a semiconductor that meets these energy levels requirements and, at the same time, is characterized by a relatively small band gap energy that allows a good absorption of the visible range of the solar spectrum is an extremely challenging task.[37,38]

As the water splitting process is a challenging route to generate hydrogen, a lot of research has been focused, in the last years, on developing novel materials to be employed as photocatalysts. These materials have to meet numerous features, such as absorption curves peaked around desired wavelengths, efficient separation of the generated electron-hole pairs and a fast water splitting reaction kinetics. Moreover, from a practical standpoint and for a cost-effective and sustainable implementation, issues such as cost, abundance, low-toxicity and long-term stability in water and under strong illumination must be addressed.[38,39] As already mentioned, the materials that meet these requirements and are thus employed for photocatalytic water splitting applications are semiconductors, and particularly transition-metal oxides. The characteristics of this class of materials and their behaviour under illumination and in contact with an electrolyte in a photoelectrochemical cell will be described in detail in the following chapter.

References

1. UNFCCC, Kyoto Protocol, **1997**. treaties.un.org.
2. UNFCCC, Paris Agreement, **2015**. unfccc.int.
3. S. Agrawala, *Clim. Change* 39 (**1998**) 605–620.
4. P.A. Owusu, S. Asumadu-Sarkodie, *Cogent Eng.* 3 (**2016**) 1167990.
5. C. Le Quéré, L. Barbero, J. Hauck, R.M. Andrew, J.G. Canadell, S. Sitch, J.I. Korsbakken, *Earth Syst. Sci. Data* 11 (**2019**) 1783–1838.
6. M.R. Allen, D.J. Frame, C. Huntingford, C.D. Jones, J.A. Lowe, M. Meinshausen, N. Meinshausen, *Nature* 458 (**2009**) 1163–1166.
7. H.D. Matthews, N.P. Gillett, P.A. Stott, K. Zickfeld, *Nature* 459 (**2009**) 829–832.
8. IPCC, Global Warming of 1.5°C, **2018**. ipcc.ch.
9. BP plc, Statistical Review of World Energy, **2020**. bp.com.
10. G. Semieniuk, L. Taylor, A. Rezai, D.K. Foley, *Nat. Clim. Chang.* 11 (**2021**) 313–318.
11. S. Sorrell, *Renew. Sustain. Energy Rev.* 47 (**2015**) 74–82.
12. REN21, Renewables 2021 Global Status Report, **2021**. ren21.net.
13. N.L. Panwar, S.C. Kaushik, S. Kothari, *Renew. Sustain. Energy Rev.* 15 (**2011**) 1513–1524.
14. C.B. Field, J.E. Campbell, D.B. Lobell, *Trends Ecol. Evol.* 23 (**2008**) 65–72.
15. R. Perez, M. Perez, *Int. Energy Agency SHC Program. Sol. Updat.* 62 (**2015**) 4–6.
16. N.S. Lewis, *Sustain. Energy* 798 (**2013**) 798–802.
17. S.E. Hosseini, M.A. Wahid, *Int. J. Energy Res.* 44 (**2020**) 4110–4131.
18. M.G. Walter, E.L. Warren, J.R. McKone, S.W. Boettcher, Q. Mi, E.A. Santori, N.S. Lewis, *Chem. Rev.* 110 (**2010**) 6446–6473.
19. https://en.wikipedia.org/wiki/Sunlight.
20. American Society for Testing and Materials, Standard Tables for Reference Solar Spectral Irradiances: Direct Normal and Hemispherical for 37 ◦ Tilted Surface, **2003**.
21. H.B. Gray, *Nat. Chem.* 1 (**2009**) 7.
22. R.J. Detz, J.N.H. Reek, B.C.C. Van Der Zwaan, *Energy Environ. Sci.* 11 (**2018**) 1653–1669.
23. K. Sivula, *J. Phys. Chem. Lett.* 4 (**2013**) 1624–1633.
24. Y. Tachibana, L. Vayssieres, J.R. Durrant, *Nat. Photonics* 6 (**2012**) 511–518.

25. J. Kim, E.E. Kwon, *J. CO_2 Util.* 33 (**2019**) 72–82.

26. C. Acar, I. Dincer, *Int. J. Hydrogen Energy* 39 (**2014**) 1–12.

27. E.L. Miller, S.T. Thompson, K. Randolph, Z. Hulvey, N. Rustagi, S. Satyapal, *MRS Bull.* 45 (**2020**) 57–64.

28. H. Ahmad, S.K. Kamarudin, L.J. Minggu, M. Kassim, *Renew. Sustain. Energy Rev.* 43 (**2015**) 599–610.

29. J.D. Holladay, J. Hu, D.L. King, Y. Wang, *Catal. Today* 139 (**2009**) 244–260.

30. A. Fujishima, K. Honda, *Nature* 238 (**1972**) 37–38.

31. M.S. Prévot, K. Sivula, *J. Phys. Chem. C* 117 (**2013**) 17879–17893.

32. R. Elsenberg, H.B. Gray, *Inorg. Chem.* 47 (**2008**) 1697–1699.

33. P. Sharma, M.L. Kolhe, *Int. J. Hydrogen Energy* 42 (**2017**) 22704–22712.

34. J. Barber, P.D. Tran, *J. R. Soc. Interface* 10 (**2013**).

35. M.R. Hoffmann, S.T. Martin, W. Choi, D.W. Bahnemann, *Chem. Rev.* 95 (**1995**) 69–96.

36. B.D. Alexander, P.J. Kulesza, I. Rutkowska, R. Solarska, J. Augustynski, *J. Mater. Chem.* 18 (**2008**) 2298–2303.

37. K. Maeda, *ACS Catal.* 3 (**2013**) 1486–1503.

38. K. Maeda, K. Domen, *J. Phys. Chem. Lett.* 1 (**2010**) 2655–2661.

39. K. Sivula, R. Van De Krol, *Nat. Rev. Mater.* 1 (**2016**) 15010.

Chapter 2 – Principles of PEC water splitting

2.1 Semiconductors

A semiconductor is defined as a material whose conductivity increases as the temperature is risen. The electrical properties of a solid are determined by the distribution of its electrons; following the tight-binding approximation, the valence electrons of a solid are assumed to occupy the molecular orbitals which are delocalized throughout its structure.

Let's consider a one-dimensional solid composed of a single, infinitely long line of atoms and suppose that each atom has, for instance, one s orbital available to form molecular orbitals. We can build the linear combination of its atomic and molecular orbitals by adding N atoms to the previously described line. A single atom contributes to one s orbital at a certain energy. When a second atom is added, it overlaps the first and forms bonding and antibonding orbitals. The third atom overlaps its nearest neighbour and another molecular orbital is formed (one fully bonding, one antibonding and the third is a nonbonding orbital between the previous ones). By successively adding atoms, further orbitals are formed, spreading the range of energies covered by the molecular orbitals and filling the range of energies with more orbitals. When N atoms are added to the line, there will be N molecular orbitals covering a band of energies of finite width. The band formed by the overlap of s

orbitals is called *s band*; if the atoms also have *p* orbitals available, a *p band* will also be formed. If the atomic *p* orbitals lie higher in energy with respect to the *s* orbitals, the *p band* will lie higher in energy that the *s band*, forming a **band gap**, that is, a range of forbidden electron energies in which no orbital is present. The band lower in energy in then defined as the **valence band** (VB), while the higher energy one is the **conduction band** (CB).[1]

The occupation of these electronic states in a semiconductor is described by the Fermi-Dirac distribution (**Equation 2.1**), which indicates the population of the energetic levels at temperature T:[2,3]

$$f(\epsilon) = \frac{1}{1 + e^{(\epsilon-\mu)/k_B T}} \tag{2.1}$$

where μ is the chemical potential, that is, the free energy variation when one electron is added. The Fermi level (E_F) is the chemical potential at $T = 0\,K$ and it is defined as the energy level at which the probability of occupation by an electron is ½.[4] At 0 K, the valence band of a semiconductor is fully occupied by electrons, whereas the conduction band is empty, and the Fermi level lies in between the two bands (**Figure 2.1a**).

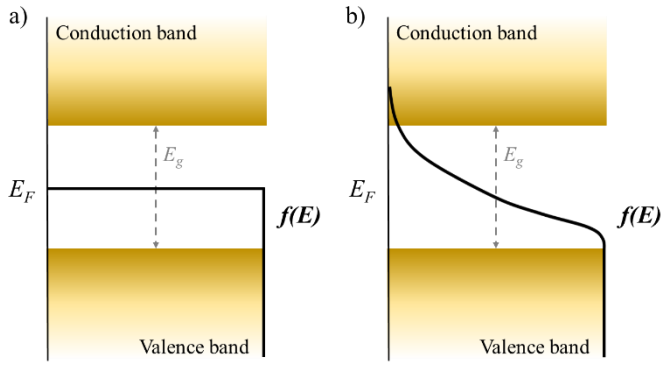

Figure 2.1 Fermi-Dirac distribution and chemical potential position in an intrinsic semiconductor at a) $T = 0$ K and b) $T > 0$ K.

If the temperature is increased the tail of the Fermi-Dirac distribution extends across the gap, and electrons can leave the lower band and populate the empty orbitals of the upper band, as shown in **Figure 2.1b**. Consequently, upon electron promotion, positively charged holes are left in the valence band. These holes and the promoted electrons can now move across the two bands, generating electrical conductivity. The definition of a semiconductor material is derived from this phenomenon, since the electrical conductivity depends on the

number of the electrons that are promoted across the band gap, and this number increases with increasing temperature.[3]

2.1.1 Intrinsic and extrinsic semiconductors

If we consider an ultrapure semiconductor that does not possess doping impurities (*i.e.*, an **intrinsic semiconductor**) at room temperature, few electrons can be thermally excited across the forbidden gap, leaving holes in the valence band. The concentration of electrons (n_e) and holes (n_h), which must be equal in these conditions, can be expressed in terms of the Fermi-Dirac probability function declined for the presence (f) or absence ($1-f$) of electrons, respectively:[5,6]

$$\begin{aligned} n_e &= \int_{\epsilon_c}^{+\infty} f(\epsilon)\rho_c(\epsilon)d\epsilon \\ n_h &= \int_{-\infty}^{\epsilon_v} (1-f(\epsilon))\rho_v(\epsilon)d\epsilon \end{aligned} \tag{2.2}$$

where $\rho_c(\epsilon)$ and $\rho_v(\epsilon)$ are the densities of states distributions or DOS (*i.e.*, the number of allowed electronic states per unit energy interval). As working conditions, we also assume that the chemical potential μ is placed in a position far enough from the bottom of the conduction band and from the top of the valence band. Under these conditions the fraction of carriers in both bands is small, since we are in a regime where just the tails of the Fermi-Dirac distribution are filling the bands. We can thus assume that $e^{(\epsilon-\mu)/k_BT} \gg 1$, and we can express f and $(1-f)$ as:

$$\begin{aligned} f(\epsilon) &\simeq e^{-(\epsilon_c-\mu)/k_BT} \\ 1-f(\epsilon) &\simeq e^{(\epsilon_v-\mu)/k_BT} \end{aligned} \tag{2.3}$$

By taking into consideration the expression of the density of states of conduction and valence band we can obtain the concentration of electrons in the CB:[7]

$$n_e = N_e \cdot e^{-(\epsilon_c-\mu)/k_BT} \tag{2.4}$$

where N_e is the effective density of states in the conduction band:

$$N_e = 2\frac{(2\pi m_c k_B T)^{3/2}}{h^3} \tag{2.5}$$

Here, m_c is the effective mass of the electron in the conduction band.

The same arguments can be applied to the concentration of holes, obtaining:

$$n_h = N_h \cdot e^{(\epsilon_v - \mu)/k_B T} \quad \text{with} \quad N_h = 2\frac{(2\pi m_h k_B T)^{3/2}}{h^3} \tag{2.6}$$

where N_h is the effective density of states in the valence band. It is worth noticing that the so-obtained density of carriers depends exponentially on temperature.

We can then write the mass action law, resembling an equilibrium between the two carriers and the vacuum condition ($O \rightleftharpoons e^- + h^+$). The equilibrium constant of this process is the product of the concentration of the two species:

$$n_e \cdot n_h = N_e \cdot N_h \cdot e^{-E_g/k_B T} \tag{2.7}$$

By taking the product of the two concentrations the chemical potential disappears from the expression and E_g is the energy gap between the two bands. This means that the concentration of the electrons and the concentration of the holes in the two bands are related to each other through a temperature-dependent factor. This law holds for any semiconductor material, with the only condition that the chemical potential must lie far enough from the two bands. The position of the chemical potential determines if there is an excess of holes with respect to electrons and vice versa, but their product is always given by **Equation 2.7**.

In an intrinsic semiconductor free of impurities, the concentration of electrons and holes is equal, *i.e.*, $n_e = n_h$. This means that the concentration of carriers is:

$$n_i = \sqrt{N_e \cdot N_h}\; e^{-(E_g/2k_B T)} \tag{2.8}$$

Considering the ratio between **Equation 2.4 2.6** we can establish where the chemical potential is positioned in the semiconductor:

$$\mu_i = \frac{\epsilon_c + \epsilon_v}{2} + \frac{k_B T}{2} + ln\frac{N_h}{N_e} \tag{2.9}$$

In this expression the middle value of the gap is summed to a negligible number, so the expression can be rounded to:

$$\mu_i \simeq \frac{E_g}{2} \tag{2.10}$$

The chemical potential (Fermi level) in an intrinsic semiconductor is thus positioned very close to the middle of the band gap, as shown in **Figure 2.1a**.[4]

The interest towards intrinsic semiconductors is however limited by the fact that their number of carriers is small and have therefore limited practical applications. If a pure semiconductor undergoes a structural modification that inserts small amounts of external ions into its structure or increases its defectivity we refer to an **extrinsic** or **doped semiconductor**. Doping can sensibly enhance the number of electrons with respect to holes or vice versa, it may enhance the optical absorption of wide band gap semiconductors,[8,9] increase the minority carrier diffusion length,[10] or enhance the catalytic activity of the material.[8,11,12] Other dopants can adversely affect their properties, by introducing midgap bulk or surface states that act as recombination centers.[13]

Two different types of doping exist, *i.e.*, acceptor or donor doping. In the acceptor-doped semiconductors, some of the material's atoms in the crystal lattice are replaced with impurity atoms that are characterized by a lower number of valence electrons. The doped material thus possesses an increased number of holes (acceptors) with respect to electrons. The acceptor-doped semiconductors are also referred to as **p-type** semiconductors. An example of p-type doping material is Si containing Al impurities. On the contrary, a donor-doped semiconductor is characterized by the presence of impurity atoms which possess extra valence electrons with respect to the matrix material. In this case, a **n-type** semiconductor, richer in electrons with respect to holes, is obtained (such as P doped Si). The effect of doping on the electronic structure of a semiconductor consists in the insertion of an energy level close to either the valence or the conduction band, depending on the nature of the doping, towards which or from which electrons can move with a much smaller energy, increasing the number of mobile charge carriers available in the material.

In extrinsic semiconductors the number of electrons and holes is not equal anymore; thus, to preserve the charge neutrality of the system the chemical potential must shift accordingly. If we consider an n-type system, in which the number of donors is higher than the number of acceptors ($N_D > N_A$) and considering that, as in intrinsic semiconductors, the

chemical potential can be derived from the ratio between the charge carriers concentrations, we obtain:[6]

$$\mu = \mu_i + k_B T \; ln\left(\frac{N_D - N_A}{n_i}\right) \tag{2.11}$$

Equation 2.11 indicates that doping results in a shift of the chemical potential with respect to the intrinsic situation of an amount that depends on the difference between the number of donors and the number of acceptors (*i.e.*, the charge excess). In this case, since $N_D > N_A$, the chemical potential shifts towards higher energies and gets closer to the conduction band.[4] The tail of the Fermi-Dirac distribution in the conduction band is then larger than in the valence band: the probability of having free electrons in the CB is greatly enhanced (**Figure 2.2a**).

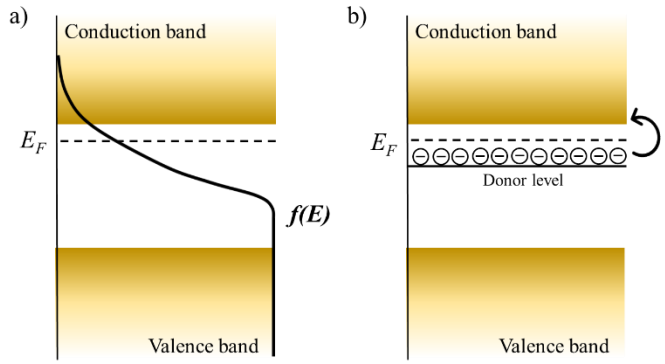

Figure 2.2 a) Fermi-Dirac distribution and chemical potential position, b) simplified band diagram under thermal equilibrium of a n-type doped semiconductor.

Fig. 2.2b represents the band model for a n-type semiconductor, in which the donor doping creates an additional energy level close to the conduction band, filled with the excess electrons present due to the impurity atoms.[14] These electrons can be promoted to the empty conduction band with a much smaller energy with respect to the electrons that are present in the filled valence band.

On the contrary, a p-doped semiconductor is characterized by a larger Fermi-Dirac distribution tail in the VB and an empty acceptor level is created closed to it due to the excess holes present in the material. The acceptor level can then host electrons that are promoted from the VB, leaving a large number of positive charge carriers behind.

2.1.2 Space charge layer and band bending

One of the key features of a semiconductor is the presence of a built-in electric field, or space charge layer (SCL). In devices for solar energy conversion, this field is responsible for the efficient separation of the photogenerated electrons and holes, thereby preventing recombination. The field is present near the surface or interface of a semiconductor, and it is formed by the transfer of charges from the semiconductor bulk across its interface.

Generally, junctions are formed when a semiconductor is put in contact with a second phase and an initial difference in Fermi levels between the two phases is present. Consequently, the majority charge carriers (*i.e.*, electrons in n-type semiconductors) are transferred from the semiconductor to the second phase to equalize the Fermi levels and establish a thermodynamic equilibrium: this equilibration creates a potential barrier at the interface between the two materials, as depicted in **Figure 2.3**.[15]

At the equilibrium, a Helmholtz double layer will be formed at the semiconductor/electrolyte interface, where the semiconductor is positively charged near its surface due to electrostatic induction and the electrolyte is negatively charged. Due to the low concentration of free charge carriers in the semiconductor, the built-in electric field cannot be properly screened in the semiconductor; this causes the concentration of charge carriers near the semiconductor surface to be depleted with respect to the bulk. In a n-type semiconductor, when $E_F > E_{redox}$ the electrons are depleted in the space charge layer and this region is therefore called the **depletion layer** and is characterized by excess positive charge.[16] In the space charge region the energy band edges in the semiconductor are thus shifted upwards due to the electric field and the consequent charge transfer between the two phases; this phenomenon is called **band bending**.[16,17]

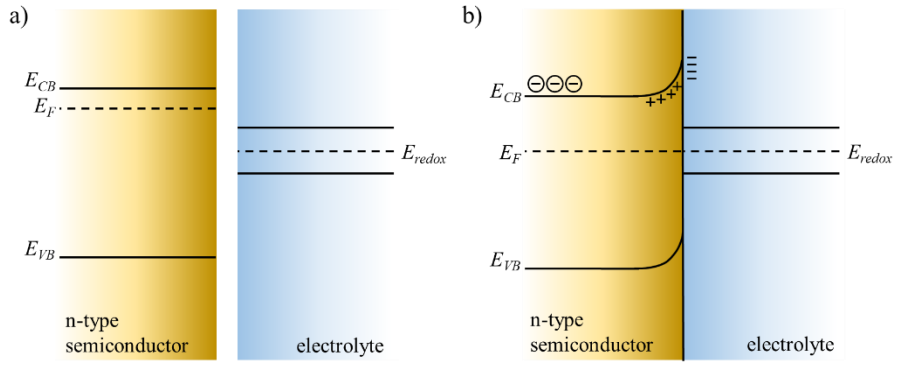

Figure 2.3 a) Band diagram of an isolated n-type semiconductor and an isolated electrolyte and b) band diagram of the two systems after equilibration, with the formation of a space charge layer (SCL) inside the semiconductor.

The width of the space charge layer (W), that is, the distance between the semiconductor surface and where its bands flatten, can be calculated as:[18]

$$W = \sqrt{\frac{2(|E - E_{fb}|)\varepsilon_r \varepsilon_0}{qN_D}} \tag{2.12}$$

where q is the elementary charge, ε_r is the relative permittivity of the semiconductor, ε_0 is the permittivity of vacuum, N_D is the donor density. $|E - E_{fb}|$ is the potential drop, and E_{fb} is the **flatband potential**, *i.e.*, the potential at which the space charge region, and consequently the band bending, is no longer present.[19,20] This condition is obtained when an external voltage E is applied, leading to the matching of the potential of the redox couple in the electrolyte (E_{redox}) and the flat band potential E_{fb} of the semiconductor: no charge is removed from the semiconductor and thus no space charge layer is formed.

The SCL can also be seen as a capacitor, where a n-type semiconductor is positively charged and the solution possesses an excess of negative charges. The total charge stored in the depletion layer is proportional to W and thus the space charge capacitance can be obtained by means of the Mott-Schottky equation (**Equation 2.13**), taking into account the surface area of the material A:[20,21]

$$\frac{1}{{C_{sc}}^2} = \frac{2}{\varepsilon_r \varepsilon_0 A^2 q N_D}\left(E - E_{fb} - \frac{k_B T}{q}\right) \tag{2.13}$$

This equation helps determining some intrinsic properties of the semiconductor material, such as the donor density and the flatband potential.

As already mentioned while introducing the concept of the flatband potential, the application of an external voltage on the system composed by a semiconductor in contact with an electrolyte can alter the SCL width, possibly even cancelling it. When a potential is applied to the system, the Fermi level of the semiconductor is shifted, depending on whether the applied potential is more positive or more negative than E_{fb}. If the Fermi level of a n-type semiconductor is shifted from its equilibrium condition under application of a more positive potential, the potential drop in the depletion layer will increase, leading to an extension of the space charge layer in the semiconductor. This will also cause an increase in the upward bending of the bands near the semiconductor/electrolyte interface. On the contrary, if a potential more negative with respect to E_{fb} is applied, the bending of the bands will be diminished.

2.1.3 Under illumination

When a semiconductor is illuminated, the incident photons can either be transmitted, *i.e.,* they pass through the semiconductor, reflected from the top surface of the material, or they can be absorbed. A semiconductor can absorb only photons whose energies are higher with respect to the band gap energy of the material ($h\nu > E_g$). This absorption can then lead to the excitation of electrons from the valence band to the conduction band. After the absorption of a photon a hole is left in the VB, while an extra electron is now present in the CB. Given the space charge layer present at the semiconductor/electrolyte interface, this newly formed electron-hole couple can more easily undergo separation, with the electron moving towards the bulk of the material, while the hole is brought towards the electrolyte interface. This means that holes can carry out oxidation reactions, while electrons driven towards the back contact can be collected to promote reduction reactions. Therefore, a n-type semiconductor under illumination behaves as a **photoanode**.[22–24]

The electrons and holes densities are varied due to light absorption and the equilibrium configuration described in **Figure 2.3** is no longer valid. The generation of these charges splits the Fermi level into two quasi-Fermi levels, representing the energy of the electron (E_{Fn}) and hole (E_{Fp}) populations.[25–27] The prefix quasi- refers to the fact that

thermalization of the excited carriers is a fast process, leaving the collection of holes (and electrons) each in quasi-thermal equilibrium under steady-state illumination.[28]

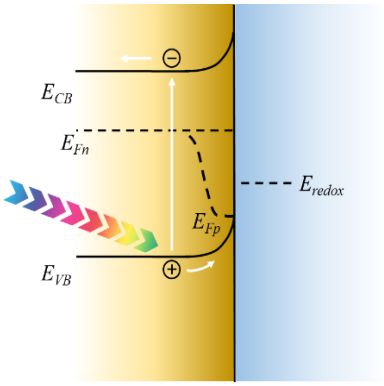

Figure 2.4 Positions of the bands at equilibrium under illumination.

Under illumination, the generated majority carriers are excited into the CB, partially repopulating the depletion layer; band banding is thus decreased with respect to dark equilibrium conditions, as shown in **Figure 2.4**. It is also worth underlining that the rise in concentration of the majority charge carriers following irradiation is negligible with respect to the increase of the minority charge carriers concentration. The quasi-Fermi level of the minority carrier, holes for a n-type semiconductor, is a crucial aspect in photoelectrochemical water splitting, since this energy level corresponds to the oxidizing power of holes of the material. The semiconductor photovoltage, defined as the difference in energy between E_{Fn} and E_{Fp}, determines the maximum theoretical energy that can be employed by the material to drive redox reactions.[29,30]

With the aim of accomplishing solar-assisted water splitting to obtain hydrogen without any additional external bias, a semiconductor possessing a photovoltage larger than 1.23 eV plus additional overpotentials and entropic losses should be used. Moreover, the energy level of the two quasi-Fermi levels (not the conduction and valence band edges) should straddle the water oxidation potentials.

2.2 PEC water splitting

As already briefly outlined in **Section 1.3.1,** in photoelectrochemical water splitting a light absorber material (usually a semiconductor) is used to provide the current flow needed for the water splitting reaction to occur.

In 1839 Henri Becquerel observed that an electric current was produced when a silver-silver halide electrode immersed in dilute acid was illuminated, thus leading to the discovery of the *photovoltaic effect*.[31] However, all studies on photoelectrochemistry performed prior to

1970 were of fundamental nature; only at the beginning of the 70s the potential application of photoelectrochemical systems for solar energy conversion and storage was recognized.[32] In the pioneer work of Fujishima and Honda, n-type TiO_2 showed the capacity of oxidating water to oxygen at significantly more negative potentials compared to the standard redox potential of the H_2O/O_2 couple, making it possible to use sunlight to split water into hydrogen and oxygen.[33]

As already mentioned in **Chapter 1**, solar water splitting is a non-spontaneous reaction with $\Delta G = 237.2$ kJ·mol^{-1} ($E^0 = 1.23$ V). To conduct this reaction, a semiconductor should be able to absorb radiation with a photon energy higher than 1.23 eV, corresponding to light with wavelengths lower than 1000 nm, which includes all the visible spectrum.[28,34] However, even if the theoretical voltage necessary to split water is 1.23 V, in practice the reaction occurs at a much higher voltage. Additional overpotentials and entropic energy losses should be accounted for to overcome the kinetic barrier of the process given by the water oxidation half-reaction, which possesses a particularly sluggish kinetics. When taking into account all of these factors the overpotential of the water splitting reaction is estimated to be *ca.* 0.4-0.6 V, leading to an overall 1.6-1.8 V.[35] Hence, only photons with wavelengths shorter than 700 nm (43% of the solar spectrum) possess enough energy to overcome the oxidation and reduction energy losses.

The general reaction mechanism is outlined as follows:[36]

$$\text{Semiconductor} + h\nu \longrightarrow e^-_{CB} + h^+_{VB}$$

$$2\ H_2O + 4\ h^+_{VB} \longrightarrow O_2 + 4\ H^+ \qquad \text{OER}$$

$$2\ H^+ + 2\ e^-_{CB} \longrightarrow 2\ H_2 \qquad \text{HER}$$

$$2\ H_2O \longrightarrow O_2 + 2\ H_2 \qquad \text{OWS}$$

where OER indicates the O_2 evolution reaction, HER the H_2 evolution reaction and OWS the overall water splitting. The oxygen evolution potential is 1.23 V vs NHE (pH = 0), while the hydrogen evolution potential has been conventionally determined to be 0 V vs NHE (pH = 0). The OWS potential is thus of 1.23 V. As already anticipated, the water oxidation semi-reaction requires the simultaneous involvement of four holes to occur. This kinetic requirement makes the OER the rate determining step of the overall reaction, *i.e.*, the **kinetic bottleneck** of the water splitting process.

Besides having a suitable band gap energy, semiconductors capable of driving the water splitting reaction must also have appropriate band positions; that is, the conduction band edge must be more negative in energy than the H_2 reduction potential, while the valence band edge must be more positive with respect to the water oxidation potential.

Light-driven water splitting catalysed by a semiconductor occurs following three main steps:[24,37]

i. absorption of light photons with energy greater than its band gap energy (see **Section 2.1.3**) and consequent generation of electrons in the CB and holes in the VB,
ii. charge separation; the photogenerated electron-hole pairs migrate towards the reaction sites: in a photoanode, holes are driven towards the photocatalyst surface, whereas electrons move towards the back contact,
iii. surface chemical reactions: holes on the photocatalyst/electrolyte interface can oxidize water molecules absorbed on the semiconductor surface.

In the case of ideal semiconductor photoelectrodes, the Fermi level in the dark is located within the band gap of the material, so no vacant states are available close to the Fermi level to accept electrons. The electron transfer step must therefore involve either electron injection into the continuum of states in the conduction band or to unfilled states (*i.e.*, holes) in the valence band. If surface states are present in a non-ideal semiconductor electrode, oxidative electron transfer may also involve vacant surface energy levels located within the band gap.

In most cases, the concentration of holes at the electrode surface depends on the rate at which they are generated by photon absorption in the bulk, transferred to the interface and removed, either by electron transfer from the electrolyte, or by recombination with electrons from the conduction band. Consequently, the rate of the oxidation step in the photoelectrochemical oxygen evolution reaction will depend on the surface concentration of holes.[38]

The separation of the photogenerated charge carriers is always in competition with charge recombination processes, *i.e.*, all processes that contribute to the re-joining of electrons

and holes, diminishing the number of carriers able to carry out redox reactions on the material's surface.

2.2.1 Metal oxides as photoelectrodes

As already outlined, a photocatalyst to be employed in the solar water splitting process must meet various requirements. Firstly, the band gap of the material must be narrow enough to maximize the absorption of visible light, bearing in mind that the longest wavelength that can be absorbed by a semiconductor is linked to its band gap by the equation $\lambda_{max} = h\nu/E_g$. At the same time, the band gap must be wide enough to efficiently drive the water splitting reaction, taking into account the overpotentials needed to overcome the losses and the slow kinetics of a real system. By combining these two requirements, a semiconductor with a band gap between 1.9 eV (corresponding to an absorption onset at 650 nm) and 3.1 eV (λ_{onset} = 400 nm) should be used. Furthermore, besides the magnitude of E_g, the relative positions of its band edges play a fundamental role in identifying a suitable material. As anticipated in **Section 2.1.3**, the quasi-Fermi levels of electrons and holes should straddle the water reduction and oxidation potentials, respectively. This means that E_{CB} should lie above $E_{red}(H^+/H_2)$, while E_{VB} should be more positive than $E_{ox}(O_2/H_2O)$.[22,39]

As shown in **Figure 2.5**, the band gap edges positions of different semiconductors are displayed differently with respect to the redox potentials of water splitting and very few of them fulfil both above-mentioned requirements. The diagram also suggests that non-oxide semiconductors usually exhibit more negative E_{CB}, making them particularly suited to reduce water, while oxide-based semiconductors typically possess a largely positive E_{VB} and are more suitable to carry out water oxidation.

Metal oxides have emerged as the most suitable class of materials to be employed for water splitting applications, mainly due to their peculiar stability in relatively harsh oxidative conditions in aqueous solutions, opposed to non-oxide semiconductors which are instead more easily oxidized or corroded when in contact with an aqueous solution.[40] Among n-type semiconductors that have been investigated as photoanodes for the water oxidation half-reaction, transition metal oxides offer many advantages.

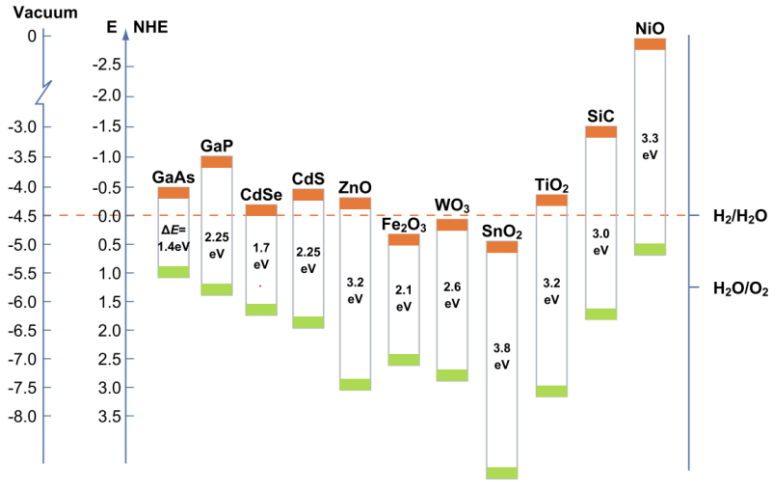

Figure 2.5 Schematic overview of the band positions of representative semiconductors. Figure taken from ref 39.

Their stability in aqueous media is due to the relatively high electronegativity of oxygen which results in the formation of stable compounds based on O^{2-} anions, combined with the fact that in most metal oxides (such as WO_3, $BiVO_4$, $CuWO_4$) metals are in their highest oxidation state, making them not susceptible of further oxidation when employed as photoanodes.[40,41] Besides their stability, many of these semiconductors have relatively narrow band gaps, ranging from 1-5 to 2.7 eV, ensuring an optimal visible light absorption. A third advantage is the fact that their valence bands usually have a *O2p* character and are located at highly oxidizing potentials (at *ca.* 3 V vs RHE), far below the 1.23 V thermodynamic potential of oxygen evolution.[42] Holes generated in these materials have therefore a large overpotential to drive water oxidation, thus enabling transition metal oxide photoanodes to easily overcome the kinetic barriers of the oxygen evolution reaction. Moreover, these semiconductors possess an easily tunable band gap, thanks to their electronic structure. The valence band is composed of *O2p* states, as already mentioned, while the conduction band position is determined by the *d* orbitals of the metal. In this way, the tuning of the metal cations can modify (usually narrow) the band gap energy of the material, while preserving the highly oxidative position of their valence band.[23]

Lastly, the composition of metal oxides is made of abundant and inexpensive elements, which makes easy and cost-effective the synthesis of these materials on a large scale.

2.2.2 Single absorber/tandem cells

Photoelectrochemical water splitting can be achieved using two different configurations. In an ideal case, a single semiconductor absorbing two photons can be used to drive the overall water splitting reaction, yielding a H_2 molecule. This approach is called **S2 scheme** (**Figure 2.6a**). In this case, a single photocatalyst meets all the requirements (E_g higher than the energy needed for water splitting and appropriate valence and conduction band edge positions) needed to drive the PEC water splitting. However, despite materials with a wider band gap have a larger overpotential to efficiently carry out the two semi-reactions, only semiconductors with $E_g < 3.2$ eV should be taken into consideration, in order to allow the harvesting of a significant portion of the solar spectrum.

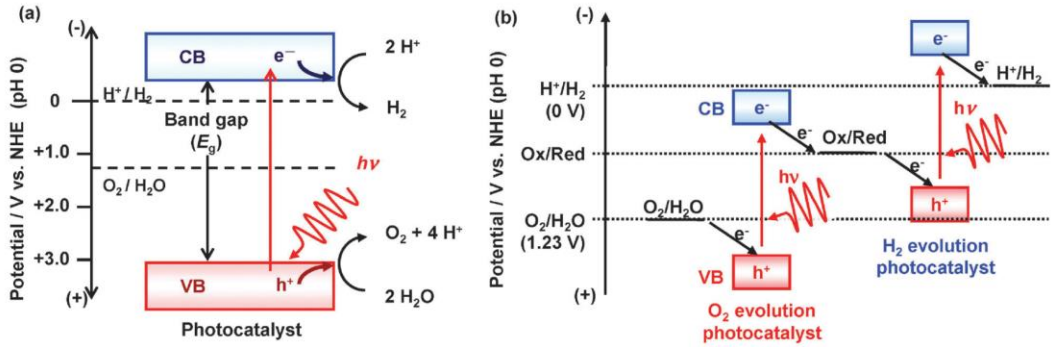

Figure 2.6 Energy diagrams of photocatalytic water splitting based on (a) one-step excitation and (b) two-step excitation (Z-scheme). Figure taken from ref. 43.

Since it is important to know the maximum expected solar-to-hydrogen efficiency (η_{STH}) of a given setup, the efficiency of the S2 approach has been calculated. By assuming losses accounting for 1 eV, a band gap of 2.23 eV should be the lowest limit for a semiconductor able to undergo complete water splitting. The maximum efficiency of the S2 scheme is therefore 11.6%.[44]

Despite the many efforts put in the development of a single material able to drive the overall water splitting reaction under solar light irradiation and some promising results that have been achieved, a more versatile strategy has been the object of increasing interest. Instead of pursuing the demanding identification of a semiconductor with a band gap

straddling the water oxidation and reduction potentials, an alternative approach appears appealing, the so-called Z-scheme depicted in **Figure 2.6b**.

In the **Z-scheme**, or tandem, or D4 approach, the overall water splitting reaction is divided into two semi-reactions and two different narrow band gap semiconductors are employed: one carries out water oxidation (the photoanode), the second one carries out water reduction (the photocathode).[28,43,45] In this case, two photons should be absorbed by each of the two separate photocatalysts to produce a H_2 molecule. The use of two separate photocatalysts allows to employ smaller band gap materials, able to harvest a larger portion of the solar spectrum. Moreover, large overpotentials become accessible without the need of absorbing highly energetic photons.[34] In the Z-scheme the majority charge carriers of each photocatalyst recombine at the junction between the two semiconductors, while photogenerated minority carriers, holes and electrons, responsible for the oxygen and hydrogen evolution reactions, respectively, are more efficiently separated. The more efficient solar light utilization and the availability of a wider range of semiconductor materials that can be employed either as photoanodes or as photocathodes are the two main advantages of the Z-scheme approach.

The double semiconductor approach can be achieved in two ways: with the photoanode and the photocathode coupled side-by-side or in a tandem configuration with the two half cells placed one on top of the other. The first way can evidently reach lower η_{STH} with respect to the second one, since coupling the cells side-by-side leads to a net loss in the irradiated area. On the other hand, this strategy allows the utilization of smaller band gap materials, since the problem of maximizing light transmission through the photoanode is absent. With such system, in the upper limit, where two 1.4 eV band gap materials are employed, a 16.6% maximum solar-to-hydrogen efficiency has been calculated,[44] which is much better than the 11.6% η_{STH} calculated for the single semiconductor approach. The determination of the upper limit for a tandem cell is more complex, since the estimation needs to take into account the absorption of the first photoelectrode that limits the activity of the second material. Taking into consideration a configuration in which the two catalysts are placed one in front of the other, we consider the first absorber to have an energy gap of E_{g1} larger than the band gap of the second absorber ($E_{g1} > E_{g2}$), in order to allow enough light to reach the second

material. Hence, the first photoelectrode must be optically transparent and have minimal scattering losses.

Most of the materials commonly used as photoanodes in photoelectrochemical systems have a band gap larger than 2.1 eV, while the photocathodes usually have narrower energy gaps. Thus, the upper absorber in a tandem cell possessing a larger E_g is assumed to be the photoanode. A contour plot obtained by plotting the theoretical maximum η_{STH} against E_{g1} and E_{g2} was built, accounting for realistic losses of 1 eV for each absorber (mainly due to overpotentials and charge separation processes) and is reported in **Figure 2.7**. This diagram gives a good estimation of the highest η_{STH} efficiency on the accounts of the band gap of one of the two semiconductors. A limit efficiency of 21.6% for $E_{g1} = 1.89$ eV and $E_{g1} = 1.34$ eV is predicted with this model. Other studies have predicted a higher 29.7% maximum efficiency with E_{g1} and E_{g2} of 1.60 and 0.95 eV, respectively.[46]

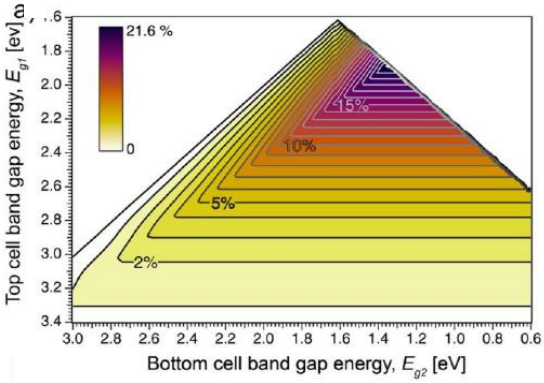

Figure 2.7 Contour plot showing the maximum predicted solar to hydrogen efficiency under AM 1.5G irradiation. The η_{STH} depends on the energy gaps of the two semiconductors. Figure taken from ref. 44.

Currently, the highest η_{STH} efficiency value obtained for a PEC tandem cell is 13.1% using III-V semiconductors (GaAs, GaInP, etc.) as light absorbers.[47] Using metal oxide semiconductors only, efficient unassisted PEC tandem cells combining a Mo-doped $BiVO_4$ photoanode with a $RuOx/TiO_2/Ga_2O_3/Cu_2O$ photocathode were designed by Grätzel et al. and obtained a solar-to-hydrogen efficiency of ~3%.[48] Domen et al. combined a $BiVO_4$-based photoanode with a Pt and CdS-modified $CuIn_{1-x}Ga_xSe_2$ photocathode and built a stand-alone tandem PEC cell that showed a 3.7% efficiency.[49]

2.3 Focus of this thesis

Given the considerations drawn in this Chapter, the key focus in the research field of photoelectrochemical water splitting is that of identifying a suitable material that could efficiently be employed as photoanode in the water oxidation semi-reaction, the rate determining step of overall water splitting. In this context, transition metal oxide semiconductors appear as the most suitable category of materials to be exploited for this purpose.

For these reasons, the aim of this thesis has been focused on the study and the optimization of well-known photoanodes to be employed in a single absorber cell, coupled with a counter electrode (usually a Pt wire). As outlined by J. R. Durrant et al., some guidelines should be followed in the choice and design of efficient materials:[24]

1) Materials should be characterized by a longer bulk charge carrier lifetime, that contributes to decreasing bulk recombination losses and increasing the minority carrier diffusion length.
2) Materials should have a faster water oxidation kinetics. Faster water oxidation kinetics decreases the density of holes that must accumulate at the photoanode surface to drive the required electron flux for water oxidation, thereby suppressing surface recombination losses.
3) The spatial separation of charge carriers shoud be improved. Materials with energy offsets should be employed to favour the separation of charge carriers. Forming type-II semiconductor heterojunctions can aid the spatial separation of electrons and holes, decreasing the need for an applied bias.
4) Dopant densities should be tuned for optimum performance. A n-type doping needs to increase the bulk conductivity and favour the formation of a SCL. However, a high doping density can be expected to decrease the minority carrier (hole) lifetime and, thus, accelerate bulk recombination losses, as well as decrease the width of the SCL.

Given these general considerations, WO_3 has been chosen as the starting material from which to build an efficient photocatalytic system, due to its favourable characteristics such as: a well positioned valence band maximum, fast water oxidation kinetics and electron

trasport properties. Given that tungsten oxide is capable of absoprting only a modest portion of the visible spectrum, the aim of my work has been then focused on overcoming this limitation. As it will be discussed in more detail in Chapters 4-7 of this thesis, two approaches have been investigated. We first studied a WO_3-based ternary oxide, $CuWO_4$, that presents a reduced band gap with respect to the binary material, and studied the effect of its doping with nickel ions, with the aim of finding the optical doping density for this material. We then proceeded with coupling WO_3 with $BiVO_4$ (characterized by a smaller band gap of *ca.* 2.3 eV), resulting a the visible-light sensitised coupled system, which also favours the spatial separation of photogenerated electrons and holes. The WO_3–$BiVO_4$ heterojunction has been extensively studied by varying its morphology and the ratio between the two materials, with the aim of further understanding the limitings factors as well as the optimal working conditions for this composite.

The experimental methods used throughout this thesis and the investigated metal oxide photoanodes that have been the subject of this work will be thoroughly detailed in the following Chapters.

References

1. H.O. Finklea, *J. Chem. Educ.* 60 (**1983**) 325–327.
2. Q. Wang, K. Domen, *Chem. Rev.* 120 (**2020**) 919–985.
3. P. Atkins, J. De Paula, Physical Chemistry, Oxford University Press, **2010**.
4. A.W. Bott, D. Ph, *Sol. Energy* 8 (**1964**) 136.
5. N.W. Ashcroft, D.N. Mermin, Solid State Physics, Saunders College Publishing, **1976**.
6. S. Giménez, J. Bisquert, Photoelectrochemical Solar Fuel Production, Springer, **2016**.
7. R. van de Krol, M. Graetzel, Photoelectrochemical Hydrogen Production, Springer US, **2012**.
8. M.V. Dozzi, E. Selli, *J. Photochem. Photobiol. C Photochem. Rev.* 14 (**2013**) 13–28.
9. A. Polo, C. Nomellini, I. Grigioni, M.V. Dozzi, E. Selli, *ACS Appl. Energy Mater.* 3 (**2020**) 6956–6964.
10. J.W. Jang, D. Friedrich, S. Müller, M. Lamers, H. Hempel, S. Lardhi, Z. Cao, M. Harb, L. Cavallo, R. Heller, R. Eichberger, R. van de Krol, F.F. Abdi, *Adv. Energy Mater.* 7 (**2017**) 1–11.
11. Y. Park, D. Kang, K.S. Choi, *Phys. Chem. Chem. Phys.* 16 (**2014**) 1238–1246.
12. F.F. Abdi, L. Han, A.H.M. Smets, M. Zeman, B. Dam, R. Van De Krol, *Nat. Commun.* 4 (**2013**) 1–7.
13. K.J. Pyper, J.E. Yourey, B.M. Bartlett, *J. Phys. Chem. C* 117 (**2013**) 24726–24732.
14. A.J. Bard, L.R. Faulkner, Electrochemical Methods - Fundamentals and Applications, John Wiley & Sons, **2001**.
15. A.J. Nozik, *Annu. Rev. Phys. Chem.* 29 (**1978**) 189–222.
16. Z. Zhang, J.T. Yates, *Chem. Rev.* 112 (**2012**) 5520–5551.
17. S. Corby, E. Pastor, Y. Dong, X. Zheng, L. Francàs, M. Sachs, S. Selim, A. Kafizas, A.A. Bakulin, J.R. Durrant, *J. Phys. Chem. Lett.* 10 (**2019**) 5395–5401.
18. Y. Ma, S.R. Pendlebury, A. Reynal, F. Le Formal, J.R. Durrant, *Chem. Sci.* 5 (**2014**) 2964–2973.
19. A. Hankin, F.E. Bedoya-Lora, J.C. Alexander, A. Regoutz, G.H. Kelsall, *J. Mater. Chem. A* 7 (**2019**) 26162–26176.
20. K. Gelderman, L. Lee, S.W. Donne, *J. Chem. Educ.* 84 (**2007**) 685–688.
21. K. Sivula, *ACS Energy Lett.* 6 (**2021**) 2549–2551.

22. B.D. Alexander, P.J. Kulesza, I. Rutkowska, R. Solarska, J. Augustynski, *J. Mater. Chem.* 18 (**2008**) 2298–2303.

23. D.K. Lee, D. Lee, M.A. Lumley, K.S. Choi, *Chem. Soc. Rev.* 48 (**2019**) 2126–2157.

24. S. Corby, R.R. Rao, L. Steier, J.R. Durrant, *Nat. Rev. Mater.* 6 (**2021**) 1136–1155.

25. C.N. Kenyon, M.X. Tan, O. Krüger, N.S. Lewis, *J. Phys. Chem. B* 101 (**1997**) 2850–2860.

26. M.X. Tan, C.N. Kenyon, N.S. Lewis, *J. Phys. Chem.* 98 (**1994**) 4959–4962.

27. B. Klahr, S. Giménez, F. Fabregat-Santiago, T. Hamann, J. Bisquert, *J. Am. Chem. Soc.* 134 (**2012**) 4294–4302.

28. M.G. Walter, E.L. Warren, J.R. McKone, S.W. Boettcher, Q. Mi, E.A. Santori, N.S. Lewis, *Chem. Rev.* 110 (**2010**) 6446–6473.

29. B.A. Gregg, A.J. Nozik, *J. Phys. Chem.* 97 (**1993**) 13441–13443.

30. M.F. Weber, M.J. Dignam, *Adv. Hydrog. Energy* 3 (**1984**) 957–968.

31. A.-E. Becquerel, *Comptes Rendus l'Académie Des Sci.* 9 (**1839**).

32. A.J. Nozik, 3654 (**1996**) 13061–13078.

33. A. Fujishima, K. Honda, *Nature* 238 (**1972**) 37–38.

34. K. Maeda, *ACS Catal.* 3 (**2013**) 1486–1503.

35. K. Sivula, *J. Phys. Chem. Lett.* 4 (**2013**) 1624–1633.

36. N. Pirrone, F. Bella, S. Hernández, *Green Chem.* 24 (**2022**) 5379–5402.

37. H. Ahmad, S.K. Kamarudin, L.J. Minggu, M. Kassim, *Renew. Sustain. Energy Rev.* 43 (**2015**) 599–610.

38. L. Peter, *Curr. Opin. Green Sustain. Chem.* 31 (**2021**) 100505.

39. J. Ke, M. Adnan Younis, Y. Kong, H. Zhou, J. Liu, L. Lei, Y. Hou, *Nano-Micro Lett.* 10 (**2018**) 69.

40. K. Sivula, R. Van De Krol, *Nat. Rev. Mater.* 1 (**2016**) 15010.

41. F.F. Abdi, S.P. Berglund, *J. Phys. D. Appl. Phys.* 50 (**2017**).

42. G. Pacchioni, *Catal. Letters* 145 (**2015**) 80–94.

43. T. Hisatomi, J. Kubota, K. Domen, *Chem. Soc. Rev.* 43 (**2014**) 7520–7535.

44. M.S. Prévot, K. Sivula, *J. Phys. Chem. C* 117 (**2013**) 17879–17893.

45. J. Low, C. Jiang, B. Cheng, S. Wageh, A.A. Al-Ghamdi, J. Yu, *Small Methods* 1 (**2017**) 1–21.

46. S. Hu, C. Xiang, S. Haussener, A.D. Berger, N.S. Lewis, *Energy Environ. Sci.* 6 (**2013**) 2984–2993.

47. K. Dongseok, L. James L., Young, Haneol, X. Walter E., Klein Huandong, Chen Yuzhou, G. Boju, Y. Todd G., Deutsch Jongseung, *Nat. Energy* 2 (**2017**) 17043.

48. L. Pan, J.H. Kim, M.T. Mayer, M.K. Son, A. Ummadisingu, J.S. Lee, A. Hagfeldt, J. Luo, M. Grätzel, *Nat. Catal.* 1 (**2018**) 412–420.

49. H. Kobayashi, N. Sato, M. Orita, Y. Kuang, H. Kaneko, T. Minegishi, T. Yamada, K. Domen, *Energy Environ. Sci.* 11 (**2018**) 3003–3009.

Chapter 3 - Methods and characterizations

3.1 Synthesis

The photoanodes presented in this thesis have all been synthetized on a conductive substrate, to ensure the formation of an electronic contact between the material and the support, that allows the extraction of the electrons from the back contact by the external applied potential. Usually, in PEC studies a transparent glass covered by a surface conducting layer is used. Thus, all electrodes prepared for this work have been assembled by using fluorine-doped tin oxide (FTO) glass slabs as substrate, due to its transparency in the visible range and resistance to temperature treatments up to 600 °C.

A general scheme of the synthetic process used to prepare the photoanodes studied in this thesis can be summarized in 3 steps: *i)* preparation of a solution containing the precursor reactants, *ii)* deposition of the solution on the conductive substrate, and *iii)* thermal treatment at high temperature. A well-known method used for the synthesis of homogeneous multicomponent metal oxide materials consists in using a hydroxycarboxylic acid such as citric acid to form stable metal complexes. A polymeric resin is formed by adding a polyhydroxy alcohol such as ethylene glycol or poly(ethylene glycol). Immobilization of metal

complexes in such rigid organic polymer networks reduces segregation of metal ions, ensuring homogeneity.[1]

After its preparation, the precursor solution was deposited on a FTO slab using either the spin coating technique or a solvothermal method, which are described in detail in the following sections. The deposited films underwent a thermal treatment aimed at eliminating the organic precursors and obtaining a crystalline film. The annealing temperature was varied and adjusted to the examined material, and thermal treatments were carried out either on a hotplate or in a muffle furnace.

3.1.1 Spin coating technique

Spin coating is an experimental procedure commonly used to deposit uniform thin films (from few nanometres to few micrometres) on flat substrates.[2] It consists in spreading a small amount of a precursor solution onto the substrate placed on a rotating disc, that spreads the liquid uniformly.

The deposition is performed in four steps: deposition, spin up, evaporation and spin off (see **Figure 3.1**). In the initial step, the solution is cast on the substrate, typically using a pipette; the deposited volumes usually lie in a range from a few tens to a few hundreds of microliters. The substrate can be already spinning (dynamic spin coating), or it is spun after the deposition (static spin coating). The second step, the spin up, allows the centrifugal motion to spread the solution across the substrate; the final rotation rate (expressed in revolutions per minute, rpm) can be reached either immediately, or after a lower speed spreading step; the acceleration can be adjusted to obtain films of the desired thickness, a key parameter which is however influenced by several factors. At this stage, most of the solution is expelled from the substrate. Initially, the fluid may be spinning at a different rate than the substrate, but eventually the rotation speeds will match up, leading to a homogeneous levelling of the fluid. The evaporation stage occurs throughout the whole process; the evaporation of the solvent is possible due to the rapid rotation of the substrate, that contributes to the removal of highly volatile components. The rate of this step will depend on the solvent volatility, vapour pressure and ambient conditions. The spin off sets forth the conclusion of the deposition procedure, as the rotation of the substrate is stopped.[3]

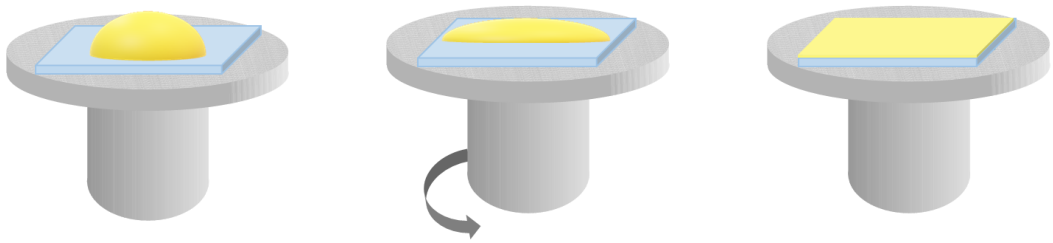

Figure 3.1 Schematic representation of the different stages of the spin coating procedure onto a substrate (deposition, spin on, spin off).

The final thickness of a film depends on a series of factors, mostly related to the nature of the precursor solution containing the material to be deposited. The final film thickness is thus influenced by the concentration of the solute, the nature of the solvent, the density and the viscosity of the solution. Other parameters influencing the width of the film are the duration of the deposition, the angular velocity of spinning and the distance of the deposited solution from the centre of rotation.

Given the difficulty of obtaining relatively thick films (>500 nm) with a single spin coating deposition, multilayer films of increasing thickness are usually obtained by repeating the deposition and annealing steps several times.[4]

This technique presents several advantages, such as:

i. only a small amount of precursor solution is used,
ii. it is relatively inexpensive,
iii. it is quick and easy to use.

On the other hand, this synthetic route presents also some disadvantages, such as:

i. the difficulty to deposit thick films,
ii. the possible presence of contaminants in the sample (traces of solvent, oxygen, humidity, etc.)
iii. the difficulty of controlling all parameters that affect the deposition.

3.1.2 Solvothermal synthesis

Solvothermal synthesis is widely used to fabricate a wide range of nanoscale and nanostructured materials such as metal oxides. It can also be used to grow nanoparticles on a conductive substrate, thus obtaining a nanostructured thin film.[5,6]

Solvothermal synthesis is generally defined as a chemical reaction taking place in a solvent at temperature above the boiling point and pressures above 1 bar. The medium used in a solvothermal synthesis can be either water (in this case, the method is called hydrothermal), an alcohol or any other organic or inorganic solvent. Nevertheless, the term solvothermal is generally used to describe all types of synthesis that occur in a closed vessel with controlled temperature and pressure. During the process, precursors with the end-product stoichiometry are mixed in a solvent with structure-directing agents. After being stirred completely, the mixture is added into a sealed autoclave, which is heated in an oven at temperatures normally ranging between 100°C and 250°C for a specific period of time. The autoclave is usually made of steel, which can tolerate the elevated pressures that are developed during the reaction. The reactants are not directly placed into the autoclave, but are placed inside a Teflon vessel which is chemically inert.

After the completion of the reaction, the autoclave is cooled to room temperature and the obtained products are washed with solvents like alcohol and water to remove the impurities or unreacted reactants from the solution.

For the preparation of nanostructured thin films, a so-called seed layer is firstly prepared by depositing a precursor solution on the support either by spin coating or by another deposition technique.[5–7] The film is then placed in the autoclave and fully covered by the solvent and the reactants. Using the seed layer as a growth germ, the solvothermal reaction contributes to the growing of the nanostructured material on the previously prepared seed layer film. There are some key factors which strongly affect the thin film growth, such as the nature of the solvent, the temperature, the reaction time, and the concentration of the precursor materials.

3.2 Physical characterizations

3.2.1 UV-Vis spectroscopy

The determination of the absorption properties of a photocatalytic material in terms of the number of absorbed photons is a crucial information to obtain, when evaluating the PEC performance of the material. However, the evaluation of the absorption of solid materials still lacks accurate expressions. Traditionally, the absorbance A of a material is defined as the inversed logarithm of the transmission, *i.e.*, the ratio between the incident and the transmitted light:[8]

$$A = -log\, T = log\, \frac{I_0}{I_t} \tag{3.1}$$

Rather than for solid samples, absorbance is usually employed to quantify the absorption properties of a given material dispersed in a homogeneous matrix (typically a liquid). However, the calculation of the absorbance via transmittance measurements can be applied to study relatively thin, optically transparent photoanode films, with A values generally lower than 1 (which correspond to 90% absorption of the incident light). Generally, the UV-Vis spectra of these transparent samples are acquired by measuring their transmission using a simple spectrophotometric set-up, consisting of a light source, a monochromator, a sample holder and a detector. In these measurements, a bare FTO glass is used as blank, and its absorption spectrum is subtracted from that recorded with the sample.

However, **Equation 3.1** is not suited to describe the properties of non-transparent films, since in this case the majority of the incident light is either absorbed or reflected, and only a minimal portion of incident light I_0 is transmitted. In these conditions, we must consider that the incident radiation will either be reflected (I_r), transmitted (I_t) or absorbed (I_a) by the sample:

$$I_0 = I_r + I_t + I_a \tag{3.2}$$

By substituting **Equation 3.2** into **Equation 3.1** we obtain a new expression for absorbance A, that applies in the case of the above-mentioned photoelectrodes:[9]

$$A = -log\left(\frac{I_t}{I_0 - I_r}\right) = -log\left(\frac{I_t/I_0}{I_0/I_0 - I_r/I_0}\right) = -log\left(\frac{T}{1-R}\right) \tag{3.3}$$

In order to apply this equation, the absorption properties of the investigated electrodes must be evaluated employing an integrating sphere. An integrating sphere is an optical component that consists in a void sphere, the internal part of which is covered with a highly reflective material (usually $BaSO_4$), which is able to scatter and diffuse the incident light. By using two different sample holders, the transmittance and the reflectance of a sample can be measured and used to calculate the absorbance of the material using **Equation 3.3**.

UV-Vis spectroscopy is used in photocatalysis to evaluate also the absorption onset of the semiconductors under study, which is the minimum photon energy required to promote electrons from the valence band maximum to the conduction band minimum. From the absorption onset an approximated value of the band gap of the material can be estimated:

$$E_g\ (eV) = \frac{1240}{\lambda_{onset}} \tag{3.4}$$

The calculation of the estimated band gap of a photocatalyst can be a first proof of the attainment of the desired material or it can highlight the modification of the electronic structure of a semiconductor following morphology alterations, surface treatments or doping with metal ions.[4,10]

In semiconductor physics, the band gap of a semiconductor can be of two types: **direct** or **indirect**. The valence band maximum and the conduction band minimum of a semiconductor are each characterized by a defined crystal momentum (k-vector). If the k-vectors of the two orbitals between which the electronic transition occurs are identical, the transition is defined as 'permitted' and the absorption of the material is increased even close to the absorption edge. If, on the other hand, the two crystal momenta are different, the material possesses an indirect band gap and the transition of an electron from the valence band to the conduction band is, in principle, forbidden, since it would require an additional momentum to occur. In practice, these transitions can take place if they are mediated by a phonon, thus obtaining a vibro-optical transition. If a semiconductor is characterized by an indirect band gap, its absorption will be less intense, especially at wavelengths close to the absorption onset.

Among the materials that have been investigated in this thesis, WO_3 and $CuWO_4$ are indirect band gap semiconductors.[11,12] The nature of $BiVO_4$'s bandgap has been debated, with theoretical predictions and some experimental observations pointing to an indirect bandgap

and other experimental studies to a direct bandgap.[9] Recently, a work conducted by I. D. Sharp et al. used a range of spectroscopic measurements to determine that the fundamental bandgap of monoclinic scheelite $BiVO_4$ is indirect, but at the same time an additional direct transition at ~200 meV above the fundamental indirect bandgap, responsible for the large absorption coefficient of $BiVO_4$, was revealed.[13]

3.2.2 Scanning electron microscopy

Electron microscopy is a technique often used to record images of nanometre-sized objects, in which a beam of electrons with a well-defined wavelength replaces the lamp found in traditional light microscopes, since the resolution of a microscope (*i.e.*, the minimum distance between two objects that leads to two distinct images) is in the order of magnitude of the wavelength of the light used as probe beam. Instead of glass or quartz lenses, electron microscopes use magnetic fields to focus the incident beam. In scanning electron microscopy (SEM), electrons scattered back from a small, irradiated area of the sample are detected, and the electrical signal is sent to a video screen; an imagine of the surface is then obtained by scanning the electron beam across the sample.

The resolution limit (d) is mathematically expressed through the Rayleigh criterion which, with a series of assumptions, can be defined as:[14]

$$d_{max} \approx \frac{\lambda}{2} \tag{3.5}$$

Hence, to obtain a resolution greater than 200 nm (the limit resolution achievable using visible light) it is necessary to turn to radiation with a wavelength shorter than those in the visible region. Electrons are suitable to be employed as illumination source, since they are easily generated from metal filaments, can have short wavelengths and, being charged, they can be easily deflected and focused by magnetic fields. The wavelength of an electron can be calculated (and tuned) for a specific accelerating voltage.

The scheme of the main components of a SEM instrument is depicted in **Figure 3.2**. As already mentioned, the source of illumination in electron microscopes is a beam of electrons, generated by a so-called electron gun. These can be classified into two types: thermoionic guns use a heated tungsten wire to produce electrons, that are then accelerated

to create an electron beam; a field emission gun, instead, uses a cold single crystal tungsten filament and electrons are extracted from it by a strong electrostatic field, that provides a much smaller source size, higher current and brightness, making field emission SEM (FE-SEM) instruments high-resolution machines. Electron microscopes are high-vacuum instruments; to produce a consistent electron beam at least two types of vacuum pumps are needed. After the beam is produced, a series of electromagnetic lenses and apertures (condenser lens, objectives, etc.) are used to reduce the diameter of the electron source and to focus the beam on the sample.

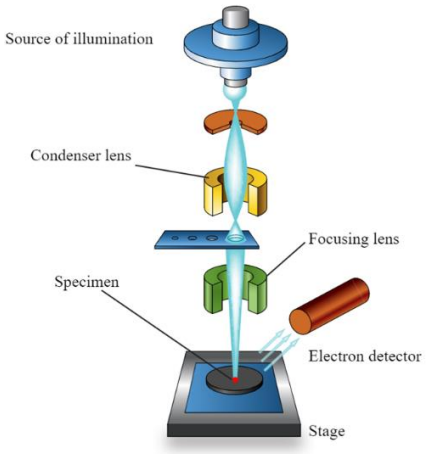

Figure 3.2 Schematic diagram of the building elements of a scanning electron microscopy instrument. Figure taken from ref. 15.

When the electron beam hits a sample, it interacts with its atoms, generating a number of different outcomes. SEM instruments collect the secondary electrons, that are the result of inelastic interactions between the electron beam and the sample and are ejected from the region close to its surface. Since secondary electrons have low energy, a small bias is applied at the front end of the detector to attract them towards the detector. The electric signal output of the detector is then displayed as a two-dimensional intensity distribution that can be viewed and photographed.

In this thesis, top-view SEM images have been acquired to have insight into the shape and morphology of the investigated photoanodes surfaces, since the collection of secondary electrons is particularly suited to provide high-resolution edge details. Cross-section images have been acquired by rotating the sample into the specimen chamber in order to expose the

side of the photoelectrode, with the aim of estimating the thickness of the sample. Since the materials investigated in this work are semiconductors and are hence sufficiently electrically conductive, no further modification of the samples was required before the analyses and no heavy metals were used to coat the films.

3.2.3 X-rays diffraction

X-rays diffraction is a versatile, non-destructive analytical method to analyse the material's properties such as phase composition, structure, lattice parameters, particles size, preferred particles orientation, etc., of powder samples, solid samples or even liquids.

The phenomenon of diffraction is the interference caused by a solid in the path of an incident wave; the pattern that results from this wave-solid interaction is called diffraction pattern. Diffraction phenomena occur when the dimensions of the diffraction object are comparable to the wavelength of the incident radiation. X-rays are electromagnetic radiation with wavelength of the order of $10^{-8} - 10^{-10}$ m. They are typically generated by bombarding a metal with high-energy electrons, generating radiation with a continuous range of wavelengths (the *Bremsstrahlung*), and with few high-intensity, sharp peaks, that arise from collisions of the incident electrons with the electrons in the inner shells of the metal atoms. A collision expels an electron from an inner shell, and an electron of higher energy drops into the vacancy, emitting the excess energy as an X-ray photon.

The basic structure of a crystal is composed of a three-dimensional, orderly arranged, infinite array of points (ions, atoms, molecules), called space lattice. A space lattice can, in turn, be seen as an aggregate of a set of parallel equidistant planes: the lattice planes. These planes can be regarded as semi-transparent mirrors and a crystal can be modelled by numerous stacking planes separated by a distance d. This model allows an easy calculation of the crystal-radiation angles that will build a constructive interference, giving rise to reflection peaks. By considering the reflection of two parallel rays of the same wavelength by two adjacent planes (**Figure 3.3**) we can

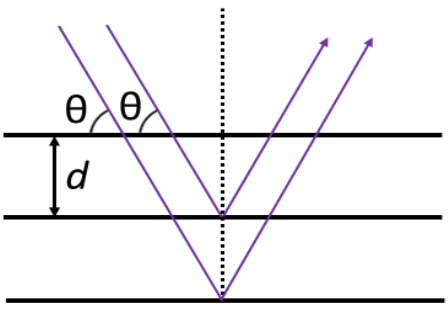

Figure 3.3 Scheme of the conventional derivation of Bragg's law.

observe that the two reflected rays will differ in path by a distance equal to $2d \cdot sin\theta$, where θ is the glancing angle. For numerous glancing angles the path length difference is not an integer number of wavelengths, and incident and diffracted waves interfere destructively. A constructive interference is instead built when the path length difference is an integer number of wavelengths $n\lambda$.

The Bragg's law then defines the conditions in which a constructive interference is observed:[16]

$$n\lambda = 2d \cdot sin\theta \tag{3.6}$$

Modern XRD instrumentations are composed by a sealed X-rays tube as radiation source, optical components used to collimate the incident and the diffracted beams, a sample holder, and an X-rays detector. In most XRD instruments, the investigated sample is irradiated with a monochromatic beam of X-rays, and it is rotated until a reflection is detected. By varying the diffraction angle 2θ *(the angle between the incident and the diffracted beam) through movements of tube or sample and detector, intensities are recorded to create a diffractogram.*

In this thesis, XRD analyses have been performed on thin films, with the following aims:

i. confirm the attainment of a crystalline sample,
ii. rule out the presence of impurities,
iii. identify the crystalline structure of the investigated materials,
iv. confirm the presence of two distinct structures in heterojunction samples.

It is important to underline that in thin film experiments the intensities of the layer peaks are not comparable to the intensities recorded with powder samples, because the number of reflecting lattice planes is much smaller.[17] The investigation has been thus mainly focused on the shape and position of the peaks building the XRD pattern under study.

3.3 Photoelectrochemical tests

3.3.1 *j-V* plots: linear sweep voltammetry

Voltammetry is a class of analytical methods characterized by great diagnostic potentials. It can provide qualitative, quantitative, and mechanistic information on all electroactive species present in the working solution and on the surface of an electrode. This information is obtained by measuring, in a 3-electrode cell, the current (*i.e.*, the rate of the electron transfer process) flowing between the working electrode W and a counter electrode C, as a function of the potential (*i.e.*, the energy) applied to the working electrode with respect to a reference electrode R. By sweeping the working electrode's potential we supply the energy necessary to perform the semi-reaction of interest but, since the potential of a single electrode is unknown, what is varied is the potential difference between W and C, providing energy to a complete redox reaction, in which each semi-reaction occurs either at the working electrode or at the counter electrode site. Moreover, since our aim is to be independent of the semi-reaction occurring at the counter electrode, the potential of the working electrode W is tuned and varied with respect to the potential of the reference electrode R which remains constant and it is a tabulated value.

The current, *i.e.*, the electron transfer rate, depends both on the transport of charges towards the electrode/electrolyte interface (related to the charge transport properties of the material in its bulk) as well as on the electron transfer process (related to activation energy of the redox reaction).

Linear sweep voltammetry (LSV) is a voltammetric method where the current at the working electrode is measured while the potential between the working electrode and a reference electrode is swept linearly in time. The result of a LSV test consists in a *j-V* (current vs voltage) plot that gives information about the photocurrent onset potential of the photoelectrode and its ability to generate photocurrent at a given applied potential (see **Figure 3.4**). The potential at which an illuminated photoanode starts to drive the oxygen evolution reaction is defined as the photocurrent onset potential (V_{onset}). At higher applied bias, in the absence of illumination, a dark current will eventually arise: the semiconductor's surface starts behaving as a metal and provides additional current to the system. The

potential at which the dark current becomes significant ($V_{dark\ onset}$) is the potential at which the measurements should be stopped.[18] If a photoelectrode shows any dark current at a given potential lower than its usual $V_{dark\ onset}$, this could result from sample corrosion and instability. Performing LSV measurements both in the dark and under illumination is required to understand how the observed current density is linked to absorption and conversion of the incident light. For this reason, the two *j-V* curves should always be compared in the sample plot, or the dark current should be subtracted from the full-lamp measurement. Alternatively, chopped illumination measurements can be carried out employing a shutter, giving a single measurement profile in which illuminated and dark periods are alternated.

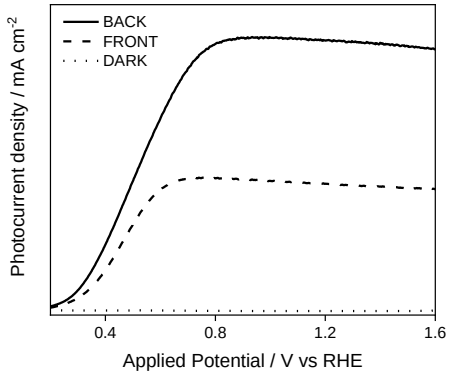

Figure 3.4 Characteristic *j-V* curves measured in a 3-electrode configuration on a WO_3-based PEC electrode in the dark (dotted curve) and under AM 1.5 G illumination in front-side (dashed curve) and back-side (solid curve) configuration.

In the ideal case where the overpotential for the electrochemical reaction approaches zero, a photocurrent can be measured at all potentials more anodic than V_{fb} (see **Chapter 2**, **Section 2.1.2**). In most cases the systems under study exhibit an overpotential, and a photocurrent is observed after an additional potential has been applied. In practice, the flatband potential of a photoanode can be measured by Electrochemical Impedance Spectroscopy.[19] The magnitude of the overpotential associated with the water oxidation reaction can be estimated by comparing the photocurrent generated by a sample in the absence and in the presence of a hole scavenger species;[20] in the presence of a sacrificial agent a more favourable oxidation reaction takes place: the direct comparison of the photocurrent onset potential recorded under both experimental conditions gives insight into the PEC properties of the investigated material.

LSV measurements can be performed using two different configurations: back- and front-side illumination, as shown in **Figure 3.5**, depending on whether the light first strikes the FTO underlayer or if it directly irradiates the photoactive material. When the sample is illuminated in a back-side configuration, photogenerated electrons and holes are formed at the FTO/electrode interface. In this case the holes must travel across the entire thickness of the film in order to react at the electrode/electrolyte interface; the electrons, instead, have to cross a much shorter distance to be collected by the FTO glass and then extracted by the outer circuit. When the sample is illuminated in a front-side setup the charge carriers are generated at the electrode/electrolyte interface and electrons must travel a longer distance than holes in order to be collected.[9,21] Performing PEC measurements using these two different configurations, keeping all the other parameters unmodified, allows one to better understand the rate determining step of the water oxidation process, and if the overall PEC performance is limited by poor electron or hole transport issues. If the photocurrent densities generated by a photoanode in back configuration are greater than those generated in front-side mode, this could suggest that in the investigated material electron transport is slower than hole transport. Instead, if comparable photocurrents are measured in both configurations, the transport properties of electrons and holes in the photoanode are similar.

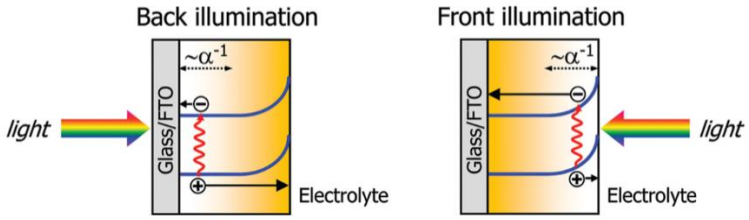

Figure 3.5 Scheme of photogenerated charge carriers upon back- or front-side irradiation. Figure taken from ref. 9.

3.3.1.1 Charge injection and charge separation efficiency

The photocurrent density J generated by a photoanode can be expressed as the combination of different contributions, according to **Eq. 3.7**:[20]

$$J = J_{abs} \cdot \eta_{sep} \cdot \eta_{inj} \tag{3.7}$$

J_{abs} is the theoretical maximum current that could be generated by the sample, which could be achieved only if every photon absorbed by the photoanode would be efficiently converted into current. η_{sep} is the charge separation efficiency, that estimates the efficient separation of photogenerated holes and electrons in the bulk of the material, whereas η_{inj} is the charge injection efficiency, *i.e.*, the percentage of photogenerated holes that, once successfully reached the electrode/electrolyte interface, are able to effectively take part in the water oxidation reaction.

η_{inj} can be easily calculated by performing LSV measurements both in the presence and in the absence of a hole scavenger species, that is, a redox couple whose oxidation reaction is favoured with respect to that of the H_2O/O_2 couple.[22] The role of a hole scavenger is to mitigate the efficiency loss due to the charge transfer at the electrode/electrolyte interface. The charge injection efficiency is thus calculated using the following equation:

$$\eta_{inj} = \frac{J_{electrolyte}}{J_{hole\ scavenger}} \tag{3.8}$$

η_{sep} can be calculated by assuming that, in the presence of a hole scavenger species, the charge injection efficiency is unitary:

$$\eta_{sep} = \frac{J_{hole\ scavenger}}{J_{abs}} \tag{3.9}$$

J_{abs} is estimated using the standard solar spectrum and the measured absorbance of the photoelectrode as:[23]

$$J_{abs} = q \int_{\lambda_1}^{\lambda_2} \phi_{ph} \cdot \left(1 - 10^{-A(\lambda)}\right)\, d\lambda \tag{3.10}$$

where q is the elemental charge ($1.60 \cdot 10^{-19}$ C), ϕ_{ph} (Ph cm^{-2} s^{-1} nm^{-1}) is the photon flux density under standard conditions[a] (AM1.5G, 100 mW cm^{-2}),[24] and $1 - 10^{-A(\lambda)}$ is the Light Harvesting Efficiency, LHE. The integration interval is based on the absorption onset and the band gap energy of the investigated material.

Numerous hole scavenger species are used to probe the intrinsic characteristics of photoanodes materials, such as hydrogen peroxide for hematite,[20] sodium sulphite for bismuth

[a] In **Eq. 3.10** and throughout this Chapter, Ph stands for number of photons.

vanadate,[25] methanol for tungsten trioxide,[26] and sodium nitrite for copper-based photoanodes.[4]

3.3.2 Experimental procedure and setup

The equipment required to run voltammetry analyses consists in:

i. A potentiostat that controls and sweeps the potential of the working electrode W with respect to the reference electrode R, following a program set by the user, and records the current flowing between W and C.

ii. A photoelectrochemical cell in which the photoanode is mounted as working electrode. Typically, a PEC cell consists in a reservoir to hold the electrolyte, the investigated sample, the counter and the reference electrodes, an optically transparent window that allows the sample to be illuminated (usually made of fused silica) and the electrical connections to the potentiostat. Other components such as inputs and outputs for a gas circulation system or a membrane to separate the anode and the cathode compartments can be present.[18,27]

iii. An electrolytic solution to fill the PEC cell, composed of a solvent which should show sufficiently good electric conductivity and of a supporting electrolyte which should not be active in the interval of investigated potentials. The pH of the electrolytic solution should be tuned carefully to ensure a good stability of the working electrode. In practice, aqueous H_2SO_4 or HCl solution are often used as an acidic electrolyte for WO_3 or TiO_2.[28] For photoanodes that require neutral or alkaline solution, such as $ZnFe_2O$, KOH or NaOH solutions are commonly used.[29] Other metal oxides are stable in neutral conditions; $BiVO_4$ is stable between pH 3 and 11 and it is usually tested in 0.5 M Na_2SO_4 aqueous solutions.[30] To avoid pH fluctuations, a pH buffer can be added to the solution, *e.g.*, the well-known phosphate buffer KH_2PO_4/K_2HPO_4.

iv. A lamp simulating the standard solar emission profile, necessary to perform voltammetry analyses under so-called full-lamp conditions. Xenon lamps are widely accepted to give the best matching with the solar spectrum and optical filters are usually used to optimize the overall spectral shape. Another option is given by solar

simulators, the performance of which is evaluated by taking into account the spectral matching, the uniformity of irradiation and the temporal stability.

All voltammetry measurements presented in this thesis have been carried out using a standard Ag/AgCl electrode as *R*. The potentials measured vs the Ag/AgCl reference electrode have been referred in this text to the Reversible Hydrogen Electrode (RHE), according to the Nernst equation:

$$E_{RHE} = E_{Ag/AgCl} + E^0_{Ag/AgCl} + 0.059 \times pH \tag{3.11}$$

in which $E_{Ag/AgCl}$ is the recorded potential versus the experimentally employed reference electrode, $E^0_{Ag/AgCl}$ is the standard potential of the Ag/AgCl redox couple (0.210 V vs. RHE at room temperature), RT/nF is equal to 0.059 at room temperature and the pH is that of the employed electrolyte solution. This allows an easy comparison of the performances of photoelectrodes operated in various pH conditions.

3.3.2.1 Set-up at the Università degli Studi di Milano

j-V measurements were performed in the laboratories of the UniMi Photocalysis Group at the Università degli Studi di Milano using the equipment described in this section.

An Autolab PGSTAT 12 (EcoChemie, Utrecht, The Netherlands) potentiostat controlled by the NOVA software was used to sweep the applied potential. The PEC cell here employed was a so-called 'cappuccino' cell, fit to host and carry out 3-electrode measurements.[31]

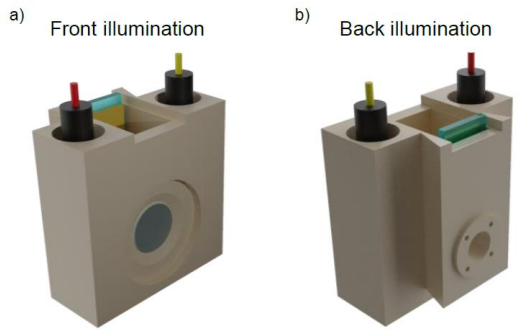

Figure 3.6 Schematic representation of a 'cappuccino' PEC cell. Figure taken from ref. 31.

The cappuccino cell depicted in **Figure 3.6** is made of PEEK (polyether ether ketone), a chemically resistant polymer. It has a small volume (~10 mL), and it is composed of two circular compartments to place the reference and counter electrodes and an additional compartment in which the sample is placed, pressed against an O-ring seal on the cell body. The design of this cell allows the proximity of the three electrodes, thus minimizing current losses. On the front side of the cell a silica window is mounted, allowing the illumination of the sample. This cell ensures that the sample area wetted by the electrolyte is the same as the illuminated area, which is 0.28 cm^2. Back- and front-side illuminations are performed by simply rotating the cell of 180°, without losing optical alignment. The reference electrode is a standard Ag/AgCl electrode (3.0 M KCl), while the counter electrode is a Pt wire.

An LCS-100 Solar Simulator Model 94011A-ES (Newport) equipped with an electronic shutter was used as irradiation source, providing full lamp illumination (**Figure 3.7**). The power density of the incident light was calibrated to 100 mW cm^{-2} using a Thorlabs PM200 power meter equipped with a S130VC power head with Si photodiode detector.

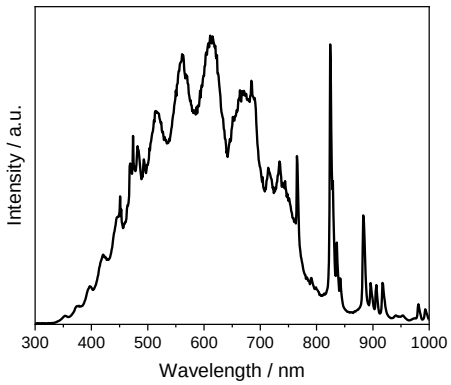

Figure 3.7 Emission spectrum of the LSC-100 Newport solar simulator used for photoelectrochemical full-lamp analyses.

3.4 Incident photon to current efficiency

Incident photon to current efficiency (IPCE) is one of the most important diagnostic figures of merit for PEC devices, describing the photocurrent collected per incident photon flux as a function of illumination wavelength. IPCE takes into account efficiencies for three fundamental processes involved in photoelectrochemistry: *i)* photon absorptance, defined as

the fraction of electron-hole pairs generated per incident photon flux (η_{e^-/h^+}), *ii)* charge transport to the solid-liquid interface ($\eta_{transport}$) and *iii)* the efficiency of interfacial charge transfer ($\eta_{interface}$). This method assumes that the counter electrode is not limiting the current flowing through the circuit.[18]

$$IPCE = \eta_{e^-/h^+} \cdot \eta_{transport} \cdot \eta_{interface} \tag{3.12}$$

In a PEC system, IPCE is obtained from a chronoamperometry measurement at a fixed applied bias when the sample is irradiated with monochromatic light. The difference between the steady-state current and the steady-state background current is the photocurrent that arises due to redox reactions occurring at the surface of the working and counter electrodes. The IPCE corresponds to the ratio of this photocurrent (converted to an electron rate) versus the rate of incident photons (converted from the calibrated power of a light source).

$$IPCE(\lambda) = \frac{electrons\ (cm^{-2}\ s^{-1})}{photons\ (cm^{-2}\ s^{-1})} \tag{3.13}$$

Practically, IPCE is obtained from the ratio between the photocurrent recorded by the sample and its theoretical photocurrent, *i.e.,* the photocurrent that the electrode would generate if all photons that reach its surface would be transformed into photogenerated electrons:

$$IPCE(\lambda) = \frac{j}{j_{ph}} \tag{3.14}$$

The photon current j_{ph} is defined by the product of the incident photon flux and the elementary charge q:

$$j_{ph}\ (Ph\ A\ cm^{-2}) = q\,(C) \cdot \phi_{ph}\ (Ph\ s^{-1}\ cm^{-2}) \tag{3.15}$$

whereas the photon flux ϕ_{ph} is obtained by dividing the intensity of the monochromatic incident light I, acquired with the use of a photodiode, for the energy of a single photon at a specific wavelength. Keeping in mind that $E = h\,c/\lambda$, ϕ_{ph} becomes:

$$\phi_{ph} = \frac{I\ (mW\ cm^{-2})}{E\,(J\ Ph^{-1})} = \frac{I\,(mW\ cm^{-2}) \cdot \lambda\,(nm)}{h\ (J\ s) \cdot c\,(m\ s^{-1})} \tag{3.16}$$

Finally, **Eq. 3.14** thus becomes:

$$IPCE = \frac{j \cdot h \cdot c}{q \cdot I \cdot \lambda} = \frac{|j\ (mA\ cm^{-2})| \cdot \frac{h(J\ s) \cdot c(m\ s^{-1})}{q(C)}}{I(mW\ cm^{-2}) \cdot \lambda(nm)} \tag{3.17}$$

By multiplying all the constants (Planck's constant *h,* the speed of light *c* and the elemental charge *q)* we obtain the value of 1240 V nm. The final expression is:

$$IPCE = \frac{j\ (mA\ cm^{-2}) \cdot 1240\ (V\ nm)}{I(mW\ cm^{-2}) \cdot \lambda(nm)} \tag{3.18}$$

To better understand the inherent performances of a material it is often helpful to subtract the efficiency losses ascribable to the incident photons that are reflected or transmitted by the sample, measuring efficiency accounting only on the actual absorbed photons, leading to the calculation of the Internal Quantum Efficiency (IQE). IQE helps to determine the optimum balance between the maximum path length for photon absorption versus the minimum effective e^-/h^+ transport distance within the material. IQE is defined as:

$$IQE = \frac{IPCE}{\eta_{e^-\,/\,h^+}} = \eta_{transport} \cdot \eta_{interface} \tag{3.19}$$

The photon absorptance ($\eta_{e^-\,/\,h^+}$) is calculated from Beer's law (**Eq. 3.1**). The assumption is that the number of generated electron-hole pairs is equal to the number of absorbed photons:

$$\eta_{e^-\,/\,h^+} = \frac{I_0 - I}{I_0} = 1 - \frac{I}{I_0} = 1 - 10^{-A} \tag{3.20}$$

From **Eq. 3.18** and **3.19**, IQE can be easily calculated as:

$$IQE = \frac{j \cdot 1240}{I \cdot \lambda \cdot (1 - 10^{-A})} \tag{3.21}$$

Additionally, IPCE measurements offer a simple method to corroborate the photocurrent values measured from the *j-V* curve of a sample.[32] The integration of the IPCE spectra over the AM 1.5G solar spectrum provides the expected photocurrent of the device under full-lamp irradiation, at the fixed potential used to perform the IPCE test. The integrated current density can be determined by **Eq. 3.22**:

$$J_{AM1.5G} = q \int (\phi_{ph} \cdot IPCE)\, d\lambda \tag{3.22}$$

A certain degree of discrepancy between the two measurements can be however expected considering that IPCE measurements are carried out at a single wavelength with a much lower incident light intensity with respect to tests carried out under one sun irradiation.

3.4.1 Experimental procedure and setup

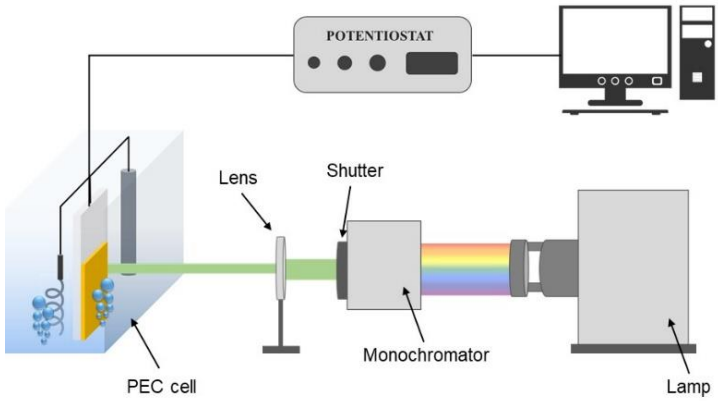

Figure 3.8 Scheme of the experimental setup used to perform IPCE measurements under monochromatic light irradiation.

A typical setup used for such measurements is shown in **Figure 3.8**. It contains many elements already present in the setup described in **Section 3.1.2** (a potentiostat, a 3-electrode PEC cell filled with a suitable electrolyte solution), but it stands out from full-lamp analyses for the illumination source, which is required to be monochromatic.

The light source is usually a Xenon lamp, and a monochromator is used to filter out a narrow part of the emission spectrum, centred around the wavelength of interest. An electronic shutter is used to control the exposure of the sample to the light, and optical lenses are used to focus the light on the sample. If dispersive elements are produced inside the monochromator generating higher orders of diffracted light, long-pass filters must be used to filter these components.[33]

3.4.1.1 Set-up at the Università degli Studi di Milano

IPCE tests were performed by using the potentiostat and the PEC cell described in **Section 3.1.2.1**. The irradiation source was a 300 W Xe lamp (Lot-Oriel). Monochromatic light was produced using a LOT-Oriel Omni-λ 150 monochromator, placed between the Xe lamp and the sample. The current was measured with a 10 nm step-size withing the 300 to 550 nm range; a 490 nm cut-off filter was placed between the monochromator and the sample to measure photocurrents generated at wavelengths longer than 500 nm, to avoid the contribution of shorter wavelength components produced by the second harmonic reflections of the monochromator's grating.

Operationally, a chronoamperometry at a given applied potential (typically the water oxidation potential, 1.23 V vs RHE) was run, while a Thorlabs SC10 automatic shutter was set to alternate 20 s period of light with a 20 s period of dark. The irradiation wavelength was then scanned to obtain a *j vs time* plot, in which every photocurrent peak was ascribed to a different incident λ. IPCE values have been then calculated according to **Eq. 3.18**.

3.5 Electrochemical impedance spectroscopy

The electrical resistance of a circuit element is defined as its ability to resist the flow of electrical current and it is described by Ohm's law, which defines the resistance as the ratio between voltage E and current I.

$$R = \frac{E}{I} \tag{3.23}$$

This well-known relationship is however suitable to describe only an ideal resistor, that is characterized by having a resistance value which is independent of frequency and by an AC current and voltage signals that are in phase with each other. Real circuit elements exhibit much more complex behaviours, leading to the use of impedance, which is a more general circuit parameter. Like resistance, impedance is a measure of the ability of a circuit to resist the flow of electric current, but, unlike resistance, impedance is not limited by the simplifying properties listed above. Electrochemical impedance is usually measured by applying an AC potential to an electrochemical cell and measuring the current after the

perturbation. By applying a sinusoidal potential excitation, the response is a sinusoidal AC current signal at the same frequency but shifted in phase (**Figure 3.9**).[34]

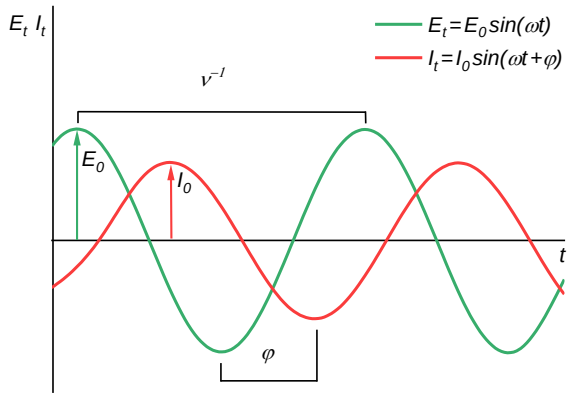

Figure 3.9 Excitation and response signals employed to carry out Electrochemical Impedance Spectroscopy measurements.

The excitation signal, expressed as a function of time, is:

$$E_t = E_0 sin(\omega t) \tag{3.24}$$

where E_t is the potential at time t, E_0 is the amplitude of the signal and ω is the radial frequency (rads/s), obtained from the frequency ν (Hz) as:

$$\omega = 2\pi\nu \tag{3.25}$$

The response signal I_t is shifted in phase (φ) and has a different amplitude I_0:

$$I_t = I_0 sin(\omega t + \varphi) \tag{3.26}$$

An expression analogous to Ohm's law allows us to calculate the impedance of the system as:

$$Z = \frac{E_t}{I_t} = \frac{E_0\, sin(\omega t)}{I_0\, sin(\omega t + \varphi)} = Z_0 \frac{sin(\omega t)}{sin(\omega t + \varphi)} \tag{3.27}$$

The impedance is therefore expressed in terms of a magnitude, Z_0, and a phase shift φ. Using Euler's relationship, $e^{(i\varphi)} = cos(\varphi) + isin(\varphi)$, impedance can be expressed as a complex function, where the potential and the current response are defined as:

$$E_t = E_0\, e^{(i\omega t)}$$
$$I_t = I_0\, e^{(i\omega t+\varphi)} \tag{3.28}$$

The impedance is then defined as:

$$Z(\omega) = \frac{E}{I} = Z_0\, e^{i\varphi} = Z_0(cos\varphi + isin\varphi) = Z' + iZ'' \tag{3.29}$$

Given **Equation 3.29,** impedance can be therefore represented as a vector in the complex plane.

The results obtained through an impedance measurement can be visualized using different plots:[35]

i. The Nyquist plot is produced by plotting the inverse of the imaginary impedance component ($-Z''$) *vs.* the real component (Z'). Each point of this graph refers to the impedance obtained with one of the investigated frequencies. ν increased by moving from the right to the left side of the plot.
ii. In the Bode Module plot the x-axis is the logarithmic scale of the frequency ν and the y-axis is the logarithm of the impedance Z.
iii. The Bode Phase plot represents the phase shift φ vs $logZ$.

3.5.1 Equivalent circuits

Electrochemical Impedance Spectroscopy (EIS) provides the decomposition of the electrical response of the photocatalyst into resistances and capacitances, whose vectorial combination is the general impedance of the sample. The interpretation of these features is a powerful tool to reveal specific kinetic and charge storage properties of the sample employed in the water oxidation reaction. The information obtained through experimental EIS measurements, displayed in the experimental plots described above, has to be analysed in terms of a suitable equivalent circuit (EC), allowing us to extract the capacitances and the resistances kept in the experimental output data, that are related to the electronic processes of charge accumulation, charge separation and charge transfer.[31,36–38] The resistances are associated to different processes of carrier flux, either inside the semiconductor or at the semiconductor/electrolyte interface. On the other side, capacitances represent a charge storage mechanism and can be distinguished among dielectric capacitances, associated to an

internal electrical field produced by a charge separation, or chemical capacitances, generated by the variation of chemical potential or carrier concentration. The discernment of resistances and capacitances is obtained by fitting the experimental data to an EC. The evolution of the capacitances and resistances following the increasing applied voltage give information about the meaning of each element.

If we consider the simple example of a photoelectrode in contact with an electrolyte solution, three electrical responses can be identified and modelled into an equivalent circuit:

1. R_{ct} is the resistance associated with the interfacial charge transfer process,
2. C_{dl} is the surface capacitance associated with the Helmholtz layer at the electrode/electrolyte interface,
3. R_s is the resistance accounting for charge transport across the FTO support, the external circuit and through the electrolyte.

These factors must be deconvoluted from the total resistance of the system by using the adequate equivalent circuit. A frequently used EC is the Randles model, depicted in the inset in **Figure 3.10**.[39,40]

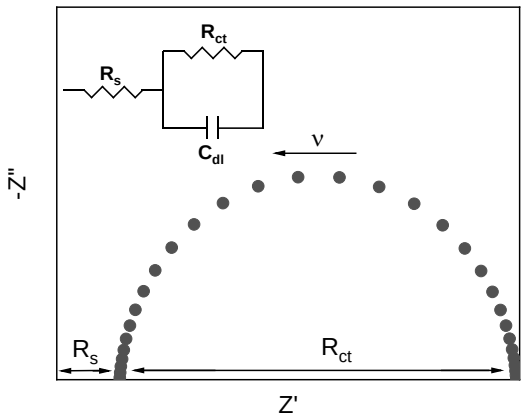

Figure 3.10 The Nyquist plot associated with the Randles equivalent circuit (depicted in the inset).

The Nyquist plot associated with the Randles model consists in a semicircle, whose diameter is equal to R_{ct} and whose initial Z' value corresponds to R_s. In the classical Randles circuit the capacitance is associated with the Helmholtz layer at the electrode/solution interface and affects only R_{ct} in parallel.[41]

In these systems, however, the double-layer capacitance at the electrode is not ideal (*i.e.*, it is not purely capacitive), but it often displays a certain frequency dispersion. Since this behaviour cannot be modelled using a simple circuit consisting of R and C elements, a Constant Phase Element (CPE) is usually used.[42] In such cases, the impedance of an ideal capacitor, $(i\omega C)^{-1}$, is replaced by the impedance of a CPE:

$$Z_{CPE} = \frac{1}{Q}\,(i\omega)^{-n} \tag{3.30}$$

where Q ($\mathrm{F \cdot s^{n-1}}$) is a parameter related to the electrode capacitance and n is the constant phase exponent ($0 < n < 1$) related to the deviation of the behaviour of the capacitor from the ideal conditions. In case in which $\mathrm{n} = 1$ **Equation 3.30** recovers a perfect capacitor.[40] The CPE value obtained by fitting the EIS data can be then used to calculate the capacitance values, using **Equation 3.31**:[43,44]

$$C = \frac{(R_1 \cdot CPE_T)^{1/CPE_P}}{R_1} \tag{3.31}$$

3.5.2 Mott-Schottky analysis

As discussed in **Section 3.3.1**, the flatband potential of a semiconductor could be, theoretically, estimated by measuring the photocurrent onset potential. However, due to the overpotential required to drive the water oxidation reaction, this method fails at estimating $\mathrm{V_{fb}}$ precisely. For this reason, the most widely employed method is the use of the Mott-Schottky equation:[45,46]

$$\frac{1}{C^2} = \frac{2}{\varepsilon\varepsilon_0 A^2 e N_D}\left(V - V_{fb} - \frac{k_B T}{e}\right) \tag{3.32}$$

where C and A are the interfacial capacitance (obtained by means of an EIS analysis) and area, ε is the dielectric constant of the semiconductor, and ε_0 is the permittivity of free space, N_D is the number of donors, V is the applied voltage, k_B is Boltzmann's constant, T the absolute temperature and e is the elemental charge. By plotting $\mathrm{C^{-2}}$ against V a straight line is obtained, from which $\mathrm{V_{fb}}$ can be determined from the intercept on the x-axis. The value of N_D can also be found from the slope of the line, knowing ε and A.

The determination of V_{fb} via the Mott-Schottky equation entails the measurement of the capacity of the electric double layer at the electrode/electrolyte interface. The total capacitance of the double layer consists of two contributions: the semiconductor capacitance and the capacitance of the Helmholtz layer. The first varies with the extent of the band bending, whereas the capacitance of the Helmholtz layer is expected to remain constant. This often leads to the assumption that the total capacitance is similar to that of the semiconductor, and the contribution of the Helmholtz layer is negligible.[47] This simplification is however not always valid and, especially for highly doped semiconductors ($N_D > 10^{23}$ m^{-3}), an experimentally determined interfacial capacitance should be corrected by the capacitance of the Helmholtz layer in order to obtain meaningful Mott–Schottky plots. Recently, an analytical resolution limit was derived, below which doping densities cannot be measured in a capacitance measurement.[48] If a calculated doping density is close or below the resolution limit, it can only be considered as an upper limit to the actual doping density in the photoanode.

3.5.3 Experimental procedure and setup

Experimentally, an Electrochemical Impedance Spectroscopy measurement is performed by superimposing a sinusoidal AC potential to our system, at a given fixed applied potential. The module of the perturbation is usually small (around 10 mV) to respect the linearity derived in **Eq. 3.29**. The module and the phase shift of the resulting alternating current are then analysed. This process is repeated amongst a large range of frequencies, typically spanning from 10^5 to 10^{-1} Hz.

3.5.3.1 Set-up at the Institute of Advanced Materials (INAM)

EIS measurements were performed using an Autolab PGSTAT 302 (Metrohm) potentiostat controlled by the NOVA software; the PEC cell was a 3-electrode glass cell equipped with an Ag/AgCl reference electrode and a Pt wire as counter electrode. Solar simulated irradiation was provided by a LED-based solar simulator (SUNBOX) electronically controlled through a PC using an Arduino microcontroller.[49]

3.6 UV-Vis-NIR Spectroelectrochemistry

As outlined in **Section 3.2.1**, UV-Vis spectroscopy is a widely used technique to study the optical properties and reaction kinetics of the photocatalysts, especially of heterogeneous ones.[50–52] When this method is coupled with electrochemical experiments the technique takes the name of UV-Vis spectroelectrochemistry (SEC), that was first implemented in the 1960s.[53] Exploiting these combined experiments the oxidation states and concentration changes in the photocatalyst can be monitored by probing their absorption fingerprint and quantified through the well-known Lambert-Beer Law.[54] In UV-Vis SEC the absorbance is measured while simultaneously monitoring the current flowing through the circuit, enabling a correlation between the current and the optical responses as a function of the applied potential. When electrochemical reactions are taking place, metal oxides undergo chemical and structural changes that can manifest in alterations of their electronic and atomic structure, directly linked to electronic transitions (d–d or ligand–metal changer transfer), which can be then monitored by UV-Vis spectroscopy, as different electronic and vibrational transitions absorb incident radiation at different wavelengths (see **Figure 3.11**).

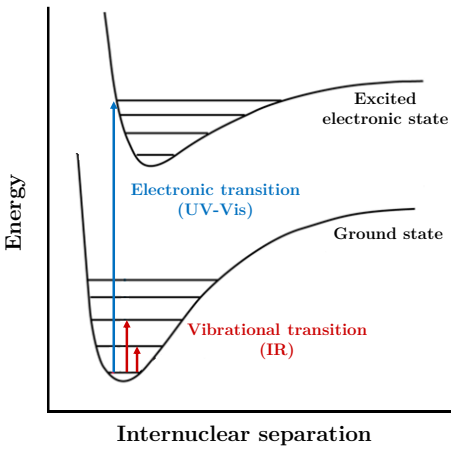

Figure 3.11 Electronic and vibrational transitions and their corresponding absorbing range.

In a typical SEC experiment, the initial potential of the cell is set such that no redox processes are initiated. The applied potential is then gradually scanned or stepped to induce electron transfer, and absorption spectra are recorded over this range of potentials. A series of reaction intermediates, as well as catalysis products, can then be detected and identified, provided each has a unique spectroscopic signature.[55]

3.6.1 Experimental procedure and setup

Spectroelectrochemical analyses are usually performed by placing a photoelectrochemical cell into the sample compartment of a chosen spectrophotometer instrument. Attention must be drawn both on the choice of a suitable PEC cell to be employed for this technique and on the investigated material: the transmission of the incident irradiation throughout the cell and the sample towards the detector of the instrument must be assured.[56] Typically, at the beginning of each experiment, a background UV-Vis spectrum of the system is taken to be employed as a blank. Successively, the sample is immersed in the PEC cell, connected to a potentiostat and its absorbance spectrum is measured. Depending on the scopes of the analysis, the absorbance of the sample can be recorded by scanning the incident wavelength over a set range, or a single incident wavelength can be chosen, performing a monochromatic analysis. Then, different spectra are recorded after the application of different biases. SEC data as a function of applied potential are generally presented as difference spectra (ΔO.D.), which are obtained by subtracting a reference spectrum (often the one recorded at the open circuit potential or the initial absorbance spectrum) from the spectra collected at the potential of interest.[57] These difference spectra are then characteristic of the species evolved or altered as a result of the applied change in the experimental conditions.

3.6.1.1 Set-up at the Institute of Advanced Materials (INAM)

UV-Vis-NIR spectroelectrochemical measurements were performed using a PerkinElmer Lambda 1050+ UV/Vis/NIR spectrophotometer. The PEC cell was a 3-electrode glass cell equipped with an Ag/AgCl reference electrode and a Pt wire as counter electrode. The external applied potential was controlled using a PalmSens4 portable potentiostat.[58]

References

1. J. Lin, *Proc. Int. Meet. Inf. Disp.* 8 (**2008**) 1247–1250.
2. C.R. Lhermitte, A. Polo, L. Yao, F.A. Boudoire, N. Guijarro, K. Sivula, *ChemSusChem* 13 (**2020**) 3645–3653.
3. N. Sahu, B. Parija, S. Panigrahi, *Indian J. Phys.* 83 (**2009**) 493–502.
4. A. Polo, C. Nomellini, I. Grigioni, M.V. Dozzi, E. Selli, *ACS Appl. Energy Mater.* 3 (**2020**) 6956–6964.
5. J. Su, L. Guo, N. Bao, C.A. Grimes, *Nano Lett.* 11 (**2011**) 1928–1933.
6. J. Su, X. Feng, J.D. Sloppy, L. Guo, C.A. Grimes, *Nano Lett.* 11 (**2011**) 203–208.
7. B.R. Lee, M.G. Lee, H. Park, T.H. Lee, S.A. Lee, S.S.M. Bhat, C. Kim, S. Lee, H.W. Jang, *ACS Appl. Mater. Interfaces* 11 (**2019**) 20004–20012.
8. T.G. Mayerhöfer, J. Popp, *ChemPhysChem* 20 (**2019**) 511–515.
9. Y. Liang, T. Tsubota, L.P.A. Mooij, R. Van De Krol, *J. Phys. Chem. C* 115 (**2011**) 17594–17598.
10. D. Sengupta, P. Das, B. Mondal, K. Mukherjee, *Renew. Sustain. Energy Rev.* 60 (**2016**) 356–376.
11. F. Wang, C. Di Valentin, G. Pacchioni, *J. Phys. Chem. C* 115 (**2011**) 8345–8353.
12. J.E. Yourey, B.M. Bartlett, *J. Mater. Chem.* 21 (**2011**) 7651–7660.
13. J.K. Cooper, S. Gul, F.M. Toma, L. Chen, Y.S. Liu, J. Guo, J.W. Ager, J. Yano, I.D. Sharp, *J. Phys. Chem. C* 119 (**2015**) 2969–2974.
14. Lord Reyleigh, *London, Edinburgh, Dublin Philos. Mag. J. Sci.* 8 (**1879**) 261–274.
15. Microscopy Australia, MyScope, n.d. https://myscope.training/.
16. W.L. Bragg, *Proceeding R. Soc. A* 89 (**1913**) 248–77.
17. K. Inaba, *Rigaku J.* 24 (**2008**) 10–15.
18. T.F. Jaramillo, T.G. Deutsch, N. Gaillard, H.N. Dinh, *J. Mater. Res.* 25 (**2010**) 3–16.
19. K. Sivula, *J. Phys. Chem. Lett.* 4 (**2013**) 1624–1633.
20. H. Dotan, K. Sivula, M. Graetzel, S.C. Warren, *Energy Environ. Sci.* 4 (**2011**) 958–964.
21. Y. Park, D. Kang, K.S. Choi, *Phys. Chem. Chem. Phys.* 16 (**2014**) 1238–1246.
22. P. Iwanski, J.S. Curran, W. Gissler, R. Memming, *J. Electrochem. Soc.* 128 (**1981**) 2128–2133.
23. X. Zhu, N. Guijarro, Y. Liu, P. Schouwink, R.A. Wells, F. Le Formal, S. Sun, C. Gao, K.

Sivula, *Adv. Mater.* 30 (**2018**) 1–6.

24. ASTM International, Standard AM0 and AM1.5 Spectra, **2007**.

25. A. Polo, I. Grigioni, M. Magni, A. Facibeni, M. Vittoria Dozzi, E. Selli, *Appl. Surf. Sci.* 556 (**2021**) 149759.

26. G.L. Chiarello, M. Bernareggi, M. Pedroni, M. Magni, S.M. Pietralunga, A. Tagliaferri, E. Vassallo, E. Selli, *J. Mater. Chem. A* 5 (**2017**) 12977–12989.

27. T. Hisatomi, J. Kubota, K. Domen, *Chem. Soc. Rev.* 43 (**2014**) 7520–7535.

28. C. Santato, M. Odziemkowski, M. Ulmann, J. Augustynski, *J. Am. Chem. Soc.* 123 (**2001**) 10639–10649.

29. A. Polo, F. Boudoire, C.R. Lhermitte, Y. Liu, N. Guijarro, M.V. Dozzi, E. Selli, K. Sivula, *J. Mater. Chem. A* (**2021**) 27736–27747.

30. I. Grigioni, A. Corti, M.V. Dozzi, E. Selli, *J. Phys. Chem. C* 122 (**2018**) 13969–13978.

31. T. Lopes, L. Andrade, H.A. Ribeiro, A. Mendes, *Int. J. Hydrogen Energy* 35 (**2010**) 11601–11608.

32. J.A. Christians, J.S. Manser, P. V. Kamat, *J. Phys. Chem. Lett.* 6 (**2015**) 852–857.

33. R. van de Krol, M. Graetzel, Photoelectrochemical Hydrogen Production, Springer US, **2012**.

34. Gamry Instruments, Basics of Electrochemical Impedance Spectroscopy, n.d.

35. J. Huang, Z. Li, B.Y. Liaw, J. Zhang, *J. Power Sources* 309 (**2016**) 82–98.

36. S. Giménez, J. Bisquert, Photoelectrochemical Solar Fuel Production, Springer, **2016**.

37. D. Klotz, D.A. Grave, H. Dotan, A. Rothschild, *J. Phys. Chem. Lett.* 9 (**2018**) 1466–1472.

38. B. Klahr, S. Giménez, F. Fabregat-Santiago, J. Bisquert, T.W. Hamann, *J. Am. Chem. Soc.* 134 (**2012**) 16693–16700.

39. J.E.B. Randles, *Discuss. Faraday Soc.* 1 (**1947**) 11–19.

40. J. Bisquert, G. Garcia-Belmonte, P. Bueno, E. Longo, L.O.S. Bulhões, *J. Electroanal. Chem.* 452 (**1998**) 229–234.

41. B. Klahr, S. Giménez, F. Fabregat-Santiago, T. Hamann, J. Bisquert, *J. Am. Chem. Soc.* 134 (**2012**) 4294–4302.

42. A. Lasia, Electrochemical Impedance Spectroscopy and its Applications, Springer, **2014**.

43. Y.Y. Proskuryakov, K. Durose, M.K. Al Turkestani, I. Mora-Seró, G. Garcia-Belmonte, F. Fabregat-Santiago, J. Bisquert, V. Barrioz, D. Lamb, S.J.C. Irvine, E.W. Jones, *J. Appl. Phys.* 106 (**2009**).

44. I. Mora-Seró, S. Giménez, F. Fabregat-Santiago, E. Azaceta, R. Tena-Zaera, J. Bisquert, *Phys. Chem. Chem. Phys.* 13 (**2011**) 7162–7169.

45. K. Gelderman, L. Lee, S.W. Donne, *J. Chem. Educ.* 84 (**2007**) 685–688.

46. K. Sivula, *ACS Energy Lett.* 6 (**2021**) 2549–2551.

47. A. Hankin, F.E. Bedoya-Lora, J.C. Alexander, A. Regoutz, G.H. Kelsall, *J. Mater. Chem. A* 7 (**2019**) 26162–26176.

48. S. Ravishankar, J. Bisquert, T. Kirchartz, *Chem. Sci.* 13 (**2022**) 4828–4837.

49. E. López-Fraguas, J.M. Sánchez-Pena, R. Vergaz, *IEEE Trans. Instrum. Meas.* 68 (**2019**) 4913–4923.

50. A. Polo, I. Grigioni, M.V. Dozzi, E. Selli, *Catal. Today* 340 (**2020**) 19–25.

51. I. Grigioni, M. Abdellah, A. Corti, M.V. Dozzi, L. Hammarström, E. Selli, *J. Am. Chem. Soc.* 140 (**2018**) 14042−14045.

52. M. Waimbo, G. Anduwan, O. Renagi, S. Badhula, K. Michael, J. Park, S. Velusamy, Y.S. Kim, *J. Photochem. Photobiol. B Biol.* 204 (**2020**) 111781.

53. T. Kuwana, R.K. Darlington, D.W. Leedy, *Anal. Chem.* 36 (**1964**) 2023–2025.

54. C.A. Mesa, E. Pastor, L. Francàs, *Curr. Opin. Electrochem.* 35 (**2022**) 101098.

55. K.J. Lee, N. Elgrishi, B. Kandemir, J.L. Dempsey, *Nat. Rev. Chem.* 1 (**2017**).

56. Y. Zhai, Z. Zhu, S. Zhou, C. Zhu, S. Dong, *Nanoscale* 10 (**2018**) 3089–3111.

57. L. Francàs, S. Corby, S. Selim, D. Lee, C.A. Mesa, R. Godin, E. Pastor, I.E.L. Stephens, K.S. Choi, J.R. Durrant, *Nat. Commun.* 10 (**2019**) 1–10.

58. R.R. Rao, S. Corby, A. Bucci, M. García-Tecedor, C.A. Mesa, J. Rossmeisl, S. Giménez, J. Lloret-Fillol, I.E.L. Stephens, J.R. Durrant, *J. Am. Chem. Soc.* 144 (**2022**) 7622–7633.

Chapter 4 - Ni(II)-doped $CuWO_4$ thin film photoanodes

4.1 Abstract

Ternary metal oxides have attracted increasing attention for their application as photoanodes in photoelectrochemical cells, due to their easily tunable band gap and band edge positions. Among these materials, $CuWO_4$ has emerged in the last years has a promising candidate thanks to its relatively narrow band gap of ~2.3 eV, its high stability and selectivity towards the oxygen evolution reaction. However, its poor charge separation efficiency highly limits its photoelectrochemical performance and very few studies have focused on exploring new strategies to overcome this limitation. In this work, for the first time we succeeded in preparing, via spin coating technique, optically transparent $CuWO_4$ thin films containing different amounts of Ni(II) ions, in order to investigate whether the substitution of Cu(II) ions in the copper tungstate structure may lead to a beneficial effect on the performance of this material. The prepared films have been fully characterized via UV-Vis spectroscopy, XRD analyses and SEM images and their PEC performances have been tested via LSV, IPCE and IQE analyses. Finally, charge injection and separation efficiencies of the prepared electrodes were derived by testing the photoanodes in the presence of a hole scavenger containing electrolyte. We successfully obtained pure-phase crystalline materials that exhibit

higher PEC performances with respect to pure $CuWO_4$, due to a significantly enhanced charge separation efficiency in the bulk of the material.

4.2 Introduction

As discussed earlier in **Chapter 2**, the majority of photocatalysts employed for the water oxidation reaction have semiconductor properties and combine high efficiency, stability and low-cost characteristics.[1,2] Interest has been recently drawn on ternary metal oxides as efficient photoanodes for the water oxidation reaction, over the largely studied binary oxides such as WO_3 and TiO_2 that are usually characterized by relatively large band gap values and are thus able to harvest only a minimal part of the visible solar spectrum.[3–5] Ternary oxides usually possess metal-based d orbitals and O(2p) orbitals that co-contribute to the building of valence band maxima, and open the possibility of fine-tuning the position of valence and conduction bands as well as the band gap energy.[6–8] As of today, $BiVO_4$ is the most studied and best-performing ternary oxide,[9–11] while other multicomponent materials such as $ZnFe_2O_4$ and $CuWO_4$ are emerging.[12–16]

$CuWO_4$ is a n-type semiconductor and it is a promising candidate to work as a photoanode in a photoelectrochemical cell, due to its relatively small band gap of ~2.3 eV, its stability when subjected to the highly oxidizing conditions of the O_2 evolution reaction and its high selectivity towards the oxygen evolution reaction.[17,18] This material could potentially mitigate frequent problems common to most oxide semiconductors such as the stability in neutral or basic aqueous solutions. In fact, it is stable and best performing when subjected to the highly oxidizing condition of PEC oxygen evolution reaction up to pH 9.[19] Despite these promising characteristics and a maximum theoretical photocurrent density of 9 mA cm^{-2},[20] the performances obtained until now with copper tungstate photoelectrodes are far from its theoretical potentials.[21,22] PEC applications of this material are penalised by its indirect band gap, a low electronic conductivity in the bulk and the presence of electronic surface states.[23–25] Bartlett et al. demonstrated through Electrochemical Impedance Spectroscopy that the onset of photocurrent in $CuWO_4$ thin-film electrodes is dictated by the presence of a midgap state that participates in water oxidation and that it is likely composed of Cu(3d) orbitals.[26] More recently, these midgap states have been energetically located at

0.51 V_{RHE} due to the presence of Fermi level pinning in Mott-Schottky plots.[27] Photogenerated holes from the VB can either directly oxidize water or become trapped in the intra-band gap state and react with water molecules. However, these midgap states may also favor detrimental charge recombination processes, limiting the carrier mobility.[24,28]

To overcome the intrinsic limitations of this material different strategies have been addressed: many studies have been conducted on building heterojunctions with other photocatalysts such as WO_3 and $BiVO_4$,[29–31] tuning its surface defectivity by treating the material with gaseous hydrogen,[7,15] or coat $CuWO_4$ with cocatalysts such as MnPO or Ni/Fe.[22,32] Doping with other metal elements has been investigated since D. Bohra and W.A. Smith firstly reported the successful doping of $CuWO_4$ attained by substituting copper with Fe(III) ions,[33] resulting in Fe(III)-doped photoanodes which presented increased photocurrent and separation efficiency. From then, only a very limited amount of studies have focused on identifying alternative suitable elements to substitute Cu^{2+} in copper tungstate's crystalline structure.[34] More attention has been drawn on substituting Mo^{6+} for W^{6+} ions, which has led to visible-light sensitised photoanodes characterized by an extended band gap energy,[35,36] and on preparing morphology-controlled photoanodes possessing increased surface areas.[37,38]

In this Chapter we investigate the optical, structural and photoelectrochemical properties of $CuWO_4$ thin films photoanodes containing different amounts of Ni(II) ions with the aim of finding alternative dopants. Nickel ions were chosen as dopants due to their ionic radius similar to that of Cu^{2+}, allowing a favorable substitution of copper ions into the lattice. Previous studies have focused on building a $CuWO_4/NiWO_4$ heterojunction,[39] and the few studies concentrated on nickel-containing copper tungstate materials have been tested in other photocatalytic applications.[40–42]

Our results evidence an increased photocurrent generated by Ni(II)-doped photoanodes with respect to pure $CuWO_4$, with 10% doping leading to the best performances, due to a comparable charge injection efficiency with respect to copper tungstate, while exhibiting a 50% increase in the charge separation efficiency.

4.3 Experimental section

4.3.1 Materials

The following chemicals were purchased from Sigma Aldrich and were used as supplied: copper(II) nitrate trihydrate (99%), ammonium metatungstate hydrate (99%), nickel(II) nitrate hexahydrate (99%), citric acid (99%), boric acid (99%), potassium hydroxide (85%) and ethanol (99%).

4.3.2 Photoelectrodes preparation

To obtain 1 ml of 0.5 M $CuWO_4$ precursor solution 0.2703 g of citric acid, 0.1220 g of $Cu(NO_3)_2{\cdot}3H_2O$ and 0.1239 g of $(NH_4)_6H_2W_{12}O_{40}{\cdot}xH_2O$ were added to 0.77 ml of a 2:1 ethanol/water solution. The solution was then stirred for about 10 min to fully dissolve the powders, thus obtaining a blue paste. This solution was later deposited on a 2 mm-thick Fluorine-doped Tin Oxide (FTO) glass (Kintec Glass, 7-ohm/sq) by spin coating at 4000 rpm for 30 s. Prior to deposition the FTO glass was cleaned by 30 min-long sonication in a soap solution, then washed carefully, sonicated in ethanol for 30 min and finally dried in air. A 15-minute UV-cleaner ozone treatment was performed onto the clean glass slices in order to increase the hydrophilicity of the FTO surface. Finally, the slices were soaked in isopropanol for a few seconds right before deposition, to reduce the light scattering of the prepared films in the long-wavelength spectral region. The so-prepared copper tungstate electrodes were then dried in air on a hotplate at 250 °C for 10 min and later annealed at 550 °C for 1 hour.

Ni(II)-doped $CuWO_4$ photoanodes were prepared following the synthesis described in a previous work.[33] In order to dope only the copper site, 50 µl of equimolar W(VI) and Ni(II) precursor solutions were added to 1 ml of the previously prepared $CuWO_4$ paste, attaining $Cu_{1-x}Ni_xWO_4$ samples. The Ni(II)-containing solutions were then deposited onto FTO glass and successively annealed with the same procedure used for the pure material. Three different doping percentages have been investigated in this work, corresponding to a Ni(II) doping content of 1, 10 and 25% with respect to the concentration of Cu(II) ions. The investigated doping percentages have been chosen to study the behaviour of the electrodes in the presence

of either very modest or significant amounts of doping, with the aim of stressing the possible differences in terms of photoelectrochemical performance of the electrodes.

4.3.3 Optical, morphological and photoelectrochemical characterizations

UV-Visible absorption spectra were recorded in transmission mode using a Jasco V-670 spectrophotometer. Structural information on the electrodes was obtained through X-Ray Powder Diffraction (XRPD) analyses, employing a X'Pert PRO PANalytical diffractrometer equipped with a Cu sealed tube. The morphologies of pure $CuWO_4$ and $CuWO_4$-Ni(II) 25% samples were investigated by means of top-view images acquired using a scanning electron microscope (SEM), model Jeol JSM-7600F with a 5 kV incident beam. Energy dispersive X-ray spectroscopy (EDX) was used to quantify the elemental composition of $CuWO_4$ and $CuWO_4$-Ni(II) 25% samples and verify the experimental atomic percentages of the prepared electrodes.

Linear Sweep Voltammetry (LSV) measurements were performed using a three-electrode glass cell with two quartz windows. The FTO/$CuWO_4$ photoanodes were employed as working electrodes, while an Ag/AgCl (3.0 M NaCl) electrode and a platinum gauze were used as reference and counter electrode, respectively; an Autolab PGSTAT 12 was employed as potentiostat. The light source was provided by an Oriel, Model 81172 Solar Simulator equipped with an AM 1.5G filter (1 Sun). The incident light intensity was fixed at 100 mW cm^{-2} and measured by means of a Thorlabs PM200 power meter equipped with a S130VC power head with Si detector.

The prepared photoanodes were tested both in back-side (through the FTO side) and front-side (through the deposited film side) illumination configuration in a 0.1 M H_3BO_3 electrolyte solution, buffered at pH 9 by the addition of KOH (KBi). LSV tests have been performed also in the presence of a hole scavenger species, $NaNO_2$. From our previous work, a 0.1 M $NaNO_2$ solution in 0.1 M KBi at pH 9 resulted to be the best suited hole scavenger-containing electrolyte to test this type of materials among numerous alternatives (Na_2SO_3, H_2O_2, NH_3), displaying a negligible dark current while increasing the photocurrent density of

the sample.[35] The potential vs. Ag/AgCl was converted to the RHE scale using the following equation: $E_{RHE} = E_{AgCl} + 0.059pH + E°_{AgCl}$, with $E°_{AgCl}$ (3.0 M NaCl) = 0.210 V at 25 °C.

Incident photon to current efficiency (IPCE) measurements were carried out using a 300 W Lot-Oriel Xe lamp as light source, equipped with a Lot-Oriel Omni-λ 150 monochromator and a Thorlabs SC10 automatic shutter in the same three-electrode cell described above. An external bias of 1.23 V vs RHE was applied in all measurements and the photocurrent was recorded with a 10 nm step within the 300 and 550 nm range. IPCE values were calculated at each wavelength λ using the following equation:

$$IPCE\% = \frac{j \cdot 1240}{P_\lambda \cdot \lambda} \cdot 100 \qquad (4.1)$$

where j is the photocurrent density (mA cm^{-2}) and P_λ (mW cm^{-2}) is the power of the monochromatic light at a specific wavelength λ (nm).

Since IPCE profiles do not include losses of incident photons that are reflected or transmitted, it is often more accurate, to understand the inherent performance of a material, to measure efficiency based only on the photons absorbed by the sample. We therefore determined the Internal Quantum Efficiency (IQE) of our photoanodes, which is defined as:

$$IQE\% = \frac{IPCE\%}{\eta_{e^- / h^+}} \qquad (4.2)$$

where η_{e^-/h^+} is the absorptance, defined as the fraction of electron-hole pairs generated per incident photon flux.

4.4 Results

4.4.1 Photoanodes characterization

The UV-Vis absorption spectra of pure and Ni(II)-doped $CuWO_4$ photoanodes are reported in **Fig. 4.1a**. The absorption profile of pure $CuWO_4$ (*i.e.* $CuWO_4$ 0%) indicates the attainment of an indirect band gap material characterized by a low absorption coefficient,

which exhibits an absorption onset located at *ca.* 530 nm, consistent with the ~2.3 eV band gap previously reported for this material.[14]

The absorption spectra of the doped samples appear similar in shape to that of the pure material. This could suggest that the investigated doping percentages of Ni^{2+} do not influence the band gap energy of copper tungstate or its electronic structure: the absorption onset is comparable for all electrodes. However, the doped samples exhibit a slightly lower absorption intensity compared to pure $CuWO_4$, with a decreasing absorbance maximum with increasing doping content.

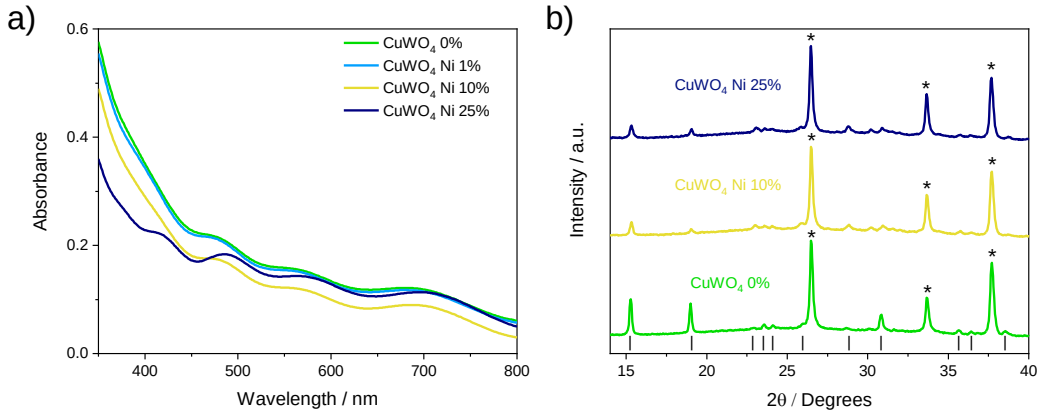

Figure 4.1. (a) UV-Vis absorption spectra of pure and Ni(II)-doped $CuWO_4$ electrodes and (b) X-rays diffraction patterns on pure, 10% and 25% Ni(II)-doped $CuWO_4$; the peaks indicated with * are ascribed to the FTO substrate and the evidenced peaks are attributed to the crystalline structure of $CuWO_4$.

Fig. 4.1b reports the XRD patterns of pure $CuWO_4$ and of the two samples containing the largest Ni(II) percentages (10% and 25%); these measurements aimed at confirming the attainment of a pure-phase, crystalline materials even in the presence of an elevated nickel content. As expected, all photoanodes display the characteristic diffraction peaks ascribable to a triclinic wolframite structure, which has been reported for pure $CuWO_4$ electrodes in previous studies.[17,18] This confirms our hypothesis that a doping amount up to 25% does not alter the crystalline structure of $CuWO_4$ and does not cause the formation of a minority phase. Although XRD patterns did not detect the presence of any impurity phase, the relative intensity of the diffraction peaks is altered by doping. Pure $CuWO_4$ presents peaks with higher relative intensity at 15.3, 19.0 and 30.8°, corresponding to the (010), (100) and (111) crystal faces of $CuWO_4$, respectively,[43,44] with respect to the nickel-containing samples. A recent experimental study, supported by DFT calculations, evidenced that

$CuWO_4$ films with a higher exposure of the (100) facet were characterized by promoted charge transport and favored oxygen evolution reaction kinetics.[44]

The top-view SEM images of $CuWO_4$ and $CuWO_4$ Ni(II) 25% are shown in **Fig. 4.2**. The surface morphology of the two electrodes can be observed with a detail in the hundreds of nanometer scale. While both samples show a planar surface and a structure composed of densely aggregated crystallites, that homogeneously cover the FTO underlayer with no sign of phase segregation, we notice a clear difference in the size of aggregates when passing from a doping-free photoanode (**Fig. 4.2a**) to that containing a fairly high Ni(II) content (**Fig. 4.2b**). In particular, pure $CuWO_4$ presents surface particles with sizes spanning from *ca.* 200 to *ca.* 250 nm, while the $CuWO_4$-Ni(II) 25% sample shows much smaller aggregates, with dimensions within the 70-100 nm range. Thus, smaller surface particles dimensions could be directly linked to a better contact between the material and the electrolyte, due to a higher surface area of the former.[19] Higher surface areas have been also linked to a facilitated separation of the photogenerated charge carries.[45]

Based on our previous work, in which samples were prepared by coating the conductive substrate with precursor solutions of comparable concentration, the thickness of which was evaluated via SEM cross-section images, we can estimate that the thickness of the monolayer photoelectrodes described in this Chapter is *ca.* 80 nm.[27]

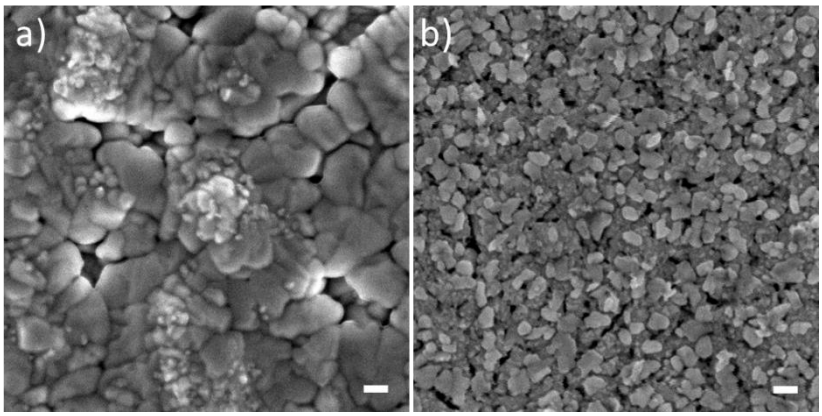

Figure 4.2. Top-view SEM images of a) pure $CuWO_4$ and b) $CuWO_4$ Ni(II) 25%. The scale bar is 100 nm.

EDX analyses were then carried out together with the acquisition of the SEM images. EDX plots resulting from these analyses are reported in their integrity in the Appendix found at the end of this Chapter (**Figure A1**). The elemental composition of the two above-

mentioned photoelectrodes has been calculated excluding the contribution of oxygen atoms and it is reported in **Table 4.1**. The composition of the pure copper tungstate electrode perfectly matches the theoretical composition of the oxide, in which the atomic percentage of the two transition metals are comparable and the 1:1 Cu/W stoichiometry is respected. The EDX results obtained with the nickel-doped sample allowed us to confirm the presence of Ni(II) ion doping into the copper tungstate structure. We also gathered evidence of effective doping of the Cu site only, the atomic percent amount of W being close to 50%, similar to that of the pure sample. This is an indirect confirmation of the validity of the experimental methodology we followed to synthesize the doped samples.

We were also able to verify the effective doping content, by calculating the ratio between the nickel content and the sum of copper and tungsten atoms content. This is ca. 8.6%, much lower than the expected nominal doping of 25%. The attainment of these divergent result could be explained with a combination of factors. An intrinsic dopant loss due to evaporation during the synthesis and annealing process should be always taken into account,[46] while at the same time the extremely reduced thickness of the samples could contribute to the failure of precise quantitative results. However, we were still able to gain a qualitative proof of the incorporation of nickel ions into the copper tungstate structure.

$CuWO_4$ 0%		**$CuWO_4$ Ni(II) 25%**	
Element	**Atom% norm.**	**Element**	**Atom% norm.**
Cu	49.93	Cu	42.56
W	50.07	W	49.56
Ni	n.d.	Ni	7.88

Table 4.1. Normalized elemental composition of pure and Ni(II) 25%-doped $CuWO_4$ photoanodes obtained through EDX analysis.

4.4.2 Photoelectrochemical tests

The linear sweep voltammetry (LSV) curves obtained by testing the photoanodes under simulated solar light illumination are reported in **Fig. 4.3**. A common trend can be identified in the spectra recorded under back- and front-side illumination. All samples display a similar

photocurrent onset at *ca.* 0.9 V vs RHE, which is ~400 mV more positive than the CB edge of the material.[19] Photoelectrochemical tests provide information not only in terms of generated photocurrent density, but also from the shape of the obtained *j-V* curves. A system with high quantum efficiency should produce a photocurrent onset starting from a potential close to the CB edge energy value. In the present case, the heavily delayed onset is a clear evidence of a slow reaction kinetics that proceeds through midgap electronic states, as anticipated in the introduction of this Chapter.[26]

The pristine copper tungstate sample is characterized by very modest performances in terms of photogenerated current, reaching a 0.2 mA cm^{-2} value at 1.8 V vs RHE, in agreement with results previously reported for electrodes of similar thickness.[47] In terms of photoactivity, the sample containing the lowest nickel concentration (1%) generates photocurrents very similar to pure $CuWO_4$ throughout all applied potential range. Possibly, as the actual doping amount is lower than 1% as hypothesized in **Section 3.1**, the effective loading of the dopant is not sufficient to produce a significant photocatalytic effect on the $CuWO_4$-Ni(II) 1% sample.

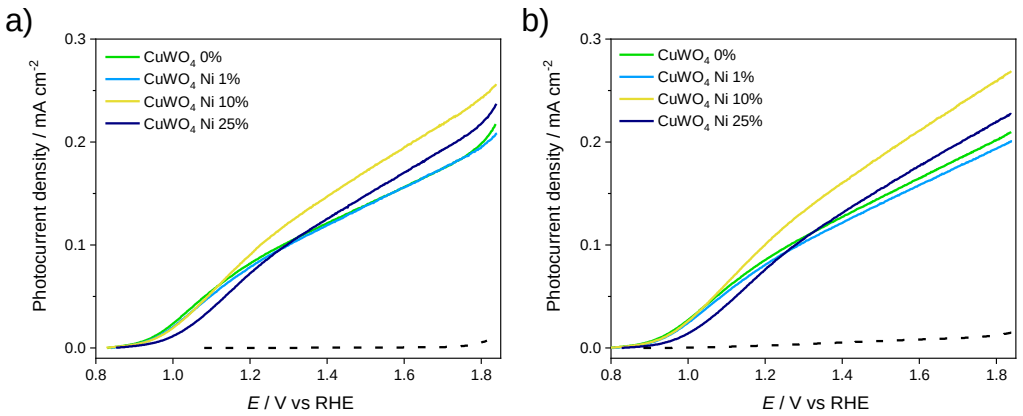

Figure 4.3. Linear Sweep Voltammetry (LSV) curves of pure and Ni(II)-doped $CuWO_4$ electrodes in KBi 0.1 M at pH 9 in (a) back- and (b) front-side illumination configuration. Dashed lines represent scans in the dark.

On the contrary, the electrodes containing the higher nickel amount shows a different trend. In particular, $CuWO_4$-Ni(II) 10% results is the best performing electrode among all the investigated photoanodes, displaying higher photocurrents already at low potentials (1.1 V vs RHE) and generating a >0.1 mA cm^{-2} photocurrent at the water oxidation potential. At the same time, $CuWO_4$-Ni(II) 25% shows a slightly delayed photocurrent onset and increased photocurrents (with respect to the 0 and 1%-Ni(II) containing electrodes) at potentials higher than 1.4 V vs RHE. Notably, comparable photocurrent intensities were

generated by the photoanodes under both illumination configurations (see **Fig. 4.3a** and **Fig. 4.3b**). This suggests that the charge carriers, *i.e.* holes and electrons photogenerated in our material have similar transport properties.[48]

An additional sample with a nominal 50% doping amount has been preliminary tested in order to assess if a higher doping content could lead to further advantages. The LSV analyses of this sample, reported in the Appendix of this Chapter (**Figure A2**), indicate that such high doping percentage was found to be detrimental for the sample's PEC performance.

The activity of the photoelectrodes under irradiation with light at different wavelengths was studied through IPCE and IQE analyses, to further investigate the efficiency trends of these samples. The results are reported in **Figure 4.4**.

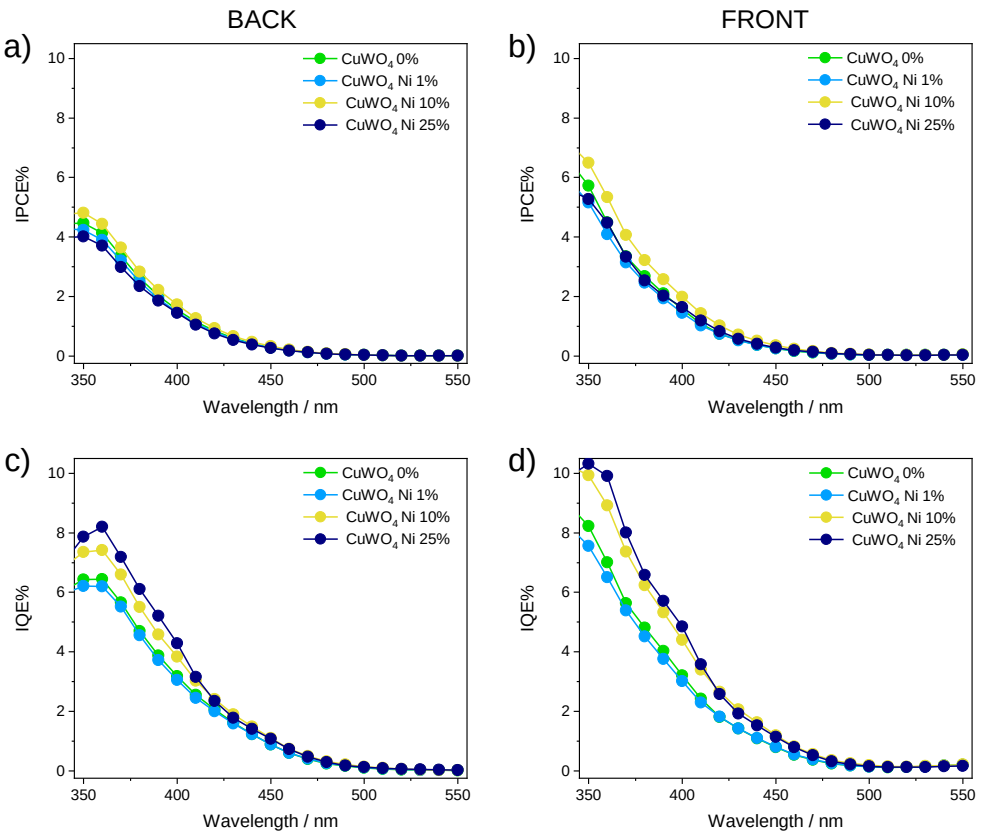

Figure 4.4. a), b) IPCE% and c), d) IQE% of pure and Ni(II)-doped $CuWO_4$ photoanodes in back- and front-side configuration.

Fig. 4.4 depicts the IPCE and IQE values calculated under monochromatic irradiation of the samples both in back- and front-side configurations. The efficiencies

reported in **Fig. 4.4a** and **b**, that do not take into account the absorptance of the samples and, hence, do not take into account the contribution of transmitted or scattered incident photons on the samples, are in accordance with the full-lamp analyses described above, in which the 10%-nickel containing electrode results to the best performing photoelectrode, displaying the highest efficiency values throughout the investigated wavelengths range, both under back-side (**Fig. 4.4a**) and front-side (**Fig. 4.4b**) irradiation configuration.

However, it is difficult to identify a clear activity trend among the other samples, since their performances both under full lamp and monochromatic irradiation are very similar at the applied potential of the water oxidation reaction. Internal Quantum Efficiency analyses could therefore offer a more accurate tool for evaluating the intrinsic efficiency of the electrodes, since the number of incident photons effectively absorbed by the investigated material are taken into account.

Fig. 4.4c and **d** show the IQE% values obtained with pure and $CuWO_4$ doped samples under back- and front-side illumination, respectively. Compared to the IPCE plots, it is easier to distinguish more clearly the performances of the different electrodes, whose activity trends result more diversified. As observed under full-lamp irradiation, pure copper tungstate and $CuWO_4$-Ni(II) 1% samples exhibit comparable performances, reaching IQE values of 6 and 8% under back- and front-side illumination, respectively. Again, samples possessing a relative high nickel content show better activity throughout the whole set of investigated wavelengths. This indicates that, as already pointed out by absorption analyses, the favorable effect generated by the doping is not linked to an extended activity in the visible spectrum or to altering the electronic structure of copper tungstate. $CuWO_4$-Ni(II) 10 and 25% samples exhibit higher IQE values of 8 and 10%, an efficiency increase of *ca.* 20-25% with respect to pure copper tungstate.

The recorded IPCE values are also in good agreement with the performances of the samples under full lamp irradiation (**Fig. 4.3**). Indeed, the photocurrent density values recorded by the samples at 1.23 V vs RHE in the LSV analyses have been compared to the photocurrent density values obtained by integrating the product between the IPCE curves and the standard AM 1.5 G solar spectrum over the entire investigated wavelengths range.[49] The comparison, reported in **Table 4.2**, shows a good matching of the j values obtained with the two different methods. Slightly lower values have been obtained through integration,

probably due to the different nature of the monochromatic irradiation which is characterized by a much lower intensity with respect to the solar simulator light source.

	Measured photocurrent / mA cm^{-2}	**Integrated photocurrent / mA cm^{-2}**
$CuWO_4$ 0%	0.093	0.085
$CuWO_4$ Ni 1%	0.088	0.079
$CuWO_4$ Ni 10%	0.111	0.099
$CuWO_4$ Ni 25%	0.086	0.082

Table 4.2. Photocurrent density measured at 1.23 V vs. RHE and integrated photocurrent values calculated from IPCE analyses at the same applied potential for pure and Ni(II)-doped $CuWO_4$ photoanodes.

4.4.3 Charge injection and charge separation efficiency

In order to investigate the origin of the enhanced photoactivity consequent to the incorporation of Ni(II) ions into copper tungstate, LSV analyses were conducted in the presence of a hole scavenger containing electrolyte, to obtain the intrinsic efficiency properties of our materials.

The maximum expected photocurrent density that can be generated by our electrodes J_{abs}, *i.e.*, the photocurrent obtained if all absorbed photons by a given electrode film were converted into electricity, was calculated from their absorption spectra. In our case, J_{abs} was calculated by integrating the product between the current theoretically generated under standard AM 1.5 G solar irradiation and the absorption spectrum of the photoelectrodes over the 300−530 nm range (up to the absorption onset of the prepared photoelectrodes, as pointed out by **Fig. 4.1a**). Usually, the experimentally measured photocurrent densities (J_{PEC}) are much lower than the predicted ones, due to the fact that not all absorbed photons are successfully converted into current. In fact, charge carriers recombination may occur at the surface and/or in the bulk of the material and the efficiency of photoanodes is consequently greatly lowered. The correlation between J_{PEC} and J_{abs} is described by the following equation:[37,50]

$$J_{PEC} = J_{abs} \cdot \eta_{sep} \cdot \eta_{inj} \tag{4.3}$$

where η_{sep} is the percent amount of photogenerated charge carriers that reaches the semiconductor/electrolyte interface, whereas η_{inj} is the percent amount of these charge carriers that are injected into the electrolyte and take part in the water oxidation reaction. If PEC tests are conducted in the presence of a hole-scavenger containing electrolyte, η_{inj} can be assumed to be equal to 1 and η_{sep} can be easily calculated from **Equation 4.3**. To calculate η_{inj}, the values of J_{PEC} attained for the water oxidation reaction can be divided by the J_{PEC} relative to the oxidation of a hole acceptor with $\eta_{inj} = 1$.

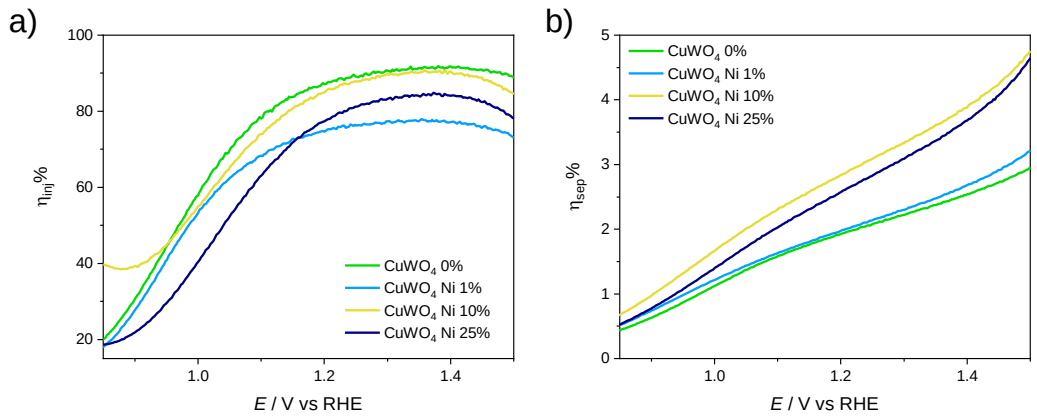

Figure 4.5. a) Charge injection and b) charge separation efficiency values calculated for pure and Ni(II)-doped $CuWO_4$ photoanodes.

The charge injection and separation efficiencies were calculated by testing our photoanodes in a KBi 0.1 M pH 9 solution containing 0.1 M $NaNO_2$, acting as hole scavenger, and are reported in **Fig. 4.5**. Sodium nitrite has been chosen as suitable hole scavenger species to be employed in contact with copper tungstate-based photoanodes after other commonly used sacrificial species were found to generate high dark currents or give rise to current doubling,[35,47] that is, the current multiplication due to the formation of unstable radicals followed by electron injection into the conduction band of a photocatalyst in the presence of hole scavenger species.

The highest charge injection efficiency over the entire range of applied potentials is displayed by the 0% sample, which shows almost quantitative surface water oxidation, as already outlined in previous studies,[47] indicating excellent surface properties for this electrode. On the other hand, the introduction of nickel ions has a detrimental effect on η_{inj}, except for

the 10% sample, which shows only slightly lower efficiencies with respect to the pure material, especially at potentials higher than 1.2 V vs RHE. In the 0% and the 10% samples injection efficiencies reach a value of ~90%, which indicates an excellent water oxidation kinetics at the electrode/electrolyte surface.

Fig. 4.5b presents the charge separation efficiencies calculated for all photoanodes. We can immediately notice that the efficiency displayed by all samples is quite low, below 5%. This indicates that the fast recombination of photogenerated electron/hole pairs in the bulk of the material is the major performance-limiting factor of our photoanodes. In this case the introduction of nickel in the copper tungstate structure has a clear beneficial effect on the separation efficiencies of the doped electrodes, since they all display comparable or higher η_{sep} with respect to pure $CuWO_4$. The $CuWO_4$ Ni 10% sample shows the highest separation efficiency, confirming to contain the ideal Ni dopant amount.

	$\mathbf{J_{abs}/mA\ cm^{-2}}$	$\mathbf{\eta_{inj}\%}$	$\mathbf{\eta_{sep}\%}$
$CuWO_4$ 0%	3.23	88	2.03
$CuWO_4$ Ni 1%	3.17	76	2.07
$CuWO_4$ Ni 10%	2.79	87	2.99
$CuWO_4$ Ni 25%	2.68	80	2.73

Table 4.3. J_{abs}, η_{inj} and η_{sep} values calculated at 1.23 V vs RHE for pure and Ni(II)-doped $CuWO_4$ photoanodes.

The calculated J_{abs} and the estimated efficiencies at the water oxidation potential are reported in **Table 4.3**. We can notice that the introduction of a small percent amount of dopant causes a decrease of the charge injection efficiency, decreasing from 88% for pure copper tungstate to the lowest η_{inj} of 76% obtained for the Ni 1% electrode. With a further increase in the nickel content, brought to 10%, the percentage of charge carriers successfully transferred to the electrolyte rises, and an injection efficiency of 87% is reached, comparable to that of $CuWO_4$ 0%. However, a higher doping of 25% lowers the efficiency to 80%.

Contrarily, the trend evidenced for the charge separation efficiency is different: pure $CuWO_4$ and the electrode containing the lowest nickel amount display comparable η_{sep} values of 2.03-2.07%, whereas the $CuWO_4$-Ni(II) 10% photoanode exhibits a conspicuous increase

(50%) in efficiency, up to 3%. As observed for η_{inj}, a slightly lower η_{sep} is obtained for the electrode containing 25% of nickel ions.

4.5 Discussion

By investigating the absorption properties and the structural characteristics of the prepared electrodes we can rule out any difference in the electronic or crystalline structure that may have been caused by the introduction of nickel ions in the copper tungstate structure, up to 25% doping. All samples indeed show a similar absorption profile and onset, as well as a comparable diffraction pattern. Morphological investigations revealed that the surface characteristics of pure and 25%-nickel containing electrodes appear quite different. The incorporation of Ni(II) ions into the synthesis of the photoelectrodes leads to a reduction in the average size of surface particles, possibly leading to a better contact and interpenetration of the electrolyte with the photocatalytic material. EDX analyses confirmed the incorporation of the dopant into the prepared materials. Given the hypothesis that the contribution of nickel ions might be confined to a modification in the surface properties of the electrodes, a $CuWO_4$ sample coated with a Ni(II) solution was prepared and tested under full lamp analyses. The results shown in **Figure A3** of the Appendix demonstrate that the enhancement of activity following the introduction of nickel ions is not entirely ascribable to surface modifications.

Full lamp LSV analyses have pointed out that samples containing 10% Ni dopant display higher photocurrent densities, under both back- and front-side irradiation. These results are then corroborated by IPCE and IQE monochromatic analyses, confirming that $CuWO_4$-Ni(II) 10 and 25% exhibit the highest conversion efficiency. Finally, the results of tests run in the presence of a hole scavenger species, from which the surface and bulk efficiencies of the electrodes were calculated, demonstrate the best performance of $CuWO_4$-Ni(II) 10%, with almost quantitative hole collection and an enhanced charge separation in material's bulk.

The superior performances of the $CuWO_4$-Ni(II) 10% electrode can be thus assigned to a combination of an increased surface area that could favor the charge injection efficiency at the electrode surface and an enhanced charge conductivity in the bulk of the material, which

contributes to lower the detrimental charge recombination processes that are the limiting factor of this class of materials.

4.6 Conclusions

Pure-phase, crystalline $CuWO_4$ thin films doped with different percentages of Ni(II) ions were prepared for the first time. UV-Vis, XRD and EDX analyses confirmed that the incorporation of nickel in the copper tungstate structure retains the pure phase crystalline structure typical of pure $CuWO_4$. SEM images evidenced that the introduction of Ni dopant ions led to the modification of the surface morphology of the photoelectrodes with respect to pure phase copper tungstate, decreasing the surface particles size. This could lead to beneficial effects such as a better contact between the material and the electrolyte. Photoelectrochemical tests evidenced the highest PEC efficiency of the 10%-Ni(II) containing electrode, with best performances under both full-lamp and monochromatic irradiation. Finally, the tests performed in the presence of a hole scavenger species, *i.e.* $NaNO_2$, allowed us to attribute the enhanced PEC performances of the $CuWO_4$-Ni(II) 10% photoanode to a marked increase in charge separation efficiency occurring in the bulk of the doped electrode with respect to pure copper tungstate, besides to a more favorable surface morphology.

Appendix A

EDX analyses on $CuWO_4$ 0% and $CuWO_4$ Ni 25% samples

Together with the acquisition of SEM images of $CuWO_4$ 0% and Ni 25% samples, EDX analyses have also been performed. The here shown EDX spectra evidence the presence of several peaks ascribed to nickel ions in the doped sample, along with the presence of signals due to both Cu and W elements, which are present in both tested photoelectrodes.

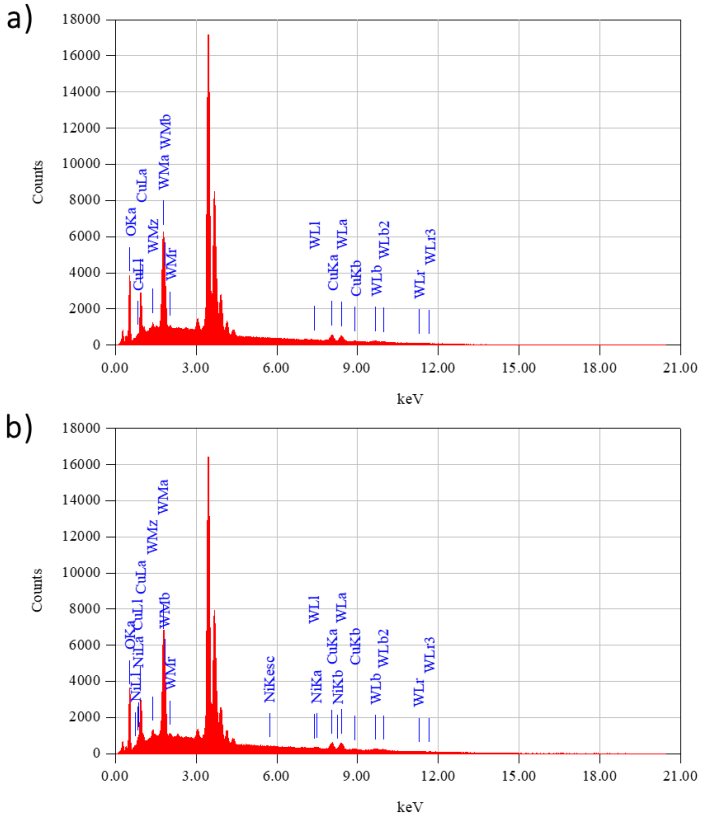

Figure A1 EDX elemental analyses of a) $CuWO_4$ 0% and b) $CuWO_4$ Ni 25%.

$CuWO_4$ sample doped with 50% of nickel(II) ions

Following the same synthetic route outlined in **Section 4.2.2,** a copper tungstate film with 1:1 Cu:Ni ratio was prepared, in order to verify if a Ni(II) dopant content higher than that of the electrodes described in this Chapter could lead to further beneficial effects on the photoelectrochemical performance. As can be observed in **Figure A2**, such a high dopant content is clearly detrimental for the sample in terms of photogenerated current.

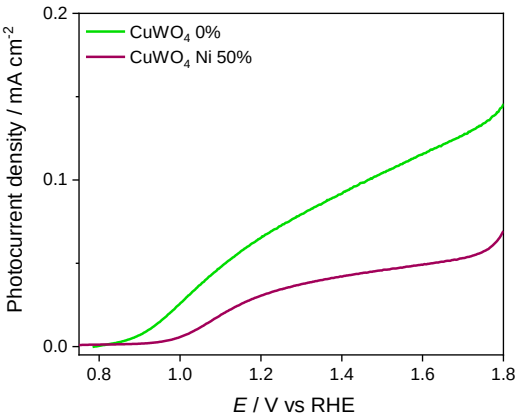

Figure A2 Linear Sweep Voltammetry (LSV) curves of pure and Ni(II)-50% doped $CuWO_4$ electrodes in KBi 0.1 M at pH 9 in back configuration.

$CuWO_4$ sample with Ni(II) surface coating

In order to assess if the beneficial effect of nickel doping could be ascribed to the accumulation of Ni(II) ions on the surface of the copper tungstate electrode, a $CuWO_4$ photoelectrode was prepared, which was then covered with a thin layer of a Ni(II) solution. LSV analyses on this sample (**Figure A3**) show that a surface layer of Ni(II) ions does not produce an enhancement in the photoelectrode performance. We can thus rule out the hypothesis that the beneficial effects generated by this type of doping are only surface related.

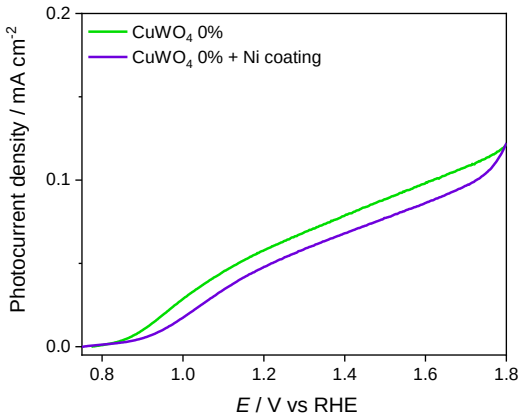

Figure A3 Linear Sweep Voltammetry (LSV) of pure and Ni(II) coated doped $CuWO_4$ electrodes in KBi 0.1 M at pH 9 in back configuration.

References

1. T.F. Jaramillo, T.G. Deutsch, N. Gaillard, H.N. Dinh, *J. Mater. Res.* 25 (**2010**) 3–16.
2. K. Sivula, R. Van De Krol, *Nat. Rev. Mater.* 1 (**2016**).
3. S. Corby, E. Pastor, Y. Dong, X. Zheng, L. Francàs, M. Sachs, S. Selim, A. Kafizas, A.A. Bakulin, J.R. Durrant, *J. Phys. Chem. Lett.* 10 (**2019**) 5395–5401.
4. X. Liu, F. Wang, Q. Wang, *Phys. Chem. Chem. Phys.* 14 (**2012**) 7894–7911.
5. A. Polo, I. Grigioni, M.V. Dozzi, E. Selli, *Catal. Today* 340 (**2020**) 19–25.
6. D.K. Lee, D. Lee, M.A. Lumley, K.S. Choi, *Chem. Soc. Rev.* 48 (**2019**) 2126–2157.
7. Y. Tang, N. Rong, F. Liu, M. Chu, H. Dong, Y. Zhang, P. Xiao, *Appl. Surf. Sci.* 361 (**2016**) 133–140.
8. H.V. Thang, E. Albanese, G. Pacchioni, *J. Phys. Condens. Matter* 31 (**2019**) 1–10.
9. H.W. Jeong, T.H. Jeon, J.S. Jang, W. Choi, H. Park, *J. Phys. Chem. C* 117 (**2013**) 9104–9112.
10. Z. Wang, X. Huang, X. Wang, *Catal. Today* 335 (**2019**) 31–38.
11. M. Tayebi, B.K. Lee, *Renew. Sustain. Energy Rev.* 111 (**2019**) 332–343.
12. J.H. Kim, Y.J. Jang, J.H. Kim, J.W. Jang, S.H. Choi, J.S. Lee, *Nanoscale* 7 (**2015**) 19144–19151.
13. N. Guijarro, P. Bornoz, M.S. Prévot, X. Yu, X. Zhu, M. Johnson, X. Jeanbourquin, F. Le Formal, K. Sivula, *Sustain. Energy Fuels* 2 (**2018**) 103–117.
14. J.E. Yourey, B.M. Bartlett, *J. Mater. Chem.* 21 (**2011**) 7651–7660.
15. W. Guo, Z. Duan, O. Mabayoje, W.D. Chemelewski, P. Xiao, G. Henkelman, Y. Zhang, C.B. Mullins, *J. Electrochem. Soc.* 163 (**2016**) H970–H975.
16. Y. Liu, M. Xia, L. Yao, M. Mensi, D. Ren, M. Grätzel, K. Sivula, N. Guijarro, *Adv. Funct. Mater.* 31 (**2021**) 2010081.
17. J.E. Yourey, K.J. Pyper, J.B. Kurtz, B.M. Bartlett, *J. Phys. Chem. C* 117 (**2013**) 8708–8718.
18. C.R. Lhermitte, B.M. Bartlett, *Acc. Chem. Res.* 49 (**2016**) 1121–1129.
19. J.C. Hill, K.S. Choi, *J. Mater. Chem. A* 1 (**2013**) 5006–5014.
20. Y. Gao, T.W. Hamann, *J. Phys. Chem. Lett.* 8 (**2017**) 2700–2704.
21. A. Venugopal, W.A. Smith, *Faraday Discuss.* 215 (**2019**) 175–191.
22. T.W. Hamann, P. Shadabipour, A.L. Raithel, *ACS Appl. Mater. Interfaces* 12 (**2020**) 50592–50599.

23. C. Tian, M. Jiang, D. Tang, L. Qiao, H. Xiao, F.E. Oropeza, J.P. Hofmann, E.J.M. Hensen, A. Tadich, W. Li, D. Qi, H. Zhang, *J. Mater. Chem. A* 7 (**2019**) 11895–11907.

24. Z. Wu, Z. Zhao, G. Cheung, R.M. Doughty, A.R. Ballestas-Barrientos, B. Hirmez, R. Han, T. Maschmeyer, F.E. Osterloh, *J. Electrochem. Soc.* 166 (**2018**) H3014–H3019.

25. P. Raizada, S. Sharma, A. Kumar, P. Singh, A.A.P. Khan, A.M. Asiri, *J. Environ. Chem. Eng.* 8 (**2020**) 104230.

26. K.J. Pyper, J.E. Yourey, B.M. Bartlett, *J. Phys. Chem. C* 117 (**2013**) 24726–24732.

27. I. Grigioni, A. Polo, M.V. Dozzi, L. Ganzer, B. Bozzini, G. Cerullo, E. Selli, *J. Phys. Chem. C* 125 (**2021**) 5692–5699.

28. B. Klahr, S. Giménez, F. Fabregat-Santiago, T. Hamann, J. Bisquert, *J. Am. Chem. Soc.* 134 (**2012**) 4294–4302.

29. D. Wang, P. Bassi, H. Qi, X. Zhao, Gurudayal, L.H. Wong, R. Xu, T. Sritharan, Z. Chen, *Materials (Basel).* 9 (**2016**) 348.

30. S.K. Pilli, T.G. Deutsch, T.E. Furtak, L.D. Brown, J.A. Turner, A.M. Herring, *Phys. Chem. Chem. Phys.* 15 (**2013**) 3273.

31. I. Rodríguez-Gutiérrez, E. Djatoubai, M. Rodríguez-Pérez, J. Su, G. Rodríguez-Gattorno, L. Vayssieres, G. Oskam, *Electrochim. Acta* 308 (**2019**) 317–327.

32. K.M. Nam, E.A. Cheon, W.J. Shin, A.J. Bard, *Langmuir* 31 (**2015**) 10897–10903.

33. D. Bohra, W.A. Smith, *Phys. Chem. Chem. Phys.* 17 (**2015**) 9857–9866.

34. C. Li, P. Diao, *Electrochim. Acta* 352 (**2020**) 136471–136479.

35. A. Polo, C. Nomellini, I. Grigioni, M.V. Dozzi, E. Selli, *ACS Appl. Energy Mater.* 3 (**2020**) 6956–6964.

36. J.C. Hill, Y. Ping, G.A. Galli, K.S. Choi, *Energy Environ. Sci.* 6 (**2013**) 2440–2446.

37. W. Ye, F. Chen, F. Zhao, N. Han, Y. Li, *ACS Appl. Mater. Interfaces* 8 (**2016**) 9211–9217.

38. D. Hu, P. Diao, D. Xu, M. Xia, Y. Gu, Q. Wu, C. Li, S. Yang, *Nanoscale* 8 (**2016**) 5892–5901.

39. L. Fan, J. Sunarso, X. Zhang, X. Xiong, L. He, L. Luo, F. Wang, Z. Fan, C. Wu, D. Han, N.H. Wong, Y. Wang, G. Chen, W. Chen, *Int. J. Hydrogen Energy* 47 (**2022**) 20153–20165.

40. P. Basyach, A.K. Guha, S. Borthakur, L. Kalita, P. Chetia, K. Sonowal, L. Saikia, *J. Mater. Chem. A* 8 (**2020**) 12774–12789.

41. S. Meng, L. Li, H. Xi, J. Yang, T. Xiao, R. Zuo, X. Xu, Z. Lei, Z. Yang, Q. Xue, *Chinese J. Chem.* 40 (**2022**) 2701—2711.

42. J. Liao, Y. Shao, Y. Feng, J. Zhang, C. Song, W. Zeng, J. Tang, H. Dong, Q. Liu, H. Li, *Appl. Catal. B Environ.* 320 (**2023**) 121973.

43. Y. Liu, L. Chen, X. Zhu, H. Qiu, K. Wang, W. Li, S. Cao, T. Zhang, Y. Cai, Q. Wu, J. Li, *J. Electroanal. Chem.* 924 (**2022**) 116859.

44. L. Chen, W. Li, W. Qiu, G. He, K. Wang, Y. Liu, Q. Wu, J. Li, *ACS Appl. Energy Mater. Interfaces* 14 (**2022**) 47737–47746.

45. B. Klahr, S. Giménez, F. Fabregat-Santiago, J. Bisquert, T.W. Hamann, *J. Am. Chem. Soc.* 134 (**2012**) 16693–16700.

46. A. Polo, I. Grigioni, M. Magni, A. Facibeni, M. V. Dozzi, E. Selli, *Appl. Surf. Sci.* 556 (**2021**) 149759.

47. Y. Gao, T.W. Hamann, *Chem. Commun.* 53 (**2017**) 1285–1288.

48. Y. Liang, T. Tsubota, L.P.A. Mooij, R. Van De Krol, *J. Phys. Chem. C* 115 (**2011**) 17594–17598.

49. J.A. Christians, J.S. Manser, P. V. Kamat, *J. Phys. Chem. Lett.* 6 (**2015**) 852–857.

50. G. V. Govindaraju, G.P. Wheeler, D. Lee, K.S. Choi, *Chem. Mater.* 29 (**2017**) 355–370.

Chapter 5 – Role of nanostructuring on WO_3 and WO_3–$BiVO_4$ photoanodes

5.1 Abstract

WO_3–$BiVO_4$ photoanode heterojunctions are among the most employed systems in photoelectrochemical (PEC) cells for the conversion of water into molecular oxygen, the kinetic bottleneck of water splitting. Composite WO_3–$BiVO_4$ photoelectrodes possessing a nanoflake-like morphology have been synthesized through a multistep process and their PEC performance investigated in comparison with that of electrodes displaying a planar surface morphology and similar absorption properties and thicknesses. Using various characterization techniques, among which Electrochemical Impedance Spectroscopy, the intrinsic limitations of nanostructured and planar samples have been discussed. Moreover, PEC tests highlighted the presence of a detrimental charge recombination path active in the planar composite, that has been successfully overcome by nanostructuring the tungsten trioxide underlayer in the nanoflake-like heterojunction. Indeed, monochromatic PEC analyses and test runs in the presence of a sacrificial agent indicate a better charge carrier transport and greatly enhanced charge separation efficiency in the nanostructured WO_3–$BiVO_4$ electrode in comparison to the planar ones.

5.2 Introduction

The path towards a sustainable society passes through the development of clean and renewable energy sources, among which hydrogen produced from solar energy is one of the most promising alternatives, given the abundance of water and the inexhaustibility of solar radiation.[1–3] Photoelectrochemical (PEC) water splitting on transition-metal oxides has been extensively studied to efficiently convert solar energy and store it in the form of chemical bonds, due to the earth abundance and stability of many semiconductor oxide photocatalysts under the relatively harsh water oxidation conditions.[4–6] However, all semiconductor oxides most largely employed as photoanode materials, such as $BiVO_4$, WO_3, and Fe_2O_3, suffer from slow water oxidation kinetics and fast recombination of photogenerated electron/hole couples.[4,7–10] Photocatalyst doping and/or surface modification, combined with heterojunction formation, were found to be effective to accelerate the rate determining step of overall water splitting.[11–16] In particular, the composite material obtained by coupling WO_3 with $BiVO_4$ combines the excellent visible light harvesting properties of bismuth vanadate (that possesses a band gap of 2.4 eV and it is thus able to absorb solar light up to *ca.* 520 nm) with the good electron conductivity of tungsten oxide (which is however characterized by a reduced absorbance in the visible due to its band gap energy of 2.7 eV). Moreover, due to their favourable band alignment, a better charge separation and consequent lower recombination of the photogenerated electron-hole couples should be achieved, leading to an increase in the charge carrier lifetime.[17,18]

To further increase the efficiency of these materials specific effects deriving from nanoscaling can also be exploited. Indeed, nanostructured photoanodes are characterized by a shortened carrier collection pathway, increased light absorption due to light scattering effects and enhanced surface area, favouring a more extended contact between the material and the electrolyte, as well as charge transfer at the semiconductor-liquid interface.[16,19,20] In recent years, nanostructured WO_3–$BiVO_4$ heterojunctions with various morphologies have been studied,[21,22] and, among these materials, vertically aligned WO_3 nanorods or nanowires coated with a thin bismuth vanadate layer have shown the best PEC performances,[16,23,24] combining an enhanced photon absorption originated from a longer optical path through the nanostructured material and improved charge separation in the $BiVO_4$ layer, favoured by the bettered charge collection efficiency provided by the tungsten oxide underlayer. Out of

numerous studies, WO_3–$BiVO_4$ photoanodes displaying a more open, nanoflake-like morphology have been little investigated, with only a single study reporting relevant performance for this heterojunctions.[15] Moreover, to the best of our knowledge, no study has been focused on the systematic comparison of the advantages and downsides between photoanodes displaying a controlled morphology and materials characterized by a planar surface, *i.e.*, photoanodes that do not display any controlled surface morphology or asperities and are composed of densely packed aggregates. The only study available on this topic is focused on heterojunctions that display different thicknesses and it highlighted only a modest increase in performance when passing from a planar WO_3–$BiVO_4$ heterojunction to a nanostructured one (the generated photocurrent passes from 0.8 to 1.6 mA cm^{-2} at 1 V vs NHE upon nanostructuring).[25]

The present chapter thus focuses on comparing the overall efficiency exhibited by WO_3–$BiVO_4$ photoelectrodes displaying different morphologies (*i.e.*, nanoflake-like and planar). Intrinsic performance limitations of planar electrodes will be successfully overcome by properly nanostructuring the WO_3 underlayer (with a fixed thickness). The peculiar role played by the WO_3 morphology will be effectively unveiled by investigating heterojunctions with similar film thickness and optical properties. In particular, in the case of planar electrodes, it has been clearly outlined that the thickness increase of the electron-carrier layer (WO_3) tends to favour an undesired recombination path of photogenerated charges,[18,26,27] while the complete coverage with $BiVO_4$ of the WO_3 underlayer simultaneously leads to a detrimental loss of the more oxidizing valence band holes photogenerated in the tungsten oxide material. Interestingly, the WO_3–$BiVO_4$ nanostructured heterojunction presented in this study shows a significant overcoming of these crucial disadvantages, generating a 6-fold increase in photogenerated current and in the charge separation efficiency of the material.

5.3 Experimental section

5.3.1 Materials

The following chemicals, all purchased from Sigma Aldrich, were employed as supplied: tungstic acid (H_2WO_4, 99%), hydrogen peroxide (H_2O_2, 30wt%), oxalic acid (HO_2CCO_2H, 99%), hydrocloric acid (HCl, 37wt%), nitric acid (HNO_3, 23.3wt%), acetonitrile (CH_3CN, 99%), ammonium metavanadate (NH_4VO_3, 99%), bismuth(III) nitrate pentahydrate ($Bi(NO_3)_3{\cdot}5H_2O$, 98%), citric acid (99%), acetylacetone (99%), ammonium metatungstate hydrate (99%, $(NH_4)_6H_2W_{12}O_{40} \cdot xH_2O$), polyethylene glycol 300 (PEG 300). Poly(vinyl alcohol) and urea (H_2NCONH_2, 99%) were purchased from Fluka. 2-methoxyethanol (99%) was purchased from Alfa Aesar. 2 mm thick fluorine-doped tin oxide (FTO) glass (7 ohm/sq) was purchased from Kintec.

5.3.2 Photoelectrodes preparation

5.3.2.1 Planar electrodes

A WO_3 precursor solution was prepared by adding 0.494 g of ammonium metatungstate to 0.3 mL of acetylacetone and 0.7 mL of 2-methoxyethanol. The solution was heated at 50 °C and kept under stirring for 3 h; lastly, 50 mg of PEG 300 were added. A 2.5 x 2.5 cm^2 FTO slab was coated with 100 µL of the so obtained paste by spin-coating at 4000 rpm for 30 s. The final spinning rate was reached with a three-acceleration step program: 500 rpm s^{-1} up to 500 rpm, then 1500 rpm s^{-1} up to 2000 rpm, and finally 2000 rpm s^{-1} up to 4000 rpm. Prior to deposition, the FTO glass was cleaned by a 30 min long sonication in an aqueous soap solution, then in ethanol. After coating, the electrode was annealed at 550 °C for 1 h on a hotplate; the final annealing temperature was reached using a 1 h heating ramp. This deposition step was repeated twice.

A $BiVO_4$ precursor solution was prepared by adding 0.386 g of citric acid, 0.495 g of bismuth(III) nitrate and 0.118 g of ammonium metavanadate to 3 mL of nitric acid. 100 µL

of this solution were deposited at 4000 rpm for 30 s by spin-coating on a previously prepared WO_3 photoelectrode, followed by annealing at 500 °C for 1 h, using the same hotplate and heating ramp as above. This deposition cycle was repeated up to 8 times in order to obtain an enough thick $BiVO_4$ layer.

Reference photoanodes containing only $BiVO_4$ were prepared by performing the same deposition-calcination cycle procedure up to 8 times on a clean FTO slab.

5.3.2.2 Nanostructured electrodes

WO_3 nanostructured films were prepared by following the experimental protocol as described by Su *et al.* with some little modifications.[28] A *ca.* 200 nm thick WO_3 seed layer was deposited on the FTO substrate by spin-coating 100 µL of a tungsten oxide precursor solution at 3000 rpm for 30 s. The solution was prepared by adding 0.417 g of tungstic acid and 0.167 g of PVA to 6 mL of H_2O_2 30%, followed by stirring for 3 h to obtain a transparent solution. The deposited film was then annealed for 2 h in a muffle at 500 °C; the final annealing temperature was reached after a 1 h heating ramp. WO_3 nanoflakes (NF) were later grown on the seed layer by solvothermal synthesis. A 0.05 M tungstic acid precursor solution was prepared by adding 0.625 g of H_2WO_4 to 9 mL of H_2O_2 30% and the volume was adjusted to 50 mL with distilled water; the solution was kept at 80-85 °C for 30 min to allow the dissolution of the powders.

The solution employed for the solvothermal synthesis was prepared as follows: 12 mL of the 0.05 M tungstic acid precursor solution, 0.08 g of oxalic acid and 0.08 g of urea were dissolved in 50 mL of acetonitrile and 1 mL of HCl 37% was added. The solution was placed in a 125 mL stainless steel autoclave, which was kept at 180 °C for 2 h. After the reaction, the electrodes were rinsed with water and calcined at 500 °C for 1 h in a muffle, using 1h heating ramp. The parameters of the solvothermal synthesis have been optimized to obtain the desired thickness of the photoanodes.

In order to obtain a nanostructured WO_3–$BiVO_4$ heterojunction, 60 µL of a $BiVO_4$ solution were deposited at 4000 rpm for 30 s on the previously prepared WO_3 NF electrode, followed by annealing at 500 °C for 1 h in a muffle. This $BiVO_4$ deposition step was repeated

twice in order to obtain a $BiVO_4$ layer with light absorption abilities comparable to those exhibited by the $BiVO_4$ coating on the planar WO_3 system.

The so prepared photoanodes were labelled as WO_3_*X* if containing WO_3 only, and WO_3_*X*–BV if consisting in a WO_3–$BiVO_4$ heterojunction. The label is referred to the morphology of the film, with *X*=P if it is characterized by a WO_3 planar morphology or *X*=NF if it possesses a WO_3 nanoflake-like nanostructure. The photoanode containing $BiVO_4$ only is labelled as BV.

5.3.3 Optical, morphological and photoelectrochemical characterizations

Absorption spectra were recorded employing a Jasco V-670 spectrophotometer. The UV-Vis absorption profiles of the photoanodes characterized by a planar surface (*i.e.*, the planar WO_3 sample, as well as the planar WO_3–$BiVO_4$ heterojunction films and the $BiVO_4$ reference film) were acquired in transmittance mode, all these photoactive films being optically transparent. The absorption spectra of the nanostructured electrodes were recorded with the same instrument equipped with an integrating sphere, working in both transmittance and reflectance mode. The absorbance of these samples was then calculated using the following equation:[29]

$$\mathrm{A} = \log\left(\frac{1-\mathrm{R}}{\mathrm{T}}\right) \tag{5.1}$$

The attainment of pure, crystalline materials was checked by X-ray diffraction analyses (XRD), performed with a Rigaku Miniflex 600 diffractometer, equipped with a Cu tube providing Kα radiation. The shown diffractograms were base-corrected employing the Origin software.

A scanning electron microscope (SEM), model Jeol JSM-7600F with a 5 kV incident beam, was used to acquire top view and cross-section images of planar and nanostructured WO_3, and of the coupled WO_3–$BiVO_4$ electrodes.

Electrochemical Impedance Spectroscopy (EIS) data were acquired by means of a Autolab potentiostat controlled by Nova software; a 10 mV amplitude perturbation ranging

from 10^5 to 10^{-1} Hz was used. The light source was a LED-operating solar simulator (SUNBOX).[30] Investigated samples, located in a 3-electrode glass cell with a platinum wire as counter and a Ag/AgCl reference electrode, were irradiated in back configuration. Data were fit using ZView software.

Photoelectrochemical tests were carried out in a three-electrode cappuccino cell,[13] with the photoanodes used as working electrodes (with an illuminated area of 0.28 cm^2), an Ag/AgCl (3 M KCl) as reference and a platinum gauze as counter electrode, respectively. The scan rate in Linear Sweep Voltammetry (LSV) analyses was 10 mV s^{-1} and the applied bias was controlled through an Autolab PGSTAT 12. The light source was a solar simulator (Newport, model Oriel LCS-100) equipped with an AM 1.5 G filter, with a light intensity fixed at 100 mW cm^{-2}. All prepared electrodes were tested under both back-side irradiation configuration, *i.e.* through the FTO glass, and under front-side irradiation, *i.e.* through the photoactive material, in contact with a 0.5 M Na_2SO_4 electrolyte solution at pH 7. The potentials *vs.* Ag/AgCl values were converted into the RHE scale using the following equation: $E_{RHE} = E_{AgCl} + 0.059\ pH + E^{\circ}_{AgCl}$, with $E^{\circ}_{AgCl}(3\ M\ KCl) = 0.210$ V at 25 °C.

Incident photon to current efficiency (IPCE) measurements were carried out at the fixed applied voltage of 1.23 V vs RHE under monochromatic light irradiation in the above described three-electrode set up; the light source was a 300 W Lot-Oriel Xe lamp equipped with a Lot-Oriel Omni-λ 150 monochromator. Percent IPCE values were calculated using the following equation:

$$IPCE\% = \frac{j \cdot 1240}{P_\lambda \cdot \lambda} \cdot 100 \qquad (5.2)$$

where j is the recorded photocurrent density (mA cm^{-2}) and P_λ (mW cm^{-2}) is the power measured at each specific wavelength λ (nm). A 490 nm cut-off filter was used when recording photocurrents at $\lambda > 500$ nm, to avoid any possible contribution from the second harmonics generated by the monochromator.

5.4 Results

5.4.1 Photoanodes characterization

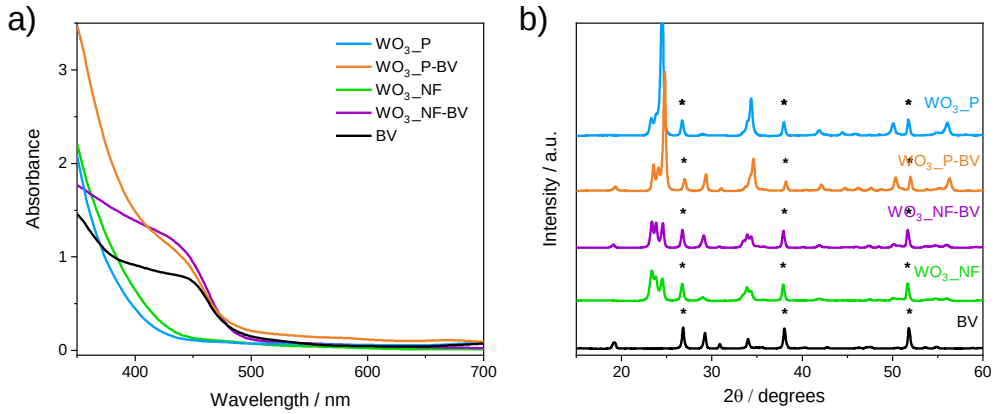

Figure 5.1 a) Absorption spectra and b) XRD patterns of planar and nanostructured WO_3, WO_3–BV and of planar BV electrodes. The reflections marked with * refer to the FTO substrate.

The absorption spectra of the prepared photoanodes are reported in **Fig. 5.1a**. Planar and nanostructured WO_3 electrodes exhibit a similar absorption profile, with an absorption onset located at *ca.* 450 nm, accounting for a 2.7 eV band gap.[8] The heterojunction electrodes exhibit an increased absorption in the visible region, extending up to *ca.* 500-520 nm, in agreement with the 2.4 eV band gap of $BiVO_4$,[31] confirming the visible light sensitisation performed by bismuth vanadate on tungsten oxide in the composite material. The absorption shoulders in the visible range, typical of $BiVO_4$, are similar for the two heterojunction systems, indicating an effective comparable loading of bismuth vanadate on the two underlying WO_3 electrodes, independently of their morphology. The planar pure $BiVO_4$ electrode exhibits the same 500 nm absorption onset observed for the two heterojunction electrodes. However, its absorption shoulder at 450 nm shows a different intensity, indicating that a slightly lower amount of bismuth vanadate was deposited directly on the FTO substrate than on the WO_3 underlayers.

The XRD patterns of the investigated systems are shown in **Fig. 5.1b**. The two WO_3 electrodes exhibit the typical peaks of a pure monoclinic structure,[32] with the reflections at 23.4°, 23.8° and 24.6° related to the {002}, {020} and {200} planes, respectively, and the

reflections at 33.5°, 34° and 34.4° associated with the {022}, {-202}, {202} planes.[14,33] In the WO_3 planar sample (WO_3_P) the intensity of the {200} and the {202} peaks is higher with respect to nanostructured WO_3 (WO_3_NF), suggesting a possible preferential orientation growth. At the same time, the WO_3_P sample also exhibits more intense reflections at 50.4° and 56.3° with respect to the WO_3_NF electrode, associated to the {140} and {142} planes, respectively.[34] The XRD patterns of the two heterojunctions show the coexistence of WO_3 and $BiVO_4$ reflections, this latter with crystalline monoclinic structure, as already reported for bismuth vanadate,[11,35] and evidenced by the 19.1°, 29.1° and the 31.1° reflections, corresponding to the {110}, {121}, {040} planes, respectively.[29]

The top-view images acquired by scanning electron microscopy (SEM) confirm the attainment of a nanostructured WO_3 electrode (**Fig. 5.2a**, top panel), characterized by three-dimensional microstructures with thin nanoflake thickness and abundant porosity. This morphology is maintained also upon $BiVO_4$ deposition, as shown in **Fig. 5.2b**, which seems to mainly alter and reduce the average porosity of the original WO_3 nanostructures. On the other hand, planar samples (**Fig. 5.2c-d**) do not present a controlled morphology and are characterized by a compact aggregated network of particles. In particular, the planar WO_3 photoanode is mainly composed of relatively small and uniformly distributed spherical aggregates, while the top of the composite material, consisting of the $BiVO_4$ layer, appears as a compact film characterized by a wormlike feature that completely covers the WO_3 underlayer.[36]

The thickness of both nanostructured and planar electrodes, estimated from cross-section SEM images (**Fig. 5.2**, lower panel) are reported in **Table 5.1**. Nanoflake-like WO_3 shows a *ca.* 150 nm thickness increase upon the $BiVO_4$ deposition, leading to a ca. 1.1 µm thick composite film. The planar WO_3 film shows a thickness comparable to that of the nanostructured counterpart and the deposition of $BiVO_4$ produced a ca. 130 nm thickness increase for the composite film, in perfect analogy with that obtained for the NF samples. The similar thickness of the $BiVO_4$ layers deposited on the two different WO_3 films is also confirmed by the comparable absorption of the two heterojunctions in the visible range, as shown by the absorption spectra shown in **Fig. 5.1a**.

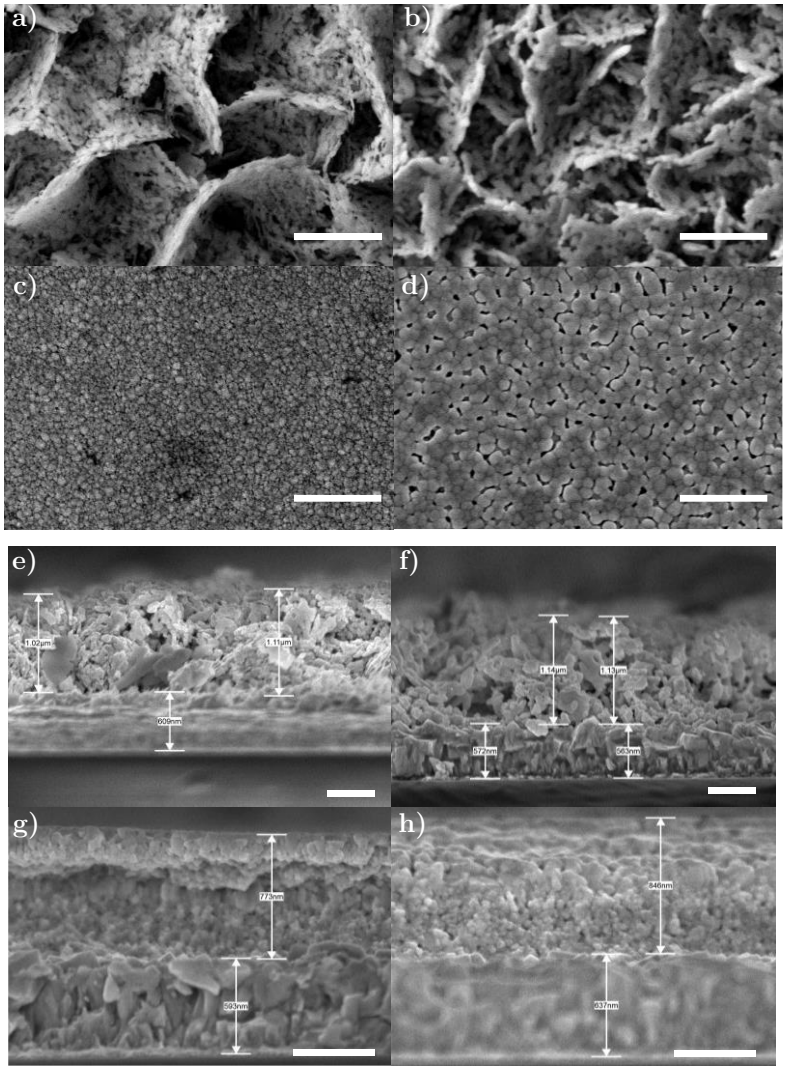

Figure 5.2 Upper panel: top view SEM images of a) WO_3_NF, b) WO_3_NF–BV, c) WO_3_P and d) WO_3_P–BV electrodes. The scale bar corresponds to 1 µm. Lower panel: cross-section SEM images of e) WO_3_NF, f) WO_3_NF–BV, g) WO_3_P and h) WO_3_P–BV electrodes. The scale bar corresponds to 500 nm.

Sample	Thickness / nm
WO_3_NF	961 ± 62
WO_3_NF–BV	1126 ± 123
WO_3_P	790 ± 41
WO_3_P–BV	914 ± 18

Table 5.1 Thickness of NF and planar electrodes estimated from SEM cross-section images.

5.4.2 Electrochemical impedance spectroscopy

Figure 5.3 depicts the Nyquist plots recorded by testing the two pure-phase tungsten oxide photoelectrodes under simulated solar irradiation generated through a LED-based solar simulator at two different applied potentials. The impedance signals of both samples appear in the form of a single semicircle, whose diameter is represented by R_{ct}, *i.e.,* the charge transfer resistance associated with the water oxidation reaction. While the two WO_3 photoanodes display a similar signal at lower applied potential (0.72 V vs RHE, half-full dots in **Figure 5.3**), the resistance of WO_3_P becomes sensibly lower with respect to that of WO_3_NF at the water oxidation potential, thus indicating that the planar WO_3 electrode drives more easily the overall water oxidation reaction.

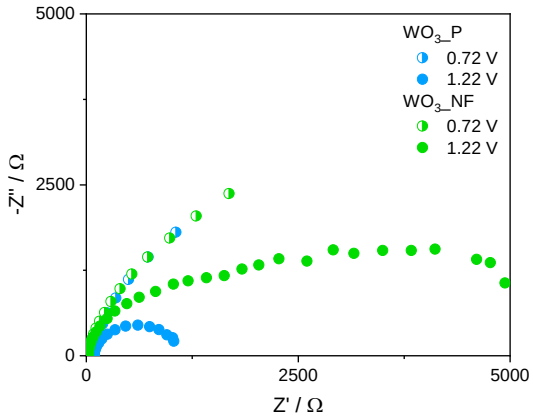

Figure 5.3 Nyquist plot of WO_3_NF and WO_3_P under 1 sun irradiation in back configuration, at 0.72 and 1.22 V vs RHE.

Since the Nyquist plots generated by both photoanodes are characterized by the presence of a single semicircle, EIS data of both samples were fitted using a simple Randles circuit,[37,38] which is composed by a system resistance R_s (accounting for charge transport across the FTO support, the external circuit and through the electrolyte), the charge transfer resistance R_{ct} associated with the water oxidation reaction and a surface capacitance C_{dl} associated with the Helmholtz layer at the electrode/electrolyte interface.

Figure 5.4 depicts the parameters obtained after the fitting, under both dark and illumination conditions of WO_3_P and WO_3_NF.

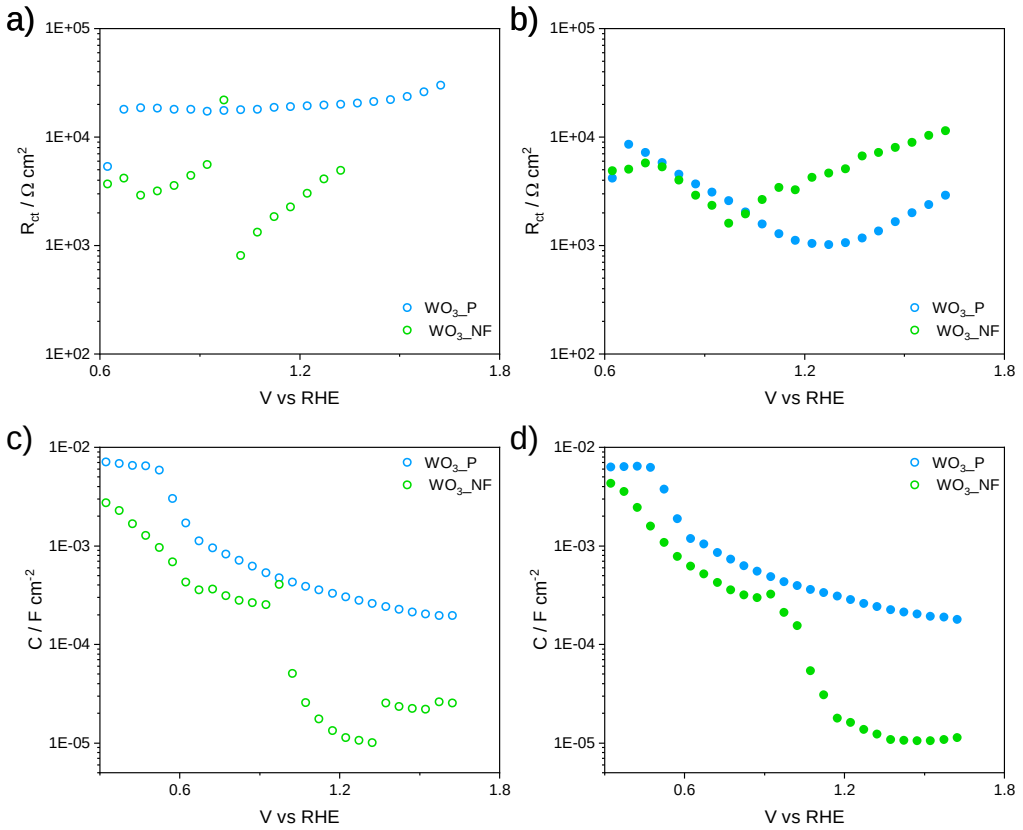

Figure 5.4 Charge transfer resistance R_1 under a) dark or b) irradiation conditions, and surface capacitance C under c) dark or d) irradiation conditions of WO_3_P and WO_3_NF samples.

Figures 5.4a,b represent the trends of the calculated charge transfer resistance as a function of the increasing applied potential. In dark conditions we do not observe a clear trend between the two parameters, since R_{ct} remains almost constant for WO_3_P, while it undergoes some fluctuations in WO_3_NF. Under irradiation we see a different trend: WO_3_P displays resistance values that decrease with increasing potential and reach a minimum value of *ca.* $1{\cdot}10^3$ Ω cm^2 at 1.3 V vs RHE. At higher applied potentials R_{ct} slightly increases up to $2\text{-}3{\cdot}10^3$ Ω cm^2. On the other hand, the behaviour of the nanostructured WO_3 sample is quite different. The charge transfer resistance of this sample exhibits a minimum at relatively lower potentials (0.9 V vs RHE) and then increases with increasing applied potential, reaching values even higher than $1{\cdot}10^4$ Ω cm^2, which indicates that the water oxidation kinetics is somehow hampered when a high external potential is applied to the system. However, this phenomenon is not observed for WO_3_P, suggesting that it is probably linked to the morphology of the nanostructured tungsten oxide sample.

Fig. 5.4c,d show the trend of surface capacitance of both photoanodes. Firstly, this parameter does not seem to be affected by the illumination conditions, the trend and calculated values of C_{dl} being similar for both samples in the dark and under simulated solar radiation. For both photoanodes we observe an exponential dependence of the capacitance on the applied voltage, which is characteristic of the chemical capacitance, and which monitors the exponential density of states below the conduction band.[39] Notably, WO_3_NF presents an abrupt decrease in capacitance at *ca.* 0.9-1.1 V vs RHE, reaching C_{dl} values of *ca.* $1 \cdot 10^{-5}$ F cm^{-2}. This sudden change in capacitance occurs at an applied voltage which is only slightly higher than the minimum charge transfer resistance observed in **Fig. 5.4b**. This may suggest the presence of a common phenomenon generating these observed trends, presence of which is limited to the nanostructured samples only.

In order to verify if the nanostructured heterojunction still presents the same behaviour of its underlayer WO_3_NF, EIS data acquired with WO_3_NF–BV have also been fitted using a Randles circuit. The so-obtained parameters are reported in **Figure 5.5**. Concerning the charge transfer resistance, in the dark the composite sample shows an almost constant R_{ct}, independent of the applied bias. Under illumination WO_3_NF–BV shows a trend similar to that of WO_3_NF, i.e., the resistance decreases up to a minimum value and then it slightly increases at higher applied potential. However, the R_{ct} minimum is attained at much higher potentials (*ca.* 1.3 V vs RHE) and its value, corresponding to *ca.* 400 **Ω** cm^2, is significantly lower with respect to what observed for the WO_3_NF electrode. We can therefore ascribe the differences between the two samples to the contribution of the bismuth vanadate coating on the WO_3 underlayer, which favours the charge transfer kinetics between the photoelectrode and the electrolyte, as testified by a decreased resistance.

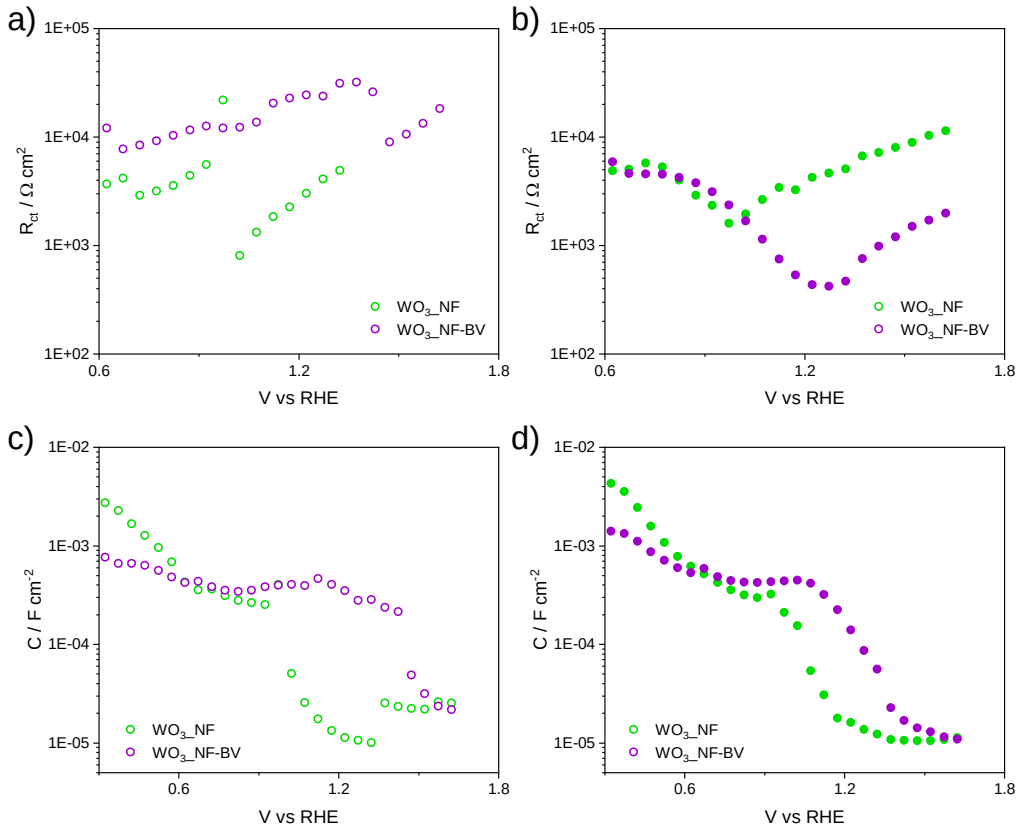

Figure 5.5 Charge transfer resistance R_1 under a) dark or b) irradiation conditions, and surface capacitance C under c) dark or d) irradiation conditions of WO_3_NF and WO_3_NF–BV.

Figures 5.5c,d depict the surface state capacitance of the heterojunction, in comparison to that of WO_3_NF. Contrary to what observed with the tungsten oxide sample, behaviour of C_{dl} in the heterojunction in the dark is different from that under illumination conditions. In the absence of irradiation, the capacitance of the composite material remains almost constant up to relatively high applied bias (1.5 V vs RHE), and then undergoes a marked decrease up to *ca.* $1{\cdot}10^{-5}$ F cm^{-2}. Under illumination, an almost constant capacitance trend is maintained only up to lower potentials: at 1.1 V vs RHE the capacitance of the heterojunction slightly decreases until it reaches the minimum value exhibited by WO_3_NF. In both irradiation conditions, however, the capacitance of the composite is higher with respect to that of tungsten oxide over the entire applied potential range. This may be related to a higher electron density due to the charge carriers injection from the $BiVO_4$ overlayer.[39]

5.4.3 Photoelectrochemical tests

The PEC performances of pure and composite nanoflake electrodes under back-side and front-side illumination can be compared in **Fig. 5.6a,c**. The limit photocurrent generated by WO_3_NF is *ca.* 0.5 mA cm^{-2}, in agreement with the performance reported previously for similarly prepared electrodes.[32,40] The lack of transient spikes in correspondence to the light on steps may suggest the absence of any current loss produced by undesired charge carriers recombination processes occurring at the electrode/electrolyte interface.[41] The photocurrent generated by WO_3_NF reaches a plateau at relatively low potentials (~1.1 V), without any further increase with increasing applied potential. This peculiar plateau form of the j-V plot may be related to the fact that the high surface area of the nanostructured WO_3 photoanodes usually brings about a great number of surface defects,[42,43] that could be directly involved in the oxidation of water molecules at the semiconductor/electrolyte interface, instead of favouring the charge transport in the bulk of the material. Consequently, the WO_3_NF sample exhibits a maximum photocurrent at relatively lower applied potentials.

Interestingly, by taking into account the EIS results discussed in the previous Section, we can observe that the WO_3_NF electrode shows a plateau of photocurrent under solar irradiation from ca. 1.1. V vs. RHE, i.e. nearby the applied potential at which the charge transfer resistance of the system is increasing after reaching a minimum (**Fig. 5.4b**), and the surface capacitance calculated for WO_3_NF has an abrupt decrease (**Fig. 5.4d**). The combination between a higher charge transfer resistance and a lower capacitance could thus explain the attainment of a photocurrent limit in the LSV measurements performed under full-lamp irradiation with the nanostructured tungsten oxide photoanode.

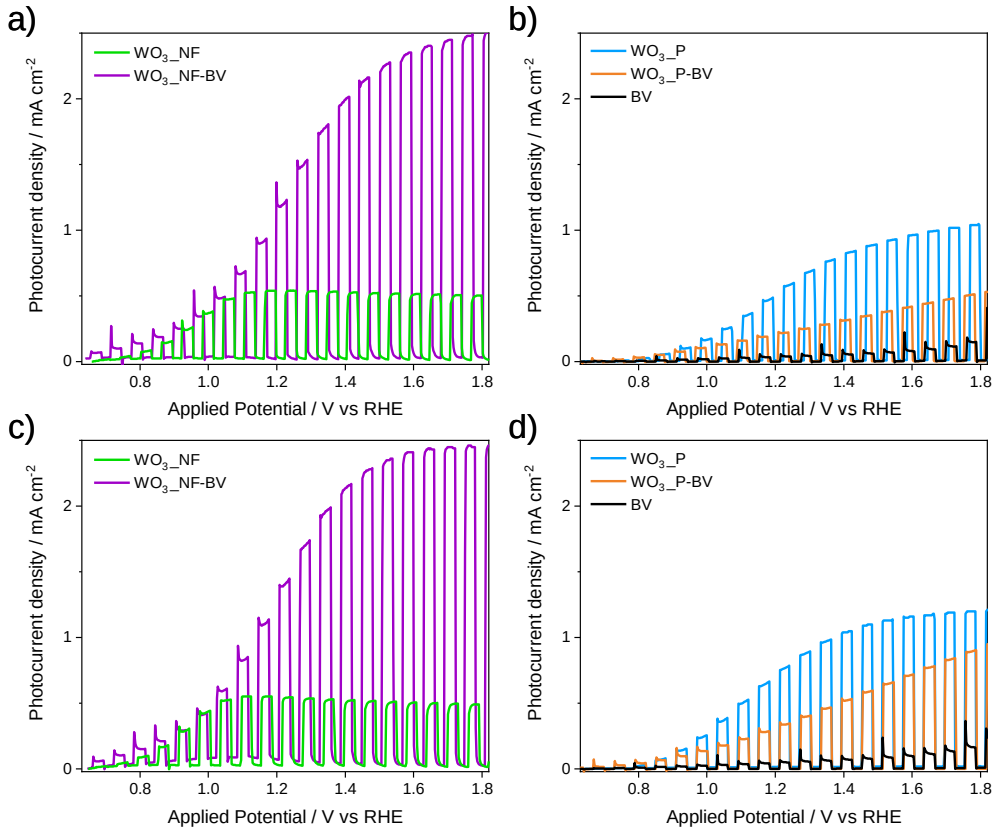

Figure 5.6 Linear Sweep Voltammetry (LSV) of WO_3, WO_3-BV and BV nanostructured and planar electrodes recorded under (a, b) back-side and (c, d) front-side irradiation in 0.5 M Na_2SO_4.

The performance of the WO_3_NF sample is considerably enhanced upon $BiVO_4$ deposition, due to the synergistic effects created by the combination of the two metal oxides. $BiVO_4$ contributes to extending the absorption onset of the system, from 470 to 520 nm, allowing the exploitation of a wider range of the incident light. At the same time, thanks to the favourable Fermi level alignment between the two oxides, the photocurrent onset of the composite electrode is sensibly anticipated to ~0.6 V vs RHE,[44] with respect to the 0.8 V vs RHE onset observed for WO_3_NF. Interestingly, the photocurrent of WO_3_NF–$BiVO_4$ does not reach a plateau value as in the case of WO_3_NF, possibly because $BiVO_4$ contributes to suppress a portion of surface defects intrinsically induced by the peculiar nanostructuring of WO_3_NF. This hypothesis is corroborated by the above-presented EIS results, showing a better charge transfer resistance and an increased surface capacitance upon deposition of BV on WO_3_NF, possibly thanks to beneficial electron injection from the bismuth vanadate overlayer to the underlying tungsten oxide.

The heterojunction generates a greatly enhanced photocurrent of *ca.* 1.3 mA cm^{-2} at 1.23 V vs RHE, that reaches the value of 2.5 mA cm^{-2} at higher applied potentials, with a 5-fold increase in performance with respect to pure WO_3_NF. By comparing the performances of the nanostructured electrode under back- (**Fig. 5.6a**) and front-side (**Fig. 5.6c**) irradiation, we observe that comparable photocurrent values are generated in the two different illumination configurations. This unexpected result attained under back-side illumination may suggest that the more oxidizing power of the tungsten oxide underlayer is to some extent preserved, possibly due to a residual direct contact between the uncovered WO_3 and the electrolyte.

Figures 5.6b,d report the LSV plots recorded with the planar electrodes under identical operating conditions. Firstly, even in the absence of a nanostructured morphology, the LSV curves of WO_3 electrodes are still characterized by a plateau photocurrent, which is however reached at a higher potential with respect to that attained with WO_3_NF. This would suggest that WO_3 electrodes with planar morphology have less surface defects compared to the nanostructured samples. This phenomenon could be also responsible for the higher photocurrent values reached by WO_3_P, which outperforms nanostructured WO_3_NF at applied potentials larger than 1.2 V, reaching a maximum photocurrent of 1 mA cm^{-2}. On the other hand, under back-side irradiation the planar WO_3–$BiVO_4$ heterojunction exhibits an even lower photocurrent than pure WO_3 on the whole range of investigated applied potential, reaching a photocurrent maximum of ca. 0.5 mA cm^{-2}. This phenomenon is observed also under front-side irradiation (**Fig. 5.6d**), because, as mentioned above, the heterojunction should work better under front-side irradiation. Poor performances under these conditions can be indicative of a detrimental mechanism in the planar heterojunction, which could affect the system also under back-side irradiation. Moreover, in back configuration, due to the uniform coverage of the tungsten oxide underlayer with $BiVO_4$, the absence of a direct transfer of the highly oxidizing photogenerated WO_3 holes towards water molecules (mainly interacting with the exposed $BiVO_4$ layer) could also contribute to the worsening of the planar heterojunction performance under such conditions.

Interestingly, the planar BV electrode generates very moderate photocurrents under both irradiation configurations, probably due to the relatively modest thickness of the

photoactive sample which does not exceed the inactive layer depth, the so-called "dead-layer", previously observed in thin $BiVO_4$ photoanodes.[45]

On the basis of the PEC tests performed under full-lamp irradiation we can thus conclude that, given two sets of electrodes with comparable thickness and absorption properties, the PEC performance of the planar WO_3–$BiVO_4$ heterojunction appears to be hampered by a detrimental phenomenon leading to a worse performance of the composite material with respect to the corresponding single-component WO_3 electrode. On the other hand, the nanostructured WO_3_NF–BV coupled sample exhibits the best performance among all investigated samples, much higher than that of pure WO_3_NF, under both back- and front-side irradiation configuration.

Single-wavelength measurements were then performed to better investigate the observed phenomenon. **Figure 5.7** shows the incident photon to current efficiency (IPCE) curves recorded with the prepared WO_3, WO_3–$BiVO_4$ and $BiVO_4$ electrodes under both back-side and front-side monochromatic illumination at the fixed applied potential of 1.23 V vs RHE.

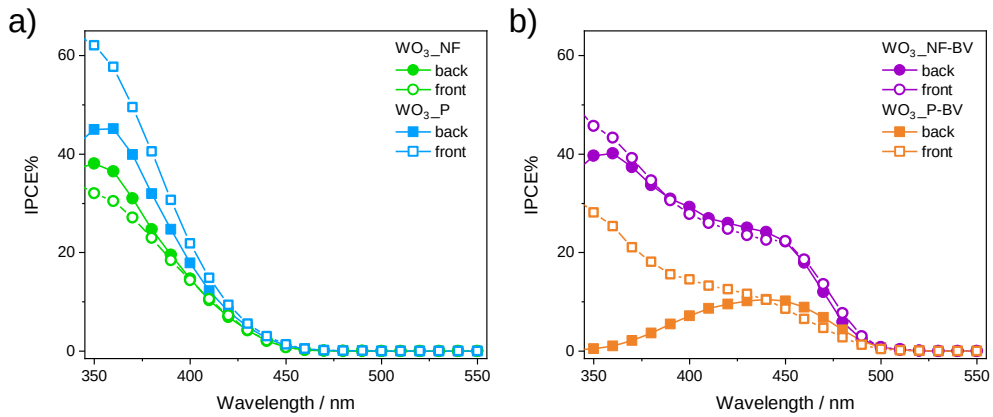

Figure 5.7 Incident Photon to Current Efficiency (IPCE) of a) WO_3 and b) WO_3–BV electrodes performed at 1.23 V vs RHE in Na_2SO_4 0.5 M under back- (full symbols) and front-side (open symbols) irradiation.

The efficiencies attained with the two pure WO_3 electrodes are compared in **Fig. 5.7a**. Both photoanodes show the same photocurrent onset at 450 nm, confirming that the nanostructured morphology does not affect the photoresponse onset of WO_3, mainly depending on the intrinsic material's band gap, rather than the peculiar light scattering properties induced by the nanoflake-like structure. WO_3_P exhibits higher IPCE values

compared to WO_3_NF at all investigated wavelengths, in agreement with the relative performance trend observed under full lamp irradiation (see **Fig. 5.6**). Furthermore, WO_3_P performs better under front-side irradiation configuration, reaching 65% efficiency at 350 nm, which suggests a better mobility of the photogenerated electrons with respect to the photogenerated holes. Differently, the WO_3_NF film displays a slightly better efficiency in back-side configuration with respect to front-side irradiation, indicating quite similar transport properties of electrons and holes in this sample. Given the relatively small (~150 nm) hole diffusion length in WO_3, hole diffusion at distances in the micrometres range is highly unlikely.[46,47] The good performance of WO_3_NF under back-side illumination, that is, when the holes are generated in proximity to the FTO/material interface, can be then related to the peculiar nanoflake-like structure of the sample itself, possibly allowing an effective electrolyte penetration within the film, with a shorter distance between the hole generation sites (across the WO_3 flakes) and the hole collector electrolyte, and a consequent overall mitigation of electron-hole pairs recombination.

IPCE results attained under both front- and back-side irradiation with the composite electrodes are compared in **Fig. 5.7b**. Even in this case, the photocurrent onset is similar for both materials and it is located at *ca.* 500 nm, in accordance with the absorption spectra shown in **Fig. 5.1a**. WO_3_NF–BV displays higher efficiency with respect to the corresponding planar electrode on the whole investigated wavelengths range and under both adopted irradiation configurations. In particular, WO_3_NF–BV shows similar IPCE values under both back- and front-side irradiation, whereas WO_3_P–BV shows higher efficiency under front-side irradiation.

In the UV region ($\lambda < 420$ nm), the IPCE values of the planar WO_3–$BiVO_4$ photoanode under back-side irradiation rapidly decrease down to a null efficiency at the shortest wavelengths. This phenomenon can be related to the activation of a detrimental charge carriers recombination path, mainly occurring upon irradiating the WO_3–$BiVO_4$ photoanode with UV light through the FTO/electrode interface, when WO_3 absorbs most of the incident UV radiation. On the other hand, upon front-side illumination, a *ca.* 25% efficiency is observed at 350 nm (to be compared with a 60% efficiency observed for pure WO_3_P), suggesting that the undesired recombination process is mitigated, but still not completely avoided, when $BiVO_4$ is the main light absorber material.

At $\lambda > 440$ nm, when the WO_3 underlayer is not absorbing incident light, comparable IPCE values in the two illumination configurations are attained for WO_3_P–BV, indicating that the undesired charge carriers recombination path is active only upon the simultaneous excitation of the two semiconductors and especially in the conditions in which the WO_3 underlayer absorbs most of the UV light, i.e., under back-side illumination. Under such conditions, as already outlined in our previous works,[18,48] a recombination channel between photoexcited electrons in WO_3 CB and photogenerated holes in $BiVO_4$ VB becomes more relevant with increasing the amount of photopromoted electrons in the WO_3 conduction band, as in the case of the here prepared, relatively thick planar WO_3 films, which absorb a considerable fraction of light (see the scheme reported in **Figure 5.8a**).

On the other hand, WO_3_NF–BV exhibits the same IPCE trend under back- and front-side irradiation, over the entire investigated wavelengths range, indicating that in this sample the detrimental charge recombination channel is not affecting the overall performance of the nanostructured coupled system. Under UV irradiation, regardless of the irradiation configuration, the peculiar morphology of the sample prevents the photogenerated carrier from recombining, favouring their collection by either the external circuit or the electrolyte solution due to a shortening of their path. In this range, the efficiencies recorded by the composite material are only slightly lower than those acquired with the single WO_3_NF sample, possibly indicating that a portion of the underlying tungsten oxide layer still benefits from its direct contact with the electrolyte solution also after having been coated with bismuth vanadate. This hypothesis has been validated by preparing a nanostructured WO_3–$BiVO_4$ heterojunction with a higher bismuth vanadate loading. As shown in **Figure B1** in the Appendix at the end of this Chapter, with this electrode higher efficiency was observed in the visible, as well as a lower performance in the UV region, with respect to the composite sample possessing a thinner bismuth vanadate overlayer, in line with the presence of a portion of uncovered tungsten oxide material in this sample.

Interestingly, the WO_3_NF–BV sample outperforms its planar WO_3_P–BV counterpart over the whole investigated wavelength range, with a maximum efficiency of ca. 25% at 420 nm, which is more than double compared to that recorded with the corresponding WO_3_P–BV photoanode. Under visible light irradiation, the charges are generated on the $BiVO_4$ layer, close to the electrolyte; the migration and collection of the electrons is favoured

by the nanostructured system, and this leads to higher efficiency also in the visible light region.

Finally, as shown in **Figure B2** in the Appendix, the IPCE of pure $BiVO_4$ is negligible under both irradiation conditions, in line with the modest performance recorded under full-lamp irradiation.

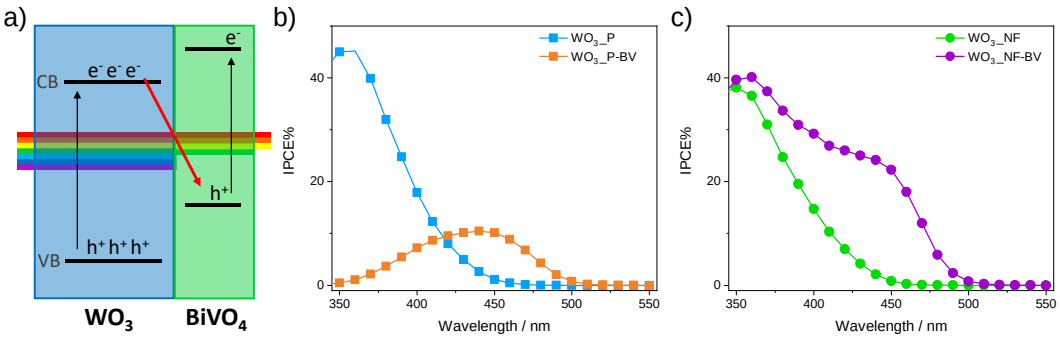

Figure 5.8 a) Proposed charge recombination mechanism active under back-side irradiation in a planar WO_3–$BiVO_4$ electrode, b) IPCE% of WO_3_P and WO_3_P–BV in back-side configuration, c) IPCE% of WO_3_NF and WO_3_NF–BV in back-side configuration.

A comparison between the IPCE curves, reported in **Fig. 5.8b-c**, evidences that the previously described detrimental recombination path, mainly active in the planar heterojunction, determines a severe reduction in efficiency of the planar composite electrode in the UV region with respect to WO_3_P. On the other hand, WO_3_NF–BV does not exhibit any reduction in activity at relatively short wavelengths with respect to the corresponding pure WO_3 electrode, the IPCE value being *ca.* 40% at 350 nm for both WO_3_NF and WO_3_NF–BV. Thus, WO_3 nanostructuring seems to play a pivotal role in enhancing the overall performance attained with the WO_3_NF–BV composite photoanode, by overcoming the undesired limitations of the planar composite. Under back-side irradiation the good transport properties of both electrons and holes are preserved in WO_3_NF, generating higher efficiency in all the investigated wavelengtsh range (**Fig. 5.8c**). In particular, upon front-side irradiation, the efficient charges separation expected for a type-II heterojunction is combined with the excellent electron transport properties of the underlying tungsten trioxide.

5.4.3.1 IPCE enhancement and efficiencies

The IPCE values of each WO_3–$BiVO_4$ heterojunction electrode recorded under back-side irradiation were compared with those obtained with the corresponding single components in terms of the so-called IPCE enhancement factor, calculated as follows:[26]

$$\text{IPCE enhancement} = \text{IPCE}_{WO_3-BiVO_4} - (\text{IPCE}_{WO_3} + \text{IPCE}_{BiVO_4}) \qquad (5.3)$$

where $\text{IPCE}_{WO_3-BiVO_4}$ is the IPCE measured with the coupled system, while IPCE_{WO_3} and IPCE_{BiVO_4} are the IPCE values of the single WO_3 sample (either planar or nanostructured) and of the *ca.* 130 nm-thick pure $BiVO_4$ electrode (reported in **Figure B2**), recorded in separate experiments, respectively.

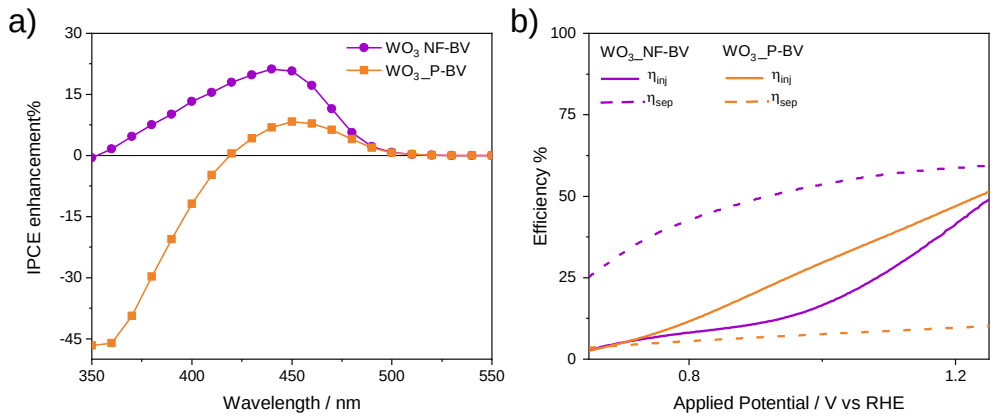

Figure 5.9 a) IPCE enhancement factor calculated according to equation (3) and b) charge separation and charge injection efficiency of nanostructured and planar WO_3–BV heterojunctions.

As already observed in **Fig. 5.8b,** the planar WO_3**–**$BiVO_4$ electrode does not preserve the performance of its underlying WO_3 in the UV region, and its IPCE enhancement factor becomes negative at wavelengths shorter than 420 nm, with a minimum of *ca.* -45% at 350 nm (orange curve in **Figure 5.9a**). Moreover, a very modest gain in activity is observed in the visible light region with respect to the single-component electrode.

Differently, the behaviour of the nanostructured WO_3_NF–BV heterojunction generates an effective photoactivity enhancement across the almost entire range of investigated wavelengths, with the WO_3_NF–BV composite showing a 25% enhancement maximum at 450 nm, that progressively decreases with decreasing irradiation wavelength, becoming zero at 350 nm (purple curve in **Figure 5.9a**). This IPCE enhancement trend

under UV light irradiation suggests that the nanostructured heterojunction retains the good performances of WO_3_NF, possibly due to the preservation of its partial direct exposure to the electrolyte.

In order to better shed light on the specific role played by the nanostructuring of the WO_3 underlayer on both the bulk charge separation and the surface charge injection properties of the heterojunction electrode, the photogenerated charge separation efficiency (η_{sep}) in the bulk and the minority charge carrier injection efficiency at the electrode/electrolyte interface (η_{inj}) of the electrodes were determined by performing experiments under back-side irradiation in the presence of sulphite anions, acting as sacrificial agents.

In fact, the water oxidation photocurrent density generated by a sample can always be expressed as: $J = J_{abs} \cdot \eta_{sep} \cdot \eta_{inj}$, where J_{abs} is the maximum theoretical current density of the sample, calculated from the integration of the product between the standard AM 1.5 G solar spectrum and the absorption spectrum of the electrode, over the proper absorption wavelength range of the film.[49] By assuming a 100% charge injection efficiency for Na_2SO_3 oxidation ($\eta_{inj} = 1$), the photocurrent attained with our electrodes in a 0.5 M Na_2SO_3 electrolyte buffered at pH 7 ($J_{Na_2SO_3}$) is $J_{Na_2SO_3} = J_{abs} \cdot \eta_{sep}$, from which η_{sep} can be simply obtained by dividing the photocurrent measured in the presence of the Na_2SO_3 hole scavenger by J_{abs}. From the combination of the two photocurrent expressions (in the presence and absence of the hole scavenger) one can finally calculate η_{inj}, which is equal to the ratio between J_{H_2O} and $J_{Na_2SO_3}$.

The calculated efficiencies for the two coupled electrodes series are reported in **Fig. 5.9b** as a function of the applied potential. The nanostructured heterojunction clearly exhibits a 6-fold higher charge separation efficiency compared to the planar heterojunction, with η_{sep} values passing from ~10% to ~60% at 1.23 V vs RHE in the case of WO_3_P–BV and WO_3_NF–BV samples, respectively. This indicates that the WO_3_NF–BV electrode is much less subjected to charge recombination in the bulk, which confirms the key role that morphology tuning has on the photogenerated charge transport properties of these materials.

The charge injection efficiencies of both samples show a similar trend, progressively increasing with increasing applied potential up to the water oxidation potential, at which η_{inj}

is ~50% for both heterojunctions. This behaviour is to be ascribed to the presence, in both samples, of the $BiVO_4$ top layer, which, in the low-potential regime, is less efficient in charge transfer to the solution.[50]

Thus, the two main factors leading to the great increase of photoelectrochemical activity of WO_3_NF–BV with respect to WO_3_P–BV are *i)* an improved charge separation guaranteed by the peculiar nanoflake-like arrangement of the underlying thick WO_3 layer, that ensures the reduction of the path that the holes generated close to the FTO/electrode interface have to travel to react with water molecules in the solution, and *ii)* possibly the preservation of a portion of exposed tungsten trioxide directly in contact with the electrolyte. The here reported WO_3 nanostructuring represents a promising strategy to exploit the beneficial effects ensured by the WO_3-$BiVO_4$ type-II heterojunction and to suppress detrimental photogenerated charge carrier recombination paths, which instead may be active in planar WO_3 – $BiVO_4$ heterojunctions.

5.5 Conclusions

WO_3 and WO_3–$BiVO_4$ electrodes of comparable thickness and absorption properties but characterized by either a planar or a nanoflake-like morphology have been prepared following two different methodologies and have been thoroughly characterized via optical, structural, morphological and photoelectrochemical analyses. This systematic investigation allowed us to ascertain the origin of the enhanced performance of the nanostructured WO_3–$BiVO_4$ electrodes with respect to the planar ones.

Full-lamp and monochromatic PEC analyses demonstrated that the severe electron-hole recombination path active in the WO_3_P–$BiVO_4$ planar electrode under back-side irradiation is successfully overcome by properly nanostructuring the tungsten trioxide underlayer. Even if WO_3_NF alone, as documented via EIS and PEC analyses, exhibited some limitations in its activity, such as higher charge transfer resistance and lower surface capacitance values, the deposition of bismuth vanadate on the nanostructured underlayer was found to be effective in overcoming such intrinsic disadvantages.

Indeed, differently from the planar composite, the WO_3_NF–$BiVO_4$ exhibits improved hole and electron transport properties, as evidenced by the similar PEC performances attained under both back- and front-side irradiation, which may be directly related to the peculiar morphology of the nanostructured composite. In fact, other properties of the photoactive material in the electrodes, such as the film thickness, the absorption properties and the crystalline phase, are the same for all investigated photoanodes. Moreover, the fact that the good PEC performance of the underlying WO_3 layer is maintained in the nanostructured composite guarantees a high oxidative power of the holes photogenerated in this system.

These factors result in a greatly enhanced charge separation efficiency in the nanostructured WO_3_NF–$BiVO_4$ photoanode, exhibiting relatively high overall photocurrents under simulated solar irradiation.

Appendix B

Nanostructured WO_3-$BiVO_4$ composite with four deposited BV layers

As outlined in **Section 5.4.3**, a nanostructured composite sample possessing four deposited layers of $BiVO_4$ (WO_3_NF–BV 4L) was prepared and its PEC performance was compared to that of the WO_3_NF–BV sample investigated in this Chapter, which was prepared by depositing two layers of $BiVO_4$ on the starting WO_3_NF sample (here indicated as WO_3_NF–BV 2L). As evidenced by the PEC results attained with such samples under full lamp irradiation (see **Fig. B1a**), the WO_3_NF–BV 4L sample possessing a larger amount of deposited $BiVO_4$ exhibits worse photocurrents compared to the WO_3_NF–BV 2L system at relatively low applied potential, whereas at relatively high applied potential its performance is superior to that of WO_3_NF–BV 2L. Under monochromatic irradiation, the efficiency of WO_3_NF–BV 4L is slightly better in the visible range (460-510 nm), but worse at $\lambda < 460$ nm. These results seem to corroborate the hypothesis according to which the electrode with only two $BiVO_4$ layers still preserves a portion of uncovered WO_3 underlayer, directly in contact with the electrolyte.

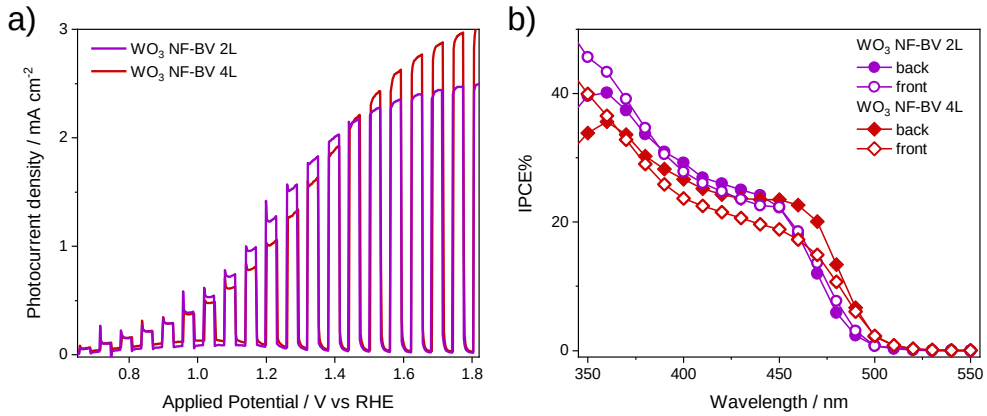

Figure B1 a) LSV plot recorded under back-side simulated solar light irradiation and b) Incident Photon to Current Efficiency (IPCE) measurements at 1.23 V vs RHE in Na_2SO_4 0.5 M in back- (full symbols) and front-side (open symbols) irradiation of WO_3_NF-BV 2L (purple) and WO_3_NF-BV 4L (red) electrodes.

IPCE of pure $BiVO_4$

In line with the results obtained under simulated solar light irradiation, the IPCE values attained with the planar BV electrode are relatively modest, *i.e.*, reaching a maximum value of 2.5% at 350 nm under back-side irradiation (**Fig. B2**).

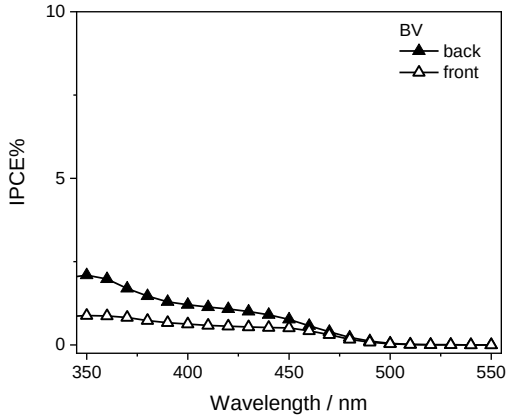

Figure B2 Incident Photon to Current Efficiency (IPCE) measurements of planar BV electrode acquired at 1.23 V vs RHE in Na_2SO_4 0.5 M under back- (full symbols) and front-side (open symbols) irradiation.

References

1. J.H. Kim, D. Hansora, P. Sharma, J.W. Jang, J.S. Lee, *Chem. Soc. Rev.* 48 (**2019**) 1908–1971.
2. M.G. Walter, E.L. Warren, J.R. McKone, S.W. Boettcher, Q. Mi, E.A. Santori, N.S. Lewis, *Chem. Rev.* 110 (**2010**) 6446–6473.
3. K. Maeda, K. Domen, *J. Phys. Chem. Lett.* 1 (**2010**) 2655–2661.
4. D.K. Lee, D. Lee, M.A. Lumley, K.S. Choi, *Chem. Soc. Rev.* 48 (**2019**) 2126–2157.
5. K. Sivula, *J. Phys. Chem. Lett.* 4 (**2013**) 1624–1633.
6. B.D. Alexander, P.J. Kulesza, I. Rutkowska, R. Solarska, J. Augustynski, *J. Mater. Chem.* 18 (**2008**) 2298–2303.
7. Y. Lu, Y. Yang, X. Fan, Y. Li, D. Zhou, B. Cai, L. Wang, K. Fan, K. Zhang, *Adv. Mater.* 34 (**2022**) 2108178.
8. C. Janáky, K. Rajeshwar, N.R. De Tacconi, W. Chanmanee, M.N. Huda, *Catal. Today* 199 (**2013**) 53–64.
9. N. Guijarro, P. Bornoz, M.S. Prévot, X. Yu, X. Zhu, M. Johnson, X. Jeanbourquin, F. Le Formal, K. Sivula, *Sustain. Energy Fuels* 2 (**2018**) 103–117.
10. S. Corby, E. Pastor, Y. Dong, X. Zheng, L. Francàs, M. Sachs, S. Selim, A. Kafizas, A.A. Bakulin, J.R. Durrant, *J. Phys. Chem. Lett.* 10 (**2019**) 5395–5401.
11. A. Polo, I. Grigioni, M. Magni, A. Facibeni, M. Vittoria Dozzi, E. Selli, *Appl. Surf. Sci.* 556 (**2021**) 149759.
12. B. Klahr, S. Giménez, F. Fabregat-Santiago, T. Hamann, J. Bisquert, *J. Am. Chem. Soc.* 134 (**2012**) 4294–4302.
13. X. Zhu, N. Guijarro, Y. Liu, P. Schouwink, R.A. Wells, F. Le Formal, S. Sun, C. Gao, K. Sivula, *Adv. Mater.* 30 (**2018**) 1–6.
14. C. Santato, M. Ulmann, J. Àugustynski, *J. Phys. Chem. B* 105 (**2001**) 936–940.
15. S. Ju, H.J. Seok, J. Jun, D. Huh, S. Son, K. Kim, W. Kim, S. Baek, H.K. Kim, H. Lee, *Appl. Catal. B Environ.* 263 (**2020**) 118362.
16. Y. Pihosh, I. Turkevych, K. Mawatari, T. Asai, T. Hisatomi, J. Uemura, M. Tosa, K. Shimamura, J. Kubota, K. Domen, T. Kitamori, *Small* 10 (**2014**) 3692–3699.
17. S.Y. Chae, C.S. Lee, H. Jung, O.S. Joo, B.K. Min, J.H. Kim, Y.J. Hwang, *ACS Appl. Mater. Interfaces* 9 (**2017**) 19780–19790.
18. I. Grigioni, K.G. Stamplecoskie, D.H. Jara, M.V. Dozzi, A. Oriana, G. Cerullo, P. V. Kamat, E. Selli, *ACS Energy Lett.* 2 (**2017**) 1362–1367.

19. F.E. Osterloh, *Chem. Soc. Rev.* 42 (**2013**) 2294–2320.

20. A. Tacca, L. Meda, G. Marra, A. Savoini, S. Caramori, V. Cristino, C.A. Bignozzi, V.G. Pedro, P.P. Boix, S. Giménez, J. Bisquert, *ChemPhysChem* 13 (**2012**) 3025–3034.

21. Y. Liu, B.R. Wygant, K. Kawashima, O. Mabayoje, T.E. Hong, S.G. Lee, J. Lin, J.H. Kim, K. Yubuta, W. Li, J. Li, C.B. Mullins, *Appl. Catal. B Environ.* 245 (**2019**) 227–239.

22. P. Wei, Y. Wen, K. Lin, X. Li, *Int. J. Hydrogen Energy* 46 (**2021**) 27506–27515.

23. P.M. Rao, L. Cai, C. Liu, I.S. Cho, C.H. Lee, J.M. Weisse, P. Yang, X. Zheng, *Nano Lett.* 14 (**2014**) 1099–1105.

24. B.R. Lee, M.G. Lee, H. Park, T.H. Lee, S.A. Lee, S.S.M. Bhat, C. Kim, S. Lee, H.W. Jang, *ACS Appl. Mater. Interfaces* 11 (**2019**) 20004–20012.

25. J. Su, L. Guo, N. Bao, C.A. Grimes, *Nano Lett.* 11 (**2011**) 1928–1933.

26. I. Grigioni, M.V. Dozzi, E. Selli, *J. Phys. Condens. Matter* 32 (**2020**) 014001.

27. M. Pedroni, G.L. Chiarello, E. Vassallo, E. Selli, *Surfaces* 3 (**2020**) 105–115.

28. J. Su, X. Feng, J.D. Sloppy, L. Guo, C.A. Grimes, *Nano Lett.* 11 (**2011**) 203–208.

29. Y. Liang, T. Tsubota, L.P.A. Mooij, R. Van De Krol, *J. Phys. Chem. C* 115 (**2011**) 17594–17598.

30. E. López-Fraguas, J.M. Sánchez-Pena, R. Vergaz, *IEEE Trans. Instrum. Meas.* 68 (**2019**) 4913–4923.

31. M. Tayebi, B.K. Lee, *Renew. Sustain. Energy Rev.* 111 (**2019**) 332–343.

32. W. Ye, F. Chen, F. Zhao, N. Han, Y. Li, *ACS Appl. Mater. Interfaces* 8 (**2016**) 9211–9217.

33. J.C. Hill, K.S. Choi, *J. Phys. Chem. C* 116 (**2012**) 7612–7620.

34. J.A. Seabold, K.S. Choi, *Chem. Mater.* 23 (**2011**) 1105–1112.

35. Y. Park, K.J. McDonald, K.S. Choi, *Chem. Soc. Rev.* 42 (**2013**) 2321–2337.

36. A. Polo, I. Grigioni, M.V. Dozzi, E. Selli, *Catal. Today* 340 (**2020**) 19–25.

37. J.E.B. Randles, *Discuss. Faraday Soc.* 1 (**1947**) 11–19.

38. J. Bisquert, G. Garcia-Belmonte, P. Bueno, E. Longo, L.O.S. Bulhões, *J. Electroanal. Chem.* 452 (**1998**) 229–234.

39. X. Shi, I. Herraiz-Cardona, L. Bertoluzzi, P. Lopez-Varo, J. Bisquert, J.H. Park, S. Giménez, *Phys. Chem. Chem. Phys.* 18 (**2016**) 9255–9261.

40. W. Li, P. Da, Y. Zhang, Y. Wang, X. Lin, X. Gong, G. Zheng, *ACS Nano* 8 (**2014**) 11770–11777.

41. K. Sivula, F. Le Formal, M. Grätzel, *ChemSusChem* 4 (**2011**) 432–449.

42. S. Corby, L. Francàs, S. Selim, M. Sachs, C. Blackman, A. Kafizas, J.R. Durrant, *J. Am. Chem. Soc.* 140 (**2018**) 16168–16177.

43. Y. Wang, W. Tian, C. Chen, W. Xu, L. Li, *Adv. Funct. Mater.* 29 (**2019**) 1–25.

44. I. Grigioni, K.G. Stamplecoskie, E. Selli, P. V. Kamat, *J. Phys. Chem. C* 119 (**2015**) 20792–20800.

45. S. Selim, L. Francàs, M. García-Tecedor, S. Corby, C. Blackman, S. Giménez, J.R. Durrant, A. Kafizas, *Chem. Sci.* 10 (**2019**) 2643–2652.

46. X. Liu, F. Wang, Q. Wang, *Phys. Chem. Chem. Phys.* 14 (**2012**) 7894–7911.

47. C. Fàbrega, S. Murcia-López, D. Monllor-Satoca, J.D. Prades, M.D. Hernández-Alonso, G. Penelas, J.R. Morante, T. Andreu, *Appl. Catal. B Environ.* 189 (**2016**) 133–140.

48. I. Grigioni, M. Abdellah, A. Corti, M.V. Dozzi, L. Hammarström, E. Selli, *J. Am. Chem. Soc.* 140 (**2018**) 14042−14045.

49. H. Dotan, K. Sivula, M. Graetzel, S.C. Warren, *Energy Environ. Sci.* 4 (**2011**) 958–964.

50. P. Vecchi, A. Piccioni, R. Mazzaro, M. Mazzanti, V. Cristino, S. Caramori, L. Pasquini, *Sol. RRL* 6 (**2022**) 2200108.

Chapter 6 – WO_3–$BiVO_4$ planar heterojunctions

6.1 Abstract

Combining different metal oxide semiconductors that present complementary characteristics to build a type-II heterojunction is an efficient strategy that aims at enhancing the photoelectrochemical performance of the composite photoanode, exploiting the synergistic effects that arise from the combination of different materials. WO_3–$BiVO_4$ photoelectrodes show indeed the most promising efficiencies in the photooxidation of water into molecular oxygen and have been thus thoroughly studied in recent years. A key factor in building these systems is to finely tune the balance between the two oxides, aiming at minimizing detrimental recombination paths that might arise in the heterojunction, while at the same time maximizing the favourable mechanisms that increase the composite's performance. In this Chapter the preparation and full characterization of single-phase WO_3 and $BiVO_4$ as well as of composite WO_3–$BiVO_4$ photoanodes displaying various under- and overlayer thicknesses is discussed in detail. PEC analyses under full-lamp and monochromatic irradiation allowed us to identify the conditions in which the detrimental charge recombination path active under back-side irradiation is mitigated, that is, by minimizing the absorption of both tungsten trioxide and bismuth vanadate layers under back-side illumination. Moreover, tests run in the presence of a sacrificial agent evidenced that the increase in performance observed by

combining the two oxides may result from a greatly improved charge injection efficiency of the composite with respect to its single components, rather than from the building of an effective type-II heterojunction.

6.2 Introduction

Tungsten trioxide (WO_3) is a well-known photoanode material, due to its modest band gap energy of 2.7 eV and its good charge conductivity.[1–3] Bismuth vanadate ($BiVO_4$) is also gathering increasing attention as another promising water oxidation photocatalyst, due to its ability to absorb visible light and a 9% theoretical solar to hydrogen conversion efficiency.[4–6] Since the first demonstration that a WO_3–$BiVO_4$ heterojunction obtained from the deposition of bismuth vanadate on tungsten trioxide electrodes led to an enhanced photocurrent and incident photon to current efficiency compared to individual materials,[7] many efforts have been directed at improving this system. Pairing WO_3 with $BiVO_4$ is indeed a very promising strategy to attain improved photoelectrochemical water splitting efficiency, due to their well-matched band edge positions that generate a staggered or so-called type-II heterojunction.[8–10] In such system the separation of photogenerated charge carriers is favoured and this is one of the main reasons responsible for the superior efficiency of the WO_3–$BiVO_4$ system, according to literature.[11–14] Indeed, the energy mismatch between the conduction (CB) and valence band (VB) edges of the two materials builds a situation in which the CB and VB band edges of $BiVO_4$ lie at more negative potentials with respect to their counterparts in WO_3. This electronic structure of the heterojunction allows electrons that are photopromoted in bismuth vanadate's CB to be effectively drawn to tungsten oxide's CB, while simultaneously photogenerated holes can be transferred from the VB of WO_3 to that of $BiVO_4$, where they react with the absorbed water molecules at the bismuth vanadate/electrolyte interface. Other synergistic effects contributing to the good performances recorded by this heterojunction are found in an increased light harvesting ability and charge conductivity.[15,16]

On a closer look, although a type-II heterojunction seems ideal to obtain an efficient spatial separation of photogenerated carriers, it also presents a number of inadequacies.[9] From a thermodynamic point of view, the increased charge separation occurs at the cost of a

reduced oxidation overpotential, since $BiVO_4$ presents a more negative VB edge with respect to WO_3, thus lowering the driving force of the overall redox reaction.[10,17] At the same time, the electrostatic repulsion between the holes present in $BiVO_4$ and those transferred from WO_3 may hamper their spatial separation. Concurrently, the attraction between holes and electrons in each and among the two individual materials may open several charge recombination channels, once more decreasing the separation efficiency of the type-II heterojunction.

In recent years, the charge carrier dynamics of the WO_3–$BiVO_4$ heterojunction has been extensively studied. Firstly, transient absorption (TA) spectroscopy studies revealed that upon excitation in the UV range the recombination rate in the heterojunction is faster compared to in BV alone.[14] Furthermore, the simultaneous excitation of both oxides may open a recombination channel, leading to the recombination of electrons in the CB of WO_3 with the holes present in the VB of $BiVO_4$.[12,18,19] The WO_3–$BiVO_4$ heterojunction would then benefit from avoiding the excitation of the tungsten trioxide underlayer, the thickness of which greatly influences the extent of this recombination path, and from tuning the thickness of the bismuth vanadate overlayer in order to shield the absorption of WO_3.[12,19] Given the theoretical operating principles of a tandem photoelectrochemical cell, detailed in **Chapter 2, Section 2.2.2**, in which the photoanode component should be the first absorber in the system, one can completely avoid WO_3 excitation only if a significant part of the solar radiation striking the cell is blocked, with unavoidable efficiency losses.

In this Chapter we therefore concentrated on preparing and fully characterizing WO_3–$BiVO_4$ planar photoanodes presenting different thicknesses of both the under- and the over-layer. Final aim would be obtaining an optimal balance between the two oxides, to maximize the performance of the heterojunction and minimize the rise of detrimental recombination paths under both back-side and front-side irradiation conditions.

Moreover, thorough studies have been conducted either by performing PEC tests in the presence of hole scavenger species or under monochromatic irradiation, in order to deepen the knowledge on the working mechanism of the heterojunction and identify the origin of its superior efficiency, besides the intrinsic building of a type-II heterojunction that is formed upon combining these two photocatalysts.

6.3 Experimental section

6.3.1 Chemicals and materials

The following chemicals, all purchased from Sigma Aldrich, were employed as supplied: ammonium metatungstate hydrate (99%, $(NH_4)_6H_2W_{12}O_{40} \cdot xH_2O$), ammonium metavanadate (NH_4VO_3, 99%), bismuth(III) nitrate pentahydrate ($Bi(NO_3)_3 \cdot 5H_2O$, 98%), citric acid (99%), polyethylene glycol 300 (PEG 300), acetylacetone (99%), nitric acid (HNO_3, 23.3% wt). 2-Methoxyethanol (99%) was purchased from Alfa Aesar. 2 mm thick fluorine-doped tin oxide (FTO) glass (7 ohm/sq) was purchased from Kintec. The WO_3 500nm-BV nL photoanodes series (see below) was prepared using Pilkington TEC 7 FTO slabs as conductive substrate.

6.3.2 Photoelectrodes preparation

WO_3 precursor solutions containing different precursor concentrations were prepared in order to obtain WO_3 photoanodes with different thickness. A 1.0 M precursor solution was prepared by adding 0.247 g of ammonium metatungstate hydrate to 0.3 mL of acetylacetone and 0.7 mL of 2-methoxyethanol. The solution was then stirred at constant rate for 3 h and heated at 50 °C. After the complete dissolution of the solid precursors, 50 mg (44 µl) of PEG 300 were added. A small amount (75 µl) of this solution was deposited on a FTO slab via spin coating at 4000 rpm for 30 s. The final spinning rate was reached with a three-acceleration step program: 500 rpm s^{-1} up to 500 rpm, then 1500 rpm s^{-1} up to 2000 rpm, and finally 2000 rpm s^{-1} up to 4000 rpm (**Table 6.1**). After coating, the electrode was annealed at 550 °C for 1 h on a hotplate. WO_3 samples displaying 200 nm and 500 nm thickness were obtained by depositing 1.0 M and 2.0 M precursor solutions. The 800 nm-thick tungsten trioxide sample was prepared by repeating twice the deposition of the 2.0 M precursor solution.

	time / s	rounds per minute	acceleration	acceleration time / s
Step 1	20	500	500	1
Step 2	2	2000	1500	2
Step 3	2	4000	2000	2

Table 6.1 Three-step spin coating program used to prepare WO_3 underlayers.

A $BiVO_4$ precursor solution was prepared by adding 0.386 g of citric acid, 0.495 g of bismuth(III) nitrate and 0.118 g of ammonium metavanadate to 3 mL of nitric acid. The paste was deposited at 4000 rpm for 30 s by spin-coating either on a clean FTO slab or on the previously prepared WO_3 photoelectrodes, followed by annealing at 500 °C for 1 h. This deposition cycle was repeated up to 8 times.

WO_3–$BiVO_4$ heterojunction samples are labelled specifying the underlayer thickness (200 nm, 500 nm, 800 nm) and the number of bismuth vanadate layers deposited on top (2, 4, 6, or 8 layers). Pure materials are labelled indicating either the thickness of the WO_3 layer or the number of deposited layers for pure $BiVO_4$.

The synthesis of each photoelectrode has been repeated at least four times; a good reproducibility between different films as well as an excellent stability over time has been achieved.

6.3.3 Methods

A Jasco V-670 spectrophotometer operating in the transmittance mode was used to record the absorption spectra of investigated photoanodes, which are all optically transparent.

X-rays diffraction analyses were performed to confirm the attainment of crystalline samples and to identify the crystalline structure of the photoanodes, and also to confirm the attainment of two distinct structures in the heterojunction samples. XRD analyses were performed with a Rigaku Miniflex 600 diffractometer, equipped with a Cu tube providing Kα radiation. The shown diffractograms were base-corrected using the Origin software.

A scanning electron microscope (SEM), model Jeol JSM-7600F with a 5 kV incident beam, was used to acquire top view and cross-section images of pure and coupled electrodes.

Photoelectrochemical tests were carried out in a three-electrode cappuccino cell,[20] in which the photoanodes under study are employed as working electrodes, an Ag/AgCl (3 M KCl) electrode was used as reference electrode and the counter electrode was a Pt gauze. Linear Sweep Voltammetry analyses were carried out with a 20 mV s^{-1} scan rate, and the applied bias was controlled through an Autolab PGSTAT 12 controlled by Nova software. The light source was a Newport (Oriel LCS-100 model) solar simulator equipped with an AM 1.5 G filter. The illuminated area of the electrodes was of 0.28 cm^2 and the incident light intensity was fixed at 100 mW cm^{-2}. All prepared electrodes were tested under both back-side irradiation configuration, *i.e.* through the FTO glass, and under front-side irradiation, *i.e.* through the photoactive material, in contact with a 0.5 M Na_2SO_4 electrolyte solution at pH 7. Photoelectrochemical analyses were carried out also in the presence of a hole scavenger species containing 0.5 M Na_2SO_3 in a Kpi buffer.[6,21]

The potential vs Ag/AgCl values were converted into the RHE scale using the following equation: $E_{RHE} = E_{AgCl} + 0.059\ pH + E^{\circ}_{AgCl}$, with $E^{\circ}_{AgCl}(3\ M\ KCl) = 0.210\ V$ at 25 °C.

Incident photon to current efficiency (IPCE) measurements were carried out at 1.23 V vs RHE under monochromatic irradiation in the above described three-electrode set up; the light source was a 300 W Lot-Oriel Xe lamp equipped with a Lot-Oriel Omni-λ 150 monochromator. Percent IPCE values were calculated using the following equation:

$$IPCE\% = \frac{j \cdot 1240}{P_\lambda \cdot \lambda} \cdot 100 \qquad (6.1)$$

where j is the recorded photocurrent density (mA cm^{-2}) and P_λ (mW cm^{-2}) is the power measured at each specific wavelength λ (nm).

6.4 Results and discussion

6.4.1 Photoelectrodes characterization

6.4.1.1 UV-Vis spectroscopy

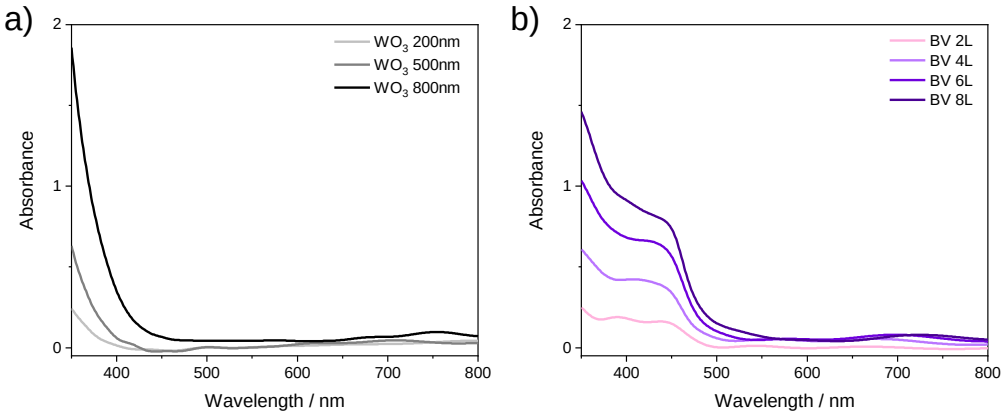

Figure 6.1 Absorption spectra of pure a) WO_3 and b) $BiVO_4$ photoanodes.

The absorption spectra of pure WO_3 and $BiVO_4$ samples are reported in **Figure 6.1**. In general, the absorption increases with increasing thickness of the samples, *i.e.*, with increasing loading of photoactive material on the conductive substrate. WO_3 samples (**Fig. 6.1a**) are characterized by an indirect band gap,[22] and exhibit an absorption onset at *ca.* 450 nm, corresponding to a 2.7 eV band gap energy.[23] $BiVO_4$ samples (**Fig. 6.1b**) show the typical absorption shoulder located at *ca.* 450 nm and are characterized by an extended visible light harvesting capability. The absorption onset is located at 520 nm, accounting for a band gap energy of 2.4 eV, much smaller than that of tungsten trioxide.[24]

The optical properties of the combined WO_3–$BiVO_4$ series have also been investigated and the absorption spectra are reported in **Figure 6.2**. By taking into consideration a particular set of samples (for example that possessing the thinner WO_3 underlayer, see **Fig. 6.2a**), we observe that the absorption shoulder typical of $BiVO_4$ becomes more pronounced with increasing number of deposited $BiVO_4$ layers, in line with an increased loading of this material on the underlying WO_3 layer in successive deposition cycles. On the other hand, by

comparing the absorption spectra of samples with the same $BiVO_4$ loading but different WO_3 thickness (**Fig. 6.2a-c**), we note that the intensity of the maximum absorption located in the UV region increases with the increasing tungsten trioxide thickness. The absorption profiles of these heterojunctions are thus the combination of the optical properties of the two pure materials; WO_3–$BiVO_4$ samples indeed possess an absorption onset and band gap similar to that of $BiVO_4$ (2.4 eV).[25]

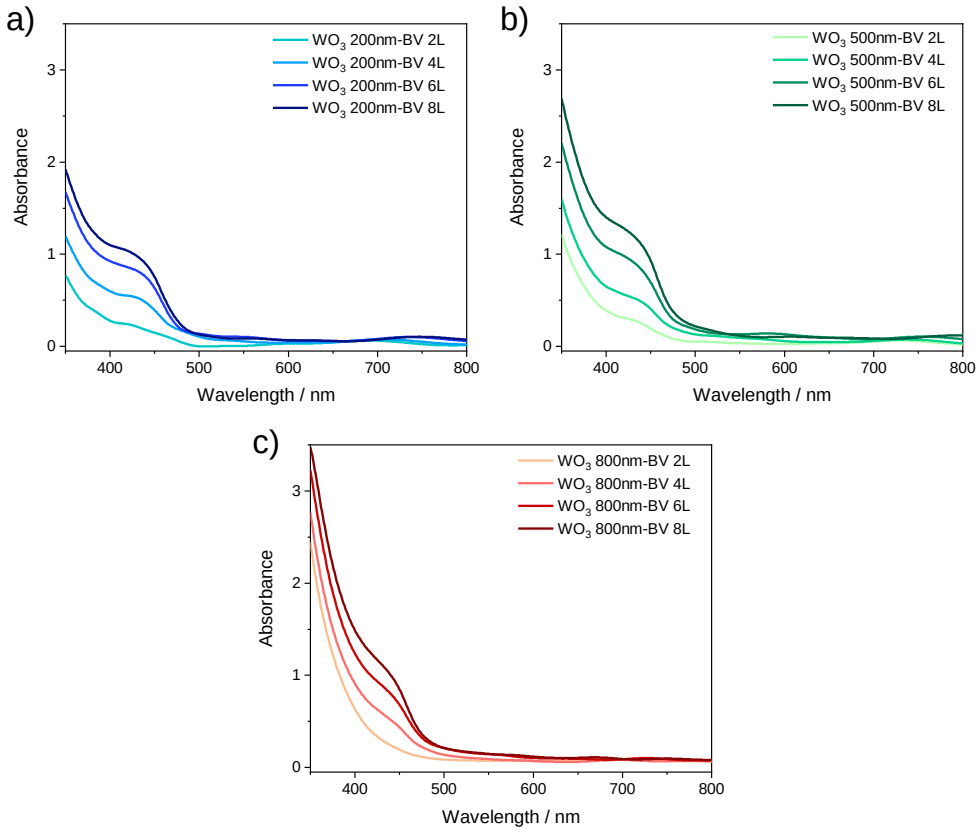

Figure 6.2 Absorption spectra of WO_3–$BiVO_4$ heterojunction photoanodes: a) WO_3 200nm–BV nL, b) WO_3 500nm–BV nL and c) WO_3 800nm–BV nL series.

6.4.1.2 XRD analyses

Figure 6.3 shows the XRD patterns of some representative samples among the investigated photoanodes. The lower pattern represents the diffraction peaks of the fluorine-doped tin oxide glass employed as support in the preparation of all photoanodes.[26] The characteristic

peaks of the FTO support (27, 34, 38 and 52°) are visible in all XRD pattern of the synthesised photoelectrodes.

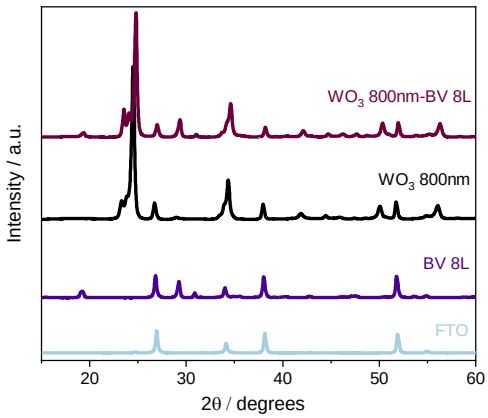

Figure 6.3 XRD patterns of the conducting oxide support (FTO), pure BV 8L, pure WO_3 800nm and WO_3 800nm–BV 8L heterojunction samples.

BV 8L sample exhibits the reflections typical of a crystalline monoclinic structure, often associated with bismuth vanadate photoanodes.[6,27] Indeed, the monoclinic scheelite structure presents a distortion for which two different V–O and four different Bi–O bond lengths exist, favouring local polarization and electron-hole separation; for this reason this crystalline structure is the most photocatalytically active for this material.[28] Moreover, this phase is also characterized by a smaller band gap energy due to the above-mentioned crystal distortion that pushes the *O2p* states towards higher energies, reducing the band gap.[29] In the pattern shown in **Figure 6.3** monoclinic scheelite is evidenced by the reflections at 19.1, 29.1 and 31.1 degrees, corresponding to the {110}, {121}, {040} planes, respectively.[30]

The WO_3 800nm sample shows the peaks of a pure monoclinic structure, which is the stable tungsten oxide phase at temperatures ranging from 20 to 339°C.[31] γ-WO_3 is characterized by the reflections at 23.4, 23.8 and 24.6° related to the {002}, {020} and {200} planes, respectively, and the reflections at 33.5, 34 and 34.4° associated with the {022}, {-202}, {202} planes.[32]

Finally, the diffraction pattern of the WO_3 800nm–BV 8L heterojunction displays the peaks and the crystalline phases of both oxides, thus confirming the coexistence of the two materials in this combined photoelectrode.

6.4.1.3 SEM images

SEM top-view images of WO_3 samples of different thicknesses are shown in **Figure 6.4**. Generally, the surface of tungsten trioxide samples is composed of densely aggregated particles of various sizes. The size of the aggregates seems to become smaller as the thickness of the underlying material increases. The WO_3 200nm sample is indeed characterized by a particles size in the 150-200 nm range, with the smallest aggregates being *ca.* 80 nm in size. WO_3 500nm is composed of slightly smaller particles, with sizes in the 100-150 nm range (the smallest being of *ca.* 50 nm). The thickest WO_3 electrode (WO_3 800nm, **Figure 6.4c**) possesses particles smaller than 100 nm; in this case the smallest aggregates are *ca.* 40 nm sized. These differences could be ascribed to the different concentration of the precursor solutions used in the synthesis. Furthermore, the smaller aggregates observed in the WO_3 800nm sample could be originated by the addition thermal treatment underwent by this photoelectrode, which was prepared by repeating the deposition cycle twice.

The lower panel of **Figure 6.4** reports the cross-section images of the above-mentioned WO_3 samples, which were used to calculate the thickness of the photoanodes by means of the ImageJ software. The so-obtained thickness values are reported in **Table 6.2**. As predicted, by tuning the precursor solution concentration used to prepare the electrodes, WO_3 samples of different thickness were obtained. The deposition of a 1.0 M solution led to a *ca.* 225 nm thick tungsten trioxide sample, while the deposition of a doubled concentrated solution (2.0 M) produced a *ca.* 460 nm-thick electrode. Repeating the deposition of the 2.0 M solution twice has led to the attainment of the thickest samples, *ca.* 800 nm thick.

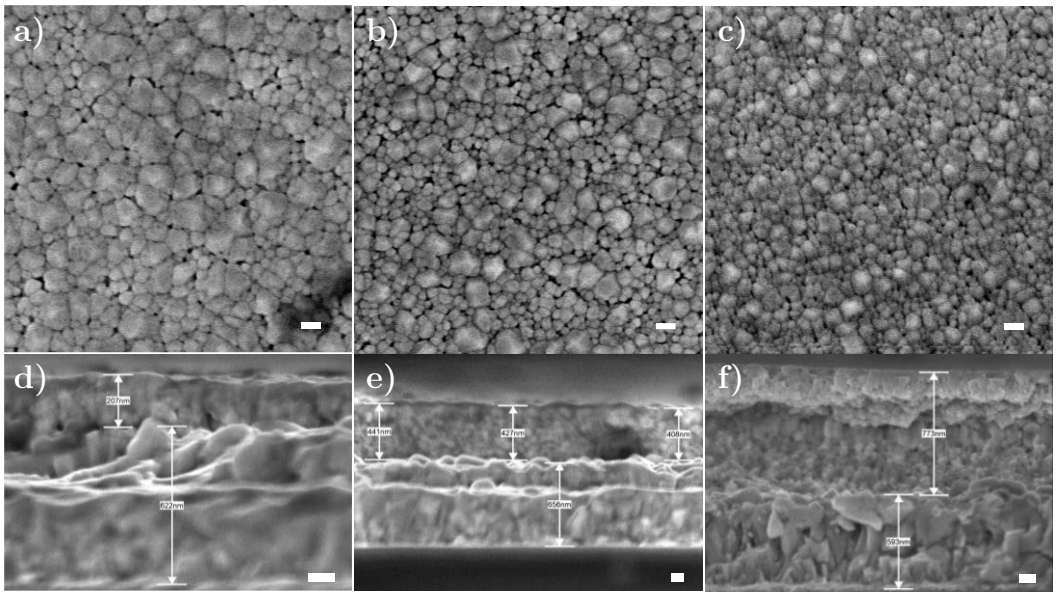

Figure 6.4 SEM top-view and cross-section images of pure a,d) WO_3 200nm, b,e) WO_3 500nm and c,f) WO_3 800nm. The scale bars are 100 nm.

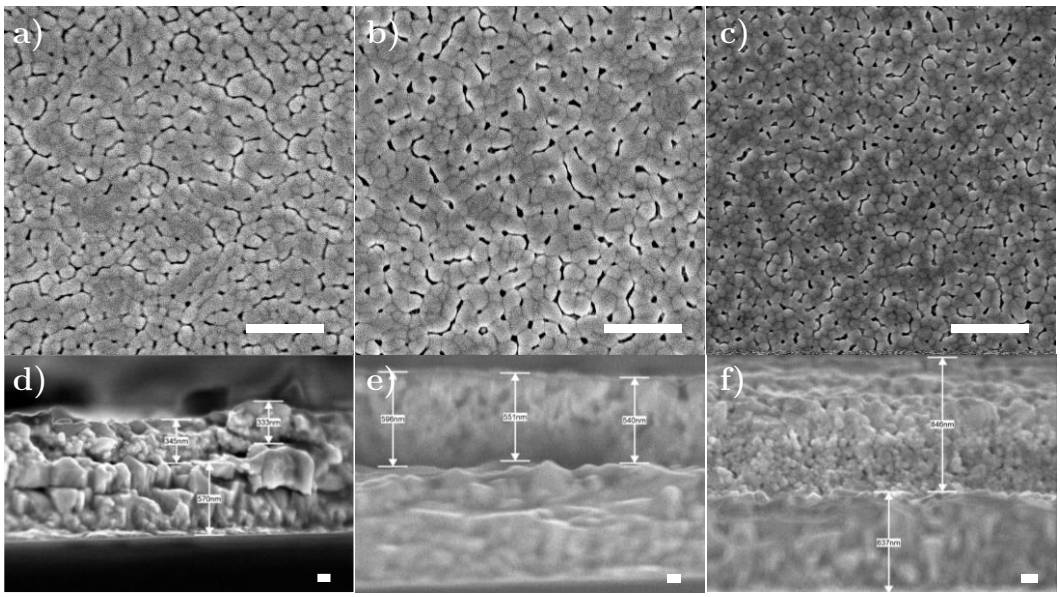

Figure 6.5 SEM top-view and cross-section images of a,d) WO_3 200nm–BV 8L, b,e) WO_3 500nm–BV 8L and c,f) WO_3 800nm–BV 8L. The scale bar of the top panel is 1 µm, that of the lower panel is 100 nm.

Figure 6.5 shows the SEM top-view images of three heterojunction samples, all characterized by the presence of eight layers of bismuth vanadate on top of the WO_3 underlayer. Notably, the surface morphology of these three samples is similar, the top $BiVO_4$ layer displaying an already-observed worm-like feature,[6,30] independently of the thickness of the WO_3 substrate. The bismuth vanadate layers completely cover the tungsten oxide underlayer.Moreover, **Figure 6.5** also shows the cross-section images of the heterojunctions, from which the thickness of the BV 8L overlayer can be estimated (see **Table 6.2**). As the thickness of eight $BiVO_4$ layers is *ca.* 140 nm, an increase in the $BiVO_4$ top layer around 35 nm can be estimated to occur after two deposition cycles.

Sample	Thickness / nm
WO_3 200nm	226 ± 24
WO_3 500nm	458 ± 17
WO_3 800nm	790 ± 41
BV 8L	136 ± 15

Table 6.2 Estimated thickness of WO_3 underlayers and BV 8L samples obtained from SEM cross-section images.

6.4.2 Photoelectrochemical tests

Numerous PEC tests have been carried out with the prepared sets of photoanodes, with the aim of evaluating their performances and fully characterizing their intrinsic properties.

6.4.2.1 Linear Sweep Voltammetry in Na_2SO_4

j-V plots recorded with single-material (WO_3 and $BiVO_4$) photoanodes under both irradiation configurations are reported in **Figure 6.6**. **Figure 6.6a** shows that the photocurrent generated by the tungsten oxide photoanodes increases proportionally to the increase in the material's thickness. The highest recorded photocurrent (at 1.8 V vs RHE) under back-side irradiation passes from 0.3 to 0.6 to 1.2 mA cm^{-2} for the 200, 500 and 800 nm samples, respectively. These performances are in perfect agreement with previous studies focusing on WO_3 samples of similar thickness.[19]

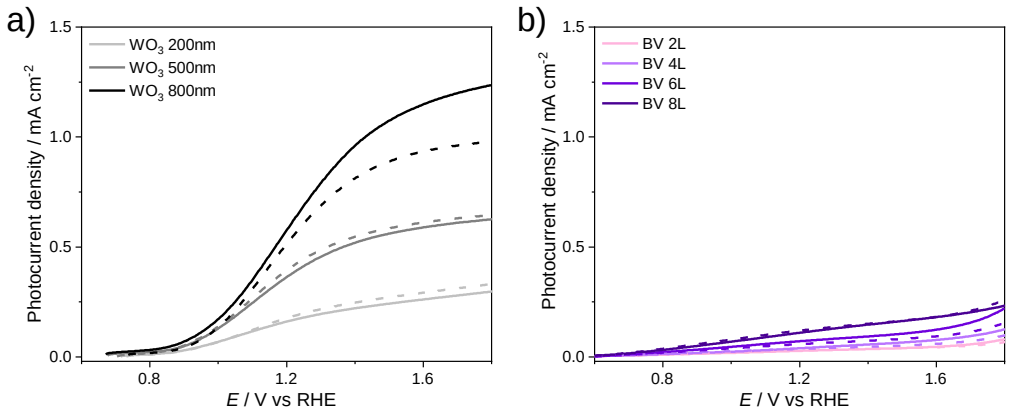

Figure 6.6 Linear Sweep Voltammetry (LSV) of a) WO_3 200, 500 and 800nm and b) BV 2, 4, 6, 8L recorded under back-side (solid lines) and front-side (dashed lines) irradiation in 0.5 M Na_2SO_4.

Moreover, the two samples with lower thickness display comparable performances when the material is directly irradiated in a front configuration, while the thickest sample shows a lower photocurrent in this configuration. This indicates a comparable efficiency in transporting both holes and electrons in the WO_3 200 and 500nm samples, while WO_3 800nm exhibits lower efficiency in the transport of electrons. Considering that tungsten trioxide is known to have excellent electric conductivity,[1,33] this could indicate that this sample exceeds the limit thickness above which the transport of electrons throughout the WO_3 becomes difficult.

Fig. 6.6b displays the LSV analyses of the $BiVO_4$ nL series of samples. Also for this set of samples the performances increase with increasing thickness, but in this case the enhancement is by far more modest. All recorded photocurrents, under both back- and front-side irradiation, reach moderate photocurrent values; the BV 8L samples generate a photocurrent of 0.2 mA cm^{-2} only at high applied bias. The activities recorded under front-side irradiation do not exhibit a clear trend and assumptions on the materials' transport properties can hardly be made, considering the low generated photocurrents and small performance differences among all BV samples. Nevertheless, also in this case these performances are in agreement with previously studied similar $BiVO_4$ photoanodes.[27]

LSV tests performed with the WO_3–$BiVO_4$ series of samples are reported in **Figure 6.7**. Notably, besides the WO_3 800nm–BV nL series, the photocurrents generated by the two

coupled materials are much higher than those generated by the corresponding single components.

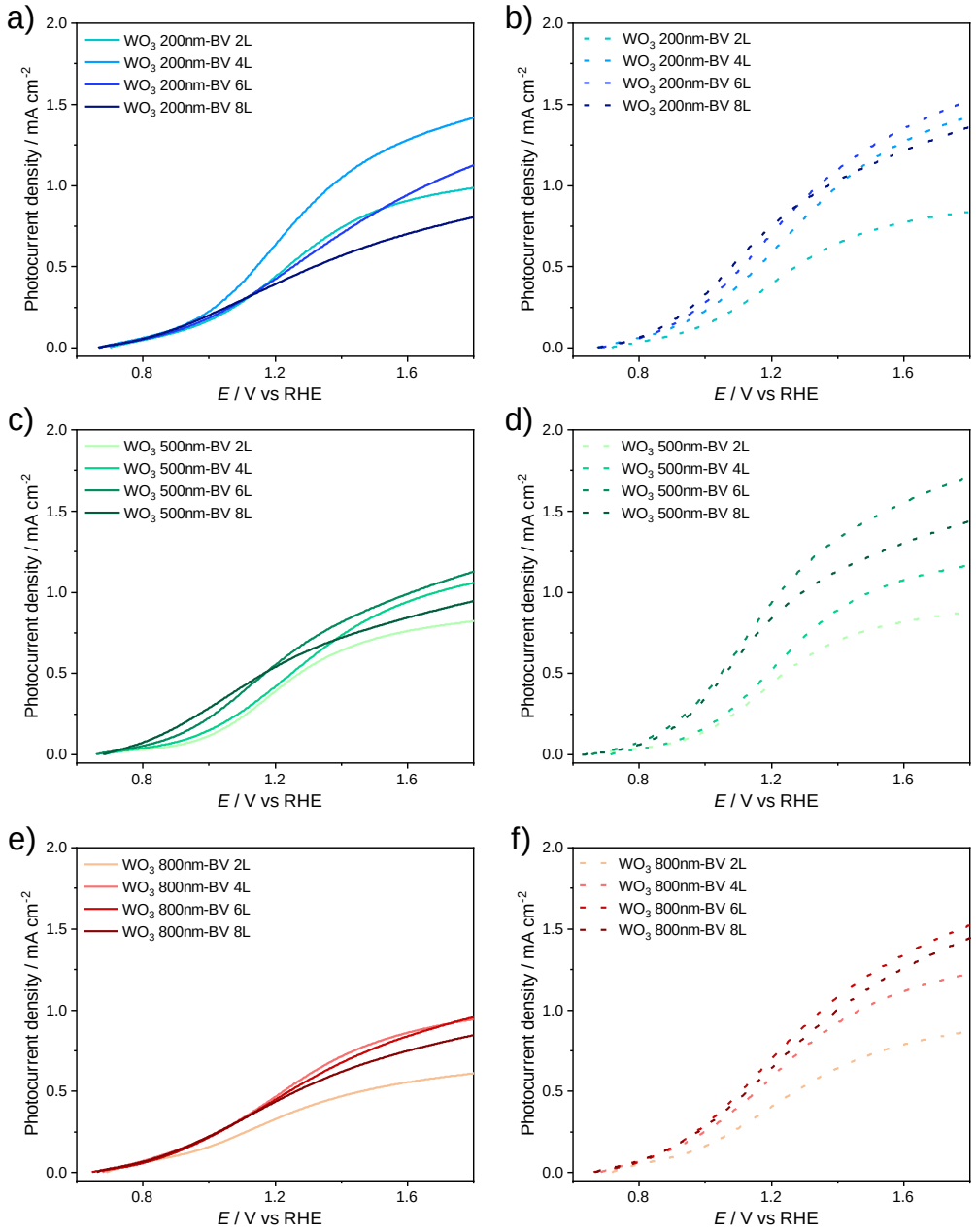

Figure 6.7 Linear Sweep Voltammetry (LSV) of a,b) WO_3 200nm–BV nL, c,d) WO_3 500nm–BV nL 500 and e,f) WO_3 800nm–BV nL series recorded under back-side (continuous lines) and front-side (dashed lines) irradiation in 0.5 M Na_2SO_4.

As already mentioned, the combination of the charge transport properties of WO_3 and the visible light-sensitising capability of $BiVO_4$ create a synergist effect on the PEC properties of the photoanodes.[34,35] **Fig. 6.7a,b** depict the performances of the heterojunction series characterized by the thinner WO_3 underlayer. Under back-side irradiation, the performance of the photoanodes increases with increasing $BiVO_4$ thickness up to the WO_3 200nm–BV 4L sample, that displays the highest, *ca.* 1.5 mA cm^{-2}, photocurrent at 1.8 V vs RHE. Upon further increase in the thickness of the deposited BV layers the current diminishes and the worst performance of the series is recorded with the heterojunction having 8 bismuth vanadate layers.

Moreover, there is a correlation between the generated photocurrents and the shape of the *j-V* curve: as the performance worsens, the LSV curve tends to become more flat. The slope of the *j-V* curve is directly connected to the fill factor of the material, that is, the efficiency of the holes exchange with the electrolyte at the material/electrolyte interface.[6,36] The sharp increase in the photocurrent just after the onset potential and the attainment of a plateau photocurrent indicate a fast electron transfer reaction limited by mass transfer phenomena. The best performing WO_3 200nm–BV 4L sample, as well as the WO_3 electrodes (see **Fig. 6.7a**), retains these characteristics. When irradiated in front configuration (**Fig. 6.7b**), the activity trend of the samples is different and the best performing electrodes are those with the thickest BV layers, all retaining a good fill factor. This could be explained by considering the type-II heterojunction that is built when coupling WO_3 with $BiVO_4$: in front configuration bismuth vanadate is the main absorber and the electrons photopromoted in its CB are much more easily transferred to the CB of tungsten oxide,[18,37] increasing the efficiency of the combined system.

Figures 6.7c,d show the LSV scans of the WO_3 500nm–BV nL series that, under back side illumination, generally produces lower photocurrents with respect to the previous set of samples. WO_3 500nm–BV 6L generates the highest photocurrent that however reaches a maximum value of *ca.* 1.1 mA cm^{-2} only, while the best photocurrent onset is that of the WO_3 500nm–BV 8L electrode. The differences in activity between the samples are however modest, which may point out that in this configuration a fairly thick WO_3 underlayer could act as the main absorber, leading to fewer photons reaching the bismuth vanadate layer, the thickness of which is thus not so influent on the overall performance. On the contrary, when

the BV overlayer is directly irradiated (**Figures 6.7d**) an activity trend among the set of samples is much easier to pinpoint. The activity of the samples increases with increasing $BiVO_4$ thickness and WO_3 500nm–BV 6L confirms to be the most active sample also in this configuration, reaching a 1.7 mA cm^{-2} photocurrent. Additional bismuth vanadate layers lead however to a lower activity.

The performances under full lamp irradiation generated by the set of heterojunctions having the thickest WO_3 underlayer are reported in **Figures 6.7e,f**. By comparing **Figures 6.7a,c,e** we see that under back-side irradiation the activity of the heterojunctions decreases with increasing tungsten oxide thickness. Here, the effect of the large WO_3 underlayer becomes more pronounced and, aside from WO_3 800nm-BV 2L, all other samples of the series exhibit very similar activities. When the irradiation configuration is changed (**Fig. 6.7f**), the heterojunction with six bismuth vanadate layers generates higher photocurrents and the performance trend is the same as that observed for the WO_3 500nm-BV nL series, even if the overall generated photocurrents are lower with respect to the previous set of photoelectrodes possessing a *ca.* 500 nm-thick underlayer.

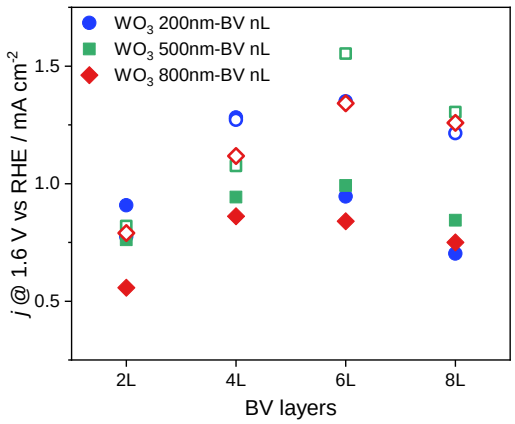

Figure 6.8 Photocurrent density at 1.6 V vs RHE of WO_3–BV heterojunctions recorded with 200 nm (circles), 500 nm (squares) and 800 nm-thick WO_3 layers (diamonds) as a function of the number of BV overlayers (2, 4, 6 and 8L), under both back- (full symbols) and front-side (void symbols) irradiation configurations, in 0.5 M Na_2SO_4.

Further highlights on the activities of the heterojunctions as a function of the thicknesses of the two photoactive materials under both irradiation configurations can be obtained from the data shown in **Figure 6.8**, which reports the photocurrent generated by

the heterojunction anodes at a fixed potential as a function of the number of BV layers that cover each composite material.

By taking into consideration the effect of the bismuth vanadate thickness on the activity of the composite system, we note that the performances attained under back- and front-side irradiation more clearly diverge with increasing number of deposited BV layers. When WO_3 is coated with 2 or 4 BV layers similar photocurrents are generated under back-side or front-side, while when the BV layers are 6 and 8 the performance under front-side irradiation becomes clearly better than that recorded under back-side illumination. At the same time, if the thickness of the bismuth vanadate layers is larger (6 and 8 layers roughly correspond to a *ca.* 110 and 140 nm), the activity of the samples is similar independently of the WO_3 underlayer thickness. On the other hand, if BV is thin (2 or 4 layers), the nature of the tungsten oxide layer becomes more relevant. Among the heterojunctions having four BV layers, that with the 200 nm-thick WO_3 underlayer shows the best performances under both irradiation configurations.

6.4.2.2 Internal Quantum Efficiency

Photoelectrochemical measurements under monochromatic irradiation have been performed on the photoanodes with the aim of further investigating the characteristics and behaviour of the prepared photoanodes. As outlined in **Chapter 3**, **Section 3.4**, IPCE and IQE values have been calculated for all electrodes; in this Section only IQE plots related to the heterojunction materials will be shown and discussed, while IPCE and IQE plots of WO_3 and $BiVO_4$ as well as IPCE plots of the WO_3–$BiVO_4$ series are reported in **Appendix C** at the end of this Chapter (**Figures C1** and **C2**). IQE plots of the three series of WO_3–$BiVO_4$ heterojunctions have been calculated by testing the samples at the fixed applied potential of 1.23 V vs RHE in 0.5 M Na_2SO_4 using the set-up described in **Chapter 3**, **Section 3.4.1**.

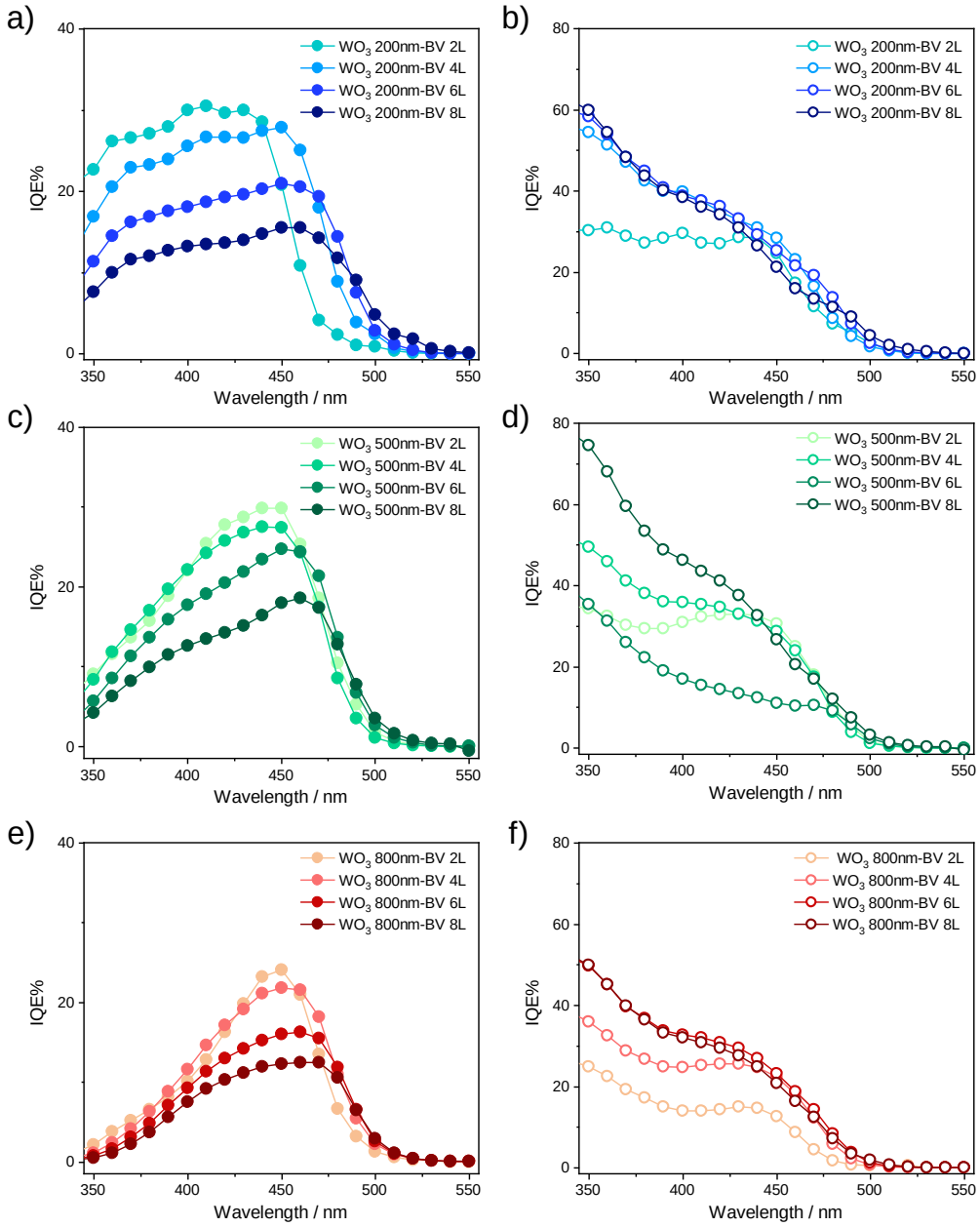

Figure 6.9 Internal Quantum Efficiency (IQE) plots of a,b) WO_3 200nm–BV nL, c,d) WO_3 500nm–BV nL 500 and e,f) WO_3 800nm–BV nL series recorded under back-side (full circles) and front-side (void circles) irradiation at 1.23 V vs RHE fixed applied potential in 0.5 M Na_2SO_4.

Figures 6.9a,b show the efficiency values of the WO_3 200nm–BV nL series under back- and front-side irradiation, respectively. The composite materials are photoactive up to 500-520 nm, confirming the *ca.* 2.4 eV band gap value estimated from absorption analyses.

As in this type of analysis the photocurrent is normalized by the absorption spectrum of the sample, we note that, differently to what has been observed under full lamp irradiation, under back-side irradiation the efficiency of the photoanodes decreases with increasing amount of $BiVO_4$ deposited on the heterojunction. Under such conditions, WO_3 200nm–BV 2L and WO_3 200nm–BV 4L are the best performing photoanodes amongst the series. Furthermore, higher IQE values were recorded upon direct irradiation in front-side configuration, especially at wavelengths lower than 420 nm. In this region, the anodes (except those possessing only two bismuth vanadate layers) exhibit higher performances, much higher than those attained by individual WO_3 200nm, reaching IQE% values up to 60% under front-side irradiation.

With increasing thickness of the underlying tungsten oxide the behaviour of the samples changes, especially at $\lambda < 450$ nm and under back irradiation, as shown in **Fig. 6.9c**. The calculated efficiencies tend to strongly decrease at lower wavelengths, reaching values around 5%. This behaviour is in great contrast with respect to the efficiencies recorded by the single WO_3 500nm anode, which shows very good performances under such conditions (see **Fig. C1b**). The IQE plots of the WO_3 500nm–BV nL series drastically change when varying the irradiation configuration: the efficiencies of the photoanodes are good at wavelengths around 420-450 nm, while at lower wavelengths their performances increase, outperforming also in this case the efficiencies recorded by single component photoanodes.

The already observed activity trend is confirmed when studying the IQE plots of the WO_3 800nm–BV nL series, reported in **Fig. 6.9e,f**. The activity decrease in the UV range under back-side illumination is here even more evident, with the efficiency of all photoanodes reaching a null value at 350 nm. The activities recorded near the visible portion of the solar spectrum are also affected, the best performing photoanodes reaching 20-25% efficiencies at 450 nm, a worse result than those obtained with the two other photoanodes series. The general activity reduction observed for this photoanodes series is evident also when they are irradiated in front-side configuration. Indeed, the efficiency values in the UV region are higher with respect to those attained under back-side configuration, but do not reach the values recorded with the corresponding single tungsten oxide electrode or with the other composites having a thinner WO_3 underlayer.

Considering the results obtained with photoelectrochemical tests under both full lamp and under monochromatic illumination, some conclusions can be drawn and hypotheses can

be made on the working mechanism of the WO_3–$BiVO_4$ system in relation to the thickness of the two photoactive materials. Starting from the considerations drawn in the previous Chapter of this thesis, concerning the recombination mechanism observed in a planar heterojunction material, we can identify two different cases:

i. the BV overlayer is fairly thick, corresponding to 6 or 8 coated layers and,
ii. the BV coating is fairly thin, corresponding to the samples possessing 2 or 4 BV layers.

Let's start with considering the first case. We can hypothesize that, when a WO_3–BV composite, in which the absorption of the bismuth vanadate is relevant, is irradiated from the back (*i.e.*, light first strikes the WO_3 underlayer), we are in the conditions of a favoured recombination mechanism involving electrons in the WO_3 CB and the holes in $BiVO_4$ VB. In this case, in fact, electron-hole couples will be generated in significant amounts in both materials. A confirmation of the relevance of this recombination mechanism is obtained by the IQE values recorded with the heterojunctions under back-side irradiation (**Fig. 6.9a,c,e**), which become progressively lower at $\lambda < 450$ nm. On the other hand, if the same system is irradiated from the BV-side of the heterojunction, the working mechanism of the type-II heterojunction is favoured, since the majority of the charge carriers will be photogenerated in the bismuth vanadate overlayer. In this case, electron migration towards the underlying WO_3 layer or holes migration towards the electrolyte interface will both be boosted, yielding better activities independently of the thickness of the tungsten oxide component. This is confirmed by PEC analyses under front-side irradiation that evidenced the superior performances of photoanodes possessing 6 or 8 BV layers, such as those reported in **Fig. 6.8** (top-right section of the panel).

In the second case, under back-side irradiation, BV is capable of absorbing only a modest portion of the incident light due to its reduced thickness. The heterojunction activity is promoted when the thickness of the WO_3 layer is modest (*i.e.*, 200 nm in this case), see **Fig. 6.8** (top-left section) and **Fig. 6.9a,b**. This is due to the fact that, being the tungsten oxide layer fairly thin, the number of carriers photogenerated within it is modest, and their recombination with the holes present in the valence band of the bismuth vanadate overlayer is limited. If the WO_3 thickness is increased, a larger number of electron and hole couples will be available to recombine with the charges generated in $BiVO_4$, leading to lower activities. Under front-side irradiation the situation appears similar. In fact, a thin BV layer does not

entirely absorb the incident radiation and the best-performing sample is that possessing a relatively thin WO_3 layer, in which only a small amount of charge carriers is generated.

Scheme 6.1 depicts the two most favourable working conditions of the WO_3–$BiVO_4$ heterojunction under back- and front-side irradiation. The best performances of the composite under back irradiation are built when both oxide layers are fairly thin, allowing the system to mitigate the detrimental recombination channel here depicted by the dashed red arrow (**Scheme 6.1a**). On the other hand, when $BiVO_4$ is first struck by incident radiation, the highest activities are recorded with the photoanodes possessing a modestly thick bismuth vanadate overlayer; in this case, the type-II working mechanism represented by the green arrows is favoured (**Scheme 6.1b**).

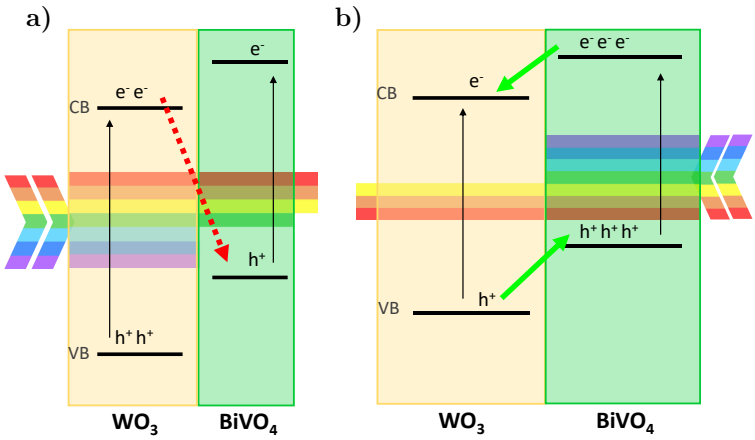

Scheme 6.1 Best operating conditions for a WO_3–$BiVO_4$ heterojunction under a) back-side and b) front-side irradiation configuration.

6.4.2.3 Linear Sweep Voltammetry in Na_2SO_3

For the purposes outlined in **Chapter 3**, **Section 3.1.1.1**, LSV analyses in the presence of a sacrificial agent, in this case sodium sulfite, have been carried out with all investigated materials and the key parameters of J_{abs} (the theoretical maximum current that could be generated by the sample), η_{inj} (the charge injection efficiency) and η_{sep} (the charge separation efficiency) have been calculated as outlined in the above mentioned Section. Tests have been carried out under back-side irradiation, since this is the irradiation configuration that needs to be implemented in order to fabricate efficient PEC solar cells.

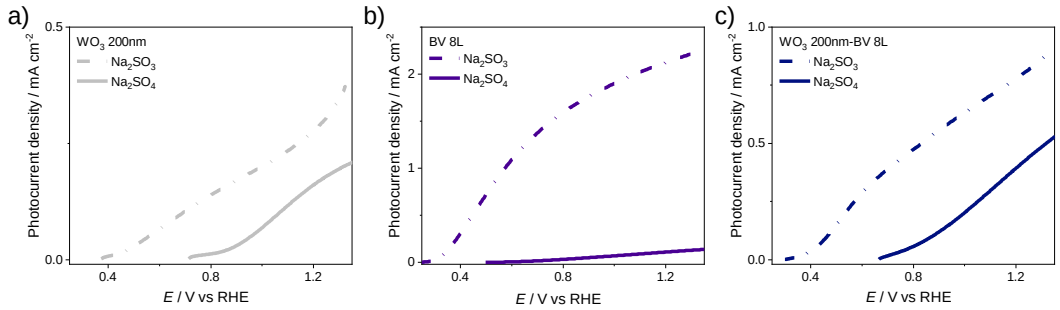

Figure 6.10 LSV scans of a) WO_3 200nm, b) BV 8L and c) WO_3 200nm-BV 8L photoanodes in 0.5 Na_2SO_4 (solid lines) and 0.5 Na_2SO_3 (dashed lines) under back-side irradiation.

The calculated J_{abs} values of the investigated samples are reported in the **Appendix C** at the end of this Chapter. **Figure 6.10** compares the photocurrents generated by three representative samples under full lamp irradiation in a standard electrolyte (Na_2SO_4) and in the presence of a hole scavenger species (Na_2SO_3). For the WO_3 film (**Fig. 6.10a**) the current density is only modestly enhanced in the presence of the sacrificial agent, while the onset potential is sensibly anticipated to 0.4 V vs RHE, which is much closer to the estimated CB edge position of the material.[38,39] These results, in agreements with previous studies,[40] indicate that hole transfer is often not the rate-limiting process for water oxidation on WO_3 films. On the contrary, the PEC activity of the BV 8L sample (**Fig. 6.10b**) is drastically enhanced in the presence of Na_2SO_3, and the photocurrent generated by the sample is 20 times larger than that recorded in the sodium sulfate electrolyte. This could be ascribed to the accumulation of holes at the $BiVO_4$ surface due to a sluggish water oxidation kinetics, which may cause severe recombination issues.[6,24,41] Lastly, the WO_3–$BiVO_4$ heterojunction (**Fig. 6.10c**) behaves more similarly to the tungsten oxide anode in the presence of a hole scavenger. The photocurrent is moderately enhanced while its photocurrent onset is sensibly shifted towards lower potentials.[40]

The kinetic competition between charge relaxation or recombination and catalysis is arguably the biggest challenge for designing efficient photocatalyst materials and devices. Moreover, metal oxide photoelectrodes face an additional issue: the lifetime of electrons and holes generated in the oxide bulk range from a few picoseconds to a few nanoseconds, whereas the timescales of interfacial water oxidation and reduction are milliseconds to seconds.[42] Preparing photocatalysts that maximise the charge separation efficiency in the bulk is thus a key challenge.

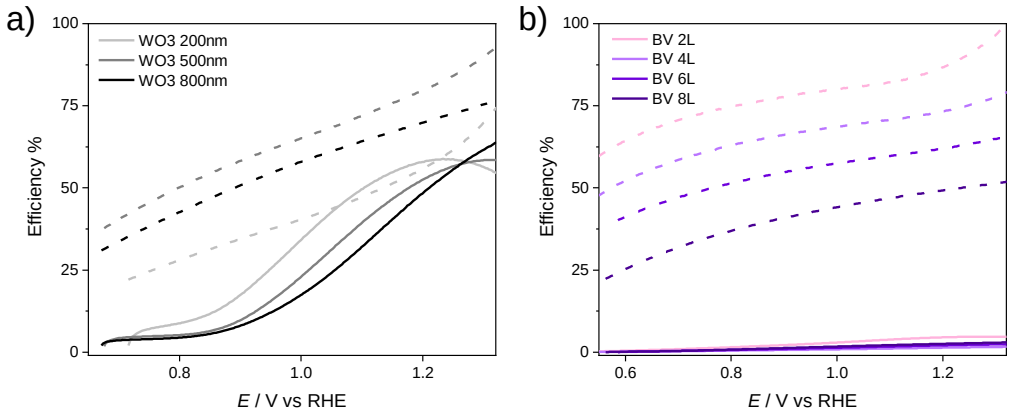

Figure 6.11 Calculated charge injection (solid lines) and charge separation (dashed lines) efficiencies of a) WO_3 200, 500 and 800nm and b) BV 2, 4, 6, 8L.

Figure 6.11a depicts η_{inj} and η_{sep} calculated for the prepared WO_3 samples (see **Chapter 3**, **Section 3.1.1.1** for the detailed procedure). The charge injection efficiencies (solid lines) of the three samples follow the same trend: the initial separation at low potentials is very low, between 5 and 10%, and increases at higher applied potentials, reaching a separation efficiency of *ca.* 55% at 1.23 V vs RHE. These results, in accordance to those of previous studies,[34] show that a relatively high overpotential is required to drive the water oxidation reaction at the electrode/electrolyte interface. On the other hand, the charge separation efficiency (dashed lines) of tungsten oxide samples rises with increasing applied potential. Recently, the ultrafast kinetics of WO_3 photoanodes has been monitored as a function of the applied potential; these studies evidenced that a rising external potential is directly linked to an enhancement in the space charge layer (SCL), that inhibits recombination, leading to longer-living holes and electrons,[43] justifying an increasing charge separation. Moreover, η_{sep} is influenced by the thickness of the WO_3 layer. In fact, the highest efficiencies among the entire range of applied potentials are generated by the WO_3 500nm photoanode, reaching >80% at the water oxidation reference potential. Thicker tungsten oxide yields slightly lower efficiencies, while WO_3 200nm displays the worst performances in term of separation efficiency, even if η_{sep} at $E > 1.2$ V vs RHE reaches values comparable to those of WO_3 800nm. This behaviour could be explained by taking into consideration a recent study, that correlates the degree of oxygen vacancies in tungsten oxide photoanodes with the degree of charge separation: an optimal (neither too high nor too low) concentration of oxygen vacancies is required to maximise the separation of the charges.[44] The intermediate thickness

of the WO_3 500nm sample could balance off the path to photogenerated charge carriers and a beneficial increased concentration of oxygen defects, as well as intermediate absorption properties.

The efficiencies calculated for the BV nL samples are reported in **Figure 6.11b**. Clearly, for this set of samples the limiting factor to their PEC activity is the poor charge injection efficiency recorded for all samples, independently of their thickness. η_{inj} is far below 5% for all bismuth vanadate photoanodes at all applied potentials. Even if it is well known that the PEC performance of bismuth vanadate photoelectrodes is mainly limited by its slow surface kinetics,[24,45] the attainment of so low injection efficiencies is peculiar and partially in contrast with the higher calculated η_{inj} values reported in the literature.[46–48] The here prepared $BiVO_4$ photoanodes could suffer from the accumulation of holes at the film/electrolyte interface that can act as surface states, recently revealed through PEIS analyses,[27] that lead to a particularly sluggish water oxidation kinetics. Much higher efficiency values have been reached when considering the separation of the photogenerated carriers in the material bulk. For all samples, η_{sep} gently increases with increasing external applied potential. The maximum efficiency value is obtained with BV 2L, which displays a *ca.* 90% efficiency at 1.23 V vs RHE, indicating an excellent separation between electrons and holes, while thicker samples display progressively lower separation efficiencies. In general, present results seem linked to the thickness of the investigated sample: BV 2L should be only *ca.* 40 nm thick and as the number of deposited BV layers and hence material's thickness increases, the charge separation efficiency of the photoanode decreases. The thickest sample, *i.e.*, BV 8L, which is ~140 nm thick (see **Table 6.2** in **Section 6.4.1.3**), displays the lowest separation efficiency, being only 50% at the water oxidation potential. Ultrafast Transient Absorption Spectroscopy tests recently demonstrated that the recombination rate of trapped holes with trapped electrons greatly increases as the thickness of a $BiVO_4$ layer increases, due to more holes trapped in bulk sites.[12]

The addition of under- or overlayers and the formation of solid-state junctions has shown promising results in increasing the charge carrier lifetimes, in passivating surface states, increasing charge separation or injection efficiencies.[12,49–51] The calculated charge injection (**Figure 6.12**) and separation (**Figure 6.13**) efficiencies of the coupled series, that

could contribute to further understand the role of the thickness of the two materials on the overall heterojunction performances, are reported below.

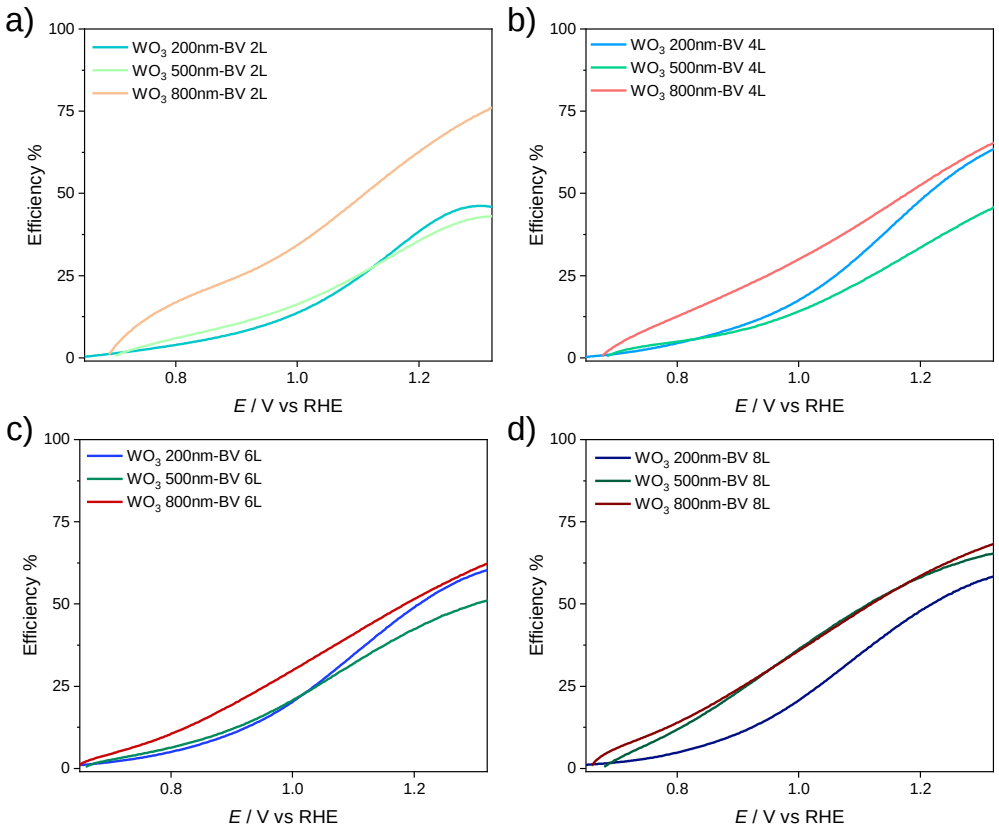

Figure 6.12 Calculated charge injection efficiencies of WO_3–$BiVO_4$ heterojunctions for different number of deposited BV layers a) 2L, b) 4L, c) 6L and d) 8L, on differently thick WO_3 underlayers.

The trend of η_{inj} for the composite samples clearly shows that this parameter follows the shape observed for the pure WO_3 electrodes (see **Figure 6.11a**), with efficiency values that are relatively low at low applied bias and progressively increase up to values ranging from 50 to 70%. The charge injection recorded for pure $BiVO_4$ samples (see **Figure 6.11b**) is dramatically increased upon its deposition over a tungsten oxide underlayer. This peculiar behaviour could indicate that the WO_3 underlayer possibly contributes to the passivation of BV surface states that hinder its surface kinetics, analogously to the effect observed upon doping bismuth vanadate with Mo^{6+} ions.[27] Moreover, the correspondence of the injection efficiencies calculated for the composite material and for pure WO_3 may indicate that, upon a sufficiently high applied bias, the holes generated in tungsten oxide's valence band are

efficiently transferred to the VB of bismuth vanadate, after the generation of the heterojunction. Moreover, the heterojunctions with the thickest WO_3 layer always exhibit the highest injection efficiency, independently of the number of deposited BV layers. The efficiency enhancement observed for the WO_3 800nm–BV 2, 4, 6, 8L samples is particularly evident at low applied biases. In fact, at 1.0 V vs RHE, η_{inj} passes from 17% (WO_3 800nm) to 30-35% for the composite photoanodes with different BV thickness. Composite electrodes with thinner WO_3 generally display lower efficiencies, especially when the number of BV coatings and the applied potentials are lower (**Figure 6.12a,b**), reaching under these conditions lower efficiencies compared to the corresponding pure WO_3 photoanodes.

When the deposited bismuth vanadate layer grows, the recorded efficiencies for all sets of heterojunctions become similar (**Figure 6.12c,d**). The observed fluctuating efficiency trends could be originated from the combination of different factors. In fact, the highest η_{inj} values generated by the WO_3 800nm–BV nL series of photoanodes could be affected by an enhanced contact between the two materials within the built heterojunctions, due to the different morphology observed for the WO_3 800nm sample (see **Figure 6.4c**). Its surface displays smaller surface grains, which could be more homogeneously coated by bismuth vanadate, increasing the contact surface between the two metal oxides and thus favouring the beneficial effects generated by WO_3 on BV's injection efficiency. Moreover, the different thickness of the $BiVO_4$ overlayer could play a crucial role in defining the overall water oxidation kinetic as the concentration of surface states in bismuth vanadate is tightly linked to the thickness of the material itself, as already discussed.

The surface properties of WO_3–$BiVO_4$ heterojunctions have been investigated by means of Intensity Modulated Photocurrent Spectroscopy (IMPS) in previous studies, which showed similar trends, indicating surface recombination up to 1.1 V vs RHE. Only upon sufficiently strong anodic polarization, electrons are drawn away from $BiVO_4$ and the electron/hole recombination at the surface is mitigated.[52]

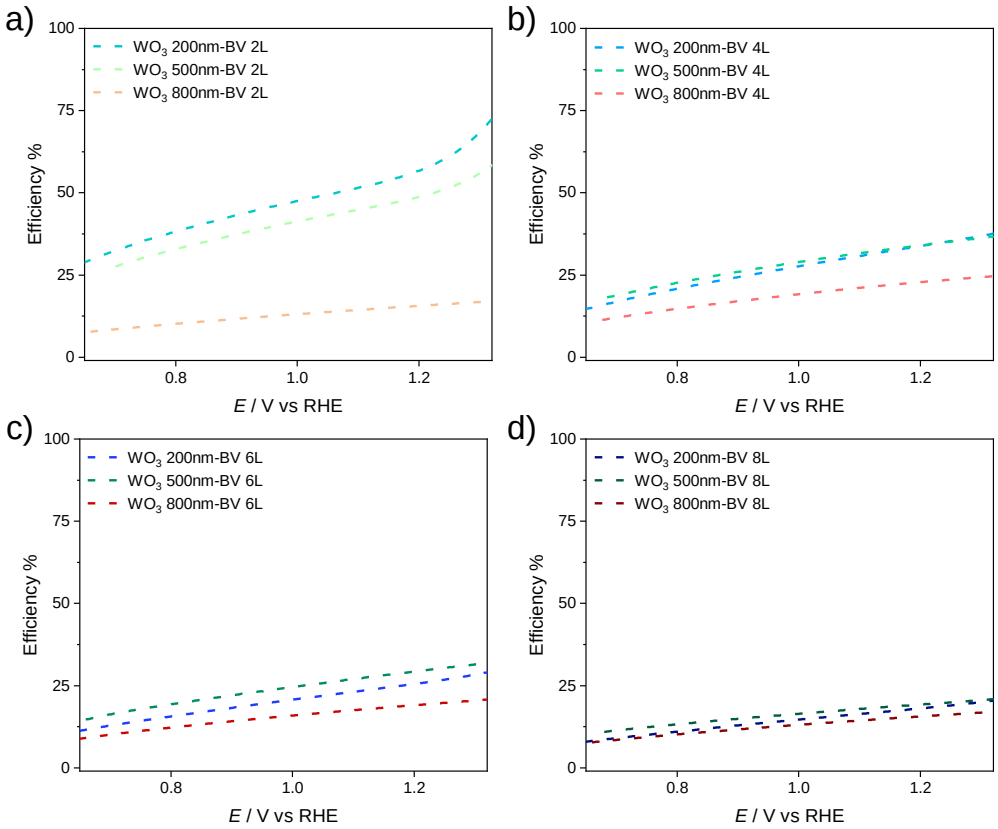

Figure 6.13 Calculated charge separation efficiencies of WO_3–$BiVO_4$ heterojunctions for different number of deposited BV layers: a) 2L, b) 4L, c) 6L and d) 8L, on differently thick WO_3 underlayers.

The charge separation efficiencies calculated for the composite materials reported in **Figure 6.13** show an already observed trend, slowly rising with increasing applied potential. All composites show sensibly lower charge separation efficiencies with respect to those recorded by the single component photoelectrodes. The only exceptions are the WO_3 200nm–BV 2L and WO_3 500nm–BV 2L samples that show modest performances, which however still do not reach the efficiencies of their individual components. The heterojunctions having the thickest WO_3 layer (800 nm), that showed the best charge injection efficiencies, exhibit instead the lowest η_{sep} values, independently of the number of BV layers. However, being these efficiencies lower than those recorded for the single WO_3 800nm sample, this behaviour is hardly influenced by the overall thickness of the heterojunctions. WO_3 800nm–BV 2L shows among the lowest separation efficiencies, even if the bismuth vanadate overlayer is estimated to be only *ca.* 30 nm thick.

Additionally, heterojunctions with various WO_3 thicknesses and 4, 6 or 8 BV layers all show charge separation efficiencies between 20 and 30%, with little variations correlated to the overall thickness of the investigated sample. These results appear in contrast with the well-established and thoroughly investigated working mechanism of a type-II heterojunction, in which conduction and valence band mismatch promote a more efficient separation of the photogenerated charge carriers. Other IMPS analyses studies have indeed shown increased charge separation efficiencies for heterojunction systems with respect to the single-phase ones.[34,40] A crucial parameter could be the irradiation configuration, which is not specified in the above-mentioned studies. The results reported in the present Section have been obtained under back-side irradiation. Of course, a different irradiation configuration determines where charge carriers are generated in the system and alters their dynamics following excitation. As already outlined in this Chapter, back-side irradiation of WO_3–$BiVO_4$ heterojunctions leads to the rise of a detrimental charge recombination pathway, that can however be mitigated by irradiating the system in a front configuration and by tuning the WO_3 and $BiVO_4$ thickness.[12,19] Indeed, the highest separation efficiencies are displayed by the WO_3 200nm–BV 2 and 4L samples, resulting the best performing ones according to the results outlined in **Section 6.4.2.2**.

Thus, despite the well-known advantages of combining two photocatalysts, the rise of recombination processes related to the building of a heterojunction must be carefully taken into account.[52] The working mechanism and the superior performances obtained with the WO_3–$BiVO_4$ combined system cannot be simply ascribled to the formation of a type-II heterojunction. Further studies on the charge recombinations paths and on charge redistribution or surface states passivation must be carried out to ascertain the origin behind its increased PEC performances.

6.5 Conclusions

WO_3, $BiVO_4$ and WO_3–$BiVO_4$ photoanodes displaying various thicknesses were prepared via spin coating and underwent optical, structural and morphological characterization. LSV tests performed under simulated solar radiation allowed us to observe different activity trends, influenced by both the irradiation configuration and the ratio between the two oxides in the

composite materials. Monochromatic measurements support the hypothesis that all heterojunction photoanodes suffer from charge recombination, under back-side irradiation. This detrimental path is mitigated by decreasing the thickness of both semiconductors, thus diminishing the generation of photogenerated charge carriers possibly susceptible to recombination. On the other hand, upon front-side illumination, the heterojunction's activity benefits from having a relative thick $BiVO_4$ overlayer, able to absorb most of the incident radiation, with a consequent more efficient separation between photogenerated electrons and holes. Lastly, the intrinsic efficiencies of the composite materials calculated from the results of tests run in the presence of a sacrificial agent evidence that, contrary to what is commonly associated with this type of systems, the charge separation efficiency is lower with respect to the single-component materials, whereas the charge injection efficiency is good at the water oxidation potential.

We can conclude that the thickness of both metal oxide materials plays a crucial role in the overall activity of the composite photoanodes and that the balance between the two semiconductors must be carefully tailored on the scopes and uses of the final photoelectrode. Moreover, we may speculate that the greatly increased efficiency of the WO_3–$BiVO_4$ system does not lie in the building of a type-II heterojunction, but must be searched in the charge redistributions mechanisms that may arise upon the combination of the two single oxides.

Appendix C

Theoretical maximum photocurrents

J_{abs} values have been calculated by correlating the standard solar spectrum with the measured absorbance of the samples:[20]

$$J_{abs} = e \int_{\lambda_1}^{\lambda_2} (N(\lambda)_{AM1.5G} \cdot LHE)\, d\lambda \qquad (C.1)$$

where $N(\lambda)_{AM1.5G}$ is the photon flux density under standard conditions, LHE is the light harvesting efficiency of the sample calculated as $LHE = (1\text{-}10^{-A})$ and e is the elemental charge.

Sample	J_{abs}/mA cm^{-2}	Sample	J_{abs}/mA cm^{-2}
WO_3 200nm	0.50	BV 2L	1.36
WO_3 500nm	0.87	BV 4L	2.79
WO_3 800nm	1.70	BV 6L	3.74
		BV 8L	4.31

Table C.1 J_{abs} of pure WO_3 and $BiVO_4$ photoanodes.

Sample	J_{abs}/mA cm^{-2}	Sample	J_{abs}/mA cm^{-2}	Sample	J_{abs}/mA cm^{-2}
WO_3 200nm – BV 2L	1.95	WO_3 500nm – BV 2L	2.53	WO_3 800nm – BV 2L	2.96
WO_3 200nm – BV 4L	3.47	WO_3 500nm – BV 4L	3.67	WO_3 800nm – BV 4L	3.90
WO_3 200nm – BV 6L	4.11	WO_3 500nm – BV 6L	4.45	WO_3 800nm – BV 6L	4.58
WO_3 200nm – BV 8L	4.31	WO_3 500nm – BV 8L	4.83	WO_3 800nm – BV 8L	4.77

Table C.2 J_{abs} of WO_3–$BiVO_4$ heterojunction series.

IPCE and IQE plots of pure WO_3 and $BiVO_4$ samples

The monochromatic measurements performed with WO_3 samples yield IPCE and IQE values which are in accordance with the activity trend observed under simulated solar irradiation, with the efficiencies growing with the thickness of the electrodes.

$BiVO_4$ samples display a different performance trend with respect to full-lamp analyses but, given the very low photocurrents generated by these samples and that the differences in performance at 1.23 V are very modest, the general behaviour in which thicker films generate higher efficiencies, especially under back-side irradiation, is maintained.

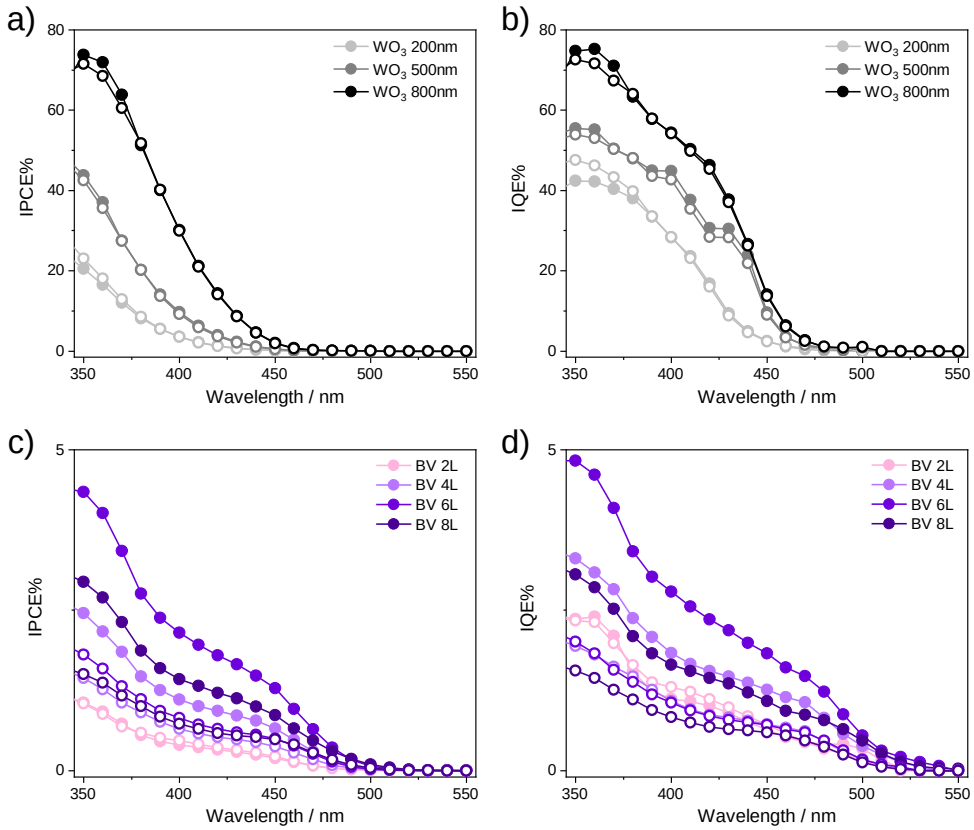

Figure C.1 Incident Photon to Current Efficiency (IPCE) and Internal Quantum Efficiency (IQE) plots of a,b) WO_3 200, 500 and 800 nm and c,d) BV 2, 4, 6, 8L BV nL recorded under back-side (full symbols) and front-side (void symbols) irradiation at 1.23 V vs RHE fixed applied potential in 0.5 M Na_2SO_4.

IPCE plots of the WO_3–$BiVO_4$ heterojunction series

The general trend of activities observed and discussed for the IQE analyses of these samples is maintained.

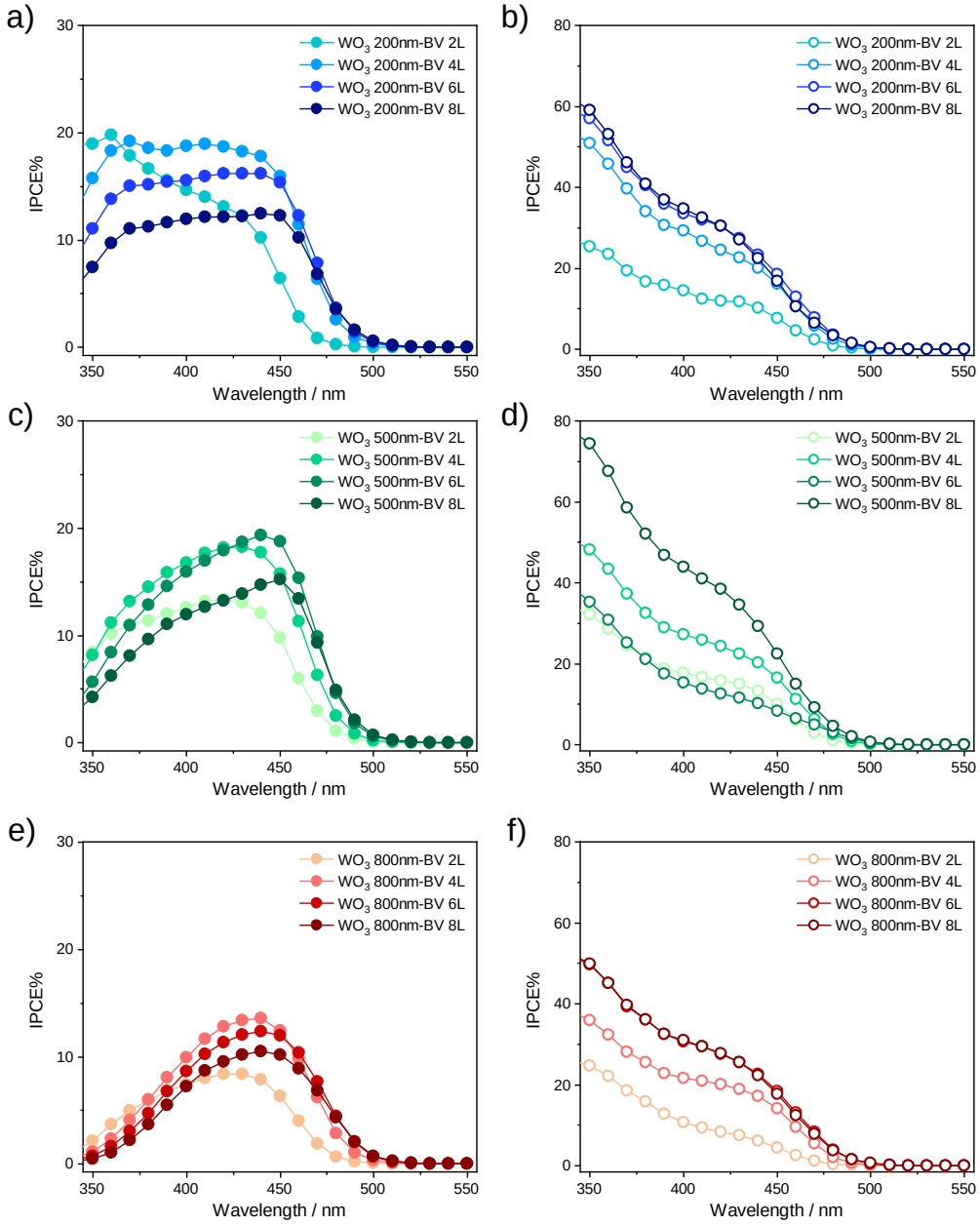

Figure C.2 Incident Photon to Current Efficiency (IPCE) plots of a,b) WO_3 200nm–BV nL, c,d) WO_3 500nm–BV nL 500 and e,f) WO_3 800nm–BV nL series recorded under back-side (full dots) and front-side (empty dots) irradiation at 1.23 V vs RHE fixed applied potential in 0.5 M Na_2SO_4.

References

1. Z. Huang, J. Song, L. Pan, X. Zhang, L. Wang, J. Zou, *Adv. Mater.* 27 (**2015**) 5309–5327.
2. J. Huang, P. Yue, L. Wang, H. She, Q. Wang, *Chinese J. Catal.* 40 (**2019**) 1408–1420.
3. C. Santato, M. Ulmann, J. Àugustynski, *J. Phys. Chem. B* 105 (**2001**) 936–940.
4. F.F. Abdi, L. Han, A.H.M. Smets, M. Zeman, B. Dam, R. Van De Krol, *Nat. Commun.* 4 (**2013**) 1–7.
5. M.S. Prévot, K. Sivula, *J. Phys. Chem. C* 117 (**2013**) 17879–17893.
6. A. Polo, I. Grigioni, M. Magni, A. Facibeni, M. Vittoria Dozzi, E. Selli, *Appl. Surf. Sci.* 556 (**2021**) 149759.
7. P. Chatchai, Y. Murakami, S. ya Kishioka, A.Y. Nosaka, Y. Nosaka, *Electrochim. Acta* 54 (**2009**) 1147–1152.
8. B.S. Kalanoor, H. Seo, S.S. Kalanur, *Mater. Sci. Energy Technol.* 1 (**2018**) 49–62.
9. Q. Xu, L. Zhang, B. Cheng, J. Fan, J. Yu, *Chem* 6 (**2020**) 1543–1559.
10. J. Low, J. Yu, M. Jaroniec, S. Wageh, A.A. Al-Ghamdi, *Adv. Mater.* 29 (**2017**) 1601694.
11. S.J. Hong, S. Lee, J.S. Jang, J.S. Lee, *Energy Environ. Sci.* 4 (**2011**) 1781–1787.
12. I. Grigioni, A. Polo, M.V. Dozzi, K.G. Stamplecoskie, D.H. Jara, P. V Kamat, E. Selli, *ACS Appl. Energy Mater. Energy Mater.* 5 (**2022**) 13142–13148.
13. G. Di Liberto, S. Tosoni, G. Pacchioni, *J. Phys. Condens. Matter* 31 (**2019**) 434001.
14. I. Grigioni, K.G. Stamplecoskie, E. Selli, P. V. Kamat, *J. Phys. Chem. C* 119 (**2015**) 20792–20800.
15. P.M. Rao, L. Cai, C. Liu, I.S. Cho, C.H. Lee, J.M. Weisse, P. Yang, X. Zheng, *Nano Lett.* 14 (**2014**) 1099–1105.
16. P. Wei, Y. Wen, K. Lin, X. Li, *Int. J. Hydrogen Energy* 46 (**2021**) 27506–27515.
17. J. Low, C. Jiang, B. Cheng, S. Wageh, A.A. Al-Ghamdi, J. Yu, *Small Methods* 1 (**2017**) 1–21.
18. I. Grigioni, K.G. Stamplecoskie, D.H. Jara, M.V. Dozzi, A. Oriana, G. Cerullo, P. V. Kamat, E. Selli, *ACS Energy Lett.* 2 (**2017**) 1362–1367.
19. I. Grigioni, M.V. Dozzi, E. Selli, *J. Phys. Condens. Matter* 32 (**2020**) 014001.
20. X. Zhu, N. Guijarro, Y. Liu, P. Schouwink, R.A. Wells, F. Le Formal, S. Sun, C. Gao, K. Sivula, *Adv. Mater.* 30 (**2018**) 1–6.
21. H. Dotan, K. Sivula, M. Graetzel, S.C. Warren, *Energy Environ. Sci.* 4 (**2011**) 958–964.

22. S.H. Baeck, K.S. Choi, T.F. Jaramillo, G.D. Stucky, E.W. McFarland, *Adv. Mater.* 15 (**2003**) 1269–1273.

23. C. Janáky, K. Rajeshwar, N.R. De Tacconi, W. Chanmanee, M.N. Huda, *Catal. Today* 199 (**2013**) 53–64.

24. Y. Park, K.J. McDonald, K.S. Choi, *Chem. Soc. Rev.* 42 (**2013**) 2321–2337.

25. I. Grigioni, G. Di Liberto, M.V. Dozzi, S. Tosoni, G. Pacchioni, E. Selli, *ACS Appl. Energy Mater.* 4 (**2021**) 8421–8431.

26. K. Subba Ramaiah, V. Sundara Raja, *Appl. Surf. Sci.* 253 (**2006**) 1451–1458.

27. A. Polo, M.V. Dozzi, I. Grigioni, C.R. Lhermitte, N. Plainpan, L. Moretti, G. Cerullo, K. Sivula, E. Selli, *Sol. RRL* 6 (**2022**) 2200349.

28. S. Tokunaga, H. Kato, A. Kudo, *Chem. Mater.* 13 (**2001**) 4624–4628.

29. Z. Zhao, Z. Li, Z. Zou, *Phys. Chem. Chem. Phys.* 13 (**2011**) 4746–4753.

30. Y. Liang, T. Tsubota, L.P.A. Mooij, R. Van De Krol, *J. Phys. Chem. C* 115 (**2011**) 17594–17598.

31. V.I. Shapovalov, A.E. Lapshin, A.G. Gagarin, L.P. Efimenko, *Glas. Phys. Chem.* 40 (**2014**) 553–569.

32. C. Santato, M. Odziemkowski, M. Ulmann, J. Augustynski, *J. Am. Chem. Soc.* 123 (**2001**) 10639–10649.

33. S. Corby, L. Francàs, S. Selim, M. Sachs, C. Blackman, A. Kafizas, J.R. Durrant, *J. Am. Chem. Soc.* 140 (**2018**) 16168–16177.

34. S.Y. Chae, C.S. Lee, H. Jung, O.S. Joo, B.K. Min, J.H. Kim, Y.J. Hwang, *ACS Appl. Mater. Interfaces* 9 (**2017**) 19780–19790.

35. X. Shi, I. Herraiz-Cardona, L. Bertoluzzi, P. Lopez-Varo, J. Bisquert, J.H. Park, S. Giménez, *Phys. Chem. Chem. Phys.* 18 (**2016**) 9255–9261.

36. M.G. Walter, E.L. Warren, J.R. McKone, S.W. Boettcher, Q. Mi, E.A. Santori, N.S. Lewis, *Chem. Rev.* 110 (**2010**) 6446–6473.

37. H. Wang, L. Zhang, Z. Chen, J. Hu, S. Li, Z. Wang, J. Liu, X. Wang, *Chem. Soc. Rev.* 43 (**2014**) 5234–5244.

38. Y. Ping, G. Galli, *J. Phys. Chem. C* 118 (**2014**) 6019–6028.

39. F. Wang, C. Di Valentin, G. Pacchioni, *J. Phys. Chem. C* 115 (**2011**) 8345–8353.

40. I. Rodríguez-Gutiérrez, E. Djatoubai, J. Su, A. Vega-Poot, G. Rodríguez-Gattorno, F.L. Souza, G. Oskam, *Sol. Energy Mater. Sol. Cells* 208 (**2020**) 110378.

41. F.F. Abdi, R. Van De Krol, *J. Phys. Chem. C* 116 (**2012**) 9398–9404.

42. S. Corby, R.R. Rao, L. Steier, J.R. Durrant, *Nat. Rev. Mater.* 6 (**2021**) 1136–1155.

43. S. Corby, E. Pastor, Y. Dong, X. Zheng, L. Francàs, M. Sachs, S. Selim, A. Kafizas, A.A. Bakulin, J.R. Durrant, *J. Phys. Chem. Lett.* 10 (**2019**) 5395–5401.

44. S. Corby, L. Francàs, A. Kafizas, J.R. Durrant, *Chem. Sci.* 11 (**2020**) 2907–2914.

45. J.A. Seabold, K.S. Choi, *J. Am. Chem. Soc.* 134 (**2012**) 2186–2192.

46. T.L. Kim, M.J. Choi, H.W. Jang, *MRS Commun.* 8 (**2018**) 809–822.

47. Y. Lu, Y. Yang, X. Fan, Y. Li, D. Zhou, B. Cai, L. Wang, K. Fan, K. Zhang, *Adv. Mater.* 34 (**2022**) 2108178.

48. S. Wang, P. Chen, J.-H. Yun, Y. Hu, L. Wang, *Angew. Chemie* 129 (**2017**) 8620–8624.

49. I. Grigioni, L. Ganzer, F. V. A. Camargo, B. Bozzini, G. Cerullo, E. Selli, *ACS Energy Lett.* 4 (**2019**) 2213–2219.

50. M. García-Tecedor, D. Cardenas-Morcoso, R. Fernández-Climent, S. Giménez, *Adv. Mater. Interfaces* 6 (**2019**) 1–8.

51. L. Steier, I. Herraiz-Cardona, S. Giménez, F. Fabregat-Santiago, J. Bisquert, S.D. Tilley, M. Grätzel, *Adv. Funct. Mater.* 24 (**2014**) 7681–7688.

52. P. Vecchi, A. Piccioni, R. Mazzaro, M. Mazzanti, V. Cristino, S. Caramori, L. Pasquini, *Sol. RRL* 6 (**2022**) 2200108.

Chapter 7 – Advanced analyses on WO_3–$BiVO_4$ heterojunctions

7.1 Abstract

In this chapter WO_3, $BiVO_4$ and WO_3–$BiVO_4$ photoanode materials are further analysed by means of two advanced characterization techniques: Electrochemical Impedance Spectroscopy (EIS) and Spectroelectrochemistry (SEC). Impedance measurements were performed on the electrodes and the results were analysed by means of different equivalent circuits, in order to best mimic the experimental characteristics of the photoelectrodes. Insights into the water oxidation kinetics as well as the charges stored in the samples have thus been acquired and compared. Composites possessing a relatively thin WO_3 underlayer (200 nm) showed a surface capacitance behaviour similar to that of $BiVO_4$, while heterojunctions possessing a thicker WO_3 layer (800 nm) evidenced electron diffusion issues. By spectroelectrochemical analyses further differences were highlighted between the properties of the single component materials and those of their composites. Difference spectra obtained with the heterojunction materials showed either a lack of the optical features typical of their WO_3 underlayer, or an absorption intensity reduction of the characteristic peaks associated to the $BiVO_4$ overlayer. Stepped potential measurements provided quantitative information on the electronic charges associated with the investigated optical transitions.

7.2 Introduction

The heterojunction obtained from the combination of tungsten oxide (2.7 eV band gap, good water oxidation kinetics and electron transport properties) with bismuth vanadate (2.4 eV band gap, good charge separation efficiency) is one of the most promising systems to be employed as photoanode in a photoelectrochemical tandem cell.[1–3] Generally, its superior photoelectrochemical properties have been assigned to the visible light sensitisation induced by $BiVO_4$ and to the favourable band edges mismatch between the two oxides, which is considered responsible for an enhanced photogenerated electrons and holes spatial separation.[1,4,5] However, literature reports,[6,7] as well as the results outlined in the previous Chapter of this thesis, point out to a reduction of the charge separation efficiency in the WO_3–$BiVO_4$ composite with respect to its single components. The work presented in this Chapter thus aims at analysing more in depth the intrinsic characteristics of this heterojunction, in order to evidence other possible factors involved in the PEC activity enhancement of the WO_3–$BiVO_4$ system, employing advanced characterization techniques, such as Electrochemical Impedance Spectroscopy (EIS) and Spectroelectrochemistry (SEC).[8–11]

Frequency-based characterization techniques such as impedance spectroscopy allow to gather information on the intrinsic kinetic and charge storage characteristics of a given photoelectrode, in order to disclose the working mechanism of the system and identify the reasons regulating its efficiency.[12] Even if EIS is relatively easy to perform experimentally, the interpretation of the results is often complex and requires the use of suitable theoretical models.[13] The use of adequate electrical equivalent circuits is a fundamental tool to interpret the charge transfer phenomena occurring in the cell under the operating conditions (see **Chapter 3, Section 3.4.1** for details). Despite its great potential, EIS is often used to provide a basic characterization of photoanode materials by limiting the interpretation of impedance data to the qualitative analysis of the Nyquist plot, by solely assessing a decrease/increase in the charge transfer resistance upon the incorporation of the bismuth vanadate overlayer and/or other surface modifications such as cocatalysts deposition.[14–18] Only few works report a detailed analysis and interpretation of EIS data, for example by focusing on the fitting of experimental parameters and on their trend as a function of the external applied potential for different materials. In this scenario the work published by S.

Gimenéz et al.[19] is distinctive and represents a good example of EIS data presentation and fitting. In particular, the authors succeeded in modelling the carrier dynamics of the WO_3–$BiVO_4$ system and highlighting that the mesoporous tungsten oxide underlayer controls the capacitive and charge transport behaviour of the overall heterojunction, leading to enhanced charge extraction properties at the counter electrode contact.[19,20]

Spectroelectrochemistry monitors the steady-state changes in optical absorption as a function of the external applied potential; this technique thus monitors both kinetic and thermodynamic processes triggered by electrochemistry as well as vibrational processes through spectroscopy.[21] UV-Vis-NIR spectroelectrochemistry is thus a powerful characterization technique, especially for catalysts and photocatalysts, since the extended range of wavelength that can be probed (300-3000 nm) allows studies in multiple reaction configurations, probing specific electronic transitions and thus providing interesting information on the electronic structure of the investigated systems.[11,21–23] Recent studies reported the use of spectroelectrochemistry to study hematite,[24,25] zinc ferrite,[26] and bismuth vanadate photoanodes.[27,28] However, this technique has been so far very scarcely employed to study the WO_3–$BiVO_4$ heterojunction. In fact, an analysis of the SEC spectra of this heterojunction has been reported only in the work of I. Grigioni et al.,[29] in comparison to the behaviour of single $BiVO_4$ only.

The work outlined in this Chapter thus aims at providing an extensive and detailed characterization of WO_3, $BiVO_4$ and WO_3–$BiVO_4$ photoelectrodes with different thicknesses by means of both impedance spectroscopy and spectroelectrochemical analyses, with the scope of thoroughly investigating the properties of pure-phase photoanodes and their variations upon combining such materials in a heterojunction.

7.3 Experimental section

7.3.1 Tested photoelectrodes

The synthesis as well as the optical, structural, morphological and photoelectrochemical characterization of the photoelectrodes have been thoroughly discussed in **Chapter 6**. To

summarize, we prepared several WO_3, $BiVO_4$ and WO_3–$BiVO_4$ photoelectrodes possessing various thicknesses. In particular, tungsten trioxide samples of increasing width (200, 500 and 800 nm) as well as bismuth vanadate electrodes prepared by subsequent coating of numerous (2, 4, 6, 8) layers have been prepared as single-phase photoanodes and have been successively combined to form three series of WO_3/$BiVO_4$ heterojunction electrodes, displaying different under- and overlayers thicknesses.

Single-phase
BV 2, 4, 6 and 8L
WO_3 200, 500 and 800 nm
Composites
WO_3 200nm–BV 2, 4, 6 and 8L
WO_3 500nm–BV 2, 4, 6 and 8L
WO_3 800nm–BV 2, 4, 6 and 8L

Table 7.1 Photoelectrodes investigated in this Chapter.

A complete overview on data regarding the characterization of these electrodes can be found in **Chapter 6, Section 6.4.1**.

7.3.2 Methods

Electrochemical Impedance Spectroscopy (EIS) data were acquired by means of an Autolab potentiostat controlled by the Nova software, using a 10 mV amplitude perturbation ranging from 10^5 to 10^{-1} Hz. The light source was a LED-operating solar simulator (SUNBOX).[30] Samples, located in a 3-electrode glass cell with a platinum wire as counter and a Ag/AgCl as reference electrode, were irradiated in back configuration. Further details on the experimental procedures are reported in **Chapter 3, Section 3.4.3**. Data were fitted according to a Randles equivalent circuit by using the ZView software.[31] In the cases for which the capacitance (C) of the circuit has been substituted with a constant phase element, C was calculated as follows:[32,33]

$$C = \frac{(R_{ct} \cdot CPE_T)^{(1/CPE_P)}}{R_{ct}} \tag{7.1}$$

where R_{ct} is the charge transfer resistance, while CPE_T and CPE_P are two fitting parameters correlated to the constant phase element.

Spectroelecrochemical analyses were performed according to the procedures detailed in **Chapter 3, Section 3.5.1**. A Perkin Elmer Lambda 1050 UV-Vis-NIR spectrophotometer was used in combination with a PalmSens4 portable potentiostat. In particular, the experimental conditions used to test the single-phase as well as the composite WO_3–$BiVO_4$ photoanodes are the following:

- wavelength range, from 350 nm (UV) to 1350 nm (NIR)
- applied potentials, from 0.523 V to 1.823 V vs RHE

SEC analyses are presented in terms of ΔO.D., that is, the difference in optical absorption spectrum. Each difference spectrum is referred to a spefic applied bias and it is calculated by subtracting from the absorption spectrum recorded at that given potential the spectrum recorded at the first applied potential. As an example, ΔO.D.@1.8V is determined using:[28]

$$\Delta \mathrm{O.\,D.\,@1.8V} = \mathrm{O.\,D.\,@1.8V} - \mathrm{O.\,D.\,@0.5V} \tag{7.2}$$

7.4 Results and discussion

7.4.1 Electrochemical impedance spectroscopy

We first focused on characterizing both individual metal oxide materials (WO_3 and $BiVO_4$) and later analysed the composite samples displaying different thicknesses of each counterpart oxide. In order to rule out any contribution eventually produced by the conductive substrate on the impedance results, we performed EIS measurements on a clean FTO slab under either dark and 1 sun irradiation conditions. As demonstrated by the so obtained Nyquist plots, reported in the Appendix at the end of this Chapter (**Figure D1**), no significant signal may be attributed to the tested reference substrate (under both dark and irradaition conditions).

Thus, the signals recorded with the prepared photoanodes could be safely attributed only to the photoactive materials themselves.

We then proceeded to test the three WO_3 samples with increasing thickness. The Nyquist plots generated by the electrodes under simulated solar irradiation at approximately the water oxidation potential are shown in **Figure 7.1**. All photoanodes give rise to a single semicircle Nyquist plot, allowing us to fit these impedance data using as equivalent circuit a Randles model in which the capacitance has been substituted by a constant-phase element.[34]

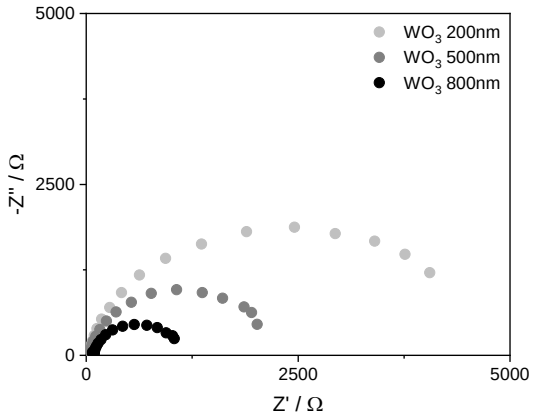

Figure 7.1 Nyquist plots of WO_3 samples with different thickness recorded under 1 sun illumination at 1.22 V vs RHE.

As described in **Chapter 3, Section 3.4.1**, the diameter of the semicircle corresponds to R_{ct}, the resistance associated with the interfacial charge transfer process, that in this case is the water oxidation reaction occurring at the electrode/electrolyte interface. In general, as the resistance associated with this process grows, the corresponding charge transfer becomes less efficient.

The results reported in **Figure 7.1** show that the water oxidation reaction is favoured by an increase in the WO_3 thickness, with the WO_3 800nm sample exhibiting a R_{ct} of $1.2 \cdot 10^3$ **Ω** at 1.22 V vs RHE. These EIS results are in line with the photoelectrochemical performances trend attained with such electrodes under simulated solar irradiation and discussed in the previous Chapter.

Using the Randles equivalent circuit we were then able to extract the surface capacitance C values and the R_{ct} values for the three WO_3 electrodes, both in the dark and under simulated solar irradiation, as a function of the external applied bias, as depicted in **Figure 7.2**.

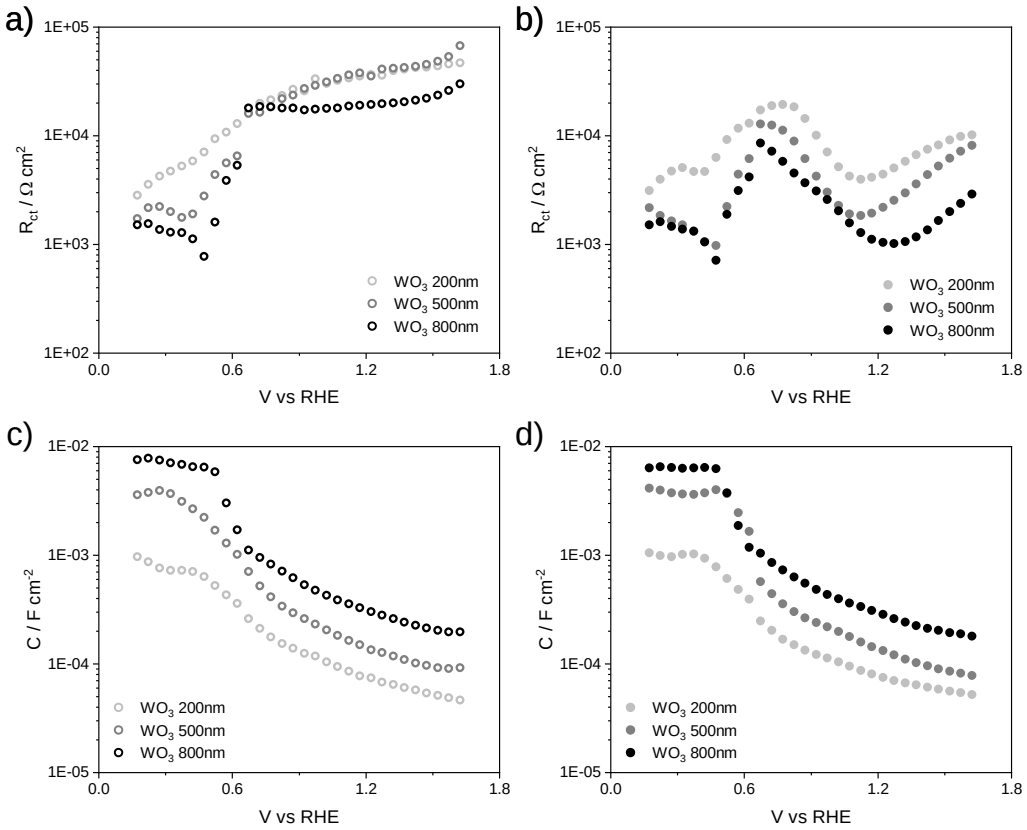

Figure 7.2 Charge transfer resistance R_{ct} and surface capacitance C determined under a,c) dark and b,d) irradiation conditions of WO_3 200, 500 and 800nm samples.

The calculated charge transfer resistances show, as expected, different behaviours depending on the irradiation conditions. In particular, in the absence of illumination and for applied potentials higher than 0.6 V the calculated R_{ct} remains constant for all electrodes, whereas under simulated solar irradiation the resistance of the films decreases up to *ca.* 1.1-1.2 V vs RHE, reaching a minimum value. At higher applied potentials R_{ct} slightly increases. WO_3 800nm exhibits the lowest calculated R_{ct} of $1{\cdot}10^3$ Ω cm^2, confirming that this is the most active sample for the water oxidation reaction, in agreement with data reported in **Figure 7.1** and photoelectrochemical tests results discussed in the previous Chapter.

The surface capacitances of the WO_3 electrodes are instead indipendent of the irradiation conditions. Under both dark and illumination conditions the capacitance C is almost constant for applied potentials lower than 0.6 V vs RHE, and then systematically decreases with increasing applied bias, reaching a minimum value, ranging from $8{\cdot}10^{-4}$ F cm^{-2}

for the thinnest film to $9 \cdot 10^{-3}$ F cm^{-2} for the WO_3 800nm sample. A correlation can be outlined between the C value and the electrode thickness. In fact, the surface capacitance increases with increasing the WO_3 layer thickness, producing a higher electron density, possibly related to the stabilization of a higher concentration of oxygen defects.[19,35,36] These factors point out to the fact that the calculated capacitance is likely associated with the chemical processes occuring at the interface, since C scales linearly with the film thickness.

By applying the Mott-Schottky (M-S) equation reported in **Chapter 3, Section 3.5.2** to the impedance data recorded at a low applied potential, the flat band potential of each WO_3 electrode has been calculated. The M-S plots and the flat band potentials estimated from the intercept of the fitted curve with the x-axis are reported in **Figure 7.3**.

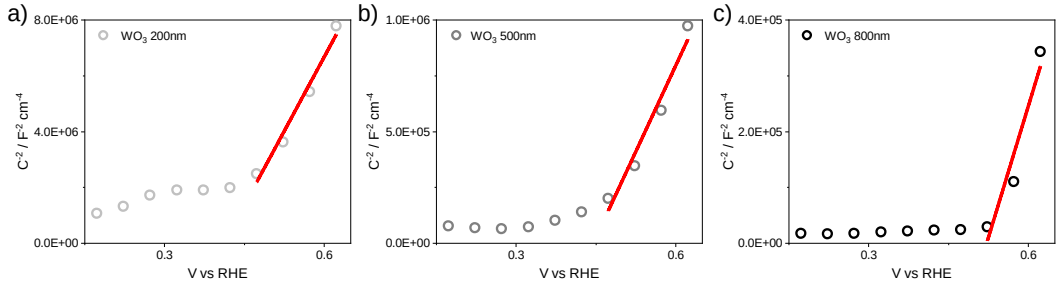

	WO_3 200nm	WO_3 500nm	WO_3 800nm
E_{FB} / V vs RHE	0.41	0.44	0.52

Figure 7.3 Mott-Schottky plots recorded in the dark for a) WO_3 200nm, b) WO_3 500nm, c) WO_3 800nm and estimated flat band potentials.

The calculated flat band potentials E_{fb} for the here investigated samples are in perfect agreement with the values reported for WO_3 of *ca.* 0.3-0.5 V vs RHE.[37–39] The photocurrent onset reported for these samples in the previous Chapter is located at *ca.* 0.8 V vs RHE, which is positively shifted with respect to the estimated flat band potentials. This is commonly observed for n-type semiconductors, and it is caused by slow kinetics and surface charge recombination that concurr to delay the photocurrent onset. Even if not directly observable in the here reported plots, the slope of the M-S curve decreases with increasing the material's thickness. Since the slopes of the plots are inversely proportional to the charge carrier densities of the films,[40] we can assess that WO_3 800nm exhibits the highest carrier density among the investigated WO_3 samples. The calculated values of the donor density of the three electrodes are comprised between $1 \cdot 10^{23}$ and $1 \cdot 10^{24}$ cm^{-3}; given the elevated density

obtained, close to the resolution limit discussed in **Chapter 3**, **Section 3.5.3**, further analyses will be needed to assess if a contribution to these results comes from the FTO substrate.

We then tested bismuth vanadate samples characterized by varying thickness; **Figure 7.4** reports the Nyquist plot obtained by performing impedance measurements at the water oxidation potential with the BV nL films. Also in this case all photoanodes display an impedance signal composed of a single semicircle and the data have been fitted using a Randles equivalent circuit. Under these operating conditions the lowest resistance is generated by the BV 4L sample, which however does not correspond to the sample exhibiting the best PEC performance under full lamp irradiation (see **Chapter 6, Section 6.4.2**). Generally, bismuth vanadate samples display resistance values much higher than those recorded with the previous set of tungsten oxide films.

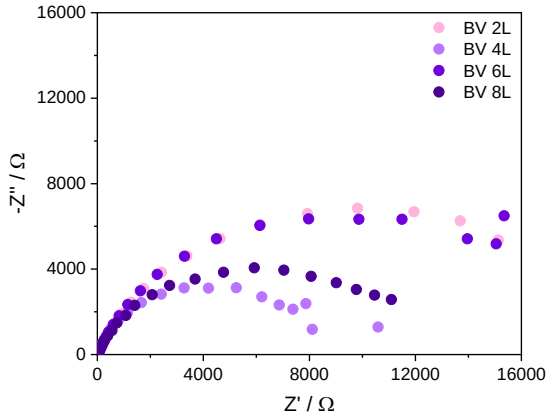

Figure 7.4 Nyquist plots recorded with $BiVO_4$ samples of variable thickness under 1 sun illumination at 1.22 V vs RHE.

Figure 7.5 depicts the calculated values of the charge transfer resistance R_{ct} and of the surface capacitance C in the absence or in the presence of simulated solar illumination for the $BiVO_4$ samples. Under dark conditions the investigated samples exhibit very high resistance values (reaching $1{\cdot}10^{15}$ Ω cm^2), which are consistent with the absence of any charge transfer process. Upon irradiation the calculated R_{ct} decrease to the $1{\cdot}10^5$–$1{\cdot}10^4$ Ω cm^2 range. Interestingly, for all investigated samples, R_{ct} systematically decreases with increasing applied potential, the estimated resistance values being pretty similar among the investigated

samples, making it difficult to draw conclusions on the best performing sample under the adopted experimental conditions.

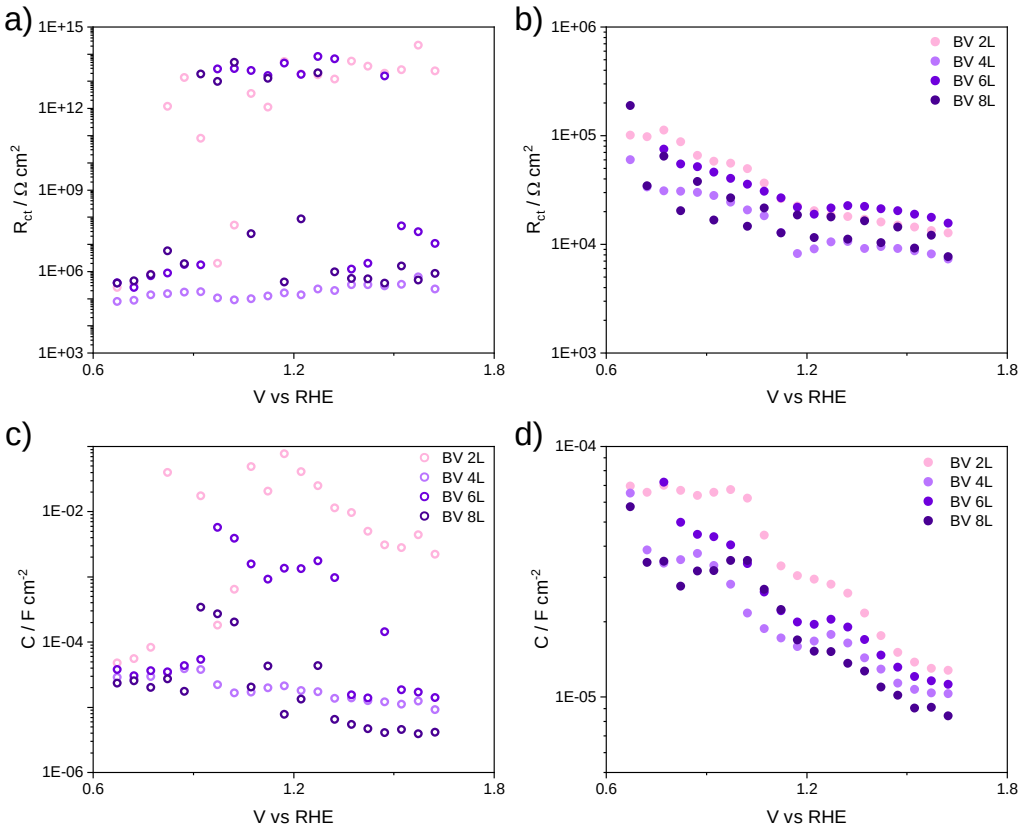

Figure 7.5 Charge transfer resistance R_{ct} and surface capacitance C determined under a,c) dark and b,d) irradiation conditions of BV 2, 4 6 and 8L samples. Please note that the y-axis scales are different between dark and irradiation conditions.

The calculated surface capacitances are reported in **Figures 7.5c,d**. A peculiar trend is observed in the capacitance under dark conditions of almost all samples, with the exception of BV 4L. In the range of applied potentials spanning from *ca.* 0.7 to 1.4 V vs. RHE an abrupt jump is observed in the calculated C value, that reaches values around $1 \cdot 10^{-2}$ F cm^{-2}. These measurements conducted in the dark may have undergone some intereference issues, yielding non coherent results. BV 4L sample, instead, is characterized by an almost costant capacitance of $2 \cdot 10^{-5}$ F cm^{-2}. Under illumination the trend of C is more clear. For all samples, the capacitance slightly decreases with increasing applied bias, retaining however the same order of magnitude of 10^4 F cm^{-2}. At approximately 0.8-0.9 V vs RHE a capacity peak can be

observed, which is probably related to the V^{4+}/V^{5+} change in the vanadium oxidation state.[41,42]

As for the WO_3 samples, attemps have been made to calculate the flat band potential of the bismuth vanadate electrodes. A good linearity of the results has been obtained with the BV 8L sample only; its Mott-Schottky plot is reported in **Figure 7.6**.

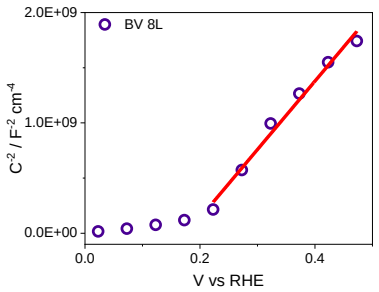

	BV 8L
E_{FB} / V vs RHE	0.18

Figure 7.6 Mott-Schottky plot measured in the dark with the BV 8L sample and its estimated flat band potential value.

The flat band potential E_{fb} estimated for the BV 8L sample corresponds to 0.18 V vs RHE, perfectly in line with literature values (between 0.1 and 0.3 V vs RHE) for bismuth vanadate.[43,44]. Also in this case, the observed photocurrent onset (*ca.* 0.8 V vs RHE) is positively shifted to higher applied potentials with respect to the calculated flat band potential. The N_D value calculated for this sample is $3.3 \cdot 10^{20}$ cm^{-3}, which results to be slightly higher than the donor density calculated previously in our group on similar electrodes.[45] Also in this case, further investigations will be needed to clarify the factors contributing to these results.

The heterojunction photoanodes series possessing different under- and overlayer thicknesses have been then tested via Electrochemical Impedance Spectroscopy. Some representative Nyquist plots are collected in **Figure 7.7** and refer to heterojunctions possessing different WO_3 thickness (200, 500 and 800 nm) coated with four or six $BiVO_4$ layers. Each panel of this Figure reports the Nyquist plots recorded with a specific composite photoelectrode under two different applied potentials (0.92 and 1.22 V vs RHE).

The major differences in the shape of the acquired impedance plots are mainly related to the different WO_3 underlayer thickness, especially for experiments performed at 1.22 V vs RHE. In particular, among electrodes with four BV layers (**Fig. 7.7a-c**), the WO_3 200nm–BV 4L sample exhibits a single semicircle, while with increasing tungsten oxide layer thickness the shape of the Nyquist plot changes and a straight line can be observed in the high frequency region (bottom left) of the plot. This line is slightly appreciable for the WO_3 500nm–BV 4L film, while it becomes more relevant in the case of WO_3 800nm–BV 4L sample.

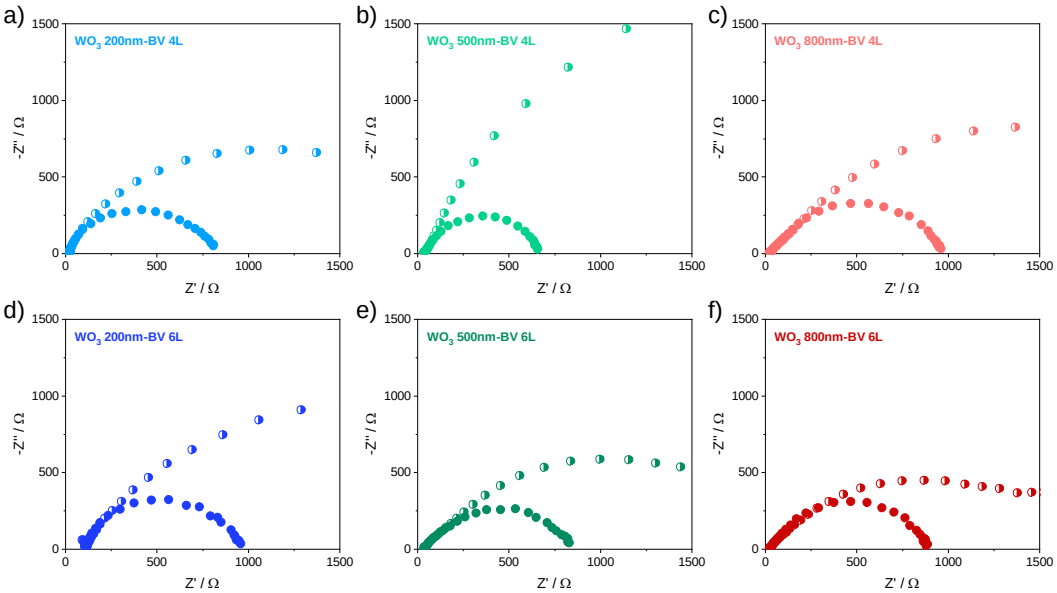

Figure 7.7 Nyquist plots recorded under simulated solar irradiation at 0.92 V (half-filled circles) and 1.22 V (full circles) vs RHE of heterojunctions with variable WO_3 underlayer thickness and a-c) four, or d-f) six $BiVO_4$ layers.

Similar EIS data trends can be attained with the composite materials possessing six BV layers (**Fig. 7.7d-f**). Also in this case, the sample with the thinnest WO_3 layer shows a regular semicircle-shaped plot, while samples with thicker WO_3 underlayers exhibit a straight line at high frequencies. The presence and the length of this straight line seem thus to be influenced by the thickness of both oxides in the composite material.

Analogous impedance signals can be identified as a so called *transmission line*, that manifests in an impedance plot as a straight line with a 45° angle inclination, and which is characteristic of electron diffusion.[19,32,46] These impedance data cannot be fitted using the

simple Randles circuit, but require to be fitted with a more complex circuit able to mimic the charge transfer processes occuring in the photoelectrodes.

Figure 7.8 reports the fitting of the EIS data relative to the WO_3 200nm–BV nL series, using a Randles EC.

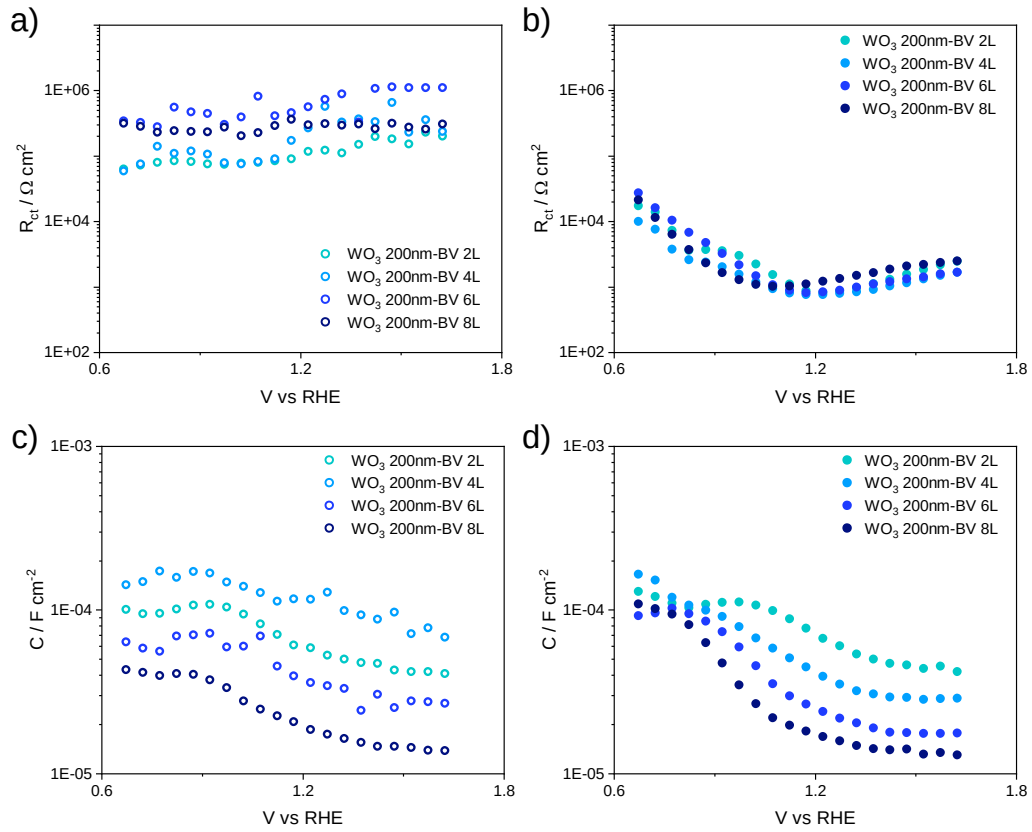

Figure 7.8 Charge transfer resistance R_{ct} and surface capacitance C determined under a,c) dark and b,d) irradiation conditions of WO_3 200nm–BV 2, 4, 6 and 8L samples.

In the absence of irradiation the composite systems exhibit very high charge transfer resistance values, remaining almost constant with increasing applied potential. Under illumination, for all samples, the charge transfer resistance tends to decrease up to 1.1 V vs RHE and then remains almost constant, at *ca.* $1{\cdot}10^3$ Ω cm^2. The samples show very similar R_{ct} values, indipendently of the number of coated bismuth vanadate layers.

The surface capacitances of the heterojunctions (**Fig. 7.8c,d**) appear almost constant under dark conditions, with C only slightly decreasing at higher applied potential. Differently,

under illumination, a marked capacitance decrease is observed with increasing external bias. Furthermore, C tends to decrease as the number of BV coated layers increases, with the WO_3 200nm–BV 8L sample reaching a *ca.* $1 \cdot 10^{-5}$ F cm^{-2} minimum value at 1.7 V vs RHE. Notably, the surface capacitance trend of the composite materials resembles that of pure-phase $BiVO_4$ samples, with the same order of magnitude of estimated C values. Differenty, pure WO_3 200nm exhibits much higher C values (two orders of magnitude higher at low potentials, see **Fig. 7.2c,d**) and shows an exponential behaviour, which is not detectable in the composites. Thus, $BiVO_4$ seems to control the capacitance of the resultant heterostructured material, even if its coating is only some tens of nanometers thick. EIS data do not evidence any enhancement in terms of electron density upon the $BiVO_4$ combination with WO_3. This finding is in contrast with what observed in the case of EIS measurements performed on nanostructured WO_3 and WO_3–$BiVO_4$ (**Chapter 5**, **Section 5.4.2)**, for which the surface capacitance of the composite resulted greater than that of the corresponding pure WO_3. We thus find no evidence of charge injection from the WO_3 underlayer to the $BiVO_4$ in this series of heterojunctions.

As previously stated, we also tried to use a different equivalent circuit to fit the data of the samples showing the trasmission line in the high frequency area. The EIS data acquired with the WO_3 800nm–BV nL series samples were thus fitted by adopting the EC reported in the following scheme (**Scheme 7.1a**). This circuit is characterized by the presence of the following parameters: R_s, that is the system resistance accounting for the transport of the charges through the FTO support and the external circuit; C_1, representing the surface capacitance and DX1, which is a Bisquert-2 extended element, normally used to fit transmission lines.[47]

Scheme 7.1b represents the transmission line element, including: the electron transport parameter (r_{tr}) along the electron transport level, the transversal element, depending on charge accumulation and charge transfer, and the lower rail, indicating fast charge transport in the electrolyte.[12,19]

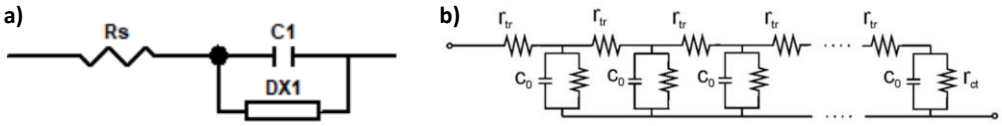

Scheme 7.1 a) Equivalent Circuit and b) detail of the transmission line element used to fit impedance data of the WO_3 800nm–BV nL series samples.

Upon fitting, different parameters have been calculated: DX1-R and C(DX1) refer to the resistive and capacitive elements of the extendend element, while C1 refers to the water oxidation charge transfer. These fitted parameters are reported in **Figure 7.9**.

The resistance associated with the extended element (DX1-R) appears to slightly increase upon increasing potential in the absence of illumination, while under simulated solar irradiation the resistance decreases up to 0.9 V vs RHE and then it increases at higher bias. Notably, the resistance of the sample possessing only two BV layers is sensibly lower with respect to those recorded with other series samples. This is consistent with the hypothesis that the diffusion issues encountered for these systems are closely connected to the thickness of both oxides in the composite material.

The capacitance associated with the transmission line, C(DX1), is almost constant under dark conditions if the bismuth vanadate coating in fairly thin (2 and 4 layers), while it decreases more rapidly if the thickness of the overlayer increases. Under illumination, the capacitance of all samples has very similar, constant values at low applied bias, while it starts to decrease at potentials higher than 1 V vs RHE.

On the other hand, C1 remains constant both under dark and simulated solar irradiation; this parameter exhibits much lower values (between $1{\cdot}10^{-5}$ and $1{\cdot}10^{-7}$ F cm^{-2}) with respect to the transmission line capacitance. Also in this case, the values calculated for the WO_3 800nm–BV 2L sample are much lower than those recorded with the other composites.

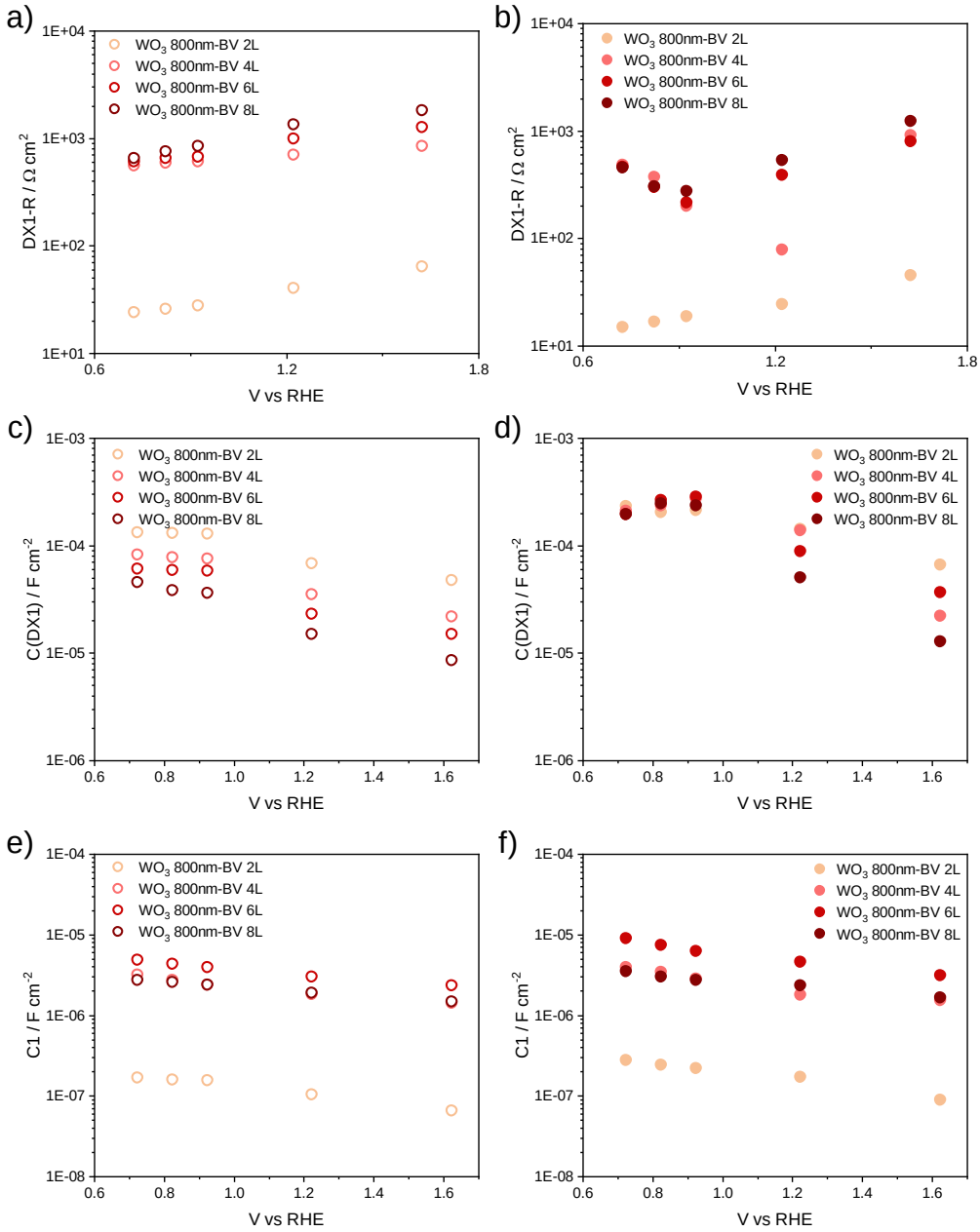

Figure 7.9 a,b) DX1-R, c,d) C(DX1) and e,f) C1 under dark (void circles) or irradiation conditions (full circles) of the WO_3 800nm–BV 2L, 4L, 6L and 8L samples.

The use of a more complex equivalent circuit to fit the impedance data of the WO_3 800nm–BV nL series has thus provided us a first confirmation of the presence of electron diffusion issues occuring in the bulk of the heterojunctions, whose entity seems to be closely connected to the thickness of the two oxide materials composing the heterojunction.

The behaviour of these photoelectrodes has been then investigated by means of spectroelectrochemical measurements, reported in the following Section, aimed at further investigating the difference in the properties of the composites depending on the thickness of both oxides.

7.4.2 Spectroelectrochemical analyses

As for the previously discussed impedance measurements, SEC analyses were firstly performed on a clean FTO electrode, the substrate used to synthesise all the here investigated photoanodes, in order to verify the absence of any significant SEC signal that may affect the interpretation of the photoanodes' absorption spectra. As can be seen in **Figure D2** of the Appendix, the fluorine-doped tin oxide slab does not generate significant absorption. The shifts from the baseline at 990, 1160 and 1240 nm have very low intensity, around $1 \cdot 10^{-3}$ ΔO.D. Moreover, in few of the spectra discussed in this section, a small peak at 534 nm can be ascribed to the lamp change of the employed instrument.

SEC spectra have been recorded for all pure and coupled photoanodes. The results obtained by testing the tungsten oxide samples with different thicknesses are reported in **Figure 7.10**.

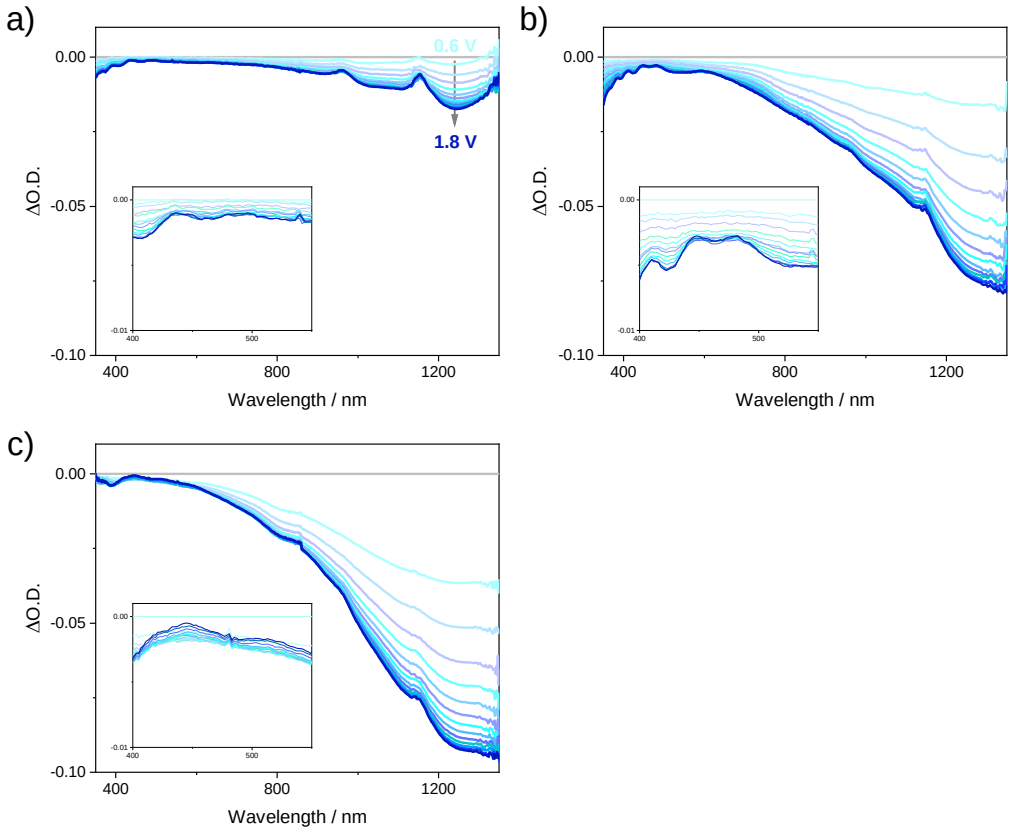

Figure 7.10 ΔO.D. spectra of a) WO_3 200nm, b) WO_3 500nm and c) WO_3 800nm. Insets represent the ΔO.D. spectra magnification in the 400-550 nm range.

All WO_3 samples exhibit a broad negative peak stretching from ~450 nm up to the NIR region, that becomes more pronounced as the thickness of the sample increases and the external applied potential grows. This signal may thus be ascribed to a progressive depletion of occupied electronic states of the metal oxide induced by increasing the applied bias; the absorption intensity associated to the optical transition of electrons originally located at such states progressively diminishes with the consequent formation of the observed negative peak.

In particular, WO_3 is generally reported to be a material with a high doping density resulting from the presence of a large number of oxygen vacancy defects,[35,36] that can generate new electronic and optical levels within the band gap of the semiconductor. In tungsten oxide, these oxygen defects often manifest as reduced tungsten centres (W^{5+}).[48] W^{5+} is an optically active *d1* centre, which results in a distinct blue coloration. The concentration of reduced tungsten centres can be modified in different ways, *e.g.*, by applying electrochemical, photochemical and thermal excitations. The depletion of these reduced W^{5+} centres under

the application of an external anodic bias gives rise to the above observed characteristic broad absorption feature extending from red wavelengths up to the NIR, thus confirming that the occupancy of these states and the degree of band bending (also affected by the external bias) in WO_3 are tightly correlated.[22] These states lie energetically below the conduction band edge of the material and present a fairly large energetic distribution.[38] The nature of this signal is thus tightly linked to the thickness of the material (*i.e.,* the concentration of electronic defects). Other studies reporting SEC analyses on tungsten oxide samples did not evidence such absorption feature because of the extremely low thickness of the studied photoelectrodes.[29]

Moreover, the insets of **Figure 7.10** show a second absorption in the visible region, peaked at *ca.* 445 nm. Also in this case the absorption difference signal becomes more pronounced and broader with increasing film thickness and/or applied potential. In this case the external anodic bias generates a positive peak with respect to the underlying background signal. Upon the electrochemical stimulus, the excitation of electrons from occupied intra band gap states toward empty energy levels located few hundred of meV below the CB of WO_3 may determine the observed positive optical peak.

Figure 7.11 depicts the difference absorption spectra recorded by applying an external bias to $BiVO_4$ samples with different thickness. Two positive absorption signals, each with a corresponding negative peak located at higher wavelengths, are visible at 960 and 1155 nm, while their negative counterparts are located at 1025 and 1240 nm. The relative intensity of these signals seems to be partially connected to the overall thickness of the analysed sample. In fact, the relative intensity of such peaks increases when passing from the 2L to the 4L sample, and again when increasing the thickness from 6 to 8 BV layers. We can hypothesise that these signals are linked to a depletion/population mechanism concerning some intraband gap states, that causes the rise of negative and positive peaks in the NIR region of the spectrum, respectively.

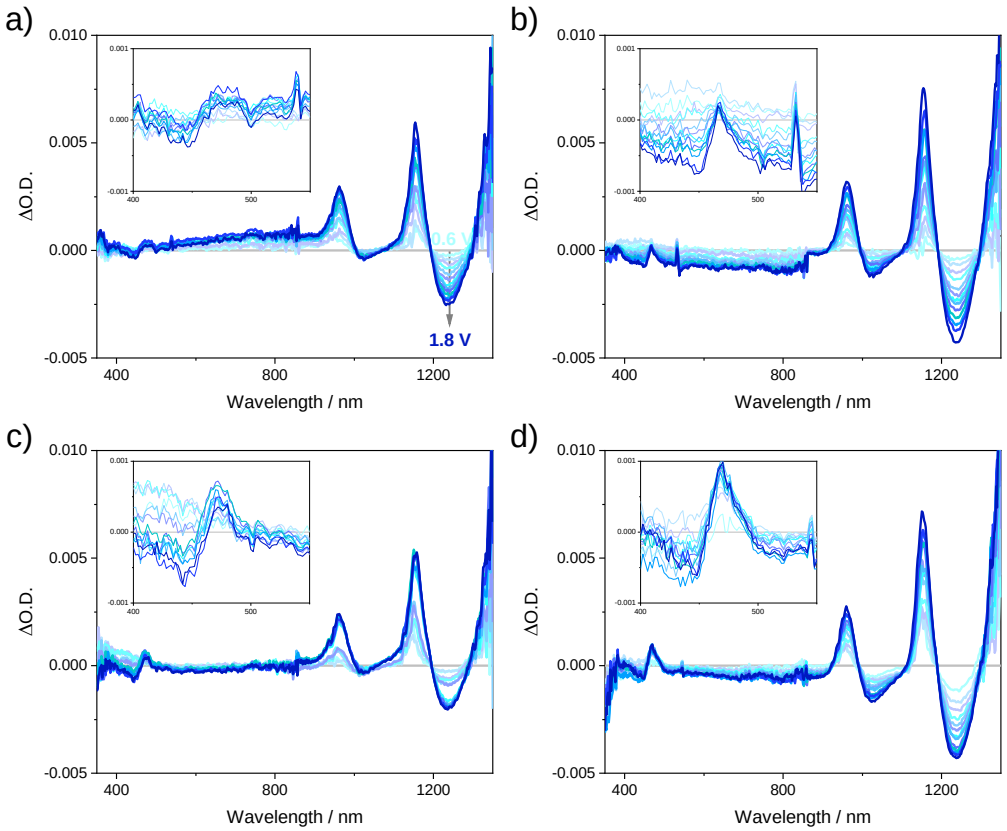

Figure 7.11 ΔO.D. spectra of a) BV 2L, b) BV 4L, c) BV 6L and d) BV 8L. Insets report the ΔO.D. spectra magnification in the 400-550 nm range.

Also in this case the samples exhibit an additional absorption peak in the UV region of the spectrum. Particularly, at ~470 nm a positive peak emerges as the applied bias is increased. Since the here applied potentials E are much more anodic than the flat band potential of $BiVO_4$ (which is located at *ca.* 0.02 V vs RHE, see **Section 7.4.1**),[15,49] the rise of a positive absorption feature can be assigned to the formation of oxidized states at energies few meV below the conduction band of the material.[29] In the absence of any applied bias, these intraband states are occupied by electrons, which are depopulated following the application of an external potential, thus leading to the appearance of a new optical transition, involving the promotion of electrons from the populated VB states towards the now empty intraband gap states. This peak is more evidently linked to the overall thickness of the electrode under study, since it becomes more pronounced and sharper as the number of coated bismuth vanadate layers increases.

After the spectroelectrochemical analyses of the two single-component series photoelectrodes, SEC measurements have been performed on the heterojunction materials characterized by different under- and overlayer thicknesses. **Figure 7.12** shows the difference spectra of the composite samples having a *ca.* 200 nm-thick WO_3 underlayer and coated with 2, 4, 6 or 8 $BiVO_4$ layers.

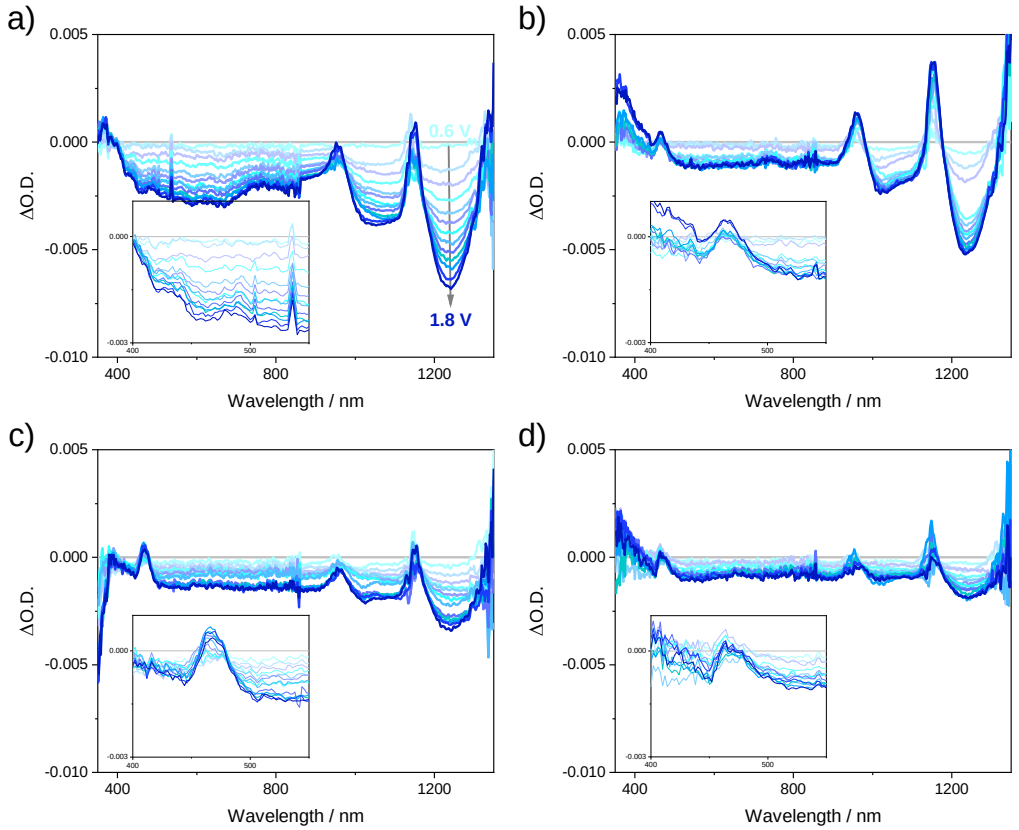

Figure 7.12 ΔO.D. spectra of a) WO_3 200nm–BV 2L, b) WO_3 200nm–BV 4L, c) WO_3 200nm–BV 6L and d) WO_3 200nm–BV 8L. Insets report the ΔO.D. spectra magnification in the 400-550 nm range.

The behaviour of the WO_3 200nm–BV nL samples strongly differs from that showed by the corresponding single WO_3 and $BiVO_4$ materials. In particular, the broad negative absorption feature characteristic of WO_3 in the NIR region is absent (see **Figure 7.10a** for comparison). Instead, the two positive and negative signals characteristic of $BiVO_4$ are maintained, even if their relative intensities are much lower than those recorded for the corresponding pure bismuth vanadate samples. Moreover, the intensities of these peaks are reduced with increasing thickness of the BV coating, once again in contrast to previous observations for pure $BiVO_4$. WO_3 200nm–BV 8L shows indeed negligible absorption features

in the NIR region up to 800 nm. In the UV-Vis range of the spectrum, the behaviour of the composite materials is much more similar to that observed for $BiVO_4$ alone. As the thickness of the overlayer grows, a positive absorption peak, centered at *ca.* 465-470 nm, appears. Its intensity, however, is not clearly linked to the number of coated BV layers, the most marked peak being exhibited by the WO_3 200nm–BV 6L sample, as evidenced in the inset of **Figure 7.12c**.

Generally, the trends in SEC spectra emerged for the WO_3 200nm–BV nL set of heterojunctions are visible also when taking into consideration composite materials with increased WO_3 thickness, with some minor differences. **Figures 7.13a-d** report the difference spectra recorded with the composite photoanodes with a tungsten oxide underlayer of *ca.* 500 nm. Also this series samples does not exhibit the typical NIR absorption feature due to the depletion of W^{5+} centers in WO_3 and the peaks at *ca.* 960 and 1155 nm which are instead characteristic of $BiVO_4$ show a reduced intensity. Interestingly, for the WO_3 500nm-BV nL series the positive ΔO.D. peak located in the visible region does not show any significant intensity variation with increasing thickness of the $BiVO_4$ overlayer.

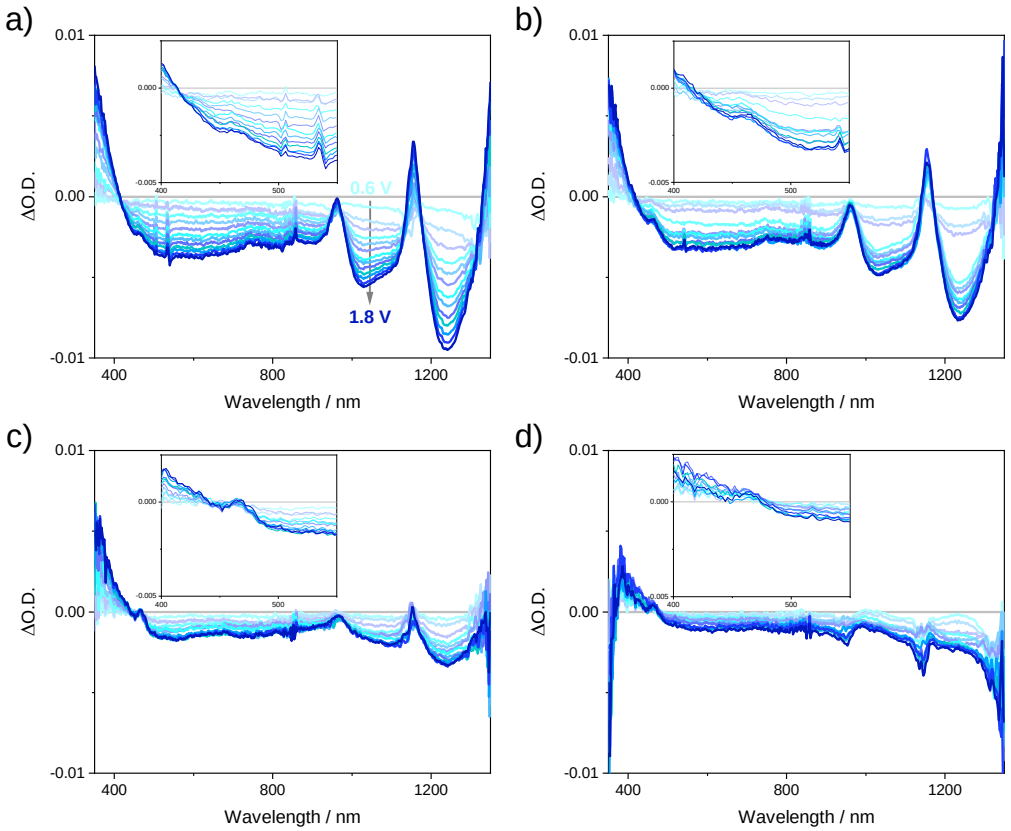

Figure 7.13 ΔO.D. spectra of a) WO_3 500nm–BV 2L, b) WO_3 500nm–BV 4L, c) WO_3 500nm–BV 6L and d) WO_3 500nm–BV 8L. Insets report the ΔO.D. spectra magnification in the 400-550 nm range.

Lastly, difference spectra recorded with the set of heterojunctions possessing a 800 nm-thick WO_3 underlayer are reported in **Figure 7.14**. This set of composites shows a behaviour similar to that of the previously discussed samples. The broad negative signal in the NIR attained with the single WO_3 800nm sample is lacking and the absorption features displayed by the BV nL samples are much less intense. In particular, with the 800 nm thick WO_3 underlayer, the characteristic NIR signals of $BiVO_4$ are almost completely toned down upon the deposition of at least four layers of BV (**Figure 7.14b**). At the same time, the band at *ca.* 470 nm shows a relatively small intensity.

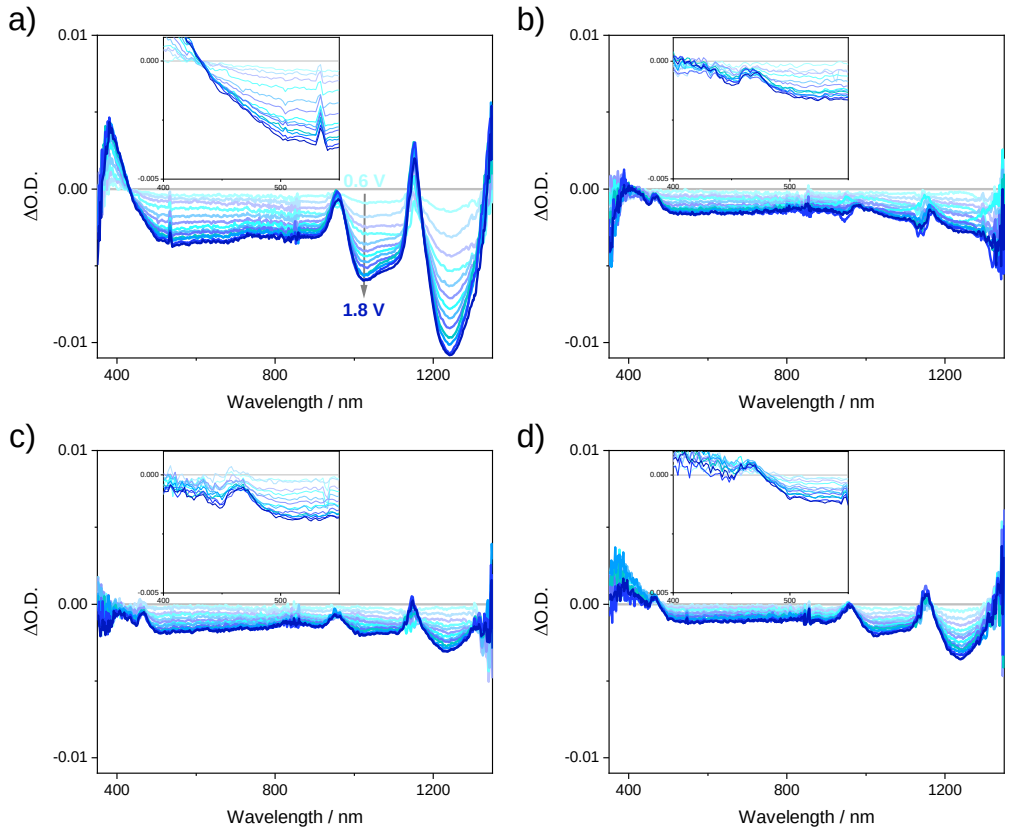

Figure 7.14 ΔO.D. spectra of a) WO_3 800nm–BV 2L, b) WO_3 800nm–BV 4L, c) WO_3 800nm–BV 6L and d) WO_3 800nm–BV 8L. Insets report the ΔO.D. spectra magnification in the 400-550 nm range.

In order to better compare the change in the spectroelectrochemical response attained with the coupled samples with respect to the single-component oxides, the ΔO.D. spectra recorded at the highest applied potential (1.83 V vs RHE) of three representative samples (WO_3 800nm, BV 8L and WO_3 800nm–BV 8L) are collected in **Figure 7.15**. A very peculiar behaviour is observed, the difference spectra of the WO_3–$BiVO_4$ heterojunctions being sensibly different from those of the corresponding individual components. The modification of the typical absorption features of the separated oxides attained upon their coupling in a composite system is a clear indication of the activation of specific charge carriers recombination/separation paths possibly determining the superior photoactivity of the investigated heterojunctions.

In particular, the disappearance of the negative NIR broad peak in the heterojunction may suggest that in the WO_3–$BiVO_4$ system reduced W^{5+} centers are no longer present or

available to be depleted by an external applied bias. Hence, the oxygen vacancy defects originally present in pure WO_3 may be absent when the material is coupled with bismuth vanadate, thus suggesting a new energy distribution of tungsten oxide intraband gap states. The abrupt disapperance of WO_3 defectuality may be also consequent to the thermal treatments undergone by the sample following the deposition of $BiVO_4$ layers on its surface, which may further contribute to a redistribution of electronic charges between the two materials.

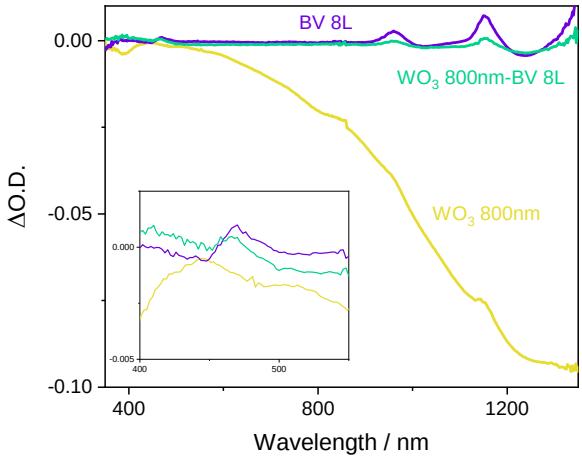

Figure 7.15 ΔO.D. spectra of WO_3 800nm, BV 8L and WO_3 800nm–BV 8L recorded at 1.83 V vs RHE. The inset reports the ΔO.D. spectra magnification in the 400-550 nm range.

At the same time, the absorption features recorded with BV 8L are still present in the composite, although displaing lower intensity. This observation may further support the presence of charge recombination and redistribution paths that are at work only upon coupling $BiVO_4$ with WO_3.

Lastly, all three photoanodes exhibit a positive ΔO.D. in the visible light range, with that ascribed to the composite material being slighty blue-shifted and less pronounced with respect to that of the BV 8L sample. Also this phenomenon could point out a different charge carriers amount/distribution in the heterojunction.

In order to further analyse the above described phenomena we performed additional measurements known as 'stepped potential spectroelectrochemistry', that will be discussed in the following Section.

7.4.2.1 Stepped potential spectroelectrochemistry

A series of measurements was performed on few selected samples under monochromatic irradiation, varying the external applied potential between the estimated flat band potential (E_{fb}) of each photoelectode and a higher E using a step modulation. In these experiments, the current density generated from the system and the change in optical density of the sample were simultaneously tracked as a function of time. WO_3 samples (200nm and 800nm) were irradiated with monochromatic light at 445 nm, while $BiVO_4$ and WO_3–$BiVO_4$ samples (BV 8L, WO_3 200nm–BV 8L and WO_3 800nm–BV 8L) were tested under irradiation at 468 nm. The chosen incident monochromatic wavelengths correspond to the maximum of the absorption peak in the visible range observed in SEC analyses (see **Figures 7.10-14**).

An example of a stepped potential SEC measurement is shown in **Figure 7.16**. Upon increasing the applied potential from E_{fb} to E_2 an increase in absorption (black line) of the sample was detected, which then returned to its original value when the potential was stepped down. At the same time, the photocurrent generated by the system (blue line) under increasing applied bias was recorded.

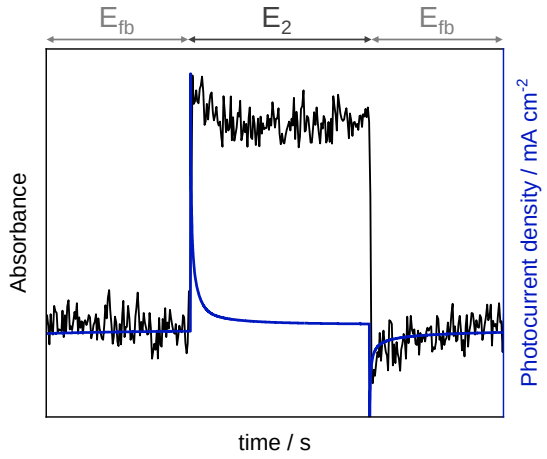

Figure 7.16 Example of a performed stepped potential spectroelectrochemical analysis.

The starting potential (E_{fb}) was 0.5 V vs RHE for the WO_3 samples and 0.2 V vs RHE for $BiVO_4$ and WO_3–$BiVO_4$ samples. E_2 was chosen with the aim of increasing the potential of 0.1 V after each step; the first measurement consisted in a 0.1 V difference between E_{fb} and E_2, the second measurement applied a 0.2 V difference, and so on.

The measured reduction current (corresponding to the $E_2 \rightarrow E_{fb}$ transition, bottom right section of the blue line in **Figure 7.16**) was then integrated to quantify the total charge stored in the tested oxide associated with the detected optical change, in terms of number of electrons involved in the building of the current signal.[28] At the same time, the optical change in terms of ΔAbs has been also calculated. The extracted charge can be used to provide insight into the density of oxidized species formed following the application of the stepped potential. In particular, by correlating the calculated ΔAbs with the extracted charge, the extinction coefficient of the oxidized species can be computed to determine their density as a function of applied potential.[28,50,51]

We first verified the accordance of the results obtained via the stepped potential technique with those obtained through SEC measurements, to check the compatibility of the results obtained by the two techniques. The difference in optical density linked to the optical transition occurring at the chosen incident wavelength was measured either *i)* by normalizing the ΔO.D. value recorded at that wavelength and discussed in the previous section (the so-obtained results are labelled as *SEC*), or *ii)* by calculating the difference in absorbance related to the same optical transition using the results obtained in stepped potential analyses (*SP_SEC*).

Generally, as evidenced in **Figure 7.17**, the ΔO.D. values obtained with the two different techniques show similar trends, especially in the case of pure-phase WO_3 200nm and BV 8L samples. On the other hand, composite samples show a lower agreement between the two sets of results, probably due to the extremely low intensity of the investigated signals obtained in SEC analyses (see **Figures 7.12d** and **7.14d**).

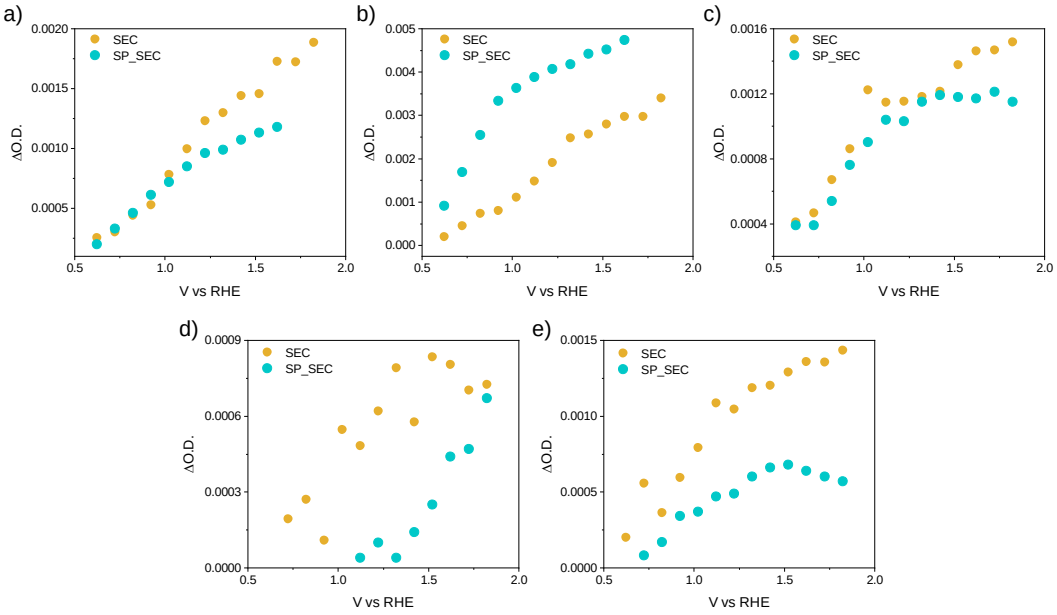

Figure 7.17 ΔO.D. values of a) WO_3 200nm, b) WO_3 800nm, c) BV 8L, d) WO_3 200nm–BV 8L and e) WO_3 800nm–BV 8L samples derived either from SEC or from stepped potential SEC (SP-SEC) analyses.

As previously stated, upon the integration over time of the photogenerated current (Q) during SP-SEC analysis, the number of electrons involved in the specific bias-induced optical transition has been calculated as follows, with e representing the elemental charge:

$$number\ of\ electrons = \frac{Q}{e} \tag{7.3}$$

Figure 7.18 reports the comparison of the calculated number of electrons generated by the irradiation of $BiVO_4$ 8L, WO_3 200nm–$BiVO_4$ and WO_3 800nm–$BiVO_4$ with the 468 nm incident radiation. It is possible to notice that both heterojunctions, in particular the one possessing the thickest tungsten oxide underlayer, generate a much higher number of electrons upon the excitation with the same incident radiation with respect to pure phase $BiVO_4$. These evidences suggest that upon the combination of the two oxides, the number of electrons associated with the same optical transition occurring in bismuth vanadate is enhanced, maybe due to an electron injection from the WO_3 substrate towards $BiVO_4$. This hypothesis seems to be validated by the enhancement of the calculated number of electrons upon the presence of a thicker tungsten oxide underlayer.

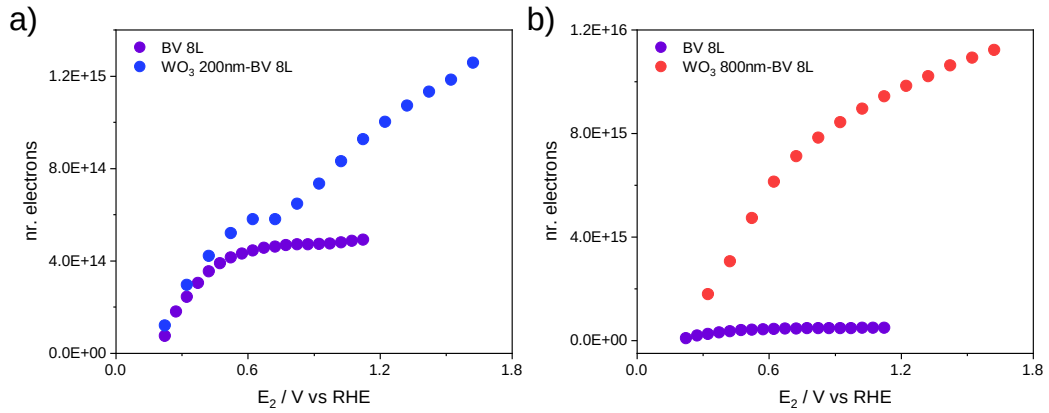

Figure 7.18 Number of electrons as function of applied potential E_2 for a) BV 8L and WO_3 200nm–BV 8L and b) BV 8L and WO_3 800nm–BV 8L.

The calculated number of electrons was then correlated with the ΔO.D. values corresponding to the specific optical transition (*i.e.*, recorded during the same potential step $E_{fb} \rightarrow E_2$) to verify the existance of a linear correlation between these two variables. These results are reported in **Figure 7.19** for all photoelectrodes. A linear fitting was then performed using the Linear Fit option of the Origin software in order to check the linear correlation and to extract the slope of the obtained lines which are reported in **Table 7.2**. The complete fitting parameters are reported in the Appendix at the end of this Chapter. A good linear fitting ($R^2 > 0.95$) was obtained for all samples, with the occasional discard of a few data points located at low or high applied potentials.

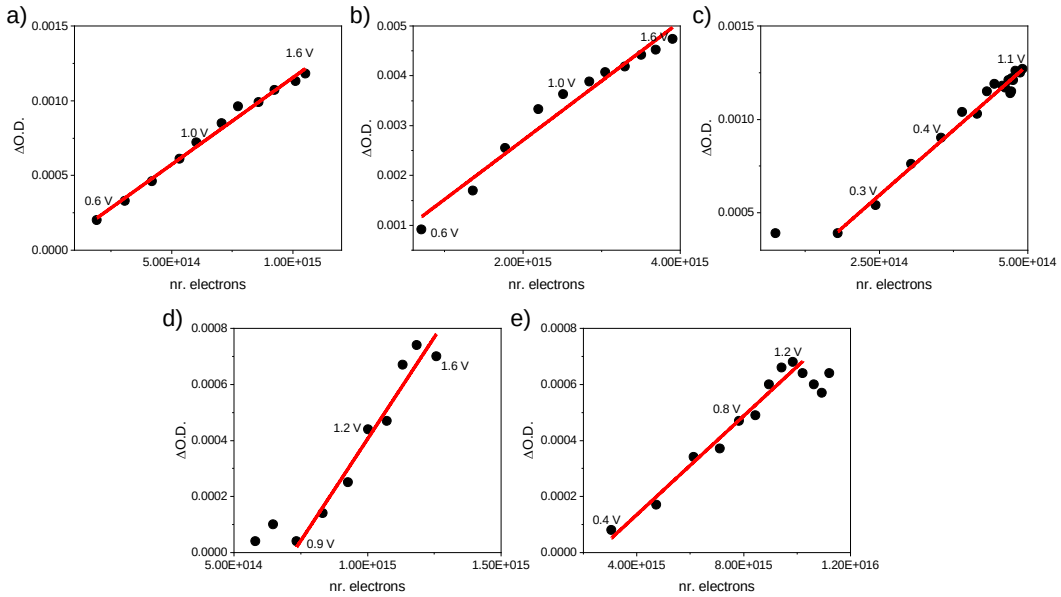

Figure 7.19 Correlation between number of electrons and ΔO.D. calculated in stepped potential SEC measurements of a) WO_3 200nm, b) WO_3 800nm, c) BV 8L, d) WO_3 200nm–BV 8L and e) WO_3 800nm–BV 8L samples.

The extinction coefficients of the optical transition observed during SEC analyses thus correspond to the slope of the linear plots reported in **Figure 7.19**. As shown by the data collected in **Table 7.2**, the coefficients obtained for the two tungsten trioxide are very similar (*ca.* $1.2E^{-18}$), while the coefficient of $BiVO_4$ results to be more than doubled (*ca.* $2.8E^{-18}$). As both materials are present in a composite system, the extinction coefficient has a value intermediate to those of the two single oxides in the case of the WO_3 200nm–BV 8L sample ($1.5E^{-18}$), while the heterojunction presenting the same BV overlayer and a much higher WO_3 underlayer thickness exhibits the lowest coefficient ($8.8E^{-20}$), two orders of magnitude smaller than the previously observed values.

As already anticipated when discussing the results evidenced by spectroelectrochemical analyses, the number of electrons involved in the same optical transition changes as the two oxides are brought together in a heterojunction, clearly indicating an electronic redistribution between the materials.

Sample	Slope / (nr. e)$^{-1}$
WO_3 200nm	1.16E^{-18}
WO_3 800nm	1.19E^{-18}
BV 8L	2.79E^{-18}
WO_3 200nm–BV 8L	1.45E^{-18}
WO_3 800nm–BV 8L	8.81E^{-20}

Table 7.2 Slope values calculated by performing a linear fitting of the curves reported in **Figure 7.19**.

Stepped potential spectroelectrochemistry was thus able to provide some quantitative data further confirming the hypothesis on the occurrence of charge redistribution in the coupled systems, since the extinction coefficient associated with the same optical transition in $BiVO_4$ results greatly decreased upon the combination of bismuth vanadate with tungsten oxide.

7.5 Conclusions

In this Chapter, advanced characterization techniques have been used to study the intrinsic behaviour of pure-phase WO_3 and $BiVO_4$ samples, as well as that of three WO_3–$BiVO_4$ series of heterojunctions, displaying variable under- and overlayer thicknesses. Electrochemical Impedance Spectroscopy and Spectroelectrochemistry are two powerful investigation methods that can provide useful information on the intrinsic kinetic and charge storage characteristics, as well as on the electronic transitions taking place in a photoelectrocatalytic material. Despite their potential, both techniques have been little exploited to analyse the WO_3–$BiVO_4$ system.

The fitting of EIS data using a Randles equivalent circuit allowed us to calculate the charge transfer resistance and surface capacitance of pure-phase electrodes and of the WO_3 200nm–$BiVO_4$ nL series, and to study their behaviour as a function of the external applied potential. We observed that the bismuth vanadate overlayer controls the overall capacitance of the heterostructured material and, in particular, the deposition of BV on WO_3 leads to an overall decrease of surface capacitance in the composite with respect to underlying WO_3, thus showing no sign of enhanced charge density in the $BiVO_4$ overlayer under illumination.

The impedance data of the composite series displaying higher tungsten oxide thickness (WO_3 800nm–$BiVO_4$ nL) have been fitted with an equivalent circuit containing an extented element, accounting for the presence of a transmission line in the high frequency region, associated with electron diffusion issues. This finding directly proved the occurrence of charge transport issues upon the combination of the two oxides in the composite material.

Spectroelectrochemical analyses have then highlighted further differences in the behaviour of the heterojunction photoanodes with respect to single component materials. The disappearance in the composites of the broad NIR absorption feature typically ascribed to WO_3 oxygen defects, as well as the reduction in intensity of the optical peaks observed for pure $BiVO_4$ point out to electron redistribution mechanisms at work when the two materials are coupled in the heterojunction. Finally, stepped potential measurements allowed us to quantify the number of charges effectively involved in the investigated optical transitions in the visible range, providing evidence of a greater availability of charges on $BiVO_4$ upon its combination with WO_3.

Appendix D

EIS on a clean FTO slab

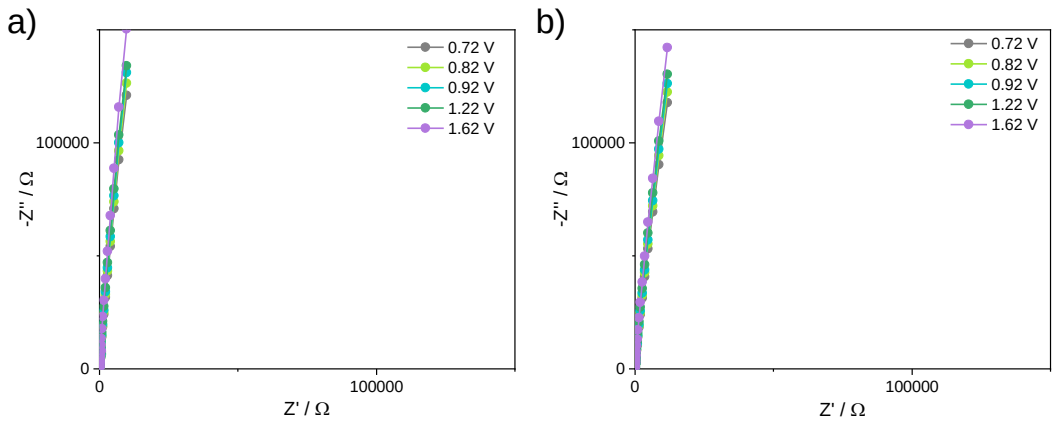

Figure D1 Nyquist plots of a clean FTO substrate in a) dark and b) under 1 sun illumination.

The absence of any electrochemical reactions occurring in the FTO conductive glass has been demonstrated by *i*) the extremely high impedance values recorded (up to $1.5 \cdot 10^5$ **Ω**), *ii*) the absence of a correlation between the signals and the external applied bias, and *iii*) the absence of any difference in the results obtained under dark or irradiation.

SEC spectra of a clean FTO slab

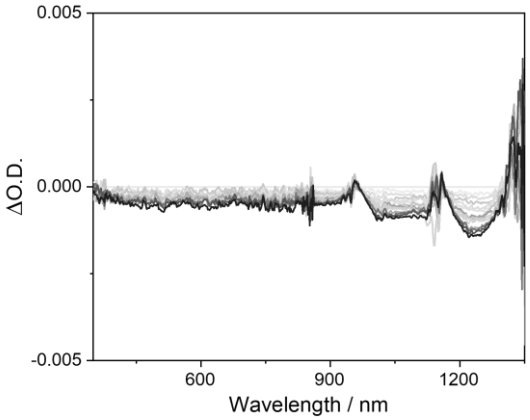

Figure D2 ΔO.D. spectra of a clean FTO substrate.

Spectroelectrochemical analyses have been performed on a clean conductive substrate in order to rule out the possibility of any contribution of the FTO to the signals recorded with the prepared photoelectrodes.

Linear fit results

a)

Equation	y = a + b*x
Plot	ΔAbs
Weight	No Weighting
Intercept	-8.97959E-6 ± 2.71924E-5
Slope	1.16425E-18 ± 3.75178E-2
Residual Sum of Square	1.03819E-8
Pearson's r	0.99536
R-Square (COD)	0.99074
Adj. R-Square	0.98971

b)

Equation	y = a + b*x
Plot	ΔAbs
Weight	No Weighting
Intercept	3.30146E-4 ± 2.14061E-4
Slope	1.18889E-18 ± 7.65465E-2
Residual Sum of Square	5.48782E-7
Pearson's r	0.98185
R-Square (COD)	0.96403
Adj. R-Square	0.96004

c)

Equation	y = a + b*x
Plot	ΔAbs
Weight	No Weighting
Intercept	-1.02856E-4 ± 4.20878E-5
Slope	2.78865E-18 ± 9.88637E-2
Residual Sum of Square	2.15228E-8
Pearson's r	0.99009
R-Square (COD)	0.98029
Adj. R-Square	0.97905

d)

Equation	y = a + b*x
Plot	ΔAbs
Weight	No Weighting
Intercept	-0.00105 ± 1.31886E-4
Slope	1.45248E-18 ± 1.27839E-1
Residual Sum of Square	2.20693E-8
Pearson's r	0.97754
R-Square (COD)	0.95558
Adj. R-Square	0.94818

e)

Equation	y = a + b*x
Plot	ΔAbs
Weight	No Weighting
Intercept	-2.171E-4 ± 4.07825E-5
Slope	8.8085E-20 ± 5.16835E-2
Residual Sum of Squares	1.04909E-8
Pearson's r	0.98651
R-Square (COD)	0.9732
Adj. R-Square	0.96985

Figure C3 Fittings values of linear correlations evidenced in **Figure 7.18**.

References

1. B.S. Kalanoor, H. Seo, S.S. Kalanur, *Mater. Sci. Energy Technol.* 1 (**2018**) 49–62.
2. P. Chatchai, Y. Murakami, S. ya Kishioka, A.Y. Nosaka, Y. Nosaka, *Electrochim. Acta* 54 (**2009**) 1147–1152.
3. X. Shi, I.Y. Choi, K. Zhang, J. Kwon, D.Y. Kim, J.K. Lee, S.H. Oh, J.K. Kim, J.H. Park, *Nat. Commun.* 5 (**2014**) 1–8.
4. Q. Xu, L. Zhang, B. Cheng, J. Fan, J. Yu, *Chem* 6 (**2020**) 1543–1559.
5. J. Low, J. Yu, M. Jaroniec, S. Wageh, A.A. Al-Ghamdi, *Adv. Mater.* 29 (**2017**) 1601694.
6. P. Vecchi, A. Piccioni, R. Mazzaro, M. Mazzanti, V. Cristino, S. Caramori, L. Pasquini, *Sol. RRL* 6 (**2022**) 2200108.
7. S.Y. Chae, C.S. Lee, H. Jung, O.S. Joo, B.K. Min, J.H. Kim, Y.J. Hwang, *ACS Appl. Mater. Interfaces* 9 (**2017**) 19780–19790.
8. Gamry Instruments, Basics of Electrochemical Impedance Spectroscopy, n.d.
9. A. Lasia, Electrochemical Impedance Spectroscopy and its Applications, Springer, **2014**.
10. T.E. Keyes, R.J. Forster, Spectroelectrochemistry, in: Handb. Electrochem., **2007**: pp. 591–635.
11. C.A. Mesa, E. Pastor, L. Francàs, *Curr. Opin. Electrochem.* 35 (**2022**) 101098.
12. S. Giménez, J. Bisquert, Photoelectrochemical Solar Fuel Production, Springer, **2016**.
13. T. Lopes, L. Andrade, H.A. Ribeiro, A. Mendes, *Int. J. Hydrogen Energy* 35 (**2010**) 11601–11608.
14. J. Liu, W. Chen, Q. Sun, Y. Zhang, X. Li, J. Wang, C. Wang, Y. Yu, L. Wang, X. Yu, *ACS Appl. Energy Mater.* 4 (**2021**) 2864–2872.
15. S.J. Hong, S. Lee, J.S. Jang, J.S. Lee, *Energy Environ. Sci.* 4 (**2011**) 1781–1787.
16. P. Chatchai, S. ya Kishioka, Y. Murakami, A.Y. Nosaka, Y. Nosaka, *Electrochim. Acta* 55 (**2010**) 592–596.
17. S. Ju, H.J. Seok, J. Jun, D. Huh, S. Son, K. Kim, W. Kim, S. Baek, H.K. Kim, H. Lee, *Appl. Catal. B Environ.* 263 (**2020**) 118362.
18. P.M. Rao, L. Cai, C. Liu, I.S. Cho, C.H. Lee, J.M. Weisse, P. Yang, X. Zheng, *Nano Lett.* 14 (**2014**) 1099–1105.
19. X. Shi, I. Herraiz-Cardona, L. Bertoluzzi, P. Lopez-Varo, J. Bisquert, J.H. Park, S. Giménez, *Phys. Chem. Chem. Phys.* 18 (**2016**) 9255–9261.
20. S. Selim, L. Francàs, M. García-Tecedor, S. Corby, C. Blackman, S. Giménez, J.R. Durrant,

A. Kafizas, *Chem. Sci.* 10 (**2019**) 2643–2652.

21. Y. Zhai, Z. Zhu, S. Zhou, C. Zhu, S. Dong, *Nanoscale* 10 (**2018**) 3089–3111.

22. S. Corby, E. Pastor, Y. Dong, X. Zheng, L. Francàs, M. Sachs, S. Selim, A. Kafizas, A.A. Bakulin, J.R. Durrant, *J. Phys. Chem. Lett.* 10 (**2019**) 5395–5401.

23. R. Holze, *J. Solid State Electrochem.* 8 (**2004**) 982–997.

24. C.A. Mesa, L. Francàs, K.R. Yang, P. Garrido-Barros, E. Pastor, Y. Ma, A. Kafizas, T.E. Rosser, M.T. Mayer, E. Reisner, M. Grätzel, V.S. Batista, J.R. Durrant, *Nat. Chem.* 12 (**2020**) 82–89.

25. B. Klahr, T. Hamann, *J. Phys. Chem. C* 118 (**2014**) 10393–10399.

26. Y. Liu, M. Xia, L. Yao, M. Mensi, D. Ren, M. Grätzel, K. Sivula, N. Guijarro, *Adv. Funct. Mater.* 2010081 (**2021**) 1–7.

27. L. Francàs, S. Selim, S. Corby, D. Lee, C.A. Mesa, E. Pastor, K.S. Choi, J.R. Durrant, *Chem. Sci.* 12 (**2021**) 7442–7452.

28. S. Selim, E. Pastor, M. García-tecedor, M.R. Morris, M. Sachs, B. Moss, S. Corby, C.A. Mesa, S. Giménez, A. Kafizas, A.A. Bakulin, J.R. Durrant, *J. Am. Chem. Soc.* 141 (**2019**) 18791–18798.

29. I. Grigioni, L. Ganzer, F. V. A. Camargo, B. Bozzini, G. Cerullo, E. Selli, *ACS Energy Lett.* 4 (**2019**) 2213–2219.

30. E. López-Fraguas, J.M. Sánchez-Pena, R. Vergaz, *IEEE Trans. Instrum. Meas.* 68 (**2019**) 4913–4923.

31. J.E.B. Randles, *Discuss. Faraday Soc.* 1 (**1947**) 11–19.

32. J. Bisquert, G. Garcia-Belmonte, P. Bueno, E. Longo, L.O.S. Bulhões, *J. Electroanal. Chem.* 452 (**1998**) 229–234.

33. A. Hankin, F.E. Bedoya-Lora, J.C. Alexander, A. Regoutz, G.H. Kelsall, *J. Mater. Chem. A* 7 (**2019**) 26162–26176.

34. B. Klahr, S. Giménez, F. Fabregat-Santiago, J. Bisquert, T.W. Hamann, *J. Am. Chem. Soc.* 134 (**2012**) 16693–16700.

35. T. Zhu, M.N. Chong, E.S. Chan, *ChemSusChem* 7 (**2014**) 2974–2997.

36. H. Zheng, J.Z. Ou, M.S. Strano, R.B. Kaner, A. Mitchell, K. Kalantar-Zadeh, *Adv. Funct. Mater.* 21 (**2011**) 2175–2196.

37. J.A. Seabold, K.S. Choi, *Chem. Mater.* 23 (**2011**) 1105–1112.

38. S. Corby, L. Francàs, S. Selim, M. Sachs, C. Blackman, A. Kafizas, J.R. Durrant, *J. Am. Chem. Soc.* 140 (**2018**) 16168–16177.

39. M. Ma, K. Zhang, P. Li, M.S. Jung, M.J. Jeong, J.H. Park, *Angew. Chemie - Int. Ed.* 55 (**2016**)

11819–11823.

40. B. Klahr, S. Giménez, F. Fabregat-Santiago, T. Hamann, J. Bisquert, *J. Am. Chem. Soc.* 134 (**2012**) 4294–4302.

41. D.D. Qin, T. Wang, Y.M. Song, C.L. Tao, *Dalt. Trans.* 43 (**2014**) 7691–7694.

42. L.H. Mascaro, A. Pockett, J.M. Mitchels, L.M. Peter, P.J. Cameron, V. Celorrio, D.J. Fermin, J.S. Sagu, K.G.U. Wijayantha, G. Kociok-Köhn, F. Marken, *J. Solid State Electrochem.* 19 (**2015**) 31–35.

43. S. Wang, P. Chen, Y. Bai, J.H. Yun, G. Liu, L. Wang, *Adv. Mater.* 30 (**2018**) 1–7.

44. A.J.E. Rettie, H.C. Lee, L.G. Marshall, J.F. Lin, C. Capan, J. Lindemuth, J.S. McCloy, J. Zhou, A.J. Bard, C.B. Mullins, *J. Am. Chem. Soc.* 135 (**2013**) 11389–11396.

45. A. Polo, M.V. Dozzi, I. Grigioni, C.R. Lhermitte, N. Plainpan, L. Moretti, G. Cerullo, K. Sivula, E. Selli, *Sol. RRL* 6 (**2022**) 2200349.

46. J. Bisquert, *J. Phys. Chem. B* 106 (**2002**) 325–333.

47. J. Bisquert, G. Garcia-Belmonte, F. Fabregat-Santiago, N.S. Ferriols, P. Bogdanoff, E.C. Pereira, *J. Phys. Chem. B* 104 (**2000**) 2287–2298.

48. M. Sachs, J.S. Park, E. Pastor, A. Kafizas, A.A. Wilson, L. Francàs, S. Gul, M. Ling, C. Blackman, J. Yano, A. Walsh, J.R. Durrant, *Chem. Sci.* 10 (**2019**) 5667–5677.

49. J.A. Seabold, K.S. Choi, *J. Am. Chem. Soc.* 134 (**2012**) 2186–2192.

50. R.R. Rao, S. Corby, A. Bucci, M. García-Tecedor, C.A. Mesa, J. Rossmeisl, S. Giménez, J. Lloret-Fillol, I.E.L. Stephens, J.R. Durrant, *J. Am. Chem. Soc.* 144 (**2022**) 7622–7633.

51. L. Francàs, S. Corby, S. Selim, D. Lee, C.A. Mesa, R. Godin, E. Pastor, I.E.L. Stephens, K.S. Choi, J.R. Durrant, *Nat. Commun.* 10 (**2019**) 1–10.

Chapter 8 - Conclusions and perspectives

The aim of the work presented in this PhD thesis was to further investigate the photoelectrochemical properties of various ternary and binary metal oxides that are studied as promising photoanode materials for the solar assisted water oxidation reaction. The choice of this class of materials is detailed in Chapter 2, that describes the main characteristics of these semiconductors, such as visible light harvesting properties and chemical stability.[1,2] By using different experimental techniques, described in detail in Chapter 3, the properties of the investigated materials have been tested and compared, with the aim of both identifying the materials with optimized photoelectrochemical properties and gaining further insight into the intrinsic features and working mechanisms of these photoelectrodes.

The starting material of my investigation is tungsten trioxide, WO_3, which is one of the most studied photoanode systems, due to its high stability, fast water oxidation kinetics due to a favourable location of its valence band edge, and good electron transport properties that facilitate the spatial separation between photogenerated charge carrier.[3,4] The main drawback of this material is however represented by its band gap value, which is *ca.* 2.7 eV, accounting for an absorption onset located at 460 nm, thus greatly limiting the possibility of this material to harvest the majority of the incident solar radiation, consisting in visible light.

During my studies I thus tried to overcome the main drawback of WO_3 by adopting different strategies, such as the synthesis of copper tungstate, $CuWO_4$, i.e. a ternary oxide directly deriving from tungsten oxide.[5] I then proceeded with the investigation of the coupled system obtained by combining WO_3 with another well-known photoanode material, i.e. bismuth vanadate ($BiVO_4$). $BiVO_4$ exhibits a smaller band gap (ca. 2.4 eV) and it is thus able to sensitise tungsten oxide towards the visible portion of the solar spectrum.[6,7]

Chapter 4 - Ni(II)-doped $CuWO_4$ thin film photoanodes

The results detailed in this Chapter deal with the synthesis and characterization of pure-phase, crystalline $CuWO_4$ thin films doped with different percent amounts of Ni(II) ions. Copper tungstate is indeed characterized by a smaller band gap with respect to WO_3 due to the introduction of copper in the structure, which causes the shift of the valence band of the material towards more negative values, increasing its light harvesting capability. As shown in previous studies, the PEC performances of this material is hampered by the presence of mid gap electronic states that severely affect the charge separation efficiency of this photoanode.[8–10] In order to partially overcome these limitations, we tried to incorporate into the copper tungstate's structure a variable percentage of doping ions. Nickel ions have been chosen due to the similarity between the ionic radii of Cu^{2+} and Ni^{2+}, that could favor the insertion of the doping element into $CuWO_4$ structure. Analytical techniques such as UV-Vis, XRD and EDX allowed us to confirm the incorporation of nickel into copper tungstate's structure with no evidence of secondary phases. The incorporation of Ni^{2+} ions has been proved by either morphological and activity alterations. SEM images showed that upon the introduction of doping ions the surface morphology of the photoelectrodes resulted altered with respect to pure phase copper tungstate samples. The smaller surface particles observed upon doping most likely lead to an increased contact between the material and the electrolyte, favoring the extraction of holes accumulated on the surface of the photoactive material. Photoelectrochemical tests were carried out and evidenced a higher PEC efficiency of the 10%-Ni(II) containing electrode, which shows better performances under both full-lamp and monochromatic irradiation. By testing the materials in the presence of a hole scavenger species, $NaNO_2$, we were able to evidence that the $CuWO_4$-Ni(II) 10% photoanode showed a

50% increase in charge separation in the bulk of the material with respect to pure copper tungstate, whilst showing comparable charge injection properties.

We prepared, for the first time, doped $CuWO_4$ samples that showed enhanced photoelectrochemical properties with respect to pure materials, but the intrinsic limitations of copper tungstate have only been partially overcome: a further study on the enhancement of the charge separation properties of this material is due, other strategies such as the synthesis of multilayer electrodes aiming at maximizing PEC activities can be tackled in the future.

Chapter 5 – Role of nanostructuring on WO_3 and WO_3–$BiVO_4$ photoanodes

This Chapter introduces the subject of the experimental researches that will be discussed also in the following chapters of this thesis, that is, the WO_3–$BiVO_4$ heterojunction. $BiVO_4$ has often been coupled with WO_3 to sensitise it towards visible radiation, and the mismatch between the conduction and valence band edges of these materials should also further favour the separation of photogenerated electrons and holes.[11,12] We concentrated our attention on the study of a peculiar aspect of this system, the morphology of the tungsten oxide underlayer, by investigating its role on the overall performances of the composite material. We therefore prepared WO_3 and WO_3–$BiVO_4$ electrodes of comparable thickness and absorption properties characterized by either a planar or a nanoflake-like morphology, using two different synthetic procedures. By taking into account pure phase WO_3 samples, nanostructuring seems to bring about several drawbacks, such as the attainment of a limit photocurrent at low applied bias, a higher charge transfer resistance and a lower surface capacitance observed through electrochemical impedance measurements. However, upon the deposition of bismuth vanadate, the behaviour of the planar and nanostructure heterojunctions is overturned, and we observe a much higher PEC activity for the WO_3_NF–$BiVO_4$ sample. Indeed, the severe electron-hole recombination path which is active in the WO_3_P–$BiVO_4$ planar electrode is successfully overcome by nanostructuring the tungsten oxide underlayer.

The morphology of the nanostructured sample leads to a better holes and electrons transport properties, contributing to the greatly increased charge separation efficiency detected in this sample as opposed to the planar heterojunction. Moreover, nanostructuring

allows the retaining of the good oxidative power of WO_3 also in the heterojunction, as opposed to the planar composite in which $BiVO_4$ completely covers its underlayer.

The major drawback of nanostructured samples is however their lack of optical transparency, making them not suitable to be employed in a tandem photoelectrochemical cell.[13] The following step was then to study various WO_3–$BiVO_4$ planar electrodes with the aim of identifying the planar heterojunction in which the above mentioned detrimental charge recombination path is mitigated.

Chapter 6 – WO_3–$BiVO_4$ planar heterojunctions

With the aim of studying in depth the working mechanism of the WO_3–$BiVO_4$ heterojunction and to identify the conditions in which the previously observed detrimental recombination path is most active, WO_3, $BiVO_4$ and WO_3–$BiVO_4$ photoanodes displaying various thicknesses have been prepared via spin coating. Theoretically, the working mechanism of this system is represented by a type-II heterojunction, in which the spatial separation of photogenerated electrons and holes is promoted by the energy mismatch between the band edges of the two oxides. However, this heterojunction type could also lead to a loss in oxidation power of photogenerated VB holes and electrostatic repulsion may hamper the separation of the charges.[14,15] By testing our materials under simulated solar irradiation, we observed that the PEC activity is influenced by both the irradiation configuration (back- or front-side illumination) as well as by the relative thickness of the two oxides in the heterojunction. PEC analyses conducted under monochromatic irradiation evidence that the electron-hole recombination path discussed in Chapter 5 is present in all planar heterojunctions when the samples are irradiated in a back-side configuration. However, due to the systematic study of the thickness of the two oxides, we were able to identify the conditions in which this detrimental path is mitigated, that is, when the thickness of both WO_3 and $BiVO_4$ is relatively low (*ca.* 200 nm and 70 nm for the two oxides, respectively), and thus the number of generated carriers available for recombination is lower. On the other hand, we verified that upon front-side illumination, the working mechanism of the type-II heterojunction is brought out, favouring separation. Tests run in the presence of a hole scavenger species demonstrated that the charge separation efficiency in the heterojunction is lower than that recorded with the

pure-phase oxides, while the charge injection efficiency is enhanced upon the combination of tungsten oxide and bismuth vanadate.

With this work we therefore gained further insight into the working mechanism of the WO_3–$BiVO_4$ heterojunction and evidenced that the increased PEC activity generated upon the combination of the two oxides cannot be simply ascribed to the generation of a type-II heterojunction, since a lower charge separation efficiency with respect to single component oxides has been observed for all studied heterojunctions. Instead, other phenomena possibly concerning charge redistribution between the two materials must be taken into account and studied through advanced characterization methods, as it is the case of the experimental work detailed in Chapter 7.

Chapter 7 – Advanced analyses on WO_3–$BiVO_4$ heterojunctions

Frequency-based techniques such as Electrochemical Impedance Spectroscopy have the great potential to acquire information on the charge transfer and charge storage characteristics of an investigated photoelectrode, but the sometimes complex interpretation of the experimental results still prevents it to be a vastly employed, routine characterization technique in the field of photoelectrochemistry. In particular, an extensive impedance study on the WO_3–$BiVO_4$ heterojunction is still lacking. Similar to EIS, also spectroelectrochemistry is a powerful tool to gain insight into the electronic transitions occurring in photocatalysts upon application of an external bias. In this Chapter an extensive study is reported on the single component and composite materials described in Chapter 6. EIS measurements allowed us to calculate the charge transfer resistance and surface capacitance of a series of electrodes, and to study the behaviour of these parameters as a function of the external applied bias, as well as to compare the characteristics of different electrodes. By fitting impedance results of WO_3, $BiVO_4$ and WO_3 200nm–$BiVO_4$ samples with a Randles circuit, we verified that the capacitance of the heterojunction is controlled by the bismuth vanadate overlayer, contrary to previous reports.[16] Moreover, the addition of $BiVO_4$ on planar WO_3 did not cause an increase in the surface charge of the composite. At the same time, heterojunctions possessing a thick tungsten oxide underlayer showed evidence of electron diffusion issues in the bulk of the material; it is the first time that this behaviour is reported for a planar WO_3–$BiVO_4$ heterojunction.

Spectroelectrochemical measurements shed light on the optical transitions occurring in the tested photoanodes upon application of an increasing external bias. The broad absorption feature recorded with WO_3 films (associated to W^{5+} centres[17]) and the positive and negative peaks exhibited by $BiVO_4$ samples in the NIR were altered as the two materials were brought together in the heterojunction. Indeed, energetic redistribution mechanisms may be occurring upon combination of the two oxides; a quantitative confirmation of this hypothesis was provided by stepped potential measurements, that evidence a decrease in the extinction coefficient of the same optical transition in $BiVO_4$ once it is coated upon WO_3. Again, this is the first report of a thorough SEC study of this system and further attention will be dedicated in the future to further characterizing this heterojunction with the above mentioned advanced techniques.

References

1. K. Sivula, *J. Phys. Chem. Lett.* 4 (**2013**) 1624–1633.
2. K. Sivula, R. Van De Krol, *Nat. Rev. Mater.* 1 (**2016**) 15010.
3. C. Janáky, K. Rajeshwar, N.R. De Tacconi, W. Chanmanee, M.N. Huda, *Catal. Today* 199 (**2013**) 53–64.
4. C. Santato, M. Ulmann, J. Àugustynski, *J. Phys. Chem. B* 105 (**2001**) 936–940.
5. H.V. Thang, E. Albanese, G. Pacchioni, *J. Phys. Condens. Matter* 31 (**2019**) 1–10.
6. A. Polo, I. Grigioni, M.V. Dozzi, E. Selli, *Catal. Today* 340 (**2020**) 19–25.
7. I. Grigioni, K.G. Stamplecoskie, E. Selli, P. V. Kamat, *J. Phys. Chem. C* 119 (**2015**) 20792–20800.
8. K.J. Pyper, J.E. Yourey, B.M. Bartlett, *J. Phys. Chem. C* 117 (**2013**) 24726–24732.
9. Y. Gao, T.W. Hamann, *J. Phys. Chem. Lett.* 8 (**2017**) 2700–2704.
10. I. Grigioni, A. Polo, M.V. Dozzi, L. Ganzer, B. Bozzini, G. Cerullo, E. Selli, *J. Phys. Chem. C* 125 (**2021**) 5692–5699.
11. M. García-Tecedor, D. Cardenas-Morcoso, R. Fernández-Climent, S. Giménez, *Adv. Mater. Interfaces* 6 (**2019**) 1–8.
12. Q. Xu, L. Zhang, B. Cheng, J. Fan, J. Yu, *Chem* 6 (**2020**) 1543–1559.
13. M.S. Prévot, K. Sivula, *J. Phys. Chem. C* 117 (**2013**) 17879–17893.
14. J. Low, J. Yu, M. Jaroniec, S. Wageh, A.A. Al-Ghamdi, *Adv. Mater.* 29 (**2017**) 1601694.
15. J. Low, C. Jiang, B. Cheng, S. Wageh, A.A. Al-Ghamdi, J. Yu, *Small Methods* 1 (**2017**) 1–21.
16. X. Shi, I. Herraiz-Cardona, L. Bertoluzzi, P. Lopez-Varo, J. Bisquert, J.H. Park, S. Giménez, *Phys. Chem. Chem. Phys.* 18 (**2016**) 9255–9261.
17. S. Corby, E. Pastor, Y. Dong, X. Zheng, L. Francàs, M. Sachs, S. Selim, A. Kafizas, A.A. Bakulin, J.R. Durrant, *J. Phys. Chem. Lett.* 10 (**2019**) 5395–5401.

List of scientific contributions

Publications

1. "Effective visible light exploitation by copper molybdo-tungstate for enhanced photoelectrochemical water oxidation"
   Polo A., Nomellini C., Grigioni I., Dozzi M. V., Selli E.
   ACS Appl. Energy Mater. **2020**, 3, 7, 6956-6964

2. "Nature of charge carrier recombination in $CuWO_4$ photoanodes for photoelectrochemical water splitting"
   In preparation

3. "WO_3/$BiVO_4$ heterojunction photoanodes: effects of WO_3 nanostructuring on their photoelectrochemical performance"
   In preparation

4. "Ni(II)-doped $CuWO_4$ thin film photoanodes for increased photoelectrochemical performances and charge separation efficiency"
   In preparation

Communications

1. Italian Photochemistry Meeting (Ferrara, 15-17 December 2022)
   "Planar and nanostructured $WO_3/BiVO_4$ heterojunction photoanodes: effects of the morphology on the photoelectrochemical performance"
   Nomellini C., Polo A., Dozzi M.V., Selli E.
   Flash oral communication

2. 9th Forum on New Materials, CIMTEC 2022 (Perugia, 25-29 June 2022)
   "Molybdenum doped $CuWO_4$-based photoanodes for solar energy conversion"
   Dozzi M.V., Polo A., Grigioni I., Nomellini C., Selli E.
   Oral communication

3. Merck Young Chemists' Symposium 2021 (Rimini, 22-24 November 2021)
   "WO_3-$BiVO_4$ photoanodes: influence of the nanostructuring of the WO_3 underlayer"
   Nomellini C., Polo A., Dozzi M.V., Selli E.
   Oral communication

4. Giornate Italiane di Fotochimica (Virtual Conference, 23-24 September 2021)
   "Nanostructured WO_3 photoanodes: effects on the coupled WO_3-$BiVO_4$ system"
   Nomellini C., Polo A., Dozzi M.V., Selli E.
   Flash oral communication

5. XXVII Congresso Nazionale Società Chimica Italiana (Virtual Conference, 14-23 September 2021)
   "WO_3-$BiVO_4$ heterojunction: effects of WO_3 nanostructuring on photoelectrochemical performance"
   Nomellini C., Polo A., Marra G., Dozzi M.V., Selli E.
   Oral communication

6. International Conference on Photochemistry (Virtual Conference, 19-23 July 2021)
   "Molybdenum doped $CuWO_4$-based photoanodes for efficient visible light exploitation"
   Dozzi M.V., Polo A., Nomellini C., Grigioni I., Selli E.
   Oral communication

7. 7th International Conference on Semiconductor Photochemistry (Milano, 11-14 September 2019)
   "Molybdenum doped copper tungstate for extended visible light induced photoelectrochemical water oxidation"
   Polo A., Nomellini C., Grigioni I., Dozzi M. V., Selli E.
   Flash oral communication + poster presentation

8. UK-IT Joint Meeting on Photochemistry 2019 (Lipari, 24-26 June 2019)
   "$CuW_{0.5}Mo_{0.5}O_4$ as efficient visible light harvester for photoelectrochemical water oxidation"
   Polo A., Nomellini C., Grigioni I., Dozzi M. V., Selli E.
   Poster presentation

Research activity abroad

JANUARY 2022 – AUGUST 2022

Institute of Advanced Materials (INAM)

Supervisor: prof. Sixto Giménez

Universitat Jaume I, Castellon de la Plana, Spain

Acknowledgements

My gratitude goes to my supervisor Professor Elena Selli, that has welcomed me in her research group more than five years ago, and has encouraged me to enroll for my PhD, giving me the chance to carry on a challenging scientific research project and experience all sides of a research career.

Heartfelt thanks to my co-supervisor Professor Maria Vittoria Dozzi and to Doctor Annalisa Polo for their constant support throughout my PhD. MaVi, your unceasing presence in the lab and your natural inclination to help others bring an irreplaceable scientific and human contribution to our work and research group. Anna, thank you for always believing in me and for the crucial scientific support you have given me during these years, reinforced by the right amount of honesty in difficult times.

A big thank to all the members, past and present, of the Unimi Photocatalysis Group, for creating in our sunless basement a space full of laughter and comfort.

My PhD would have not been the same without the seven months that I spent in Castellon, under the supervision of Professor Sixto Gimenez. Thank you for your warm welcome, for giving me the opportunity to work in your laboratories and for your scientific guidance. Thanks to Doctor Camilo A. Mesa for your light-spirited support, your enthusiasm and for sharing with me some of your great knowledge in this field.

Words cannot express how grateful I feel for having met all the incredible people that animate the INAM institute. You have showed me what it means to have a family, even when far from home, and this I'll never forget.

Thanks to my family for supporting me through my ups and downs, for their unshakable faith in my abilities and for gracefully guiding me towards the positive side of it all.

Lastly, my gratitude goes to my friends, who have always been by me side during this journey, that at times must have appeared hazy and difficult to read. Thank you for accepting me in my silences as well as in my liveliness.